AN ABSTRACT OF THE THESIS OF

Kevin T. Lewis for the degree of Master of Science in Mechanical Engineering

presented on December 16, 2011.

Title: Investigations into the Effects of a Vibrating Meniscus on the Characteristics of Drop Formation

Abstract approved:

_____

James A. Liburdy

As drop-on-demand (DOD) applications continue to gain ground in desktop inkjet-printing, 3D printing, fluid mixing, and other areas the demand for higher frequency operations are beginning to push against the current physical boundaries in DOD technology. The current research is exploring the possibility of controlling drop volume and velocity at high frequency ranges where meniscus vibrations can occur between drop formations and affect drop formation characteristics.

A periodic voltage is applied to a piezoelectric disk in order to generate pressure fluctuations in a single nozzle droplet generator, causing the fluid meniscus at the nozzle to vibrate. A single stronger pulse is then superimposed over the periodic waveform at different phases in order to drive drop ejection. The characteristics of the resulting drop, specifically the volume and velocity, are experimentally measured

using a high speed camera with precise timing control. The results of these experiments are then compared to a lumped element model (LEM) developed for the droplet generator geometry used. Within the LEM model framework, special attention was given to the definition of a novel method by which one can measure drop volume within an electroacoustic circuit and also allow meniscus dynamics to affect present and future drop formations.

Experimental results indicate a strong dependence of both drop volume and drop velocity on the phase of the vibrating meniscus at the start of drop formation. Positive meniscus displacements and momentums resulted in large drop volumes and velocities while negative displacements could reduce drop volume or altogether eliminate drop formation. Specifically, positive displacements and momentum of a vibrating meniscus could lead to drop volumes approximately 50% larger than the original drop volume without a vibrating meniscus. Meanwhile, negative meniscus displacements and momentums were shown to have the ability to completely prevent drop formation. Additional potential for drop characteristic control with a vibrating meniscus is discussed alongside observations on the stabilizing affect the vibrating meniscus appears to have on drop velocity as a function of time. Also, flow visualization of the drop formation is provided to demonstrate the added affect the meniscus vibrations have on the drop shapes and break-off profiles.

The LEM model presented demonstrates qualitative agreement with the experimental model, but fails to quantitatively predict drop volumes. Sources of error for the LEM model and potential improvements are discussed.

Investigations into the Effects of a Vibrating Meniscus on the Characteristics of Drop Formation

by
Kevin T. Lewis

A THESIS

Submitted to

Oregon State University

in partial fulfillment of
the requirements for the
degree of

Master of Science

Presented December 16, 2011

Commencement June 2012

Master of Science thesis of Kevin T. Lewis presented on December 16, 2011.

APPROVED:

_____

Major Professor, representing Mechanical Engineering

_____

Head of the School of Mechanical, Industrial, and Manufacturing Engineering

_____

Dean of the Graduate School

I understand that my thesis will become part of the permanent collection of Oregon State University libraries. My signature below authorizes release of my thesis to any reader upon request.

_____

Kevin T. Lewis, Author

ACKNOWLEDGEMENTS

First, I would like to thank the Xerox Corporation for the fellowship that funded my way through my graduate program. I would also like to thank Xerox Corporation engineers Dave Tence and Brian Daniels for their knowledgeable advice and aid as I progressed through this project.

I also wish to thank my mentor and advisor, Jim Liburdy, for his consideration of me as a candidate for the Xerox fellowship. I would also like to thank him for all his help, guidance, and knowledge he has shared with me over the years as an undergraduate and graduate student at Oregon State University.

I extend much appreciation to the members of the Oregon State University Mars Rover Electrical Team, 2010-11, for their help with my circuit design. In particular, I would like to thank Tyler Slone for the hours he spent sharing his knowledge of LT Spice and advanced circuit elements with me.

Special thanks to all the graduate students in Mechanical Engineering. Many of you were always willing help me with the problems I would encounter, always willing to bounce ideas off the wall with me. Vishal, your presence in the lab was always welcome and your knowledge of experimental setups was helpful and on hand whenever I needed it, thank you.

Lastly, I would like to thank my wife, Katherine, for her ever present love and support. Without your patience and kindness throughout this project, I never could have finished. Thank you for everything you have done!

TABLE OF CONTENTS

TABLE OF CONTENTS (CONTINUED)

Page

TABLE OF CONTENTS (CONTINUED)

Page

LIST OF FIGURES

LIST OF FIGURES (CONTINUED)

Figure Page

LIST OF FIGURES (CONTINUED)

Figure Page

LIST OF FIGURES (CONTINUED)

Figure Page

LIST OF FIGURES (CONTINUED)

Figure Page

LIST OF TABLES

Table Page

LIST OF APPENDICES

Appendix Page

LIST OF APPENDIX FIGURES

Figure Page

LIST OF APPENDIX TABLES

NOMENCLATURE

f	=	Frequency
h	=	Height of Meniscus
I	=	Current
L_{max}	=	Maximum acoustic domain length scale
λ	=	Wavelength
P	=	Pressure
ρ	=	Density
St	=	Stokes Number; $St = \frac{\omega a^2}{\nu}$
t	=	Time
T	=	Vibration cycle period
θ	=	Phase
ν	=	Kinematic Viscosity
V_d	=	Drop Volume
v	=	Velocity
$\bar{v}$	=	Overall Case-averaged Velocity
V	=	Voltage
$\dot{V}$	=	Volume Flow Rate
Z	=	Impedence

Subscripts:

avg	=	Average of data, often referring to the 'instantaneous' average of velocity
$trial$	=	Trial-Averaged Data; all the data from a single case is averaged into one reported value.
adj	=	Adjusted
a	=	Acoustic
d	=	Drop
m	=	Meniscus
$trig$	=	Trigger

Investigations into the Effects of a Vibrating Meniscus on the Characteristics of Drop Formation

1. INTRODUCTION

Droplet formation has been a research interest for many years. Starting in the 1800's, where liquid jet break-up was the primary form of droplet formation, the scientific community has sought to better understand the fluid mechanics behind droplet formation. With the advent of Drop-on-Demand (DOD) droplet formation in the 1970's, research in the area was rekindled. Seeking to better understand both jet breakup and DOD droplet formation, the number of publications in this area has increased drastically in recent years.

DOD droplet formation differs from liquid jet droplet formation in its ability to theoretically produce single or multiple droplets at specified times. There are a few different methods of DOD droplet formation, all of which require the generation of a pressure pulse which travels to a nozzle and ejects a droplet. The two primary forms are a thermally-driven method and a piezoelectrically-driven method. The more commonly used method is the piezoelectrically-driven pressure pulse which is used in many areas in industry ranging from inkjet printing and pharmaceuticals to printing of electronic circuits and 3D rapid prototyping. The wide range of applications for DOD drop formation gives rise to the demand for a well established understanding of how the process works. One of the larger areas of interest has been in trying to properly model DOD drop formation.

The instinctual action would be to directly solve the Navier-Stokes equations for a droplet emerging from a nozzle. However, this process proves to be highly difficult, as is the case in almost any real-world scenario when trying to solve the Navier-Stokes equations. In the past, the ability to gather enough computational power to even attempt a direct solution to the Navier-Stokes solutions (DNS) was all but impossible. Although the computational power exists today to accomplish this, the computational time required is still too long to make DNS a viable method of predicting DOD droplet formation in all but the simplest cases. In particular, when one solely desires the droplet velocity, volume and break-off time, a DNS solution method becomes overly ambitious and costly.

In the past, a number of alternative methods for predicting droplet characteristics, such as the velocity or volume of a droplet, have arisen. Among the leading methods are one dimensional approximations to the Navier-Stokes equations and Lumped Element Models (LEMs). The one dimensional approximation to the Navier-Stokes equations is the natural result from following a classical approach. One identifies the key variables of interest in the Navier-Stokes equation through an order of magnitude analysis, considers the remaining terms to be negligible, and solves the simplified governing equation. The current project, however, focuses on using and exploring the latter of the two leading methods, LEMs. An LEM assumes an analogous relationship between fluid acoustics and electrical circuits. By making this simplifying assumption, one is able to transform each component of a fluid system, in this case the DOD droplet generator, into an equivalent electrical component. The

result is a one-dimensional approximation of the fluid system as an electrical circuit. Solving the system of ordinary differential equations one can construct for the circuit will yield voltages and currents, which can be transformed back into pressures and volume flow rates, respectively. In short, an LEM may simplify the problem such that droplet characteristics can be determined computationally for a number of different scenarios with relative ease and over shorter times.

The other apparent goal in the body of the literature has been to find methods of achieving more predictability and reliability in droplet size, volume and speed. Each droplet characteristic is important in producing acceptable results at the end of the droplet formation process, whether it is the formation of a spot of ink on a piece of paper or the application of the correct volume of fluid in a cooling application. In addition, many have sought to control the existence of satellite droplets, or at least control their behavior, as well as meniscus dynamics and maximum drop production frequencies. All these factors lead to better control and efficiency in DOD systems. Being able to predict these characteristics, and identify control potential, is the primary goal of this research.

The literature is well versed in mathematical, computational, and experimental knowledge on the formation of single droplets with desired size, volume, and speed. However, DOD droplet formation is not well understood when droplet production reaches very high frequencies. At higher frequencies, previous drop formations start to have an effect on the formation of the following droplet. In low frequency droplet formation, the meniscus left behind in the nozzle has enough time for the fluid to

damp out residual vibrations or motion that may interact with the next drop. As the frequency of drop formation increases, the meniscus has less time for this damping to occur. The end result is a meniscus that may have a number of different vibration modes which can impact the following drop's formation process. The result is that higher frequency applications make it more difficult to create repeatable, predictable droplets with desired droplet properties. The current project simulates these higher frequency dynamics by producing a pre-vibrating meniscus and observing and characterizing how the vibrating meniscus affects droplet formation at different phases within the vibrating meniscus's wave cycle.

2. LITERATURE REVIEW

Some of the earliest research on drop formation was done by Rayleigh with his publication of "On the Instability of Jets" (Strutt and Rayleigh 1878). His research focused on drop formation as it relates to jetting. At his time, earlier experiments by Savart (1833) and Magnus (1855) had demonstrated that drop break-up of jets could be controlled by supplying a dominating vibration mode to the jet at the source. Rayleigh took this a step further in 1878 and 1879 when he studied the linear instability of an infinitely long liquid jet and the subsequent drop formation from the break-up of the liquid column. From his work, he was able to establish the Rayleigh instability, which allows one to determine which surface profile instability will grow the fastest and lead to droplet breakup. Whichever surface instability grows fastest will determine the distance at which the liquid column breaks into parent and satellite droplets, the size of parent drops, and the spacing of the parent drops. His research established some of the first investigations into many of the important characteristics that are still being investigated today with respect to drop formation. These topics include the repeatability of main drops, the main drop volumes and velocities, the formation of satellite drops, and the merging direction of satellite drops. Due to the thoroughness of his research, droplet formation went largely uninvestigated until around 1960 when the technological innovation of drop-on-demand (DOD) ink-jetting was being explored for its capabilities in application to the desktop printer market (Christensen, 1997). There still has been research in this area of drop formation with the resurgence of interests in the area (Bogy, 1979; Chaudhary and Redekopp, 1980;

Chaudhary and Maxworthy, 1980; Rutland and Jameson, 1971), but these investigations have been studying what is called continuous inkjet drop formation. The current study, in contrast, is focused on researching DOD drop formation and is building primarily on the research done with respect to that field of study instead.

2.1. DROP-ON-DEMAND (DOD)

The DOD method of drop formation was invented to increase the control over drop formation timing (Sangplung and Liburdy, 2009) while maintaining control over the drop's volume and velocity. This method of drop formation is found in many applications, from desktop ink-jet printing or DNA microarray systems (Dong et al., 2006) to the mixing of liquids (Daniels & Liburdy, 2009) or dispensing solder balls for circuit boards. In contrast to the drop formation from a liquid jet, the drops formed in DOD formation are formed on demand with some form of local pressure pulse. However, the process by which drops are formed can vary widely, but all the processes fall into one of two main categories: thermal DOD (Burr et al., 1996) and piezoelectric DOD (Shield et al., 1986; Yang and Liburdy, 2004; Yang and Liburdy, 2007). Both forms of DOD use pressure pulses to generate the necessary force to eject a drop from a nozzle, but it is their source for that pressure pulse that differs. The current study focuses on piezoelectrically driven DOD drop formation.

2.1.1. THERMAL DOD

Thermal DOD is a method of drop formation by which the drop is ejected from the nozzle using the pressure generated from vaporizing a small amount of the ink within the ink cartridge. Therefore, it is also sometimes referred to as a phase change

driven pressure pulse (Berger et al., 1997). A heater inside the droplet generator is powered by a pulse of current which results in a pulse of heat generation. The heat is transferred into the ink and causes a local vaporization, or phase change, of the ink. The resulting pressure pulse creates a drop at the nozzle (Yang and Tsai, 2006).

2.1.2. PIEZOELECTRIC DOD

Piezoelectric driven DOD technology uses the force versus voltage principals of piezoelectric materials to generate the necessary pressure pulse for drop generation. Piezoelectric materials are crystals that will output an electric potential, or voltage, when they are strained or deformed. Since a force on a solid will result in some amount of strain, piezoelectric materials will create electric potentials when a force or pressure is applied to them. The same process can work in reverse, i.e. applying an electric potential to a piezoelectric material will result in the crystal expanding or exerting a force on its surroundings. In the absence of anything to force against, the piezoelectric crystals will deform upon the application of a voltage. The physical deformation or force over an area from the piezoelectric material is used as the pressure source needed to eject drops from a droplet generator.

Both piezoelectric DOD and thermal DOD drop generators come in many different shapes and sizes (Burr et al., 1996). Each shape and size of drop generator has its own pros and cons, but the principals of investigation for each type, and the characteristics which are being measured or controlled, are largely the same from case to case. In seeking to better understand the characteristics of drop formation, and to understand what factors may affect the drop formation process, a number of analytical

and experimental papers have been published on the topic. Many of the analytical models developed for predicting drop formation are also validated experimentally. For the most part, papers investigating the analytical aspect of the drop formation have sought to describe a mathematical model which can account for the behavior of the drop after it has started forming (e.g. Eggers and Dupont, 2002). Papers investigating the experimental aspects of the drop formation are generally made to validate an analytical model developed for determining drop formation characteristics (e.g. Wilkes et al., 1999) or to demonstrate how particular drop generators or pressure waveforms can affect the characteristics of the drop formation (e.g. Groot Wassink et al, 2006).

2.2. CHARACTERISTICS AND TERMINOLOGY

Some descriptions on the meaning of certain terminology may be helpful before continuing with further explanation of drop formation theory and experiments. The primary characteristics of interest when investigating drop formation is the volume and velocity of drops. These two characteristics define in a large degree the repeatability of drop formation as it relates to any specific process in which drop formation may be used, such as printing or fluid mixing. To measure these characteristics in a non-dimensional manner, the drop velocities and volumes are usually non-dimensionalized by the capillary scales of the drop generator and working fluid. The capillary scales are defined in the nomenclature.

Another common characteristic of interest is the break-off of the drop. This instant in time is very difficult to characterize or capture in both experimental and

analytical investigations because it represents a mathematical and experimental singularity in the drop formation process (Eggers, 1995). As the drop is nearing break-off, the thread of working fluid attaching it to the meniscus gets infinitesimally small, but still exists until some unknown point. A lot of research has been focused around the problem of finding out how to predict the separation accurately (Cohen et al., 1999).

The meniscus, when spoken about with respect to drop formation, is the fluid base to any drop formation process that remains attached to the nozzle. The meniscus of one drop formation therefore becomes the leading edge of the next drop formation cycle. At low enough frequencies of operation the meniscus will have enough time to come to rest before the next drop formation begins. Conversely, the higher the frequency of drop formation, the more likely it is that a meniscus will not have come to rest before the formation of the next drop. This can have an effect on the drop characteristics. More recently, this interaction has become a topic of interest as printers and other DOD devices have reached higher frequencies of operation (Berger et al. 1997; Burr et al. 1996).

When discussing the physical parts of a drop generator, there are a few key components that appear to be common from one design to the next. There is usually a refill port or channel through which the ink from the last drop formation can be replaced. DOD drop formation operates on the principals of pressure pulses, and therefore it is inefficient and difficult to apply a pressure pulse to the entire supply of ink for a drop generator in order to produce one drop. In most cases, there exists more

than one nozzle through which drops are ejected (Burr et al., 1996), which introduces additional complications if one were to supply a pressure pulse to the reserve fluid as a whole. Using a refill port focuses the pressure pulse in a localized area away from the bulk of the fluid volume. After the drop is ejected, the fluid volume can be recovered through the refill port. The refill port usually feeds into a local plenum, a region for storing a smaller amount of the total fluid. The pressure pulse generally originates from this location. The pressure pulse then travels through the plenum and to the nozzle. The nozzle is the final step to the drop generator. The pressure builds on the back side of the nozzle and force fluid to push out of the nozzle. When there is enough pressure and volume flow rate out of the nozzle, a drop will be ejected. If there is not enough pressure, the forming drop will generally remain attached and flow back into the drop generator due to surface tension forces that pull it back into the nozzle.

2.3. ANALYTICAL EXPLORATIONS OF DOD DROP FORMATION

The literature has demonstrated that one can create a mathematical model from a one-dimensional approximation of the Navier-Stokes equation that represents the nature of the singularity at droplet pinch-off with near perfect accuracy (Eggers, 1995). Eggers sought to use a one-dimensional approximation to the Navier-Stokes equations because it is much less computationally intensive to solve than using the full set of three-dimensional radial coordinate system Navier-Stokes equations. His work on transforming the three-dimensional equations into simplified one-dimensional equations is quite extensive (e.g. Eggers and Dupont 1994; Eggers, 1995; Eggers,

1997; Brenner et al., 1997; Eggers, 2000) and has come to represent a benchmark for the accuracy of a drop formation model (Yang and Liburdy, 2004; Wilkes et al, 1999; Chen et al, 2002). Wilkes et al (1999) followed suit to compare Eggers' results to a full solution of the three-dimensional Navier-Stokes equations solved with a computational fluid dynamics code and adapted meshing that was intended to analyze the dynamics at finite Reynolds numbers (i.e. non-inviscid flow). During experiments, Chen et al (2002) were able to visually capture, and therefore validate, the overturned profile near pinch-off that was first predicted by the Eggers and Dupont mathematical model for pinch off (1994).

Earlier works include other one-dimensional investigations into drop-on-demand jets such as the work done by Roy and Adams (1985). In the research by Roy and Adams (1985), they demonstrated the importance of kinetic energy of the drop and surface energy on the drops characteristics. They also showed that the drop formation break-off time was relatively non-responsive to changes in input conditions, but that the drop velocity was nearly linearly dependent on driving amplitude. Another early work on one-dimensional modeling of drop formation is the work by Shield et al (1986). In their paper, Shield et al present the numerical simulation of capillary jets using two different methods to determine the effect of certain simplifications to the equations. The conclusion was that the omission of radial inertia has a greater effect on the drop profile at higher Weber numbers than at lower Weber numbers. Works of this nature, along with jet instability research (e.g. Chaudhary and Maxworthy,1980), would be the foundation upon which Eggers (1995) was finally

able to establish a one-dimensional model that would predict drop formation up to and after pinch-off.

Building upon the framework of a one-dimensional approximation to the Navier-Stokes equations are many other studies. One such study expanded upon the research of Eggers and Dupont to determine similarity solutions for capillary pinch-off of drops of one viscosity into a different viscosity surrounding fluid (Zhang and Lister, 1999). In their research, they managed to demonstrate that the self-similar structure associated with capillary pinch-off is preserved despite the asymptotically large advection induced length scales that are both much a larger than the local length scale of the necking region and much smaller than the macroscopic length scales. Zhang (1999) went in a similar direction, but was seeking to determine the importance of the effects on drop characteristics of a viscous ambient fluid. Unique to this research was the VOF/CSF numerical algorithm used which allowed for calculations to continuously pass through the pinch-off point during drop formation without numerical modifications. The model was verified against experimental measurements of the same conditions and showed good agreement. The research concluded in showing that dynamic effects of an ambient fluid affect the drop formation.

Yang and Liburdy (2004) followed suit with a similar one-dimensional approximation to the Navier-Stokes equations proposed by Eggers, but modified the boundary conditions of the equation to account for a vibrating nozzle plate from which the fluid would be ejected. Yang and Liburdy verified their model against the results presented by Eggers and Dupont (1994) and to the theory presented by Chen et al

(2002). The new model showed good agreement with both the previous models, which had both been verified against experimental results. As such, the model by Yang and Liburdy (2004) was then used to explore how a vibrating micro-nozzle affected the drop formation. Their conclusions were that the nozzle vibrations cause the primary drop velocity to increase significantly and that the break-off time and volume were weakly affected. Their study also indicated that satellite droplet velocity was dependent on the break-off phase relative to the nozzle vibration cycle.

Yang and Tsai (2006) chose to go in a different direction and instead modeled the drop formation with another computational three dimensional fluid dynamics solver. The research performed here differed from that of Wilkes et al (1999) in that the model was not developed with the intention to compare the three dimensional solution to the past theoretical derivations in the body of literature. Instead, it was designed with the purpose of exploring the practicability of a new proposed microdroplet generator. As such, the study was designed with a fixed mesh, of defined sizing, that filled the entire domain of the proposed microdroplet generator. To validate the model, the study compared the predictions to the experiments by Shields et al (1987) and showed good agreement. External to this study, their results may indicate that commercially available CFD codes could accurately predict drop formation and travel if the correct aspects are taken into consideration.

Three dimensional fluid dynamics solutions, and even one-dimensional approximations to the full Navier-Stokes equations, can be a rigorous solution technique and can requires a lot of computational power. In addition, any changes to

the inlet conditions for the drop production necessitate a mathematical redetermination of how the inlet should be represented in a model similar to the one presented by Eggers and Dupont. Take for example the model mentioned earlier that was developed by Yang and Liburdy (2004). Also, Eggers' model assumes that the drop is being formed from a quiescent, irrotational, and inviscid flow condition. As a result, there have been additional efforts in the realm of drop modeling that seek to predict the drop formation characteristics with simpler calculation techniques.

There are two main drawbacks to the solution method presented by Eggers and Dupont. The first is that the equations assume irrotational and inviscid flow. However, future research demonstrated that the equations were still relatively applicable even with many different viscosities. The remaining drawback is that it does not have a variable inlet condition. The result is that the model is unable to model the nozzle, plenum, and refill port actions at the same time; it is restricted solely to modeling the drop formation characteristics. This makes it an impractical solution technique when the application is to design a new drop generator. This becomes a problem for a lot of DOD applications because the model is unable to fully define the system from which the drop will be formed. In addition, the mathematical model is unable to account for the behavior of the meniscus after drop break-off as it may affect the following drop formation. In the one-dimensional approximation solution technique, two sets of equations for different regions in time are defined: one set for describing the drop formation behavior leading to break-off and one set for describing the drop characteristics and behavior after break-off. In the model, the equations for

describing the drop formation are accurate up to break-off but have not been validated for all the times post break-off. Therefore one cannot rely on the model from Eggers and Dupont (1994) to define the effects that the retracting meniscus will have on the rest of the system.

In order to model the full system of the drop generator and the drop formation process, a number of methods have been pursued. As mentioned earlier with the work by Wilkes et al (1999) and Yang and Tsai (2006), there have been numerical simulations that use the full set of three-dimensional Navier-Stokes equations to model the drop formation. However, these model methods are more computationally intense than the model presented by Eggers and Dupont (1994) and only add additional complexity if they attempt to model the interior of the drop generators. Other models try to do the same thing but at a lower cost, with more flexibility in the solution method, and with a greater focus on overall drop characteristics. These types of models have departed from defining the exact physical shape of the drop during the drop formation process. Whereas Eggers and Dupont (1994) were interested in better defining the physics and mathematics behind drop break-off, the newer and simpler techniques are aiming to understand the effect of drop generator design and operation on the bulk drop characteristics such as volume and velocity. These two characteristics, along with satellite drop volume and velocity, are more important to the performance of the end products than the shape of the drop at break-off for the applications that DOD formation is used in.

More recently, a notably simpler and more efficient method of analytically solving the drop ejection problem has been the Lumped-Element Modeling (LEM) method. The convenience of using the LEM method is that the model uses the principals of electroacoustics to represent the entire fluid system as a simplified electrical circuit (Merhaut 1981). The LEM method essentially reduces the full set of Navier-Stokes equations, which are partial differential equations in three directions, into simplified representations for each 'element' of the fluid system. The LEM method uses electrical elements to represent analogous acoustic pressure losses in an fluid acoustic system. Resistors, capacitors and inductors each represent acoustic resistances, compliances, and masses, respectively. An acoustic resistance is pressure loss due to viscous losses in the fluid. The acoustic compliance is the measure of the compressibility of a the fluid in a finite volume. And acoustic mass is a representation of the inertia of the volume of fluid moving through a region in the system. By following the guidelines for defining elements in the LEM method (Merhaut, 1981), most complicated geometry's one might find in a droplet generator can be simplified to a model of an analog electrical circuit. In essence, using the LEM method allows one to get away from having to solve the Navier-Stokes equations across the entire domain on some predefined computational mesh. Instead, one is able to solve for the entire systems' behavior with a single matrix that represents the acoustic circuit and its corresponding pressures and volume flow rates. Add to this the required time-stepping of the solution needed to observe the non-steady behavior, and the LEM

method captures all the same parameters that a more computationally intensive model would capture without needing nearly as much power.

Yang and Liburdy (2007), Berger et al (1997), and Burr et al (1996) are among a few of the many researchers that have chosen the LEM method as a way to model their droplet generator and drop generation calculations. Yang and Liburdy (2007) sought to determine the effects of a driving waveform and frequency on the droplet formation process. The LEM method developed in their research allowed them to demonstrate that higher frequency drop formation results in meniscus interactions with subsequent drop formations. Berger et al (1997) and Burr et al (1996) demonstrated the capabilities of the LEM method to model complex arrays of nozzles and fluid supply refill ports. While the models developed have been able to show successful measurement of drop ejection, they have not been able to demonstrate a method by which the LEM method can model the drop formation process without referring to an outside calculation. From what can be gathered in the literature, the models are not solved fully as a network of electrical elements but are still solved numerically via research based code generation.

The LEM method also has some drawbacks. As with most models, the LEM method has a restriction of its applicability to the geometry and other constraints that are actively being modeled. Also, any acoustic wavelength within the system domain must be much greater than the characteristic length of the physical system. Finally, the LEM method has no defined way of modeling the drop ejection. On the other hand, the model should be able to provide a theoretical definition of the vibrating

meniscus response to high frequency pressure oscillations up to and including the vibration modes observed by Daniels and Liburdy (2004). However, in order to do so the model requires an infinite series of circuit elements that must be truncated (Merhaut, 1981). While a truncated infinite series of elements would tend to counteract the simplicity of the calculations for this technique, there is no purely theoretical model that can predict the same vibration modes as observed in Daniels and Liburdy (2004). Daniels and Liburdy (2004) were able to demonstrate a theoretical model which included an adjustment constant, that matches their experimental results. A pursuit in modeling this same process in an LEM circuit may be able to provide insight as to what determines the value of that constant. A more detailed description of how the LEM method was used in this study can be found in Chapter 0.

2.4. ADDITIONAL MODELS AND EXPERIMENTS ON DROPS

Often times in the literature, a new model is compared to the experimental results for the same body research or from an earlier body work. An example of one such paper by Sangplung and Liburdy (2009) explores the effect on droplet formation of a flexible nozzle plate. This paper compares experimental measurements to a mathematical model developed to incorporate a flexible nozzle as a boundary condition into the Navier-Stokes equations. The plate deflection was based on the dynamics of nonlinear large deflection plate theory (Sangplung and Liburdy, 2009). Their results indicated good agreement between the computational model and their experimental results. Further investigation with the model into the affects of nozzle

plate flexibility and fluid surface tension demonstrated that drop formation could be prevented for the right combination of very large surface tensions and very flexible nozzle plates. Also, they demonstrated that the pressure at the nozzle exit was the dominant parameter in determining drop characteristics such as volume and velocity. They concluded that further studies with additional driving waveforms and generator geometries would be necessary in order to better understand the design capabilities of drop generators (Sangplung and Liburdy, 2009).

A study by Zhang et al (1995) explored the dynamics of drop formation from a purely experimental standpoint. The study explored the time evolution of drop formation from a nozzle with a very low constant flow rate. The goal of the study was to determine what effects, if any, variations of the physical and geometric parameters had on the universal features of drop formation. The conclusions from the study indicated a strong dependence of the thread length before break-up on the liquid viscosity, liquid flow rate, and the outer radius of the tube (Zhang et al 1995). The study also provides a large database of data to which future analytic models can be compared for validation purposes.

Another experimental study has demonstrated the ability to significantly reduce drop sizes without having to reduce nozzle size (Chen and Basaran, 2001). In the study, the authors demonstrate that by maintaining strict control over the drop formation process via the capillary, viscous, and inertial time scales they can produce a drop with a radius down to an order of magnitude smaller than the nozzle radius (Chen and Basaran, 2001). Experimentally, the discovery was made by observing that

a smaller radius 'tongue' sticks out ahead of the drop formation process during drop formation. By generating a strong enough negative pressure pulse within the drop generator at the maximum displacement of this 'tongue', the authors have been able to demonstrate that the 'tongue' itself becomes the drop while the rest of the meniscus retracts into the nozzle. Theoretically, this process was explained via the control of the relative time scales of the problem. Through their explanation, they were able to demonstrate why this process could not be done with water but how it is possible with water-glycerol mixtures (Chen and Basaran, 2001).

An experimental study by de Jong et al (2006) demonstrated one of the major difficulties that can arise in DOD formation, air entrapment. The principal behind the issue is that most piezoelectrically driven drop formations are triggered by a pulse with a rising and falling voltage. The pulse will usually results in a positive pressure pulse followed by a negative pressure pulse. The positive pressure pulse beings the formation of the drop and the negative pressure pulse pulls back the meniscus and allows for the drop to detach from the system. The negative pressure pulse generally leads the retraction of the meniscus into the nozzle as well. Most of the time, this is not an issue as the wetted region of the nozzle maintains contact with the nozzle edge and the fluid returns to equilibrium at the nozzle exit. However, this is not always the case and sometimes a small bubble of air will become trapped inside the nozzle. As a result of this, the bubble acts as an energy damper for the pressure pulse inside the fluid chamber and nozzle which acts to dampen or completely stop the ability for drops to form. This study found that two primary mechanisms are the cause for such

air entrapment (de Jong et al, 2006). First, a distorted droplet formation caused by small particles can induce air entrapment. And second, an accumulation of ink/working fluid on the nozzle plate will favor void formation once the meniscus is pulled back (de Jong et al, 2006).

A study by Chen et al (1998) sought to investigate the pressure rise in the droplet generator and nozzle as a function of time in a piezo-driven printhead. The study was mostly numerically solved with a small amount of experimental data collected to validate the theoretical predictions. The numerical model solved the one-dimensional wave equation to obtain the transient pressure and velocity variations in the flow channel of the printhead (Chen et al, 1998). The inexpensive experimental setup recorded the drop mass and velocity for comparative purposes. When compared to the experimental data, the wave equation numerical solution showed good agreement but tended to slightly over predict the experimental droplet mass. Also, the study indicated that the drop mass increased as the amplitude of the driving voltage into the piezoelectric printhead increased (Chen et al, 1998). This result can provide a relatively simple check for most predictive models; a correct predictive model must at least demonstrate that increasing the operating voltage will increase the predicted droplet volume.

Of particular interest to the current research is a study by Gallas et al (2003) in which the applicability of the LEM method was explored as it relates to a piezoelectric-driven synthetic jet. In this study, Gallas et al (2003) propose an LEM model that predicts the jet created from a piezoelectric-driven actuator and compares it

to experimental results. The model developed by Gallas et al (2003) also takes into account modifications to the normal LEM parameters that is based on the change to the velocity profile due to fluid oscillations. This same method of adjusting the standard LEM parameters is also observed in the work done by Yang and Liburdy (2007). Of particular interest to this study is the use of LEM method to model the piezoelectric driver in addition to the acoustic domain. By using the same theory of electroacoustics as is used to determine the rest of the LEM model elements, Gallas et al (2003) represented the piezoelectric driver in the acoustic domain as a set of capacitors and a transformer. Although including this representation of the piezoelectric drive is outside the scope of this project, it serves as topic of interest that may improve the model in the future.

3. ANALYTICAL MODEL

This chapter outlines the development of an analytical model that can predict droplet formation in the presence of a vibrating meniscus. A common form of predicting droplet formation has been to use a lumped element model (LEM), also known as a lumped parameter model. Most fluid flows are extremely complicated and difficult to model analytically. Even the most basic of flows, such as Poiseuille flow in a duct, that is non-circular in shape, may require a great deal of computational power to solve if one uses the full Navier-Stokes equations as the basis for resolving the flow. However, as is the case with Poiseuille flow in a circular duct, the full Navier-Stokes equations can sometimes be simplified to make the solution process easier.

However, even a one-dimensional approximation to the Navier-Stokes equations can start to become computationally intensive as one constructs more complicated geometries (Shah and London, 1978). In addition, there is a large time investment needed to create a CFD code, even in one-dimension. Although the investment often results in a good predictive model, the code is usually case specific and cannot be used with new or altered geometry. In order to skip the time investment, one may use a pre-coded CFD package, but these usually have a high cost and often have extra features that would not be needed in a simplified laminar flow model. While reviewing the literature to find the best model for a droplet generator, the LEM method emerged as a computationally cheap, fast, and efficient way to model simple fluidic systems (Yang and Liburdy, 2007; Burr et al, 1996; Brenner et al, 1997). Therefore, the LEM method was chosen in order to simplify the modeling of

drop generation. An LEM model applies the theories of electroacoustics to a fluidic system.

Electroacoustics is a field of study that seeks to redefine physical systems (e.g. mass-spring-damper systems often seen in controls theory or fluidic systems on the scale of a droplet generator) as electrical systems. The incentive for this transformation is to take advantage of the extensive knowledge that exists on solving electrical circuits and apply it to solving a fluidic systems. Most electrical circuits can be solved as a system of differential equations with specified parameters as opposed to the more complicated partial differential equations one would encounter when solving the Navier-Stokes equations. It also provides an illustrative diagram which can increase an individual's understanding of how each element in a particular system affects the whole. In general, an electroacoustic LEM model defines each section or component of a physical system as an analogous and equivalent electroacoustic component. These parametric components, or elements, are assembled into an electrical circuit that reflects the physical system. The elements representing each part of the physical system can be modeled in a number of complex ways. The LEM method, by the nature of its lumped parameters, takes advantage of the simplest form of electroacoustics theory, i.e. the starting point from which more complex electroacoustic theory is derived (Merhaut, 1981).

3.1. THEORY

The theory of electroacoustics starts with an analogous description of an acoustic domain problem as an electrical domain problem. Before generating the

analogous electrical elements that can represent the acoustic domain, a fundamental physical relationship must exist in order for the models' analogy to be valid.

3.1.1. FUNDAMENTAL RELATIONSHIP

Any acoustic problem must satisfy the underlying assumptions behind electroacoustic theory before the LEM method can be used. In assuming that a fluidic system can be modeled as an electrical system, one assumes that the transfer of information throughout the domain is as instantaneous as one would see in an electrical circuit. By this, it is meant that acoustic (i.e. pressure) waves are not transferred through the medium at a time lag. Note that there may be a time lag resulting from the pressure pulse traveling through individual elements in an LEM model, but this does not violate this assumption. The purpose of this assumption is to allow one to use wires, which ideally transfer circuit information instantaneously from one element to the next, to model connections between acoustic elements of a fluidic system. Physically, this assumption translates into a dimensional constraint on the size of the fluidic system one can model. If the physical constraint required by this assumption is met, then the acoustic waves can be treated like electrical waves observed in Resistor-Inductor-Capacitor (RLC) circuits, and the physical parameters and properties of the problem can be combined to form the resistors, inductors, and capacitors of an RLC circuit.

Given that acoustic and pressure waves travel through a medium at the speed of sound, the pressure at any specific point in the medium at an instant in time depends

on the phase of the sound wave passing through that point. Recall the definition of a sound wave from fundamental physics:

$$v = \lambda f \tag{3.1}$$

where v is the velocity of a wave, λ is the wavelength of a wave and f is the frequency of the wave. This equation indicates that for a given medium, an acoustic wave's wavelength will depend on the acoustic wave's frequency. The lower the frequency, the longer the wavelength.

For any continuous wave through a medium, a point along that wave will have nearly the same magnitude as the next point along that wave if the displacement between the two points is finitely small enough. And as long as the bulk fluid speed is not nearing mach speeds, the acoustic waves will be continuous. A shock wave, for example, would violate the continuity of the sound wave due to the discontinuity in pressure information transfer at the shockwave boundary. Assuming the acoustic domain is small enough, this concept can be thought of from either a spatial domain or a time domain point of view. In the time it takes for an acoustic wave to travel the full span of the acoustic domain, the time domain point of view on this concept would dictate that the pressure at a chosen point will have a negligible change from start to finish. From a spatial point of view, this same concept dictates that, for any given moment in time, the pressure difference from one side of the acoustic domain to the other should be negligible if fluid viscous, compliant, and inertial pressure losses are ignored. The spatial point of view provides an easier way to think of this concept: the acoustic pressure between two points in a given space will be the same, assuming that

the given space is small enough. This is the fundamental assumption used for LEM modeling. For there to be no change in acoustic pressure across the domain of a physical system, the size of the physical system must therefore be small enough such that the pressure through the entire system is uniform at all operating frequencies when the fluid viscous, inertial and compliant pressure losses are neglected. Mathematically, this can be expressed as:

$$L_{max} \ll \lambda \tag{3.2}$$

where L_{max} is the maximum length scale of the physical system.

The droplet generator used in the current study has an L_{max} of less than 20 mm. The working fluid used in the experiments (see Chapter 4) has a speed of sound equivalent to water, approximately 1500 m/s. Assuming a maximum operating frequency of 1000 Hz, the wavelength of the sound wave is λ=1.5 m. This indicates that L_{max} is about 75 times smaller than the wavelength of sound in the medium for frequencies 1000 Hz or lower. Therefore, an LEM model is applicable to the current research for frequencies ranging as high as 1000 Hz. The LEM model may also be operable to frequencies slightly higher than 1000 Hz. However, one must not extend to too high a frequency of operation when using the LEM model because it may begin to encroach upon the region where L_{max} is no longer much less than the wavelength of the acoustic waves in the medium.

3.1.2. PARAMETRIZING THE ELEMENTS

Ensuring that experiments are at low enough frequencies to satisfy the underlying assumption, the LEM method can be used to model the fluidic system as an

equivalent electrical circuit. Most of the components in the droplet generator's fluidic domain are classified so they can be described by either an acoustic resistance, an acoustic mass, an acoustic compliance, or some combination of the three. Some of the more complex acoustic elements, such as the piezoelectric disk bender or the drop formation, need different representative elements.

The droplet generator was broken into nine different regions, including the piezoelectric disk bender. These regions are indicated in Figure 3.1. The physical dimensions of each region can be found in Appendix A. In general, ducts were described by both an acoustic resistance and an acoustic mass whereas plenums were described by only a compliance. The definitions of these components were straight-forward with the literature available (Merhaut, 1981; Yang, 2007; Gallas, 2002). The meniscus and the droplet were non-basic components of the acoustic domain and required a deeper look into some of the literature and the physics behind the LEM model. The definitions of the meniscus and droplet will be discussed later. The piezoelectric disk was modeled as a current source, the reason for which will be discussed after establishing an understanding of the basic LEM elements.

3.1.2.1. BASIC LEM ELEMENTS

The three basic elements of LEM modeling are the resistor, inductor and capacitor. Each represents the acoustic resistance, mass, and compliance of the fluidic system, respectively. In LEM modeling, it is assumed that pressure is analogous to voltage and volume flow rate is analogous to current. This allows for one to treat fluid connections between elements in much the same way as one would treat them in an

electrical circuit. Namely, the principals of Kirchhoff's voltage and current laws translate into similar laws for pressure and volume flow rate, respectively, in an acoustic system. Finally, the relationship between voltage, current and impedance is also analogous to the relationship formed between pressure, volume flow rate and acoustic impedance, respectively.

$$V = I \cdot Z \tag{3.3}$$

$$P = \dot{V} \cdot Z_a \tag{3.4}$$

These relationships are used with the addition of physical knowledge of acoustics to determine how one defines acoustic resistance, mass and compliance (the impedances of an acoustic system).

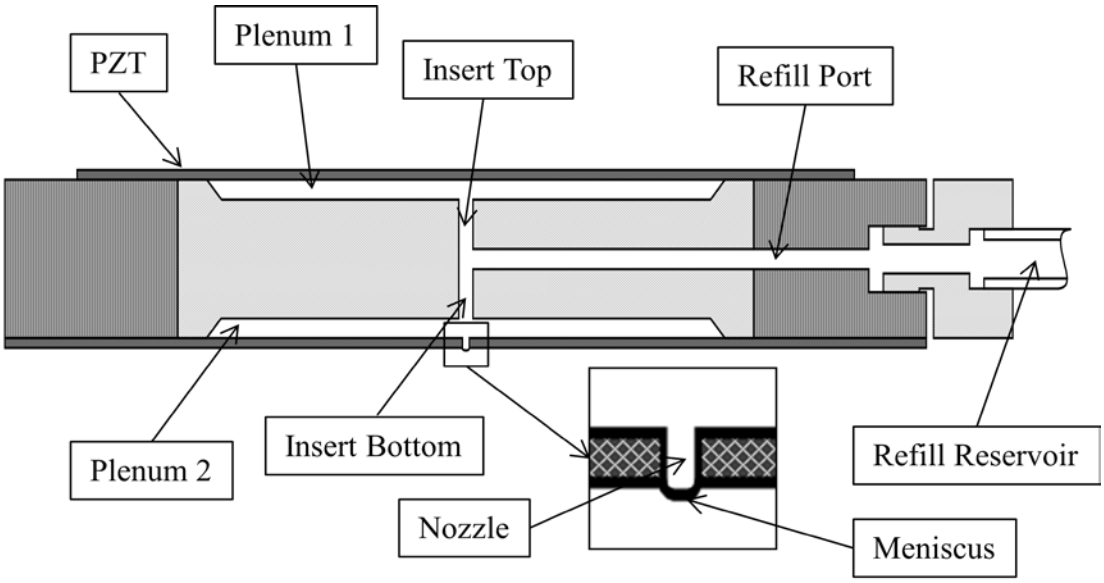

Figure 3.1: Droplet generator with indication of the different regions to model in LEM model.

In much the same manner as one would calculate total voltage drops across segments of a circuit, the total pressure drop across a segment of an acoustic system is

equal to the sum of the pressure drops across each element within the segment. In the case of the droplet generator, regions with little movement were assumed to have pressure drops due only to acoustic compliance. Regions with greater movement (e.g. the narrow duct regions of the aluminum insert) were assumed to have a pressure drop resulting from the sum of the losses due to acoustic mass and acoustic resistance.

For acoustic resistance, the laminar flow formula for the pressure drop across a duct of circular cross section, developed by Poiseuille, is used to formulate the equation that transforms the physical parameters of an acoustic system into a lumped element in an electrical system (Merhaut 1981).

$$\mathrm{P} = \frac{8\mu \mathrm{L}}{\pi a^4}\dot{\mathrm{V}} \tag{3.5}$$

$$\therefore\ \mathrm{R_a} = \frac{8\mu \mathrm{L}}{\pi a^4} \tag{3.6}$$

However, the system will be under oscillating flow, and this solution assumes a laminar profile of fully developed flow. Yang (2007) found a remedy to this problem for the LEM method by incorporating the oscillations into the definition of the acoustic resistance and the acoustic mass. Yang (2007) accounted for the flow oscillations by integrating the velocity profile developed by White (1974). White's velocity profile was obtained using the assumption that the pressure drop can be described as $\delta P = \Delta P \cdot \exp(i \cdot \omega \cdot t)$, where δP is the pressure drop at any instant in time and ΔP is the amplitude of the pressure oscillations. The integral of White's velocity profile equation allowed Yang to obtain the volume flow rate as a function of time. Yang then used the fundamental relationship between volume flow rate, $\dot{V}$,

pressure, P, and acoustic impedance, Z_a, (see equation 3.4) to describe the acoustic impedance as a function of a unit pressure and the oscillating volume flow rate.

The governing acoustic equation for pressure drop in a duct is:

$$\delta P = R \cdot \dot{V} + M \cdot \frac{d\dot{V}}{dt} \tag{3.7}$$

which can be rewritten for oscillating flow as:

$$\delta P = R \cdot \dot{V} + j \cdot \omega \cdot M \cdot \dot{V} \tag{3.8}$$

where R and M are the acoustic resistance and acoustic mass respectively. Combining equations 3.4 and 3.8, one finds that the acoustic impedance for the duct is:

$$Z = R + j \cdot \omega \cdot M \tag{3.9}$$

Substituting equation 3.9 into his equation for the acoustic impedance as a function of a unit pressure and an oscillating flow rate, Yang showed how the acoustic resistance and acoustic mass could be defined as the real and imaginary parts, respectively, of the final equation for acoustic impedance. The final definitions of the acoustic resistance and acoustic mass are omitted from the text here. The interested reader may find the full definitions in Yang (2007), also given in Appendix B.

Assuming constant properties and constant geometry, both the acoustic resistance and the acoustic mass are functions of the frequency of oscillation only. Plots were generated for acoustic mass versus frequency and acoustic resistance versus frequency in order to better understand how each element in the droplet generator may be affected by different frequencies. These plots can be seen in Figure 3.2 through Figure 3.4. The acoustic resistance and acoustic mass plots generated were non-dimensionalized by their fully developed flow equivalents and plotted as functions of

Stokes number. Therefore, the acoustic resistance was normalized by the acoustic resistance of Poiseuille flow as defined in equation 3.6.

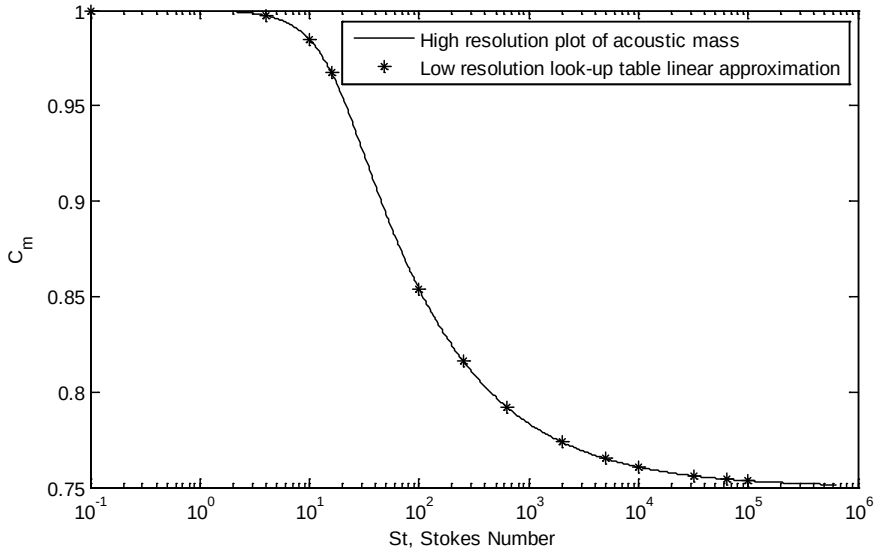

Figure 3.2: Semi-log plot of the acoustic mass modifier, C_m, as a function of Stokes number.

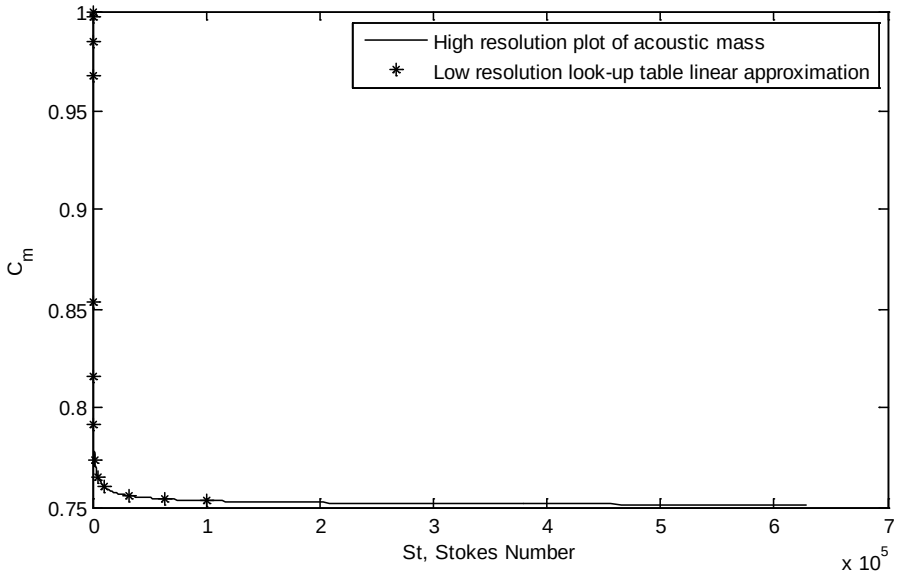

Figure 3.3: A linear scale plot of the acoustic mass modifier, C_m, as a function of Stokes number.

The acoustic mass was also normalized by the acoustic mass of fully developed flow. However, there are discrepancies in how this value is defined. In Merhaut (1981), the acoustic mass for fully developed duct flow is defined as:

$$M = \frac{\rho \cdot L}{\pi \cdot a^2} \tag{3.10}$$

and is derived by relating the kinetic energy of the fluid to the acoustic mass energy of the fluid. However, in work by Yang (2007) and Gallas et al (2002), the kinetic energy was determined for fully developed flow along with a derivation for the kinetic energy of flow through a duct using acoustic mass and volume flow rates as the basis. The two were equated and the acoustic mass for fully developed duct flow was shown to be:

$$M = \frac{4}{3} \cdot \frac{\rho \cdot L}{\pi \cdot a^2} \tag{3.11}$$

The coefficient of 4/3 was a result of equating the two forms of describing the kinetic energy shown below:

$$KE = \frac{1}{2} \cdot \rho \cdot L \cdot \int_0^a \left[u_o \cdot \left(1 - \frac{r^2}{a^2}\right) \right]^2 \cdot 2 \cdot \pi \cdot r \cdot dr = \frac{1}{6} \cdot \rho \cdot L \cdot \pi \cdot a^2 \cdot u_o^2 \tag{3.12}$$

$$KE = \frac{1}{2} \cdot M \cdot \dot{V}^2 = \frac{1}{2} \cdot M \cdot (\pi \cdot a^2 \cdot \frac{1}{2} u_0^2)^2 = \frac{1}{8} \cdot M \cdot (\pi a^2)^2 \cdot u_o^2 \tag{3.13}$$

It appears that Merhaut's reasoning makes a simplifying assumption that fails to take into account the change in the kinetic energy of the fluid due to a fully developed flow velocity profile, which is independently accounted for in both Yang (2007) and Gallas et al (2002). For this reason, fully developed acoustic mass will be defined as per equation 3.11. Therefore, the acoustic mass versus Stokes number plot will also be normalized by this definition.

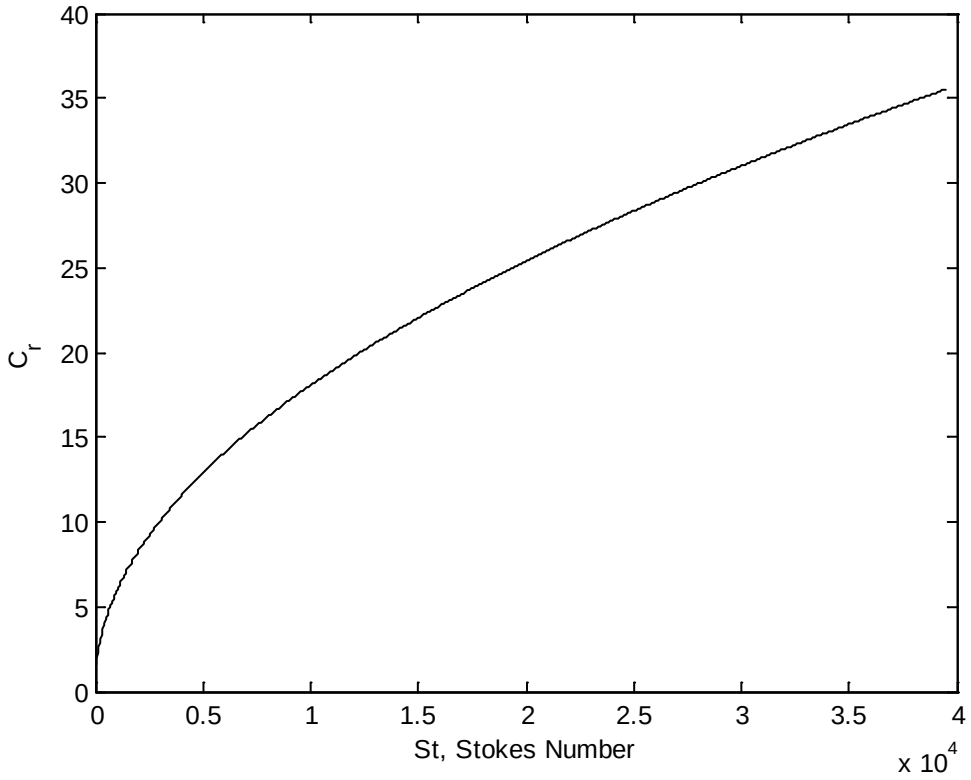

Figure 3.4: Acoustic resistance multiplier as a function of Stokes Number

A different discrepancy arose with respect to the acoustic resistance. While attempting to generate the same acoustic mass multiplier as a function of Stokes number relationship that Yang (2007) reports, a different relationship was found to exist. In Yang (2007), the acoustic resistance is said to vary linearly with respect to Stokes number. However, when the equation for acoustic resistance is integrated and the acoustic resistance multiplier is calculated as a function of Stokes number, the non-linear relationship shown in Figure 3.4 is observed. This relationship comes as a surprise because the plot from Yang (2007) was generated from the same equation as the relationship in Figure 3.4. For simplicity, the linear dependence of the acoustic

resistance on Stokes number was used in the LEM model. This should be noted, the discrepancy between these plots may be a source for error.

The acoustic mass versus Stokes number and acoustic resistance versus Stokes number plots are essentially multiplication factors by which the acoustic mass and acoustic resistance are modified from their ideal fully developed flow values due to the presence of oscillating flow. For a more accurate model, each acoustic resistance element was defined as the fully developed acoustic resistance of the element multiplied by the Stokes number dependent correction factor. The multiplier was defined using the geometry of the specific element, the fundamental frequency of system oscillations, and the relationship given in Yang (2007). The same method was used in conjunction with the relationship shown in Figure 3.2 to define the values for acoustic mass.

As can be seen in Figure 3.2, the acoustic mass multiplier was found to have a non-linear variation as a function of Stokes number. As mentioned earlier, the acoustic resistance multiplier was assumed to vary linearly with Stokes number (Yang, 2007). Since the acoustic resistance varies linearly with Stokes number, it is simple enough to incorporate the frequency dependence into the definition of the resistive elements. The linear equation describing the acoustic resistance correction factor was coded directly into the LEM model in LTspice as part of each acoustic resistance element's definition. The equation varies the correction factor value for all the acoustic resistance elements as a function of droplet generator's driving frequency.

Since the acoustic mass varies non-linearly with Stokes number, the relationship between acoustic mass and Stokes number could not be easily described with a single equation. Instead, the relationship was included in the model by using a piecewise linear approximation to the curve. The number of interpolation points used to predict the curve was increased until the piecewise linear scheme matched the theoretical solution to less than 1% deviation. The plots of the correction factor's variation were compared on both logarithmic and linear scales for the Stokes number. Anywhere the piecewise linear approximation deviated from the actual value for the correction factor by more than 1%, an additional interpolation data point was inserted into the piecewise linear scheme. Figure 3.2 and Figure 3.3 also show the final comparison of the piecewise linear scheme to the real solution. The piecewise linear scheme has been shown only with starred points so one can differentiate between the real solution and the linear approximation This selection of data points for the piece wise linear scheme became the final representation of the correction factor as a function of Stokes number. The final set of modifier-versus-Stokes number pairs was exported from MATLAB as a comparison table. The table was then imported as an interpolation lookup table for LTspice IV to use in defining the acoustic masses in the LEM model. The lookup table functions by finding the appropriate correction factor for the Stokes number of the physical element in question and applying that correction factor to the acoustic mass of the element in question.

The final basic LEM element is the acoustic compliance. The acoustic compliance is the working fluid's ability to store potential energy, as pressure, in a given volume. This relationship can be expressed as:

$$C = \frac{\delta V}{P} \tag{3.14}$$

where an incremental change in volume, δV, results in a change of pressure in the chamber. An incremental increase in the mass of fluid stored in the same amount of volume increases the pressure. Therefore, a volume flow into the chamber causes an increase in the pressure, and the chamber becomes more resistant to further volume flow into or volume compression in the chamber. For volume changes much less than the total volume of the chamber, the pressure change of the chamber can be expressed as:

$$P = \rho {c_o}^2 \frac{\delta V}{V} \tag{3.15}$$

Combining equations 3.14 and 3.15, the compliance can be simplified to:

$$C = \frac{V}{\rho {c_o}^2} \tag{3.16}$$

This acoustic compliance relationship is analogous to applying a voltage to a capacitor. The voltage drives current flow, which builds up charge on the capacitor. The greater the buildup of charge on the capacitor, the greater the voltage on the capacitor and the more resistant the capacitor is to accumulating additional charge. The fundamental assumption for the LEM method allows for the pressure wave resulting from the compression of the fluid in the chamber to be uniform since the size of the element is much smaller than the wavelength of sound in the medium.

Therefore, the acoustic compliance is modeled as a capacitor in the LEM model. The interested reader may refer to Merhaut (1981) for a more thorough theoretical derivation of each of the LEM method acoustic impedances.

3.1.2.2. MODELING OF THE PIEZOELECTRIC DISK

There are a number of different methods by which to model the piezoelectric disk of the drop generator. The method chosen for this study was to model the piezoelectric disk as a current source. There are many advantages to using this method over modeling the piezoelectric disk as a voltage source, although it does behave as both in the model. Arguably the best method would be to fully characterize the electrical characteristics of the piezoelectric disk and integrate these into the acoustic model with a transformer, as was done in Gallas et al (2003). However, the necessary instrumentation for such a route was not available, so the current source method was chosen instead.

By modeling the piezoelectric disk as a current source, the LEM model captures the displacement of the piezoelectric disk as a function of time and uses this to drive the system dynamics. The compliance elements throughout the system will help convert the volume flow rate driven by the piezoelectric disk into pressures seen throughout the system. Finally, the displacement versus time effect of the piezoelectric disk is much easier to control with the voltage input to the piezoelectric disk than is the impulse created by the piezoelectric disk. In order to properly model the piezoelectric disk as a voltage source, one would have to be able to determine the exact impulse of the piezoelectric disk on the system from whatever form of voltage

was applied to the piezoelectric disk. Not only would this be difficult, but it would then force the model to rely on experimental data input for any change to the piezoelectric disk's input waveform, since it is likely that the exact impulse felt by the system would not change linearly. Unlike the voltage source, the current source is directly related to easily measured and repeatable system parameters. By measuring the displacement of the piezoelectric disk as a function of input voltage, one can relate the driving voltage versus time to a displacement versus time. The volume displacement as a function of time can then be calculated and include in the LEM model as a current source input to the system. Recall that current in an LEM model is analogous to volume flow rate in the drop generator.

In order to correctly define the dependence of the piezoelectric displacement on the input voltage, a profilometer was used to record the relationship. The drop generator with installed piezoelectric disk, but removed insert and nozzle plate, was driven over a large range of voltages to determine how much the disk displaced at each voltage. The linear displacement was used to calculate a volume displacement in within a MATLAB code. A line of best fit was then used to approximate the relationship between the volume displacement and the applied voltage. A more detailed description of this process can be found in Appendix D. A series of function based voltage sources were embedded in the LTspice IV model that used this relationship between voltage applied and volume displacement to calculate the current source input into the drop generator.

The set of function-based voltage sources worked in the following manner:

1. The input driving waveform voltage was output into an open circuit node. Anytime a voltage is output into an open circuit node, the model is then able to use it as a variable inside any functionally defined voltage source, current source or element.
2. This open circuit voltage from step 1 is used in an arbitrarily defined voltage source to define the displacement of the piezoelectric disk at the specified driving voltage. The arbitrarily defined voltage source would calculate the volume displacement as a function of the input voltage variable. This displacement value was output as a new voltage variable into another open circuit node.
3. The time differential of the displacement value, reported as a voltage by the open circuit node from step 2, was performed by a third and final arbitrarily defined voltage source. The resulting volume displacement as a function of time is output as a voltage into one last open circuit node.
4. The current source driving the drop generator was created as a an arbitrarily defined current source. It uses the output voltage from step 3 as its input voltage. The current source therefore outputs a current (or volume flow rate) equal in magnitude to the voltage value output from step 3. This current flows into the rest of the drop generator and drives the droplet generator activity.

3.1.2.3. MODELING THE MENISCUS

A major goal of this study is to determine the affect a vibrating meniscus has on drop formation characteristics. As such, it became an important focus of the

project to determine the most suitable way in which to model the meniscus in a way that would align with the theoretical background used in LEM modeling. A few key characteristics of the physical environment had to be maintained in modeling the meniscus.

First, and most importantly, the meniscus could not be isolated from the rest of the fluid system. As discussed by Burr et al. (1996), a diode has been used in past research efforts to model a drop leaving the system. However, this method usually results in one of two methods of 'drop formation' in the model. In the first method, the diode is placed in parallel with the meniscus and a voltage source is applied to the back end to simulate the 'break through pressure' at which the fluid can now flow out of the nozzle as a drop. The down side to this method is that the meniscus all of a sudden stops behaving with the same dynamics as the rest of the system. The result is that the system has a non-realistic boundary condition and non-realistic meniscus vibration dynamics can arise. The second method usually involves placing the meniscus downstream of a diode. This method does not work because it completely separates the meniscus from the rest of the system. Since the meniscus is separated from the rest of the system, there is no way to observed the meniscus' vibration dynamics before or after drop formation.

Second, the meniscus model has to have a fundamental basis on the same acoustic principals used to derive the basic LEM elements. In the past, researchers have modeled the meniscus as an acoustic compliance in LEM models. However, the meniscus is also usually responsible for controlling the drop formation. The

theoretical derivation for the parameterization of a vibrating circular membrane element can be found in Merhaut (1981). This is essentially the same as a vibrating meniscus. The derivation provided in Merhaut (1981) is of a general form that can account for higher order membrane dynamics. The LEM element definition given directly in Merhaut (1981) lists the element equations and structures necessary to model meniscus vibration modes that resemble Bessel functions. These higher order meniscus dynamics have been observed in the work by Daniels and Liburdy (2004). Including all these elements in the LEM model is unnecessary for this study since the frequencies are too low to observe the higher order meniscus dynamics (Daniels and Liburdy, 2004).

In order to satisfy these two important characteristics, the meniscus element's definition as well as it's placement within the LEM model are important. In order to define the LEM element for the model, the meniscus was modeled by a simplified representation of the elements presented in Merhaut (1981). According to Merhaut (1981), lower frequency applications can use a single acoustic compliance element to define the meniscus. A parallel derivation was performed, with Merhaut's derivation as a guide, to determine the definition of the meniscus compliance with the parameters used in this study. The final resulting equation is:

$$C_{a,m} = \frac{\pi D^4}{128\sigma} \tag{3.17}$$

For a complete derivation of 3.17, see APPENDIX E. Conceptually, the meniscus compliance for this dominant mode is based on volume displacement and surface tension forces. The system provides a back pressure that works against the surface

tension forces of the meniscus. The meniscus region then expands with fluid accordingly to maintain force equilibrium. Note that this definition differs from the definition for meniscus compliance defined in Burr et al (1996). The meniscus compliance in Burr et al (1996) is defined as:

$$C_{a,m} = \frac{\pi D^4}{48\sigma} \tag{3.18}$$

which differs from the derived equation 3.17 by a factor of 8/3. The paper by Burr et al (1996)does not go into any further discussion around the meniscus compliance or how it was derived, so the current study decided to continue work with the equation derived from Merhaut (1981), i.e. equation 3.17.

In order to meet both the requirements for defining the meniscus in the LEM model, the meniscus must be placed at the end of the nozzle with no additional elements in between. Any and all drop modeling must therefore follow the meniscus. This is conceptually valid because the back pressure applied to the meniscus should be the same as the pressure applied to the drop, and a compliance element satisfies this requirement. Additionally, the volume flow rate into the meniscus element should be consistent with that of the total drop volume once a pressure threshold is surpassed. Allowing for the drop to form through the meniscus seems to be a valid way to capture this. Finally, establishing the model in this manner will capture the essential goal of the thesis, namely to analyze drop characteristics of drops formed through a vibrating meniscus.

3.1.2.4. LEM MODELING OF THE DROP FORMATION

The remaining part of the model to characterize is the drop formation. Unlike the vibrating meniscus, there is no existing electroacoustic theory for modeling the physical process of drop formation. However, properly modeling the drop formation in a manner that is consistent with electroacoustic theory is an important part of creating a predictive model for drop formation in the presence of a vibrating meniscus. Past research efforts were considered, but none would be able to maintain the integrity of the meniscus dynamics required in addition to the drop formation.

For a visual representation of what the model used as the drop formation circuit, see Figure 3.5. The primary challenge to designing an LEM model circuit robust enough to model the drop formation and the meniscus vibrations was finding methods with which to represent distinct flow conditions in the LEM model. These methods are subject to both the restrictions of electroacoustic modeling and the restrictions of basic circuit analysis. Essentially, the model needs to capture the act of droplet break-off in an electrical circuit; a process for which the general application of electroacoustics was not designed.

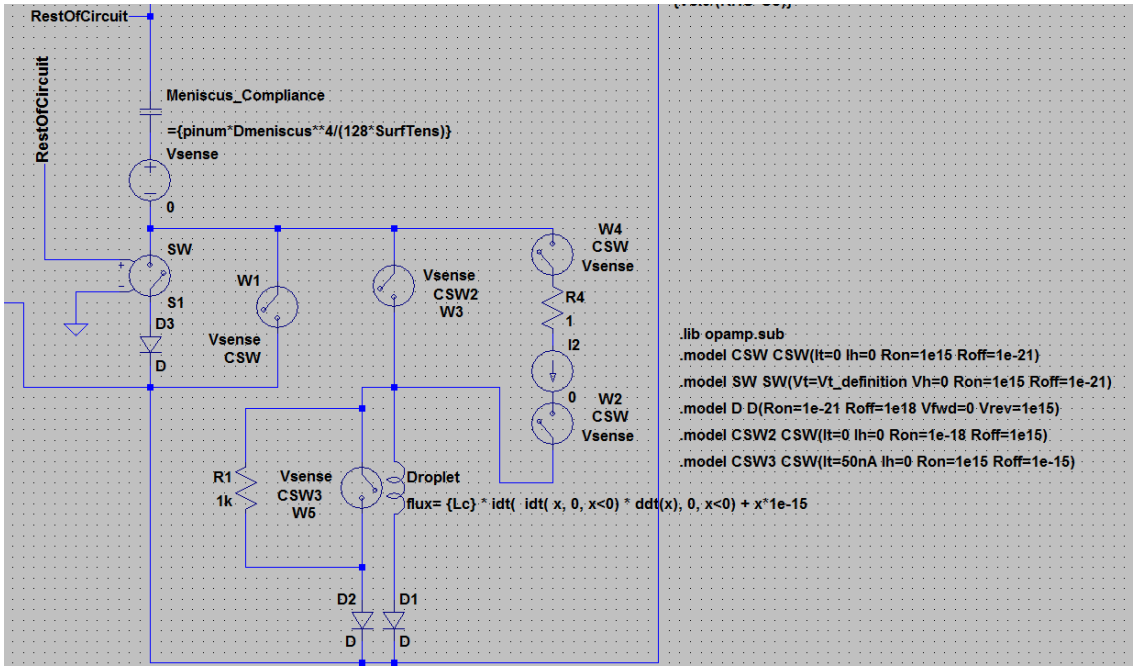

Figure 3.5: This is the GUI representation of the section of the LEM model created for modeling the drop formation.

Given the extensive history in the literature on drop break-off, and the known complexity of this problem, properly modeling the small scale dynamics of drop break-off was not a goal of this design. Much like the rest of the LEM model, the goal in the design process here is to model the drop break-off as an element, based on bulk properties and conditions. More specifically, the model was developed with the goal of measuring drop volume; and the goal of potentially measuring drop velocity and break-off time. The smaller scale dynamics of the drop break-off process were not a concern. As the literature review indicated, the scale of the break-off dynamics is much smaller than the scale of the overall drop. These smaller scale dynamics were thus ignored in the development of this model. The more important characteristics were the bulk drop properties such as the mass of the drop and the volume flow rate.

Figure 3.5 is relatively complex compared to the rest of the circuit, which can be found in APPENDIX C. At the top left of the image, one observes an open node line that reads "RestOfCircuit". This line out was created as a measuring point and also as a visual guide to indicate where the drop generator ends and the meniscus and drop begins. This wire going out to the top left leads to the nozzle and the other features of the drop generator that were modeled in the LEM model. This circuit was constructed to emulate the process of both meniscus vibrations and drop formation. Each phase of operation requires a different set of parameters to properly model the fluid flow behavior; switches were used to control the switching from one mode of operation to the next (e.g. meniscus vibration to drop formation). Within each mode there are also two additional sub-modes of operation, positive and negative current flow conditions. These sub-modes were determined by the direction of flow rate for the meniscus. In the LEM model, “Vsense” (located just below the meniscus element in the top left portion of the circuit in Figure 3.5) is a voltage element inserted to measure the current running into and out of the nozzle. “Vsense” measures the current direction and magnitude for the meniscus element and uses the measured value to control the current based switches W1 through W5.

For meniscus vibration, the goal is to have the meniscus vibrate as if it is unaffected by any drop formation. Switches S1 and W1 help to isolate this phase of operation for the drop generator. When the back pressure of the meniscus is lower than a designated pressure needed to form a drop, the flow of current in the LEM model is allowed to go directly through S1 and dump to ground. This is analogous to

modeling the pressure drop across the meniscus going from the back pressure in the nozzle to atmospheric pressure outside the nozzle. When the back pressure in the nozzle drops below ambient atmospheric pressure, however, one would expect the meniscus to be pushed back into the nozzle. The switch W1 helps model this by allowing any negative voltages behind the meniscus to pull current (volume flow rate) from the ground. Without this backflow condition, the model will blow up and proper meniscus vibrations cannot be modeled. However, from an electrical perspective, the back flow of current could also try to flow into the drop formation element ("Droplet") in this circuit because it may provide a path of least resistance. This result was prevented by introducing switches W2 & W4, the current source I2, and the resistor R4. This branch of the circuit was added to the LEM model to force negative current flow to only pass into the meniscus element. Without this branch, negative current could accidentally bleed into the drop formation element (“Droplet”) and create a false drop. The current source I2 was set to zero to force any current through the drop element “Droplet” to be equal to zero whenever there was a backflow condition in the model.

When the pressure inside the nozzle and meniscus region gets large enough, a drop will begin to form. The beginning of the drop formation through the release of the drop from the system is a new mode of operation for the model. In this mode of operation, the meniscus pressure, flow rate, and effects must continue to be calculated and included in the model but an additional element needs to be inserted that can represent the formation of a drop. The inductor element “Droplet” was added to

model the drop. How “Droplet” simulates the drop formation is discussed later. Switches W2, W3, W4, W5, and S1 all aid in the transition from the meniscus vibration mode of operation to the drop formation mode of operation.

When switching to the drop formation mode of operation, many things need to happen at once. Since it is the back pressure on a meniscus that determines when a drop will begin to form, this value is used to trigger the switch from one mode of operation to the next; more specifically, the drop formation is triggered by the “RestOfCircuit” line-out voltage. When the back pressure is large enough in the drop generator, a drop will begin to form, so analogously, when the voltage at “RestOfCircuit” reached a specified voltage (analogous to a threshold pressure), the mode of operation will switch to drop formation mode. The actions in the LEM model that occur when switching to drop formation mode are the following:

- S1 opens when the voltage of “RestOfCircuit” is high enough. This stops current flow rate from only going into the meniscus and forces the current to also flow into the drop element “Droplet” as well.
- For voltages large enough to form drops and positive current flow rates, the current flow is directed toward the “Droplet” element by opening W3.
- If the current is too small (i.e. a drop cannot realistically form), the current flow is diverted away from the drop element “Droplet”, to ground, by closing switch W6.
- If the current is large enough to indicate realistic drop formation, W5 is opened and current flows into the drop element “Droplet”

The LEM model stays in the drop formation mode for as long as it is necessary. Usually, this is a very short time but it depends on the input waveform. Over the duration of the drop formation mode, the drop element “Droplet” undergoes a time dependent change of inductance. The importance of allowing for the time dependent change of inductance and the determination of how it varies is derived from the theory behind electroacoustics. The LEM method's electroacoustic theory represents inertia as an electrical inductance. It was decided that the drop formation’s behavior would be best represented by the inertia of the drop; both viscous losses and acoustic compliance of the fluid flowing into the drop would be minimal. However, unlike calculating the acoustic mass for a duct, the actual mass of the drop, and thusly the drop’s acoustic mass, would be changing as a function of time. Therefore, it was necessary for the element representing the drop’s acoustic mass to be modeled as a time dependent value.

LTspice IV allows one to define a variable inductance for an inductor element by defining the inductors flux. It was therefore necessary to combine the elements of electroacoustic theory with the available software package to create a relationship that could describe the time dependent behavior of the drop’s acoustic mass as a function of time. Recall the relationship shown in equation 3.11. This relationship could also be described as the ratio of the mass of a given volume to the square of the cross sectional area. In equation form, this becomes:

$$M_a = \frac{4}{3}\frac{\rho V}{\pi^2 a^4} \quad 3.19$$

This form of the acoustic mass can be used to help define the acoustic mass of the drop. In particular, the relationship of the drop volume can be included in the above equation using the following:

$$V = \int_{t_0}^{t} \dot{V}(t)dt \quad 3.20$$

$$M_a = \frac{16\rho}{3\pi^2 {D_n}^4} \int_{t_0}^{t} \dot{V}(t)dt \quad 3.21$$

$$\text{and if } \mathcal{L}_c = \frac{16\rho}{3\pi^2 {D_n}^4} \quad 3.22$$

$$\text{then } M_a = \mathcal{L}_c \int_{\tau_0}^{\tau} \dot{V}(t)dt \quad 3.23$$

Here, the drop volume is a function of the volume flow rate into the drop as a function of time. Therefore, the larger the flow rate and the longer the positive flow rate period the larger the acoustic mass of the drop. Defining the drop's acoustic mass in this way maintains the validity of the electroacoustics theory in-so-far as it uses the basis of the theory to determine the LEM parameter.

With the software package used for the LEM model, it is impossible to define an inductor (the representative element for an acoustic mass) as a variable inductance. Without this ability, it is impossible to define the acoustic mass correctly because the acoustic mass is a function of time as can be seen in equation 3.21. However, LTspice IV can define a variable flux for an inductor. The flux of an inductor is related to its inductance by equation 3.24. This equation can be rearranged with the definition of the voltage drop across an inductor, see equation 3.25, to determine the definition of the flux as a function of current (equation 3.30).

$$\mathcal{L}(i) = \frac{d\Lambda}{di} \tag{3.24}$$

$$V(t) = \frac{d\Lambda}{dt} = \frac{d\Lambda}{di} \cdot \frac{di}{dt} = \mathcal{L}(i) \cdot \frac{di}{dt} \tag{3.25}$$

Integrate equation 3.25 from τ_o to τ, where τ is a indeterminate time and τ_o is an initial time, and the equation becomes:

$$\int_{\tau_o}^{\tau} V(t)dt = \int_{\tau_o}^{\tau} \mathcal{L}(i) \cdot \frac{di}{dt} \cdot dt = \int_{\tau_o}^{\tau} \mathcal{L}(i)di \tag{3.26}$$

Insert equation 3.24 , simplify, and rearrange the equation to get 3.29:

$$\int_{\tau_o}^{\tau} V(t)dt = \int_{\tau_o}^{\tau} \frac{d\Lambda}{di} di = \int_{\tau_o}^{\tau} d\Lambda \tag{3.27}$$

$$\int_{\tau_o}^{\tau} V(t)dt = \Lambda(\tau) - \Lambda(\tau_o) \tag{3.28}$$

$$\Lambda(\tau) = \int_{\tau_o}^{\tau} V(t)dt + \Lambda(\tau_o) \tag{3.29}$$

And finally, insert the definition equation 3.25 to obtain:

$$\Lambda(\tau) = \int_{\tau_o}^{\tau} \left(\mathcal{L}(i) \cdot \frac{di}{dt}\right) dt + \Lambda(\tau_o) \tag{3.30}$$

Recall the analogous relationship between acoustic mass and inductance for an LEM model. This relationship allows for the following statement to be true:

$$M_a(\dot{V}, t) = \mathcal{L}(i, t) \tag{3.31}$$

$$\mathcal{L}(i, t) = \mathcal{L}_c \int_{\tau_0}^{\tau} i(t)dt \tag{3.32}$$

Inserting equation 3.32 into equation 3.30, the definition of the flux for the LEM model inductor can be defined as:

$$\Lambda(\tau) = \int_{\tau_o}^{\tau} \left[\left(\mathcal{L}_c \int_{\tau_0}^{\tau} i(t)dt\right) \cdot \frac{di}{dt}\right] dt + \Lambda(\tau_o) \tag{3.33}$$

Equation 3.33 is the final result of an electroacoustic determination of the acoustic mass of the drop for use in an LEM model. Conceptually, the flux value determined

above is, in acoustic terms, the ratio of the kinetic energy of the drop to the square of the volume flow rate of the drop. This can be simplified to the ratio of the mass of the drop to the cross-sectional area of the drop's flow direction. Over time, this value increases due to the increased momentum that the drop will possess in both mass and velocity for a cross-sectional area of a relatively constant value. LTspice IV allows for the variable inductor to change the inductance value as a function of the current passing through the inductor. The only restriction is that the inductor can't have a value of zero. Therefore, the constant $\Lambda(\tau_o)$ was used as an arbitrarily small constant so as to have the inductor behave as if it were an open wire except for when a drop is forming.

Figure 3.5 shows that the "Droplet" inductor element is defined to reflect equation 3.33. The coding format and language of the LTspice IV program can be found in the LTspice IV help files (Englehardt, 2011). As time steps progress in the model simulation, the "Droplet" element passes current through it, changing the inductive value as necessary. The drop volume is determined by establishing a measurement code (.meas) that integrates the current flowing through the "Droplet" inductor during the drop formation mode. The integral of the current is analogous to integrating the volume flow rate into the drop, so the final value can be related to a total drop volume.

Drop break-off, and the end of the drop formation mode, occurs when the volume flow rate direction, as measured by "Vsense", changes direction. At this point in simulation time, the switch W5 closes again to short out the "Droplet" element.

The switch W1 also closes at this time to allow negative flow rate to push back in the meniscus. Meanwhile, the current in the rest of the drop formation circuit is forced to zero by opening switch W3 and closing switches W2 and W4. Closing switches W2 and W4 reintroduces the zero amp current source to the drop formation circuit, which ensures that there is no unwanted current flow through the "Droplet" element during the times when only the meniscus should be vibrating. This also serves to ensure that all the negative flow into the circuit is diverted into the meniscus, as should be the case. If the current source were not reintroduced to the system, there would be a significant amount of 'lost' current that would flow through the nearly zero resistance drop generator circuit region rather than flow into the much higher resistance circuit that is the rest of the drop generator system.

Finally, there are a few extra components that were added to the system shown in Figure 3.5 that are necessary for code stability purposes. First, there are a number of diodes placed on all but one of the connections to ground. These were necessary in order to maintain strict control over the direction in which current flow is allowed to go. This is another example of a restriction on the utility of using an electrical circuit to model a fluidic system. In more complex circuit designs, one must remove the possibility of non-real fluid flow possibilities from the circuit design. The diodes added to the model served this purpose by only allowing negative currents to pass through switch W1 and feed into the meniscus. Second, there are two resistors included on the diagram in Figure 3.5 that are strictly for code stability. R1 is used to stabilize the flow through switch W5. During all the switching periods, it is necessary

at points to have R1 in place so that the flow does not try to pass through both switch W5 and “Droplet”. R4 is added in series to the current source (located in the center of Figure 3.5) to stabilize the LTspice IV circuit. Without R4, the program will refuse to run because the current source I2 will not have an element in series with it when the switches W2 and W4 isolate it from the circuit, which creates a floating node voltage. The resistance value of 1 was arbitrarily chosen because there shouldn’t be any flow through this element at any stage of the drop formation, so it doesn’t matter what the resistance value is.

3.2. APPLICATION OF THE THEORY

Equations 3.6, 3.11, and 3.16 are used to calculate the acoustic resistance, acoustic mass, and acoustic compliance, respectively, for each region identified in Figure 3.1. The only exceptions to this are the models for the piezoelectric disk, the meniscus, and the drop formation. These three special areas of interest were modeled according to sections 3.1.2.2, 3.1.2.3, and 3.1.2.4, respectively. All the elements were built into a dynamic LTspice IV program. The program fully parameterizes the problem, such that each element is defined in terms of variables. These variables are then defined in a list of parameters. The program inserts the appropriate parameter values in to the variable positions for each element. This allows for changes to be made to the model quickly and effectively. The parameterization of the model also enables the inclusion of frequency dependence in all acoustic mass and acoustic resistance elements. A more detailed description of the LTspice IV program and parameterization is given in APPENDIX C. A drawing of the physical dimensions

pertaining to the fluidic domain of the drop generator is given in APPENDIX A. The dimensions reported in APPENDIX A are used to calculate the element characteristics, and as such, they may also be found in the list of input parameters provided to the LEM model in Figure C-4 of APPENDIX C. The methods and components of the LEM model developed for this study may also be scaled to fit different and/or smaller droplet generators in the future. Smaller geometries should allow for higher frequency operation of the model due to the fundamental electroacoustic assumption (see equation 3.2). This enables the LEM model developed in this research effort to be used as a template for future LEM models developed for industrial applications.

4. EXPERIMENTAL SETUP AND PROCEDURE

An experimental setup was designed and fabricated at Oregon State University to test the validity of the analytical LEM model developed in Chapter 3. The analytical model was constructed to reflect the geometry of the drop generator used. The rest of the experimental setup was designed to enable experimental observations that could validate the model. It was also sought to design the experiment such that conclusions could be made with regards to the effect of a vibrating meniscus on drop formation, without having to rely solely on the model to make these predictions. The full range of the experiment would then allow for the model to be validated in three distinct regions: vibrating meniscus dynamics, drop formation characteristics, and drop formation characteristics as a function of drop triggering phase in a vibrating meniscus cycle.

4.1. DROPLET GENERATOR

The droplet generator design used was based on an older drop generator used in prior research (see Hawke, 2006; Figure 4.1). This drop generator was designed with a removable nylon insert that could change the internal drop generator plenum volume. It also allowed for variable nozzle lengths and nozzle plate thicknesses. For this research, the droplet generator was modified slightly. The two modifications were to the insert and the nozzle plate. First, the nylon insert was replaced with an aluminum insert machined in such a way as to reduce the drop generator plenum volume as much as could be reasonably achieved. Secondly, the nozzle plate was kept at a uniform thickness, i.e. it was never varied. A schematic of the drop generator

used for this research can be found in Figure 3.1. More detailed dimensions of the nylon insert, and thereby the fluidic domain of the droplet generator, are given in APPENDIX A. Full schematics for the rest of the droplet generator are given in Hawke (2006).

4.2. DATA COLLECTION METHOD

In order to determine drop volumes and velocities for comparison with the model, a strobe like method of photographing the drops was used. In this method, the working fluid is illuminated by a light source at a high frequency and a high speed camera is used to capture the drop position at two different illuminations of the drop during its travel. For the light source, a Quanta-Ray PIV-400 Nd:YAG laser, by Spectra Physics, was used. This laser was designed with two laser heads in a single system. This allows for the two laser heads to be triggered independently. The independent release of laser light allows for very accurate fine tuning of the time difference between drop illuminations. Traditionally, this kind of technique is used for Particle Image Velocimetry (PIV). As seen in this study, it can also be used for tracking the velocity of a drop. The Spectra-Physics laser system, high speed camera, and waveform generator were controlled and synchronized by a pair of Stanford Research DG 535 delay generators.

Only a single laser head was used for the experiments in this study. The Spectra-Physics laser system was supplied with two independent Q-switches per laser head. This allowed for each laser crystal to be triggered twice within a single flash lamp cycle. Rather than using the two lasers independently, a single laser head could

be used to illuminate the drop twice in a single laser cycle. In order to establish equal laser intensities for drop illumination, the following procedure was followed:

- The desired time difference between lasers was set on one of the delay generators.
- The laser was turned on to low power and focused onto a blank sheet of paper.
- A photo-diode, hooked into an oscilloscope, was aimed at the focused laser light on the page.
- The trigger time of the first laser pulse was controlled by one of the delay generators. The trigger was increased or decreased until two laser pulses were detected on the oscilloscope. For all the experiments performed, the laser light pulses were set to be triggered 50 μs apart by the delay generator.
- The laser light was then increased to full power.
- The trigger time of the first laser cycle was increased or decreased until the two laser pulses had equal magnitudes on the oscilloscopes.

The high speed camera used for capturing the drop formation during the laser light illumination periods was a MicroMAX 5MHz camera. The camera has a built in feature, also designed for PIV, that allows the camera to take two very short exposures with a time delay between photos as short as 1μs. This dual-image feature of the camera was used to capture the two laser pulses independently. The camera resolution was 1300x1030 (~1.3 Megapixels) which corresponded to a field of view, after focusing through a Mitsuyo 10x microscope objective and passing through a filter, of about 4.95 mm x 3.92 mm.

In order to increase the signal-to-noise ratio for the images of the drops, a dye was introduced to the working fluid. The dye was Rhodamine 6G Chloride diluted in water to a concentration of 10^{-3} M. The unique properties of this chemical cause it to absorb a lot of light at wavelengths near 532 nm. The chemical then re-emits the absorbed energy at a higher wavelength (lower frequency), in the neighborhood of ~560 nm. Once the IR light that originates in an Nd:YAG crystal is modified to the visible light spectrum, all Nd:YAG lasers emit laser light at 532 nm. By introducing a low pass filter in front of the camera, only the lower frequency light emitted by the dye is allowed to reach the camera's sensors. Most of the laser light would be blocked by the low pass filter. Other unwanted lower frequency wavelengths of light were mitigated by performing the experiments in a dark room. The end result of these actions is a strong signal-to-noise ratio and well defined photos of drop formation.

The drops created by the droplet generator referred to in section 4.1. were triggered by an arbitrary waveform generator (Sony Tektronix AWG2021 Arbitrary Waveform Generator). However, the output voltage of the arbitrary waveform generator was not sufficient to create a drop with the experimental setup used. Consequently, prior to reaching the piezoelectric disk, the signal from the arbitrary waveform generator was amplified by a factor of 45 via an analog circuit amplifier designed at Oregon State University. Deformation of the disk results in a volume change and pressure increase in the droplet generator. Given strong enough displacement rates for the piezoelectric disk, the drop generator produced drops.

The collection of data was controlled by the delay generators, which controlled the triggering of the laser light, the camera exposure times, and the waveform generator. For time series data, the drop generation trigger time was kept as a constant. The trigger time of the camera exposure was setup to be dependent on the trigger times of the two laser pulses, thereby allowing all three to change by changing the trigger for the first laser pulse. By changing the trigger time of the laser pair and camera, the whole image capturing process could shift forward or backward in time along the drop formation process. Time series data were generated by assembling images of the drop and meniscus formation that were captured at a number of different time steps in the drop development process.

4.3. EXPERIMENTAL SUPPORT SYSTEMS

In order to maintain a reasonable amount of control over the drop generator pressure, two support systems were implemented. The systems used to stabilize the drop generator behavior are divided into two groups: physical supports and fluid supply.

4.3.1. FLUID SUPPLY SUPPORT SYSTEM

A schematic of the complete fluid system network is shown in Figure 4.1. In order to accommodate fluid loss during drop formation, a refill port was fed into the drop generator. This refill port was attached to an extra reserve of testing fluid (fluid that was used to capture data). This extra reserve was attached to a separate vertical traverse. By changing the height of the reserve testing fluid, the static pressure in the

drop generator could be maintained at a relatively constant level. The reservoir could also refill the drop generator with fluid after each drop departure.

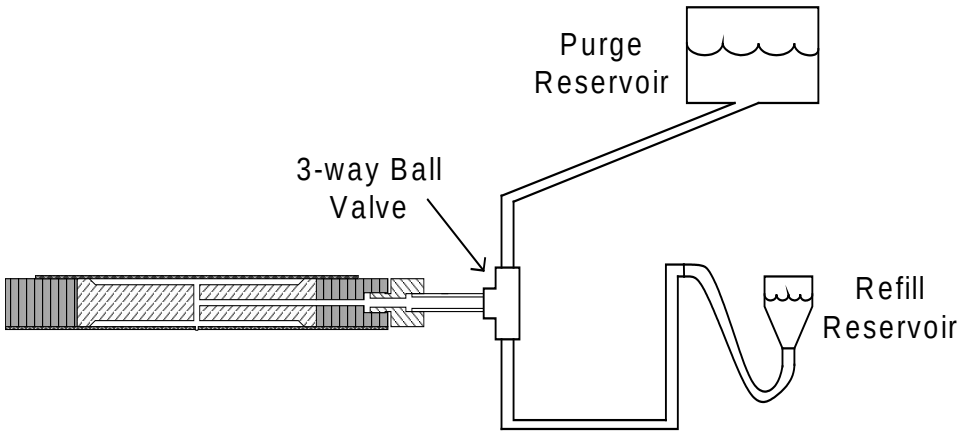

Figure 4.1: A general schematic of the droplet generator and supporting fluid systems.

Also attached to the refill port through a three-way ball valve was a distilled water purge for the drop generator. The Rhodamine 6G Chloride dye used in the working fluid for testing is a corrosive chemical. At the end of a day of testing, leaving the Rhodamine 6G dyed water in the drop generator would lead to pitting and corrosion of the aluminum insert. As such, it was necessary to provide a fluid purge of the drop generator that could help maintain the longevity of the aluminum insert. A reservoir of distilled water elevated high above the drop generator was attached to the three-way ball valve. At the end of a day of testing, the ball valve would be switched from the working fluid refill supply to the distilled water purge. The pressure head from the elevated reservoir would flush of the droplet generator clean of any Rhodamine 6G. Due to the shape of the droplet generator, it was difficult to fully remove any remaining Rhodamine 6G. As such, the droplet generator was considered

flushed clean of any Rhodamine 6G when the naked eye could not detect any remaining dye in the purge water leaving the droplet generator.

The fluid support system was made of aluminum tubing with the exception of last few inches of tubing that would lead up to the drop generator or the fluid supply reservoir. The last legs to both the drop generator and the fluid supply reservoir were polymer based tubing. The polymer based tubing was used as the last leg to the droplet generator so that the droplet generator could be worked on without having to fully disconnect it from its reservoir fluid supply. The tubing on the reservoir side was made to be flexible so that the height of the reservoir could be changed as needed to maintain pressure and sufficient volume in the drop generator.

4.3.2. SUPPORT STRUCTURE SYSTEMS

The support structure system for the drop generator consisted of a vertical traverse, mounted on a vibration isolation table, from which a rigid cantilever and mount supported the drop generator. The vibration isolation table prevents most external ground and or building vibrations to be damped out before reaching the droplet generator. Since part of the experiments were to measure meniscus vibrations, small external vibrations could potentially bias or distort the data. The vertical traverse would be used when necessary to adjust the height of the drop generator and reach a desired meniscus protrusion from the nozzle.

The rigid cantilever and mount were designed specifically for the droplet generator used in this study. The droplet generator was clamped between two aluminum plates. The aluminum cantilever was made thick enough to prevent any

noticeable deflection in the cantilever when exerting a point load equal to the weight of the drop generator at the far end of the cantilever. The plate clamping was required to maintain consistent and repeatable setups from day to day. Without the clamping, the flexibility of the tubing leading up to the droplet generator would bend the drop generator nozzle away from vertical.

4.4. TEST CONDITIONS

Experiments were split into three categories for testing: meniscus vibrations, drop formation without a vibrating meniscus, and drop formation with a vibrating meniscus. The experiments for each condition were conducted so as to have experimental data with which the analytical model could be validated. However, each category collected data beyond the model validation. In preparation for recording the experimental data, driving voltage waveforms were selected according to the results of some preliminary experiments. Repeatability was established for the selected waveforms for both drop volume and meniscus displacement. Repeatability was not established for drop velocities prior to the experiments.

4.4.1. VIBRATING MENISCUS

This experimental category was established for investigating only the vibration of the meniscus. Meniscus vibrations in terms of height change can be related to oscillations in the back pressure of the meniscus. The back pressure on the meniscus can be extracted from the LEM model presented in chapter 0 by measuring the voltage applied to the capacitor that represents the meniscus. Therefore, measuring the meniscus height as a function of time provides a source of validation for the LEM

model by comparing the measured meniscus height fluctuations to the voltage fluctuations reported in the LEM model. If the model is correct, for the same input voltage waveform to the piezoelectric disk in the model and in the experiment, the model should be able to predict the meniscus height fluctuations as a function of time. APPENDIX C provides a more detailed description of how the measured voltage from the model is transformed into a meniscus displacement.

In addition to the model validation, measuring the meniscus height as a function of time would allow for a small amount of meniscus control to be introduced to the system. From preliminary testing and model experiments, it was determined that the positive and negative displacement rate of the piezoelectric disk is the driving factor behind drop formation and meniscus dynamics. Therefore, in order to get a more sine-like wave for the meniscus vibrations, it was necessary to tune the duty time of the vibrating meniscus driving waveform to the positive and negative slopes of the naturally occurring waveform. Too early or too late of a return to zero voltage on the vibrating waveform would result in non-sinusoidal meniscus fluctuations that would be difficult to uncouple from the dominant sinusoid. By measuring the meniscus height's response to a single positive voltage step, it is possible to determine the best time at which to trigger the negative voltage step so as to maintain a sinusoidal behavior. The single positive voltage step waveform is shown in Figure 4.2. Due to the multitude of available waveforms that could be used for vibrating the meniscus, a simple semi-square wave was used for all experiments involving a vibrating meniscus. This semi-square wave is documented in Figure 4.3.

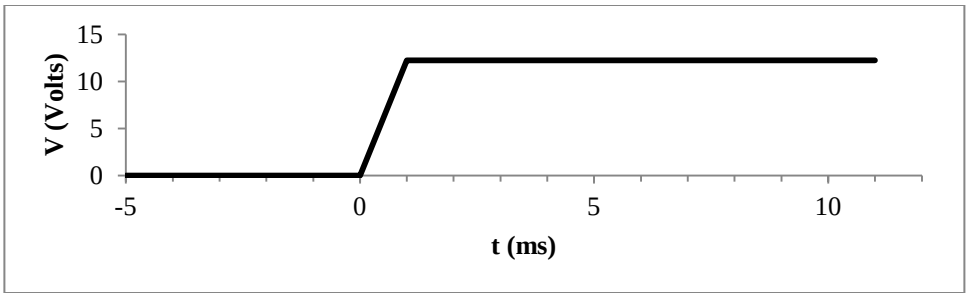

Figure 4.2: Voltage applied to piezoelectric disk as a function of time for the input step function.

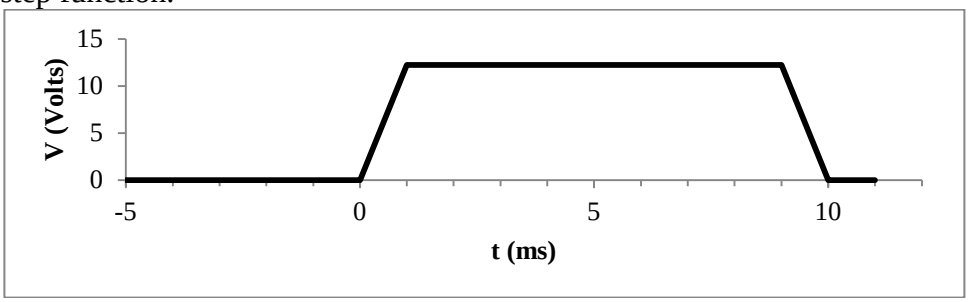

Figure 4.3: Voltage applied to the piezoelectric disk as a function of time for the input square wave function.

Figure 4.4 demonstrates the development of the vibrating meniscus waveform. The case having a step voltage input of 12.25 V zero-to-peak (0-p), shown in Figure 4.4 as diamonds, demonstrates the natural response of the meniscus height to a step voltage input to the piezoelectric disk. Note that the meniscus displacement as a function of time deviates most from that of a sinusoid at around 9 ms. Driving the piezoelectric disk at frequencies equal to or greater than the dominant frequency observed here will force the meniscus vibrations to be predominantly controlled by the input waveform. Based on this measured response of the meniscus, the semi-square voltage waveform in Figure 4.3 was created. The negative slope was triggered to start at 9 ms in order to align with the time at which the uncontrolled response deviated most from a sinusoidal behavior. This results in a full duty time of the vibration cycle of 20ms, which translates to a frequency of operation of 50 Hz. The lowest frequency

operational mode was selected in order to improve the performance of the LEM model when driving the meniscus vibrations. This waveform was then used to create two independent measurement series of the meniscus height as a function of time, which are shown in Figure 4.4 as separate cases through the use of triangle symbols and plus-sign symbols.

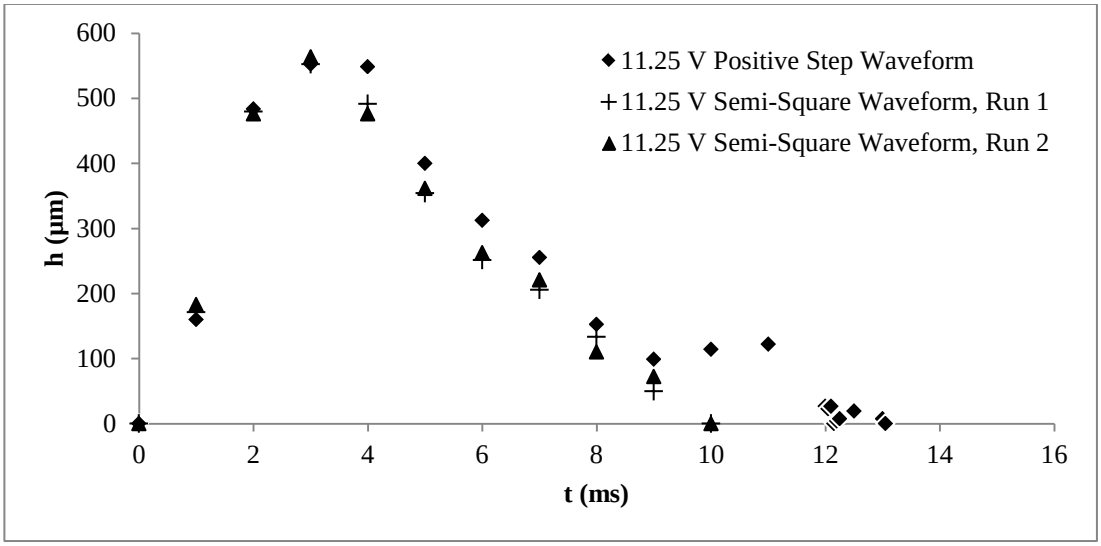

Figure 4.4: This figure shows the meniscus behavior as a function of time when triggered by two different vibration cycle waveforms. The 11.25 V Positive Step Waveform case measures the meniscus height response to the positive voltage step waveform shown in Figure 4.2. The 11.25 V Semi-Square Waveform cases, Run 1 and Run 2, are measurements of meniscus height response to the semi-square wave input shown in Figure 4.3. Time, t, is measured from the start of the driving waveform cycle.

The two square wave cases, Run 1 and Run 2, demonstrate good repeatability of meniscus vibrations and strong control over meniscus vibration mode. As an aside, it should be noted that the meniscus plot in Figure 4.4 does not indicate any negative displacement values. This is because the negative displacement of the meniscus could not be determined with the current experimental setup. It was assumed that the

negative displacement response would mirror that of the positive displacement response across the x-axis. Therefore, the driving vibration waveform shown in Figure 4.3 was selected as the background vibration input for determining the effect of meniscus vibrations on drop formation.

4.4.2. DROP FORMATION WITHOUT A VIBRATING MENISCUS

Drop formation without a vibrating meniscus is one of the critical experimental test conditions for both validating the model and for testing the abstract. The drop formation without a vibrating meniscus acts as a control for drop characteristics of drops formed by the established experimental setup. It also acts as a control for tuning the predictive model. These data were used as a means of testing the repeatability of drop production. Between tests, it was often necessary to completely dismantle the droplet generator, clean it, and reassemble it. Testing to see if drop production was consistent in drop shape and volume was the only way to see if the drop generator had been assembled correctly. Four different semi-square driving waveforms were considered for the drop generation process and are shown in Figure 4.5, Figure 4.6, Figure 4.7, and Figure 4.8 which correspond to voltage pulses with magnitudes of 20.25 , 22.5 , 33.75 , and 39.375 Volts (zero-to-peak), respectively.

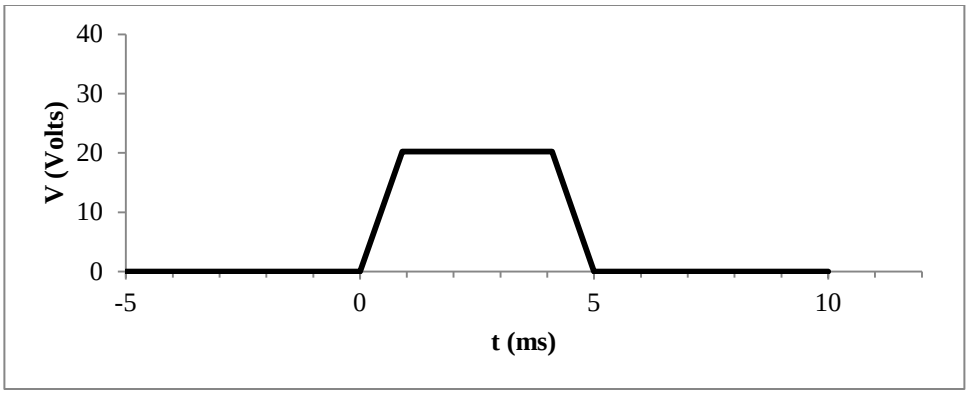

Figure 4.5: A plot of driving voltage versus time for the 20.25 V (0-p) pulse.

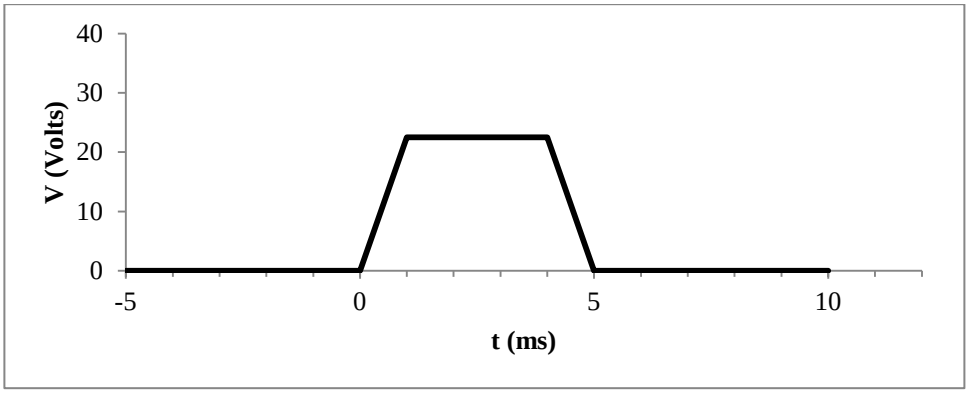

Figure 4.6: A plot of driving voltage versus time for the 22.5 V (0-p) pulse.

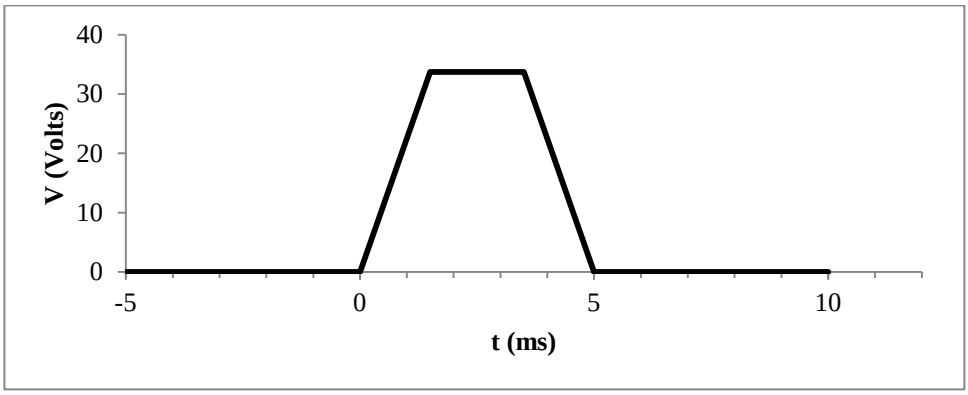

Figure 4.7: A plot of driving voltage versus time for the 33.75 V (0-p) pulse.

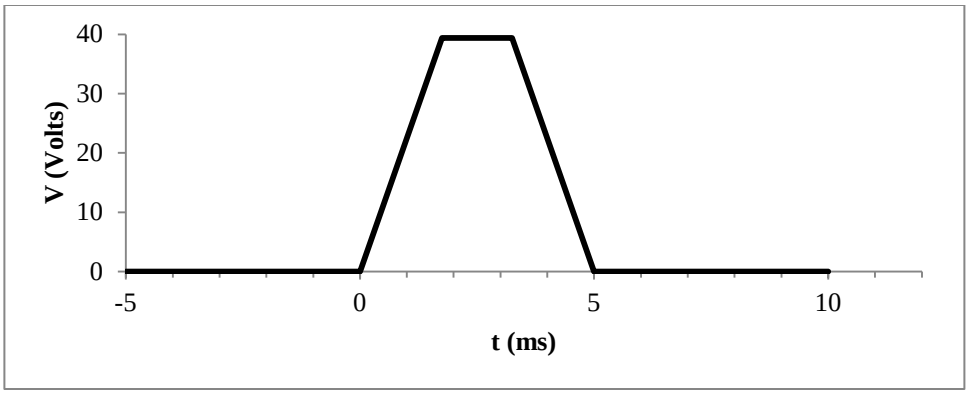

Figure 4.8: A plot of driving voltage versus time for the 39.375 V (0-p) pulse.

Take note of how the driving waveforms in Figure 4.5 through Figure 4.8 all have the same rising and falling slopes as one another; the only thing that differs in these three waveforms is the maximum amplitude of the driving waveform. The voltage pulses were defined in this way so that the voltage change only corresponded with a change in the absolute volume displaced by the piezoelectric disk, not how fast the piezoelectric disk displaces the volume. This allows for the model and experiments to isolate the effect of the amplitude of the driving waveform (increases in driving volume displacement) from the effect of stronger impulses due to the piezoelectric displacement (increases in driving volume flow rate).

In-case repeatability was verified by checking the drop position and size for consistency from one drop to the next within the same case (i.e. same droplet generator assembly run and same driving voltage waveform). This was concluded because two consecutive drops within the same case must have the same velocity if the drop's position at a given time is the same in two separate photographs. This is considered sufficient proof of repeatability for each case independently. However,

four cases of different drop generator assemblies but the same 22.5 V (0-p) voltage pulse input were explored in more detail. Although not used specifically for demonstrating across-case repeatability, the increased data sets for these four cases allow for velocity calculations later in the project.

To establish across-case repeatability, the average drop volume was calculated for seven independent assemblies of the droplet generator. Figure 4.9 demonstrates the repeatability of the drop formation and drop generator assembly across these seven independent assemblies, which were also spread out across multiple days. The drop formation for all seven assemblies was driven by the 22.5 Volts (0-p) driving waveform, as applied to the piezoelectric disk, shown in Figure 4.6. The drop volumes for this voltage, shown as filled in circles in Figure 4.9, are all approximately the same value within the error of the experiments, with one exception ,the data point for the second droplet generator assembly. A line representing the combined average drop volume for all seven assemblies is indicated by the solid horizontal line on Figure 4.9; the dotted lines above and below the solid line represent the calculated uncertainty of this average. The one case that does not lie near this average is the drop volume for the second assembly.

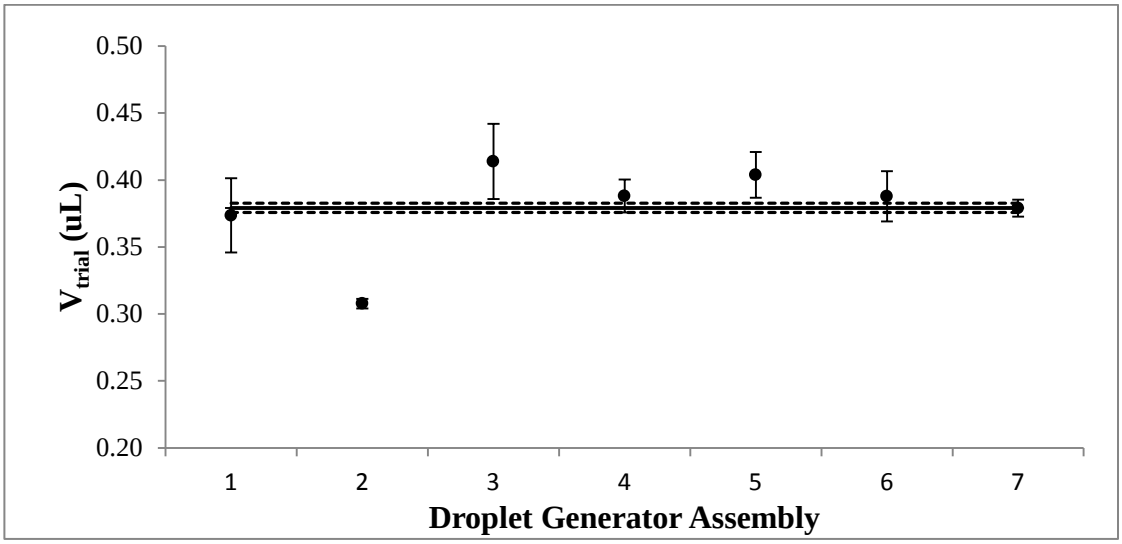

Figure 4.9: A plot of drop formation volume, V_d, repeatability from one assembly to the next. Each point represents an average drop volume for that day with the respective error of the mean bounding each data point.

The most likely explanation for why the second assemblies drop volume failed to match that of the rest of the trials for the 22.5 Volt pulse is air entrapment. Air entrapment results in a decreased pressure pulse at the nozzle exit for the same applied piezoelectric voltage. The decreased pressure is a result of trapped air bubbles compressing and absorbing some of the pressure pulse energy. The decrease in pressure pulse energy at the nozzle exit decreases the driving pressure for drop formation, which is expected to reduce the drop volume (Sangplung and Liburdy, 2009). Another indication that air entrapment could be a cause of the decreased drop volume for the second drop generator assembly case is the smaller sample variance of the drop volume (seen on the plot as a smaller error of the mean). The compression of an entrapped air bubble will act as a damper to the pressure pulse. The damper would

tend to dampen out any variation in pressure pulses from one pulse to the next and may therefore result in less variation in drop volumes for a given trial.

Despite best efforts and rigorous attempts to remove all air bubbles from within the drop generator, there were many drop generator assemblies that had to be disassembled and reassembled because of air bubble entrapment. Air entrapment was usually obvious because a drop would fail to form under the same conditions as a previous setup. Air entrapment was the only possible thing that could change from setup to setup that would reduce drop volume since the same plenums, fluids, and drop generator parts were used each time. Therefore, the majority of these failed setups were detectable prior to data collection. However, several of the earlier trials, such as the second assembly case shown in Figure 4.9, were aiming to establish repeatability. Since the drop volume data for these early trials were taken before a standard was established, the setups were susceptible to failed setup attempts that still produced drops despite the presence of a small amount of air entrapment. This may be what happened in the second assembly case.

Empirical drop volume data for drops formed by the other three drop waveforms were also collected. Using a variety of voltage waveforms provides a better opportunity with which to test the robustness of the model. The addition of these three additional driving waveform voltages makes it such that any modifications to the model must satisfy the experimental results from several test conditions. If the model can be modified so it can satisfy the experimental results for all the test conditions, then the final modified model will be more robust.

Finally, a few notes should be made in references to how the driving voltage will effect drop velocities. Similar to the drop volumes, the drop velocities will increase with increases in driving waveform maximum voltage. The important result to take away from this relationship is that higher velocity drops will traverse the distance of the field of view in less time than drops traveling at a lower velocity. As such, too large a voltage pulse may result in drops that move so fast that they do not reach break-off before the leading edge of the drop is already passing out of the field of view. This is due to the fact that break-off times are largely unaffected by the pressure pulse in the circuit (Roy and Adams, 1985). Proof of this was observed in the cases where the 39.375 V (0-p) waveform pulse shown in Figure 4.8 was used to drive drop formation. Preliminary tests were able to yield drop volumes because the drop would detach just before the leading edge passed out of the field of view for the camera, but obtaining velocities for this same case proved to be difficult because less than two milliseconds later the drop leading edge would be passing out of the field of view. To prevent this from occurring during data collection, the maximum voltage pulse waveform used to generate drops was restricted to the 33.75 V case. The lower bound was set to match the 22.5 V case because: one, preliminary data collection provided a broader set of values to compare the model too, and two, the 20.25 V case was inconsistent when forming drops. Restricting the investigation to these two voltage pulse values, the 22.5 V and 33.75 V cases, in theory captures the upper and lower bounds of the measurable drop formation range for the current droplet generator and camera setup.

4.4.3. DROP FORMATION WITH A VIBRATING MENISCUS

The purpose of the model development is to accurately predict drop formation in the presence of a vibrating meniscus. Therefore, it is essential that one have accurate data of drop characteristics for drops formed in the presence of a vibrating meniscus in order to validate the models functionality. It is equally important that real data be collected to demonstrate how a vibrating meniscus affects drop formation.

Here, the study of drop formation and of meniscus vibrations is combined. The vibration waveform was defined in section 4.4.1 and is used to vibrate the meniscus. Drop generation was then triggered with the voltage waveforms defined in Figure 4.6 and Figure 4.7. The timing of the drop generation is triggered at different phases in the vibration waveform cycle to determine the effect this has on drop formation characteristics. More specifically, the drop generating waveform is triggered at phase shifts of $\pi/3$, $2\pi/3$, $4\pi/3$, and $5\pi/3$ from the start of the vibration waveform cycle. Figure 4.10, Figure 4.11, Figure 4.12, and Figure 4.13 illustrate, in the time domain, the combined meniscus vibration and droplet pulse voltage waveforms that correlate with the 22.5 V (0-p) triggered pulse cases at phase shifts from the start of the meniscus vibration waveform of $\pi/3$, $2\pi/3$, $4\pi/3$, and $5\pi/3$, respectively. The voltage waveforms for the combined 33.75 V (0-p) pulse and vibrating meniscus waveform are omitted from the text because they are nearly identical to the Figure 4.10 through Figure 4.13, where the only changes to the figures are to replace the 22.5 V (0-p) pulses, documented in Figure 4.6, with 33.75 V (0-p) pulses, documented in Figure 4.7.

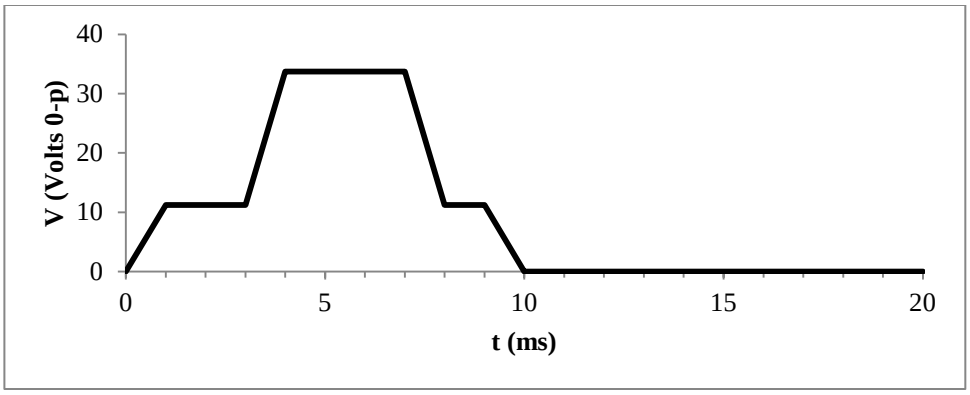

Figure 4.10: Time domain definition of the combined vibrating meniscus voltage waveform and the drop triggering pulse voltage waveform at a phase shift of π/3.

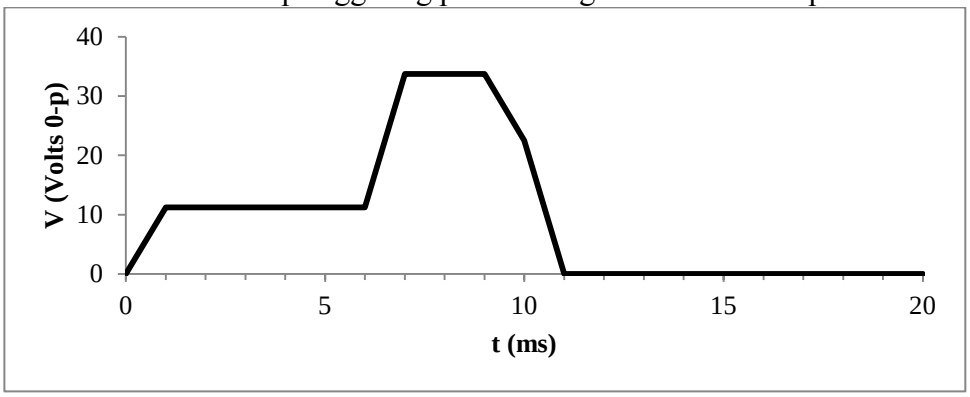

Figure 4.11: Time domain definition of the combined vibrating meniscus voltage waveform and the drop triggering pulse voltage waveform at a phase shift of 2π/3.

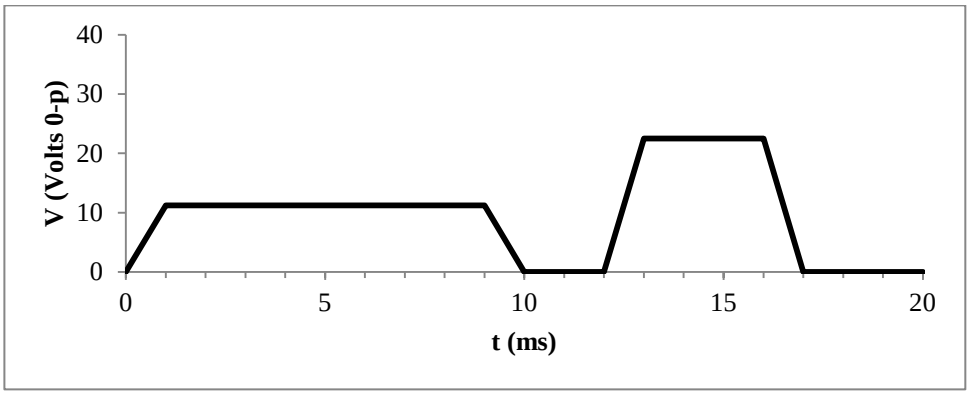

Figure 4.12: Time domain definition of the combined vibrating meniscus voltage waveform and the drop triggering pulse voltage waveform at a phase shift of 4π/3.

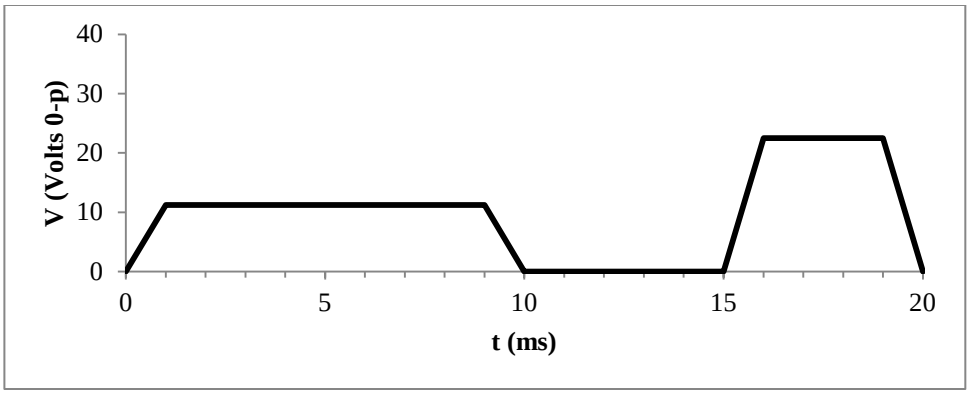

Figure 4.13: Time domain definition of the combined vibrating meniscus voltage waveform and the drop triggering pulse voltage waveform at a phase shift of $5\pi/3$.

4.5. DATA ANALYSIS

All the experimental data collected was in the form of photographs of the drops, drop formation, and meniscus vibrations. In order to make sense of these photographs and derive drop volumes, drop velocities and meniscus vibrations from them, an image analysis code was written in MATLAB. This code performed a number of permutations to an imported image in order to output a binary image that represents the fluid-only projected area.

To determine the drop volume, it was assumed that all the drops were axisymmetric. A drop's center of mass was calculated from its projected area. The code would then take half of the drop's project area to one side of the vertical axis, revolve it around the axis of symmetry, and integrate the resulting volume.

To determine the drop velocity, it was again assumed that the drops were all axisymmetric. A drops' center of mass was again determined using the projected area of the fluid. Velocity was calculated by finding the average frame-to-frame displacement of a drop from one pair of photos to the next. A more detailed

description of how this frame-to-frame velocity is calculated can be found in the next section, 4.6, on uncertainty analysis. The frame-to-frame velocity could then be related to an average time between the two pairs of photos and a velocity versus time relationship for drops can be established.

For more information on how the code processes the images and outputs the results, the reader is referred to APPENDIX F where the image analysis code has been included in its entirety. The code itself is heavily commented for ease of understanding, and an introduction in APPENDIX F outlining the code structure provides further guidance into the operation of the code.

4.6. UNCERTAINTY ANALYSIS

All the experimental data was measured using the camera and delay generator specified in section 4.2, therefore these are the two dominant sources for experimental error. The delay generator was accurate to <100 ps of jitter, which translates to a relative error of < 0.0002% for time delay triggers in the 50 μs range (the smallest time difference used in the experiments). Such a small uncertainty was considered negligible for all uncertainty calculations pertaining to velocity. The position, on the other hand, has a larger uncertainty that is determined by the uncertainty of the MicroMAX camera. The uncertainty of the position of the drop drives both the uncertainty in the drop velocity as well as the uncertainty of the drop volume.

In order to define the uncertainty of the MicroMAX camera, the dimensional resolution of the MicroMAX was calibrated with two optical slits, both 300 μm wide. One slit was a blacked out line on a clear film and the other was a slit of clear film

surrounded by black. Both slit/line types were used so as to obtain an average that was unbiased based to light diffusion around an edge. Fourteen data points for each slit were recorded, where each data point is the span in pixels across the slit. The averages of the pixel-width for the slit/line were combined for a overall average pixel-width of the slit/line. The uncertainty in the average was also determined for the pixel-width of the slit/line. The calibrated pixel-size, in um, was then calculated based on the slit/line width (300 μm) and the average pixel-width of the slit/line. To propagate the pixel-width uncertainty to the pixel-size, the same conversion was applied. This is because there is no known uncertainty for the slit/line, it was only reported as 0.3 mm. The resulting pixel size is approximately 3.8 μm/pixel with a resulting uncertainty of 0.90 nm/pixel.

The drop velocity is reported two different ways in the results. The first is an overall average drop velocity for a single waveform input case, e.g. a single representative average velocity would be reported for the case of the 22.5 V (0-p) pulse and first drop generator assembly. This method of reporting the drop velocity finds the mean of all the velocities determined using the second method of reporting drop velocity. The second method of reporting drop velocity finds the 'instantaneous' drop velocity by calculating the average drop velocity between two pairs of dual-image photos.

The two pairs of dual-image photos can be combined in a total of four different ways, without referring to a photo within the same dual-image pair, to calculate a drop

velocity. These four independent measures of drop velocity between two pairs of images are shown in equations 4.1 through 4.4:

$$v_1 = \frac{d_{2,1} - d_{1,1}}{\Delta t} \quad 4.1$$

$$v_2 = \frac{d_{2,2} - d_{1,1}}{\Delta t + dt} \quad 4.2$$

$$v_3 = \frac{d_{2,1} - d_{1,2}}{\Delta t - dt} \quad 4.3$$

$$v_4 = \frac{d_{2,2} - d_{1,2}}{\Delta t} \quad 4.4$$

$$v_{avg} = \frac{\sum_{i=1}^{4} v_i}{4} \quad 4.5$$

Equation 4.5 shows how the four velocities in equations 4.1 through 4.4 are combined to calculate an 'instantaneous' drop velocity. Note that in order to determine the numerator, the Pythagorean theorem is used to convert the 2-d coordinate displacement into a linear positional displacement. Also note that the 'instantaneous' velocity does not have a time step that corresponds with first set of photos nor the second set. The time associated with the 'instantaneous' velocity is taken to be the mean of the two times at which the two pairs of images were taken.

The dt term included in equations 5.2 and 5.3 is the increased or decreased time span between images due to the laser timing. For all the images of drops captured to determine velocities, dt was 50 µs and the value of Δt was either 1 ms or 500 µs. This value of dt may therefore have an effect on the calculation of the drop velocity. In order to assess the effect of the included dt, the average velocity and it's uncertainty was determined for a worst case scenario drop velocity calculation with and without the inclusion of the dt in equations 4.2 and 4.3. To calculate the average

velocity without the change in the time span by dt, the positional displacements of each velocity set are averaged and then the whole is divided by the time step between image pairs. To ensure a worst case scenario, the pair of photos were taken only 0.5 ms apart so as to increase the affect of the dt parameter in the final determination of the velocity. The results of this exploration are reported in Table 4.1.

Table 4.1: This table outlines the difference between calculated velocity of the drop using equations 4.1-4.5 versus using a simple average of displacements

	Value	Uncertainty in Velocity
v_1 (pix/s)	1.03E+05	2.83E-02
v_2 (pix/s)	1.00E+05	2.83E-02
v_3 (pix/s)	1.02E+05	2.83E-02
v_4 (pix/s)	9.91E+04	2.83E-02
v_{avg} (pix/s)	1.01E+05	6.24E+01
$v_{w/dt}$ (m/s)	0.385	2.38E-04
$v_{w/o,dt}$ (m/s)	0.385	
% Change	0.05%	

As can be seen in Table 4.1, the inclusion of the dt only changes the final value by 0.05%. By comparison, the error of the mean for the four velocities is 0.06% of the calculated velocity when including the dt in the definition. Assuming that 0.05% is an acceptable error for the velocity, it is more economical to calculate the drop velocity by using an average of the displacement divided by the time between image pairs rather than the average of the full defined velocity. Therefore, all drop velocities measured using the second method of velocity determination will be calculated using the following equation:

$$\mathrm{v_{avg}} = \frac{\sum_{i=1}^{4} \mathrm{d_i}}{4 \cdot \Delta \mathrm{t}} \qquad 4.6$$

where d_i is the distance between two drop centers as calculated by the Pythagorean theorem.

Returning to the first method of determining a drop velocity, one can now calculate a representative velocity and an associate uncertainty for a case as a whole. Copied below into Table 4.2 are some example velocities and their uncertainties for a selection of cases.

Table 4.2: A table demonstrating the inaccuracy of reporting the drop velocity as an individual representative average of all the 'instantaneous' velocities. The cases listed in this table are differentiated by the drop generator assembly run; they all have the same input driving waveform of 22.5 V (0-p).

Drop Generator Assembly Run #	$\bar{v}_d$	$\sigma_{\bar{v}_d}$	% Error of the Mean
3	0.083	0.039	46.83%
4	0.119	0.037	31.54%
5	0.118	0.034	29.25%
6	0.232	0.025	10.62%

The inaccuracy of measuring the droplet velocity and reporting it as an average value with the current experimental setup is shown in Table 4.2. Out of the sets of data collected, these four were the only ones with enough time series velocity data to calculate a representative mean velocity for the case as a whole, and therefore the only ones which have a representative uncertainty with respect to the representative velocity. The most important piece of information to take away from Table 4.2 with respect to uncertainties is that the case based mean velocities have significantly large sample errors, the largest of which is nearly 50% of the reported velocity. Interestingly, both the absolute and the relative uncertainty of the average drop velocity decreases with increasing drop velocity. However, despite being different

cases, the four cases in Table 4.2 all share the same driving waveform voltage. The only difference between each case is that the droplet generator has been disassembled and reassembled in between runs. A more thorough investigation of these drop velocity results is discussed in the results.

Where the uncertainty in pixel size will play the largest role is likely to be the volume of the drop, since it is calculated based off of the projected area of the drop. The equation used to calculate the volume of the drop is: V=pi*sum(r^2*h

$$V = \pi \cdot \sum_{i=1}^{n} {r_i}^2 \cdot h \qquad 4.7$$

Where h is equal to 5 pixels and n is equal to the height of the drop (in pixels) divided by h. In principal, this equation numerical calculates the integral of the droplet cross sectional area around the axis of symmetry by calculating the volume of a finite number of disks and adding them together. The uncertainty for this equation would be difficult to express in a simple equation here, so worst-case scenario will be used instead. Assuming that the drop is a perfect cylinder with a length equal to the field of view height and a diameter equal to one-third the field of view in width. This size of droplet, and thus error percent, is unrealistically large, but it provides a simple framework to work in that can be thought of as an upper bound to the volume uncertainty. For such a volume, the drop volume would be defined by the equation:

$$\mathrm{V} = \pi \mathrm{r}^2 \mathrm{h}\ ; \qquad 4.8$$

$$where\ r = \frac{1}{3} * (1030)\ and\ h = 1300$$

The resulting volume, in cubic pixels, is 4.81 x 10^8. The uncertainty for this volume is determined by the following equation:

$$\sigma_V = \pi r^2 h \cdot \sqrt{\left(2\frac{\sigma_r}{r}\right)^2 + \left(\frac{\sigma_h}{h}\right)^2} \quad 4.9$$

The uncertainty of *r* is 0.02 per pixel boundary, which becomes a total of 6.86 pixels for the radius. The uncertainty for *h* is equal to 0.02 per pixel boundary as well, which translates to a total stack potential error of 26 pixels. Note that although the height of the drop is actually fixed to be no larger than the height of the field of view, the maximum pixel error obtained above will be used for the purposes of this calculation. Substituting these values into equation 4.9, one finds that the maximum uncertainty of the volume is 1.16×10^7. The maximum relative uncertainty of the volume is therefore about 2.4%. A more realistic envisioning of the droplet size, one that occupies 20% of the width of the field of view and 75% of the height of the field of view reduces this uncertainty to a value of about 1.7%. Therefore, the smaller the drop, the smaller the relative uncertainty. As a comparison, the percent error of the mean drop volume without a vibrating meniscus was 2.94% with a maximum percent error of 4.97% and a minimum percent error of 0.82%.

5. RESULTS AND DISCUSSION

The following chapter outlines the results of the experimental and analytical investigations as obtained via the methods explained in the experimental methods and analytical model chapters. Observations and discussion of the figures and data will be presented in tandem with the results. The experimental data is discussed first to acquaint the reader with the important experimental observations made during the study. Following the discussion of the presented experimental results, the un-calibrated analytical model will be compared to the experimental results. Finally, a best attempt at a working predictive LEM model will be presented.

5.1. EXPERIMENTAL RESULTS

The drop formation data has been analyzed and grouped into two main experimental sections for comparison purposes. The first section demonstrates the behavior of drop volume and drop velocity data as a function of driving voltage. This section also explores the relationship between drop velocity and time. All data reported in the second section pertains only to drop formations without a vibrating meniscus. The second section reports drop volume and velocity data as a function of impulse waveform phase during a vibrating meniscus waveform cycle. This section of experimental data also explores the observed relationship between drop velocity and time for the drops formed with a vibrating meniscus. The reader is referred to section 4.4.1 for a demonstration of the functionality of the vibrating meniscus and how it is controlled. The results presented in the experimental section serve as a baseline against which the LTspice IV model will be compared and/or calibrated. All errors

bars on figures in this chapter are the statistical error of the mean for the data point the error bar is applied to.

5.1.1. DROP CHARACTERISTICS

The data presented in this section were not collected in the presence of a vibrating meniscus. Figure 5.1 shows the variation of drop volume as a function of the driving voltage into the piezoelectric disk. All the plots and tables of recorded data have been adjusted to reflect the voltage applied to the piezoelectric disk.

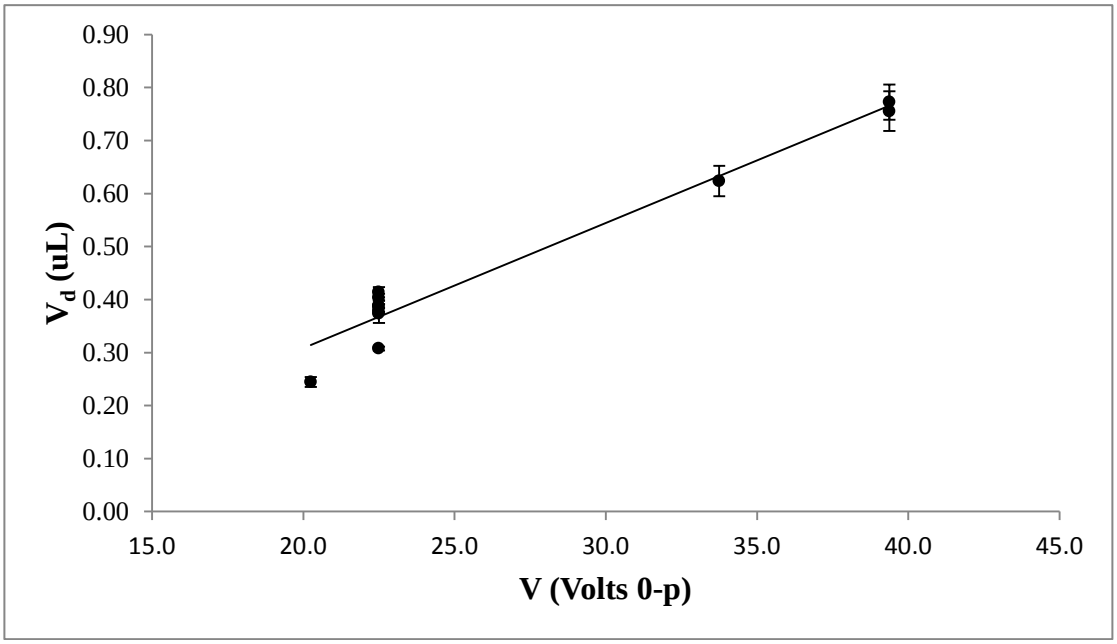

Figure 5.1: Drop volume as a function of voltage applied to the piezoelectric disk.

Figure 5.1 is a plot demonstrating the drop volume variation as a function of the driving voltage applied to the piezoelectric disk. The drop volume appears to vary linearly as a function of voltage. A linear variation is expected since the piezoelectric disk has a linear relationship between its displacement and the driving voltage. The

linearly increasing displacement would lead to linearly increasing pressures and volume flow rates within the drop generator. Increases in pressure pulse amplitude or volume flow rate will result in larger drop sizes and volumes. Therefore, the linear voltage dependence of the drop volume is a reflection of the piezoelectric disks' displacement as a function of applied voltage.

Recall from chapter 4 the wide variations in the drop velocity for cases that only different in which droplet generator assembly run they pertained to. In an attempt to further explore the source for these discrepancies between cases that should show the same mean drop velocity, plots were generated for the 'instantaneous' mean drop velocity as a function of time (Figure 5.2 through Figure 5.5) for the four cases with time series drop data, no vibrating meniscus, and a driving voltage input waveform of 22.5 Volts (0-p) as defined by Figure 4.6. Each data point on the figures is an 'instantaneous' mean drop velocity, calculated, as specified in the experimental methods, by averaging the four velocities one can calculate between one pair of images and the next.

Note that in Figure 5.2 through Figure 5.5 the time paired to a calculated mean drop velocity is the average time between the two sets of dual-image collections, t_{avg}, as discussed in the experimental methods. Time was measured with respect to the start of the voltage pulse that is driving the piezoelectric disk. Note that the linear trendlines shown on the graphs are not statistically indicative of a causal relationship, instead they attempt to demonstrate the overall trend for the mean drop velocity to increase with respect to time.

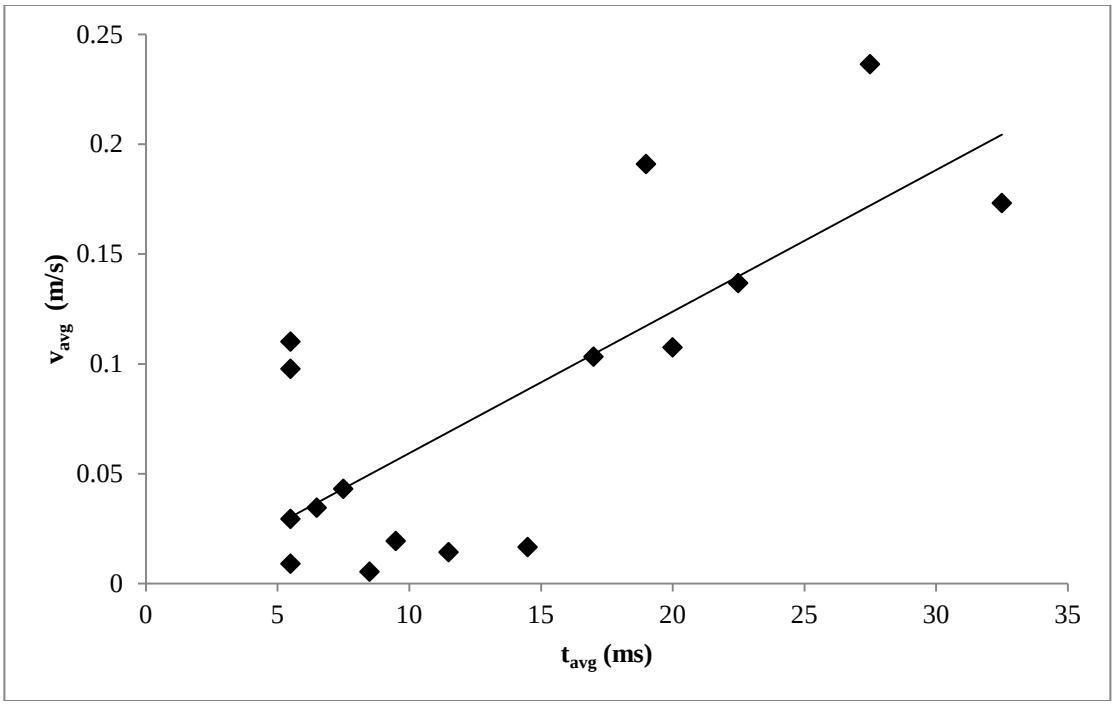

Figure 5.2: Droplet generator assembly, run 3, plot of average drop velocity versus time, no vibrating meniscus, driven by the 22.5 V (0-p) voltage waveform.

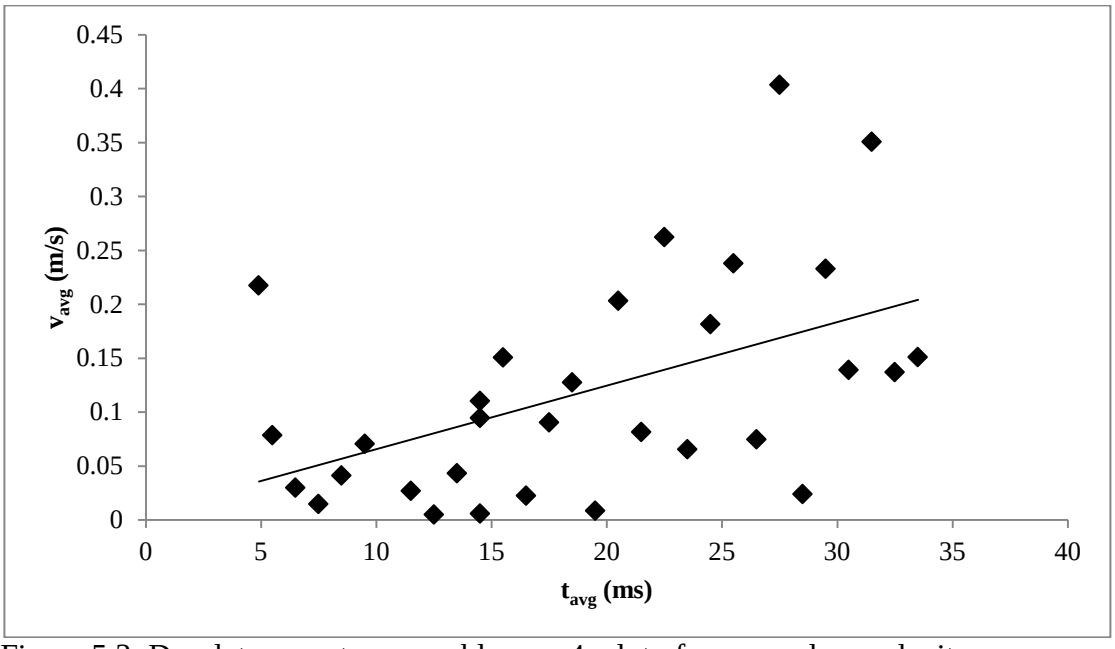

Figure 5.3: Droplet generator assembly, run 4, plot of average drop velocity versus time, no vibrating meniscus, driven by the 22.5 V (0-p) voltage waveform.

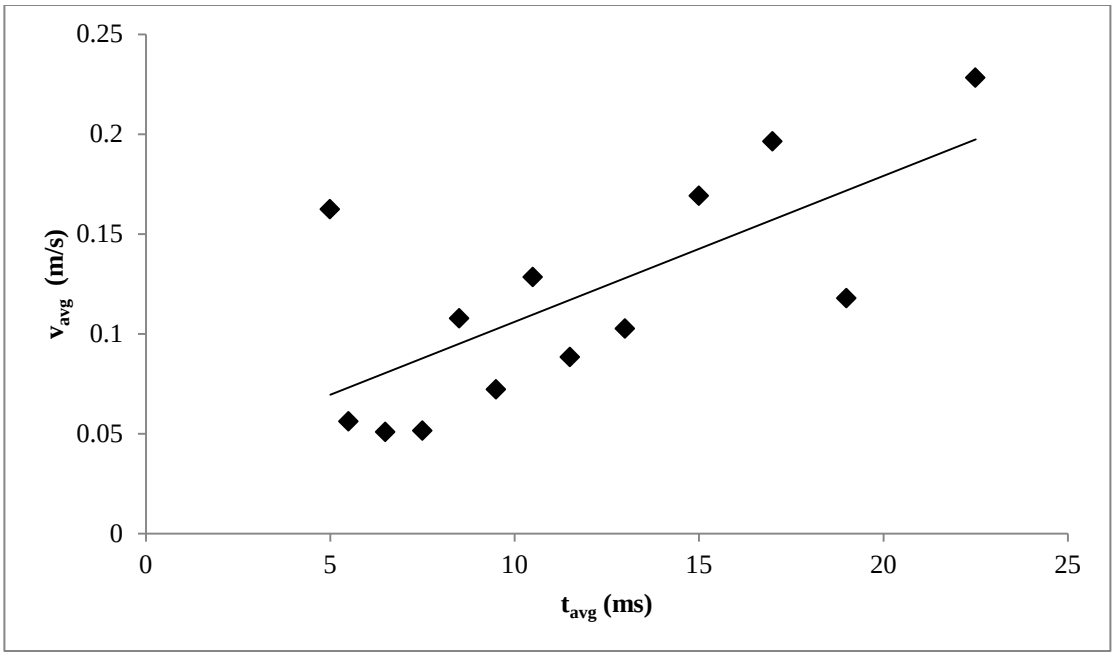

Figure 5.4: Droplet generator assembly, run 5, plot of average drop velocity versus time, no vibrating meniscus, driven by the 22.5 V (0-p) voltage waveform.

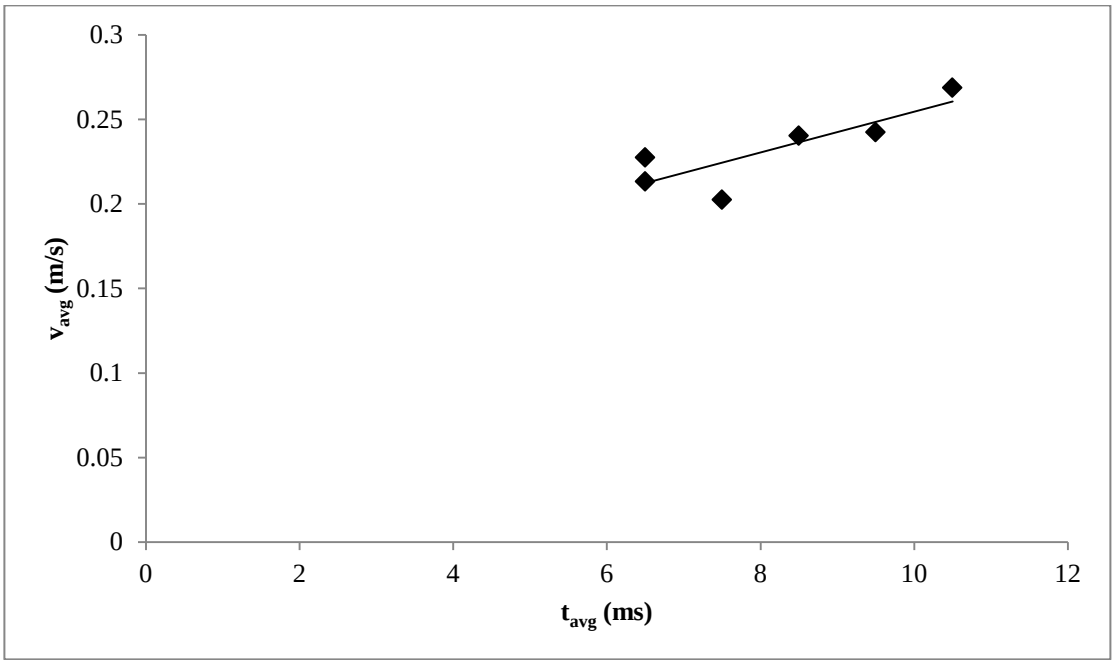

Figure 5.5: Droplet generator assembly, run 6, plot of average drop velocity versus time, no vibrating meniscus, driven by the 22.5 V (0-p) voltage waveform.

Figure 5.2 through Figure 5.5 indicate that there is a non-constant mean drop velocity. As the time after the start of the waveform increases, the general trend in all four figures if for the drop speed to increase as well. This would explain why the study found case representative drop velocities to have large uncertainties. It would also explain why the larger velocities had lower uncertainties; the faster the drop is moving the less time it has to accelerate while still in the field of view of the camera. Less acceleration results in a smaller overall change in the drop velocity versus time. From this, it can be seen that a more accurate method of comparing drop velocities from separate cases is to compare plots of the 'instantaneous' velocity as a function of time from the separate cases to each other.

Since Figure 5.2 through Figure 5.5 all showed an upward trend for the velocity with respect to time, it is instructive to observe the behavior of the mean velocities as functions of time for all four cases on a single figure, Figure 5.6. Due to the large amount of scatter observed in each case, only the general trends for each case are shown on Figure 5.6. The cleaner plot allows one to see how the overall trends relate to one another in magnitude and slope. It is odd to note the significant difference in some of the velocity magnitudes, especially for the droplet generator assembly, run 6. Despite using the same input waveforms, having the same droplet generator, and outputting approximately the same size drops, only two of the cases' trendlines lie close enough to one another to consider them to be about the same.

The most notably different trendline shown in Figure 5.6 is the trendline that corresponds to the 6th droplet generator assembly. As far as the experiments go, the only thing that could have changed between this case and the three previous is the droplet generator assembly. Despite the drop's large velocity, it still has approximately the same volume as the other cases in Figure 5.6 (see Figure 4.9 for a record of the drop volume consistency for these cases). Since the drop volume is approximately the same, the drop generator cannot have differed by having air bubble entrapment. Since nothing else could have change, the only explanation that presents itself is a contaminant ended up in one of the droplet generator plenums. The decrease in volume would increase the pressure pulse on the nozzle exit and would increase the drop velocity. One may expect the drop volume to also increase, but at most it would increase by the volume of the contaminant, whereas the pressure pulse driving the drop velocity could be increased much more, especially if the contaminant was blocking the refill port.

A higher initial velocity of the drop would also be able to explain why the trendline was steeper. The higher velocity shortens the time span during which the drop velocity can be captured, which means less data for creating the trendline which could result in a skewed trendline slope. Also, the faster moving drop would have a longer thread attaching it to the meniscus at pinch-off. The inertial forces generated on the drop due to the tail retracting back into the main body of the drop could introduce additional acceleration factors that may hasten the drop's departure from the field of view.

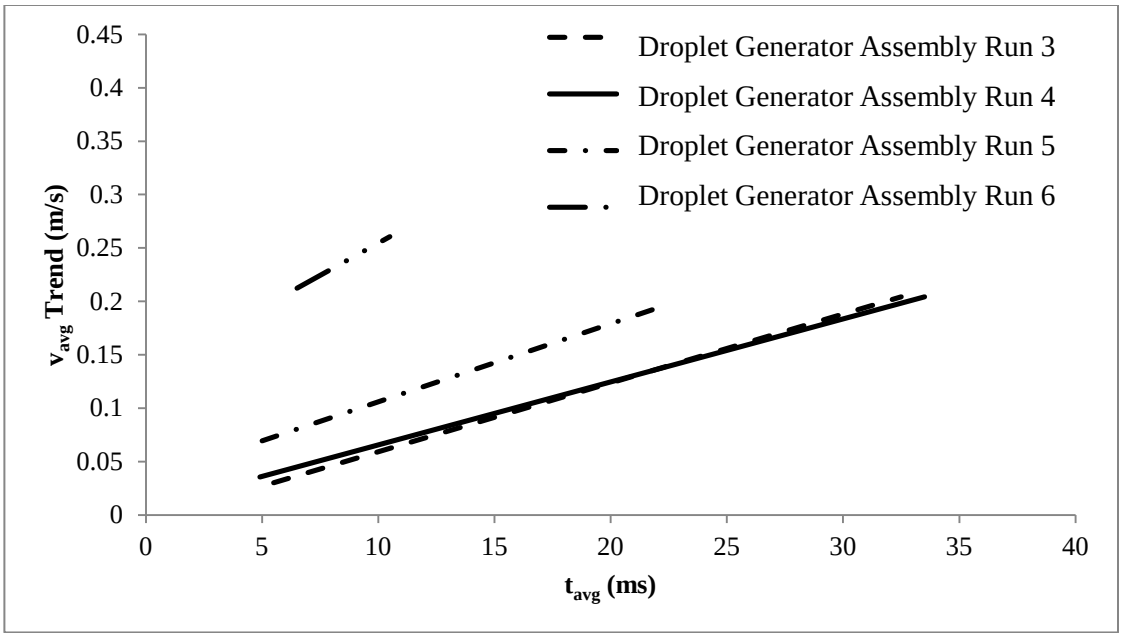

Figure 5.6: Comparative plot of general trends for the velocity versus time data generated in Figure 5.2 through Figure 5.5, same driving voltage waveform for each trendline, different droplet generator assemblies.

In conclusion, it was found that drop volume varies in a linear manner with driving waveform voltage. It was also found that the drop velocity varies greatly with respect to time but also found that, on the whole, the drop velocity tends to increase over time. Finally, it was found that air entrapment or contaminants can strongly affect the performance of a droplet generator and that utmost care should be made not to introduce any alien fluids, gases, or debris into a droplet generator when attempting to acquire high accuracy and high precision data.

5.1.2. DROP CHARACTERISTICS WITH A VIBRATING MENISCUS

Drop characteristics data were obtained for drop formation in the presence of a vibrating meniscus by combining the drop formation and meniscus vibration waveforms as explained in section 4.4.3. The resulting drop characteristics are

reported below, starting with an overall examination of the mean results, for voltage and velocity, as functions of the phase of the applied voltage pulse. In this context, the means were constructed with the more limiting process of averaging all the data for a single trial into one representative value. This was done in order to obtain qualitative comparison data of drop characteristics between trials with and without meniscus vibrations. The phase value was determined by taking the ratio of the voltage pulse trigger time, as measured from the start of the vibrating wave form in ms, to the full period (in ms) of the vibrating waveform; the phase is reported in radians.

Due to the case based averaging process, the results shown in Figure 5.7 and Figure 5.10 are qualitative representations of how the vibrating waveform affects drop characteristics at different phases in the vibration. Figure 5.7 and Figure 5.10 also show how an increase in the voltage pulse amplitude can affect the drop characteristics. Both figures have at least eight trials in them, four of which are at the low end drop production voltage pulse amplitude of 22.5 V (0-p) applied to the piezoelectric disk. The additional four trials were performed with the 50% larger 33.75 V (0-p) voltage pulse at the same phases as the original four trials.

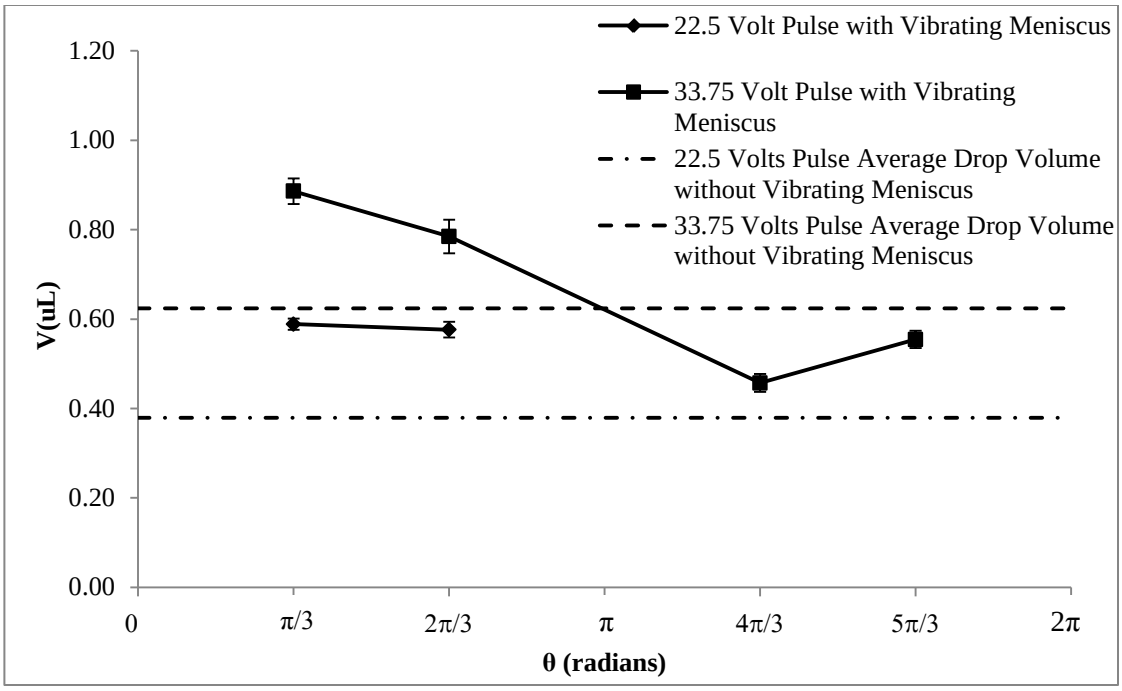

Figure 5.7: Trial-based average of drop volume, as measured from drops formed with a vibrating meniscus, as a function of the vibration phase at which drop formation was triggered.

Drop volume as a function of phase shift is plotted in Figure 5.7. Note that data for the drop volume and drop velocity was unattainable for the latter two phases of drop formation ($4\pi/3$ and $5\pi/3$) at the 22.5 V (0-p) pulse cases. This was because drop detachment did not occur in these two cases. For the $4\pi/3$ drop formation attempt at 0.5 volts zero-to-peak, the beginning of drop formation could be observed but the forming drop and meniscus were consistently pulled back into the nozzle. The negative tending slope at the end of the measured meniscus vibration cycle, seen in Figure 4.4, coupled with the negative displacement of the meniscus is most likely what prevented drop formation. The pressure pulse resulting from the 22.5 V (0-p) pressure pulse was not large enough in magnitude to overcome the multitude of adverse

conditions at this phase in the vibration waveform cycle. At this phase, one expects the meniscus to have a negative momentum. One also expects a negative displacement into the nozzle. The only aid to the drop formation would be the surface tension of the meniscus, which would be forcing the meniscus back toward equilibrium. However, once drop formation is triggered by the waveform generator and the meniscus begins to protrude out of the nozzle, the surface tension turns in toward the nozzle. All these factors combine and make it difficult for the drop to gain enough momentum for droplet break-off. The result is that the surface tension forces from the meniscus pull back the forming drop into the nozzle. An illustration of this process can be seen in below in Figure 5.8.

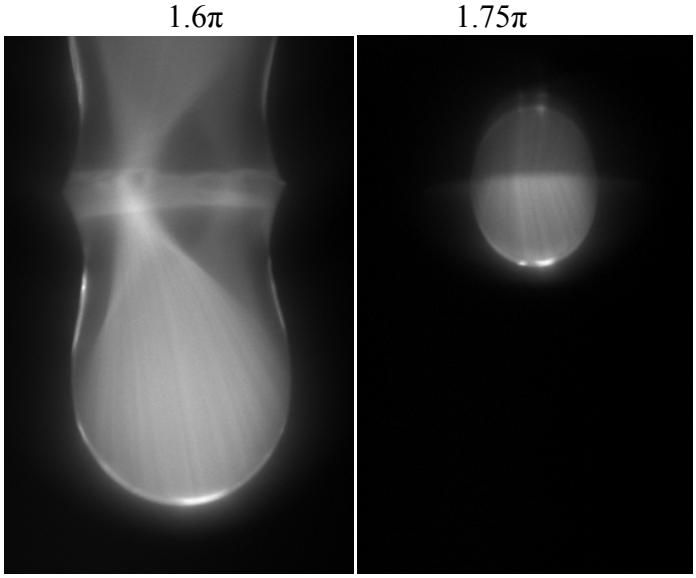

Figure 5.8: From the images above one can see that the drop formation is prevented due to the vibrations of the meniscus. These photos were taken for the 4π/3 voltage pulse phase shift. Note how the drop formation pulse has the appearance of starting to form a drop in the left image at 1.6π but by 1.75π in the right image, the drop formation has been prevented.

Many of the same conditions seen in the 4π/3 phase delay case also exist for the 5π/3 phase delay case. However, in this case the meniscus should be returning toward the equilibrium condition, which means the momentum of the meniscus should be in the same direction as the drop formation. However, the meniscus in this trial is still displaced into the nozzle, so it is not visible. Photos of the experiment appear to show the drop detach from the meniscus. However, it is inconclusive whether it realizes full detachment or not because the tail end of what appears to be a drop remains hidden inside the nozzle. The drop has such a low velocity that it is unable to travel away from the nozzle before being reabsorbed into the meniscus. A strong indication that the drop does detach is the presence of surface waves on the meniscus protrusion from the nozzle. The surface waves seen on the meniscus protrusion are similar to those seen in other trails where drops fully detach. See Figure 5.9 for a time series flow visualization of this process.

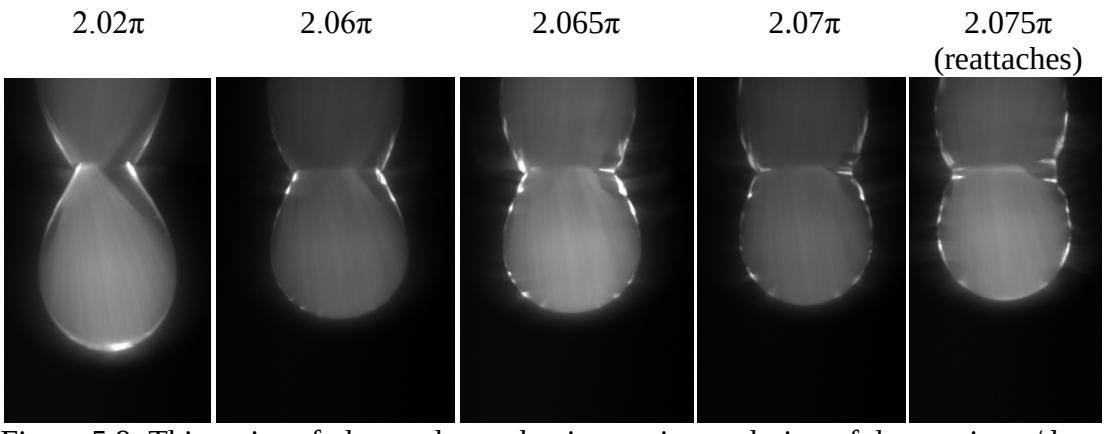

Figure 5.9: This series of photos shows the time series evolution of the meniscus/drop at the 5π/3 pulse phase test case with a vibrating meniscus and an input drop formation voltage pulse of 22.5 V (0-p)

It can be seen in Figure 5.7 that the phase at which a drop is triggered during a vibrating waveform cycle significantly affects the volume of the drop, within the error of the measurements. The average volume of drops formed during the positive displacement portion of the vibrating waveform cycle are larger for both pulse voltages during the positive displacement. As mentioned earlier, drops triggered during the latter part of the waveform cycle for the 22.5 V (0-p) trials do not have sufficient momentum. When the driving voltage for drop formation is increased to 33.75 V (0-p) and triggered in the latter part of the cycle, the average drop volume with a vibrating meniscus is lower than the trial-based average drop volume without a vibrating meniscus.

Triggering during the positive displacement part of the vibration cycle increases the drop volume over what would was observed in drop formation with a static meniscus. Triggering the drop formation while the meniscus is still expanding (i.e. while the meniscus has a forward momentum), at $\pi/3$, combines the positive momentum and pressure pulse to form larger drop volumes. If triggered while the meniscus is positively displaced but returning toward zero displacement, drop volumes are smaller than when triggered while the meniscus is both positively displaced and moving away from the nozzle. However, the volume of the drop is still larger than volumes observed when triggering a static meniscus. This indicates that both meniscus momentum and positional displacement have an effect on the final drop characteristics.

Increasing the triggering waveform voltage by 50% appears to decrease the relative effect of the vibrating meniscus. The ratio of drop volumes with vibrating meniscuses to drop volumes without vibrating meniscuses decreases when the triggering waveform voltage is increased. This demonstrates that meniscus dynamics may be mitigated by stronger driving waveforms. However, in practical applications, stronger driving waveforms could lead to larger amplitude and more complex meniscus dynamics that may take longer to dampen out or may cause unforeseen issues.

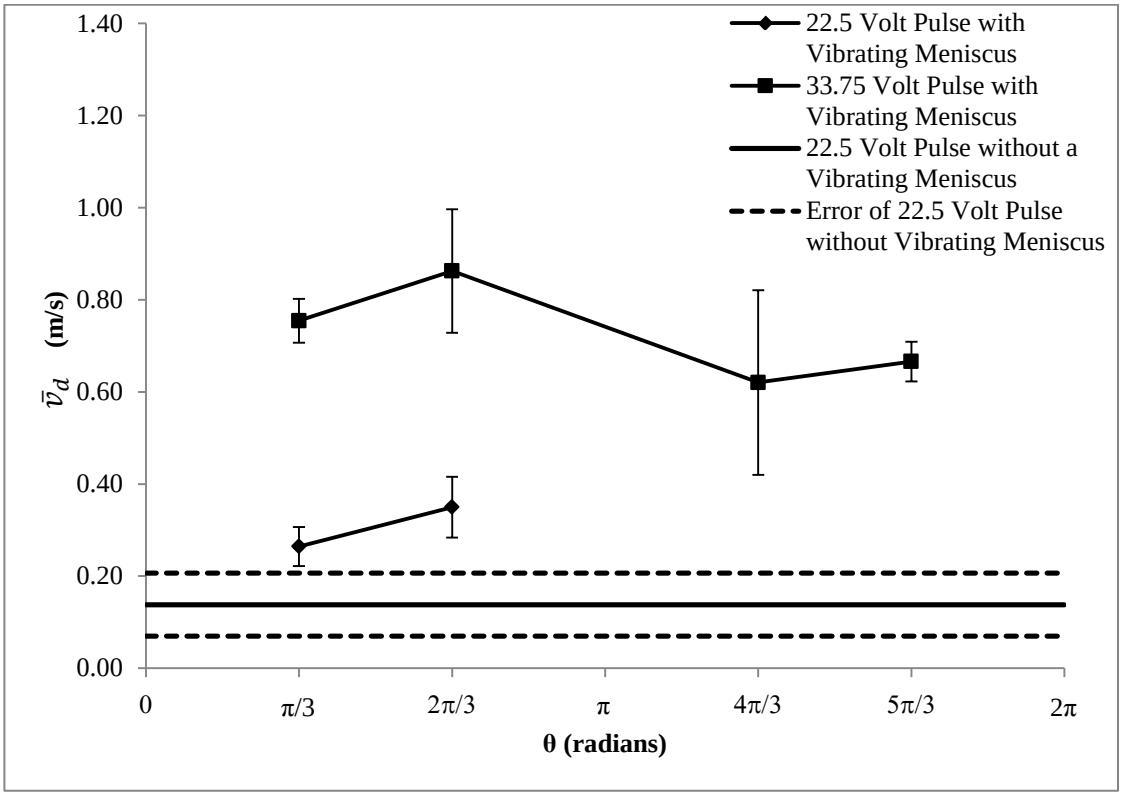

Figure 5.10: Average drop velocity, $\bar{v}_d$, as measured from drop velocities of drops formed through a vibrating meniscus. The average drop velocity is reported as a function of the vibration phase during which drop formation was triggered.

Figure 5.10 plots the average drop velocities, $\bar{v}_d$, for drop formation with a vibrating meniscus. Note that, unlike Figure 5.7 which showed comparative drop volumes for both 33.75 and 22.5 V (0-p) pulses, Figure 5.10 only shows comparison data for 22.5 V (0-p) drop velocities. This is because there is not enough data from the 33.75 V (0-p) trial condition with a quiescent meniscus to determine an average velocity for the static meniscus case. There was not enough data because sufficient time series information was not recorded to establish a base velocity for the static case with the 33.75 V driving pulse waveform; data for this case were initially collected only to demonstrate the drop volume-voltage relationship and to establish repeatability of drop formation at different input voltages. Figure 5.10 shows similar trends for the velocity of the drops as was seen in Figure 5.7 for the volume of the drops. As mentioned with respect to Figure 5.7, the 22.5 V (0-p) voltage pulse was unable to generate drops during the latter half of the meniscus vibration cycle, between π and 2π. From the average values for the velocity, it is not possible to make a definitive statement as to an observable pattern in Figure 5.10 because of the rather large error bars. However, the results do indicate that changes in the driving voltage affect the velocity of the drop at each phase. In addition, both the low and the high voltage test series indicate similar trends for the drops' velocities, at least for the first half of the waveform cycle.

When comparing the drop velocities with a vibrating meniscus to the drop velocities without a vibrating meniscus, Figure 5.10 shows that the 22.5 V (0-p) pulse resulted in larger drop velocities when triggered in the first half of the vibration cycle.

It also stands to reason that the drop velocities for this case are smaller in the second half of the vibration cycle due to the lack of drop production which, as explained earlier, is likely due to not enough drop momentum.

An interesting trend is observed for both the 22.5 and 33.75 V (0-p) pulses in the location of velocity maxima and minima for both each test series. Within a series, the peak drop velocity is observed when the drop formation pulse is triggered at $2\pi/3$. Given the trends observed in Figure 5.10, it might be expected to see a higher drop velocity at the $\pi/3$ phase, not the $2\pi/3$ phase. However, both voltage pulse series indicate a significant increase in the drop velocity from the $\pi/3$ phase pulse to the $2\pi/3$ phase pulse.

There is no definitive explanation for this behavior, but one explanation may be the large displacement of the meniscus. Given the already significantly displaced meniscus, the drop production pulse might be treating the meniscus like a solid object, rather than a compliant meniscus. When the pressure pulse reaches the nozzle and meets the slowly retracting but significantly displaced meniscus, it may create a localized increased in pressure at the nozzle exit which pushes against the full mass of the expanded meniscus. Instead of primarily pushing fluid into the meniscus, the new pressure wave may act like a jet forcing the expanded meniscus away from the nozzle like a small ball of fluid. The return to zero of the driving waveform voltage then results in a sudden retraction of the fluid in the nozzle. The fast withdrawal of the meniscus would then result in a shorter time during which the drop can be slowed by surface tension forces.

Because the 'instantaneous' mean velocity changes with respect to time within a single case (refer to: Figure 5.2, Figure 5.3, Figure 5.4, and Figure 5.5), the 'instantaneous' mean velocity as a function of time for drops formed with a vibrating meniscus may lead to greater insight into how the vibrating meniscus affects drop velocity. As such, the average velocity as a function of time was determined for each of the individual runs in Figure 5.10 and the results are reported below.

The following six plots are of velocity, in meters per second, versus an adjusted frame-to-frame average phase. The adjusted phase parameter is defined by equation 5.1:

$$\theta_{adj} = \frac{t_{avg}}{T} \cdot 2\pi - \theta_{trig} \qquad 5.1$$

where θ_{trig} is the phase at which the drop producing pulse was triggered in the vibration waveform cycle, t_{avg} is the frame-to-frame average time for the data point, and T is the vibration waveform cycle period. Using this parameter, the 'instantaneous' average phase of the data point is calculated by dividing the 'instantaneous' average time by the meniscus period and converting the ratio to radians. The phase is then adjusted to be independent of the meniscus phase by subtracting the voltage pulse's triggering phase (i.e. $\pi/3$, $2\pi/3$, etc.) used to generate the data point. This results in a run-independent phase parameter that uses the same base frequency for all the reported results. The parameter can also be thought of as a non-dimensional time since it is a linear combination of constants and the variable of frame-to-frame average time. Figure 5.11 and Figure 5.12 show the velocity versus phase for the two 22.5 V (0-p) trials recorded with a vibrating meniscus.

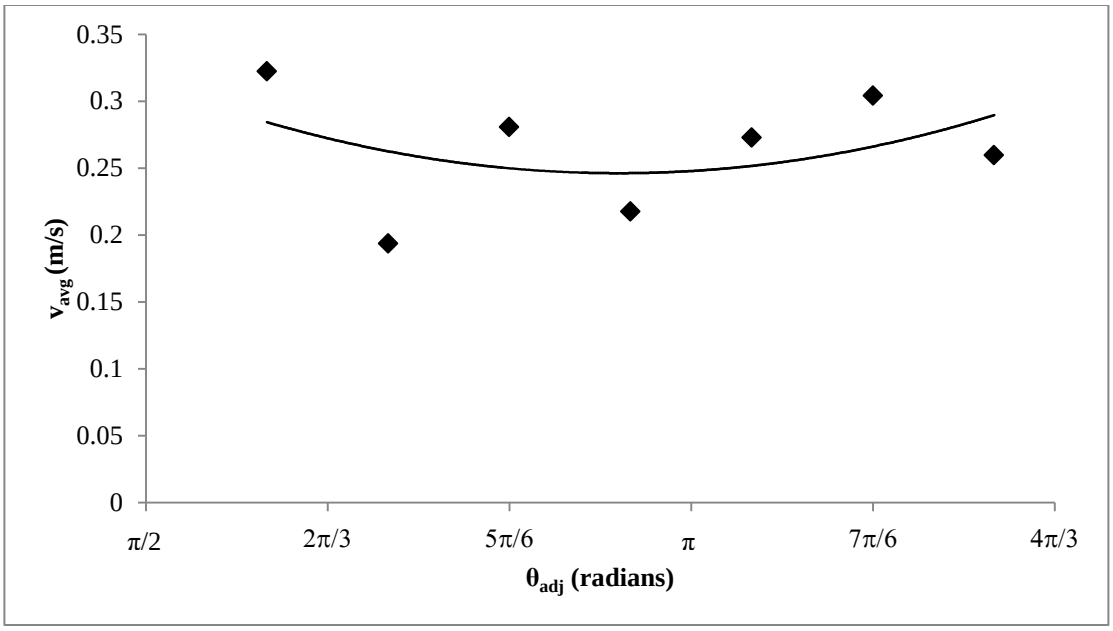

Figure 5.11: 'Instantaneous' average drop velocity, v_d, as a function of 'instantaneous' average adjusted phase, θ_{adj}, for 22.5 V (0-p) pulse, triggered at π/3 phase delay into the vibration waveform cycle. Trendline is a 2nd order polynomial line of best fit.

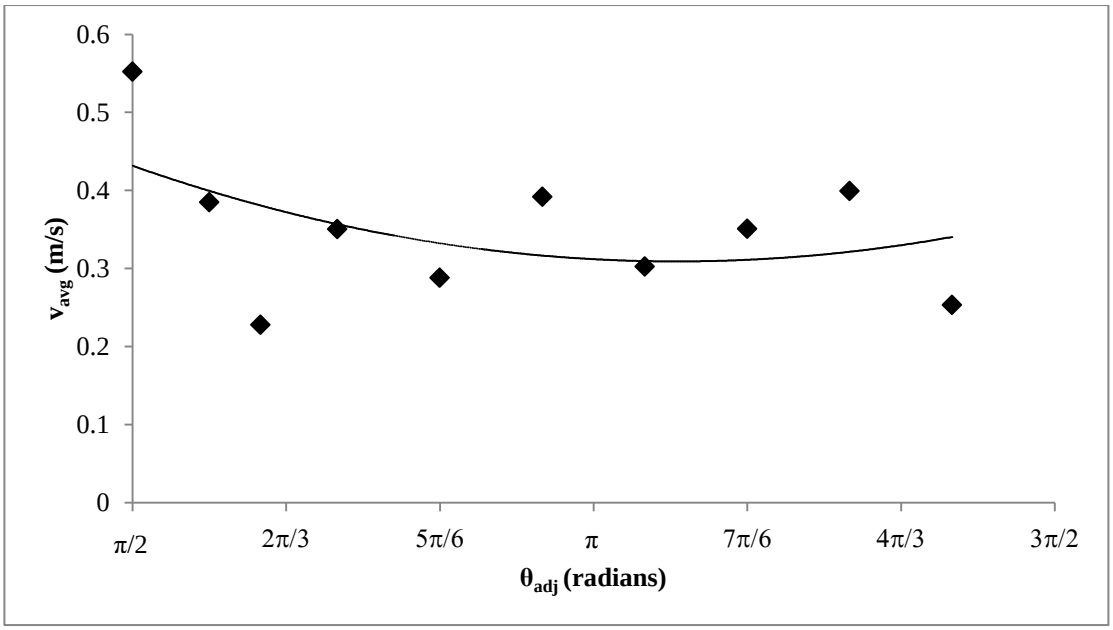

Figure 5.12: 'Instantaneous' average drop velocity, v_d, as a function of 'instantaneous' average adjusted phase, θ_{adj}, for 22.5 V (0-p) pulse, triggered at 2π/3 phase delay into the vibration waveform cycle. Trendline is a 2nd order polynomial line of best fit.

Figure 5.11 and Figure 5.12 show how the instantaneous average velocity is a function of adjusted phase. Interestingly, the velocity data appears to have far less scatter and variation than was observed for the 'instantaneous' velocity of drops formed without a vibrating meniscus. This may mean that the vibrating meniscus acted as a stabilizing effect in these two cases. This may be explained by the increase in the overall velocity of all the drop data. The drop velocity data for Figure 5.2 through Figure 5.5 were smaller in magnitude than the velocity data for Figure 5.12, which is evident in Figure 5.10. The larger overall drop velocity may have a dampening effect on the phase based variations in the 'instantaneous' average drop velocity.

Another important observation is that both Figure 5.11 and Figure 5.12 appear to indicate a non-linear trend between the drop velocity and the phase of the velocity measurement. In both cases, the maximum frame-to-frame average velocity occurs with the first phase series data point, which corresponds to phases of 0.62π and 0.5π for Figure 5.11 and Figure 5.12, respectively. This is mainly due to the high speed with which a drops tail is pulled toward the leading edge of the drop just after break-off, when surface tension forces on the tail of the drop are highest. The frame-to-frame average velocity of the drops then follow a non-linear trend as indicated on Figure 5.11 and Figure 5.12. The two plots also appear to have an oscillating drop velocity, with respect to phase, which tracks along the overall drop velocity trend.

However, data could not be obtained at sufficiently high time resolutions to discern details of this oscillatory behavior.

From the general trends shown in Figure 5.11 and Figure 5.12 it is seen that the velocity of a drop from the drop generator slows from an initial maximum speed to some minimum speed, at which point it begins to accelerate back in the direction of its travel. In order to do accelerate at all, the drop must be under some external force. The most likely force that could slow the drops speed is the surface tension along the drop. Refer to Figure 5.13 for a flow visualization of a drop immediately prior to break-off; notice how the drop is in an elongated state. The elongated state results in strong vertical surface tension forces that pull accelerate the tail into the main drop body. The reactive surface tension force on the main drop body acts to negatively accelerate the drop. When the tail has been mostly integrated into the main body of the drop, the surface tension forces' affect on the velocity would decay. As the surface tension forces decay, a different force must start to dominate in order for there to be acceleration of the drop in the direction of its travel. This force may be an overshoot of the inertia of the drop tail, which would cause the drop to accelerate in the forward direction again. Given a long enough series in time/phase, these oscillations in the drop velocity would be expected to flatten out the parabolic trend to a constant value. When the oscillating drop forces are sufficiently damped or slowed, gravitational forces will become dominant.

Figure 5.14 through Figure 5.17 show the velocity as a function of adjusted phase for the 33.75 V (0-p) piezoelectric voltage pulse. Each figure shows the frame-

to-frame average drop velocity versus drop phase for each of the four triggering phases at which the drop generation was started in the vibrating waveform cycle. Note that the data in each of these plots has fewer data points in the phase domain than for the 22.5 V (0-p) trials. The 33.75 V (0-p) trials had fewer phase domain data points because the drops were moving much faster than in the 22.5 V (0-p) trials and it was not possible to capture more than a few frames before the drops passed out of the field of view of the camera.

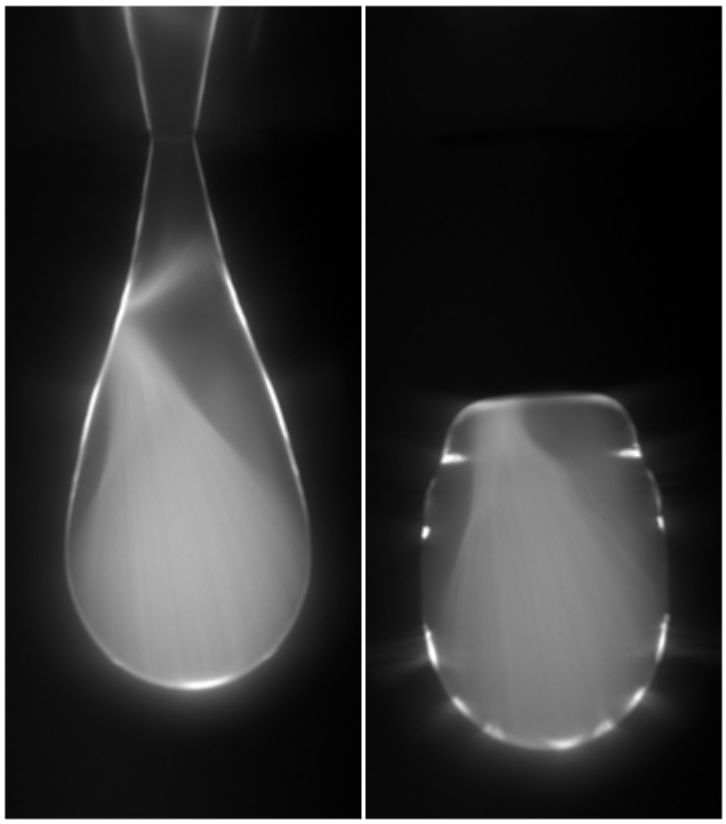

Figure 5.13: This figure demonstrates the speed with which the tail is absorbed by the main drop. The image on the left precedes the image on the right by 0.95 ms.

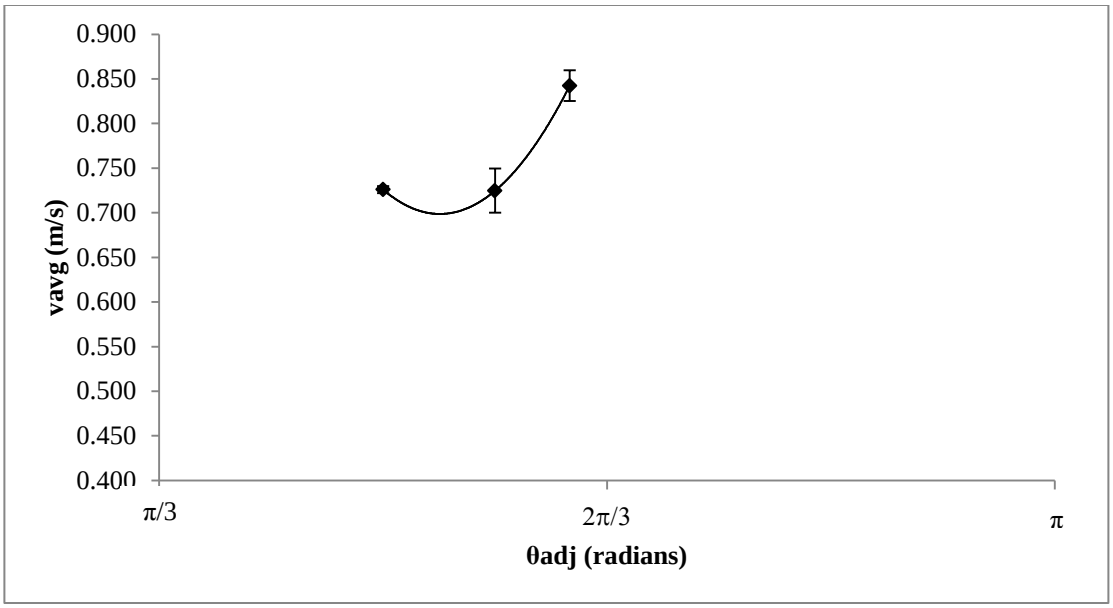

Figure 5.14: 'Instantaneous' average drop velocity, v_d, as a function of 'instantaneous' average adjusted phase, θ_{adj}, for 33.75 V (0-p) pulse, triggered at π/3 phase delay into the vibration waveform cycle. Trendline is a 2nd order polynomial line of best fit.

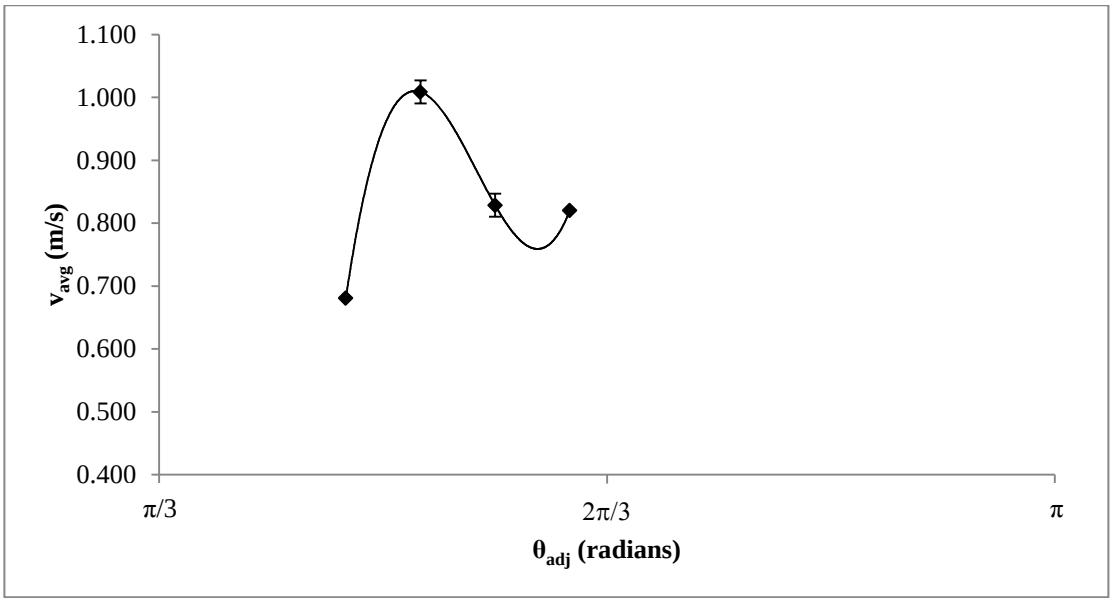

Figure 5.15: 'Instantaneous' average drop velocity, v_d, as a function of 'instantaneous' average adjusted phase, θ_{adj}, for 33.75 V (0-p) pulse, triggered at 2π/3 phase delay into the vibration waveform cycle. Trendline is a 3rd order polynomial line of best fit.

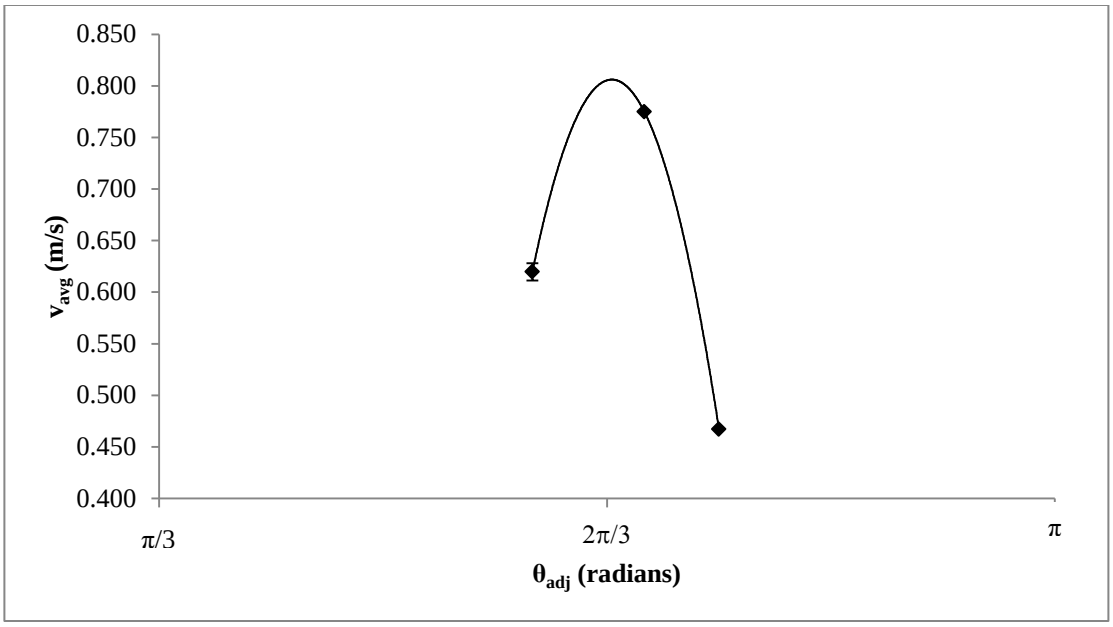

Figure 5.16: 'Instantaneous' average drop velocity, v_d, as a function of 'instantaneous' average adjusted phase, θ_{adj}, for 33.75 V (0-p) pulse, triggered at 4π/3 phase delay into the vibration waveform cycle. Trendline is a 2nd order polynomial line of best fit.

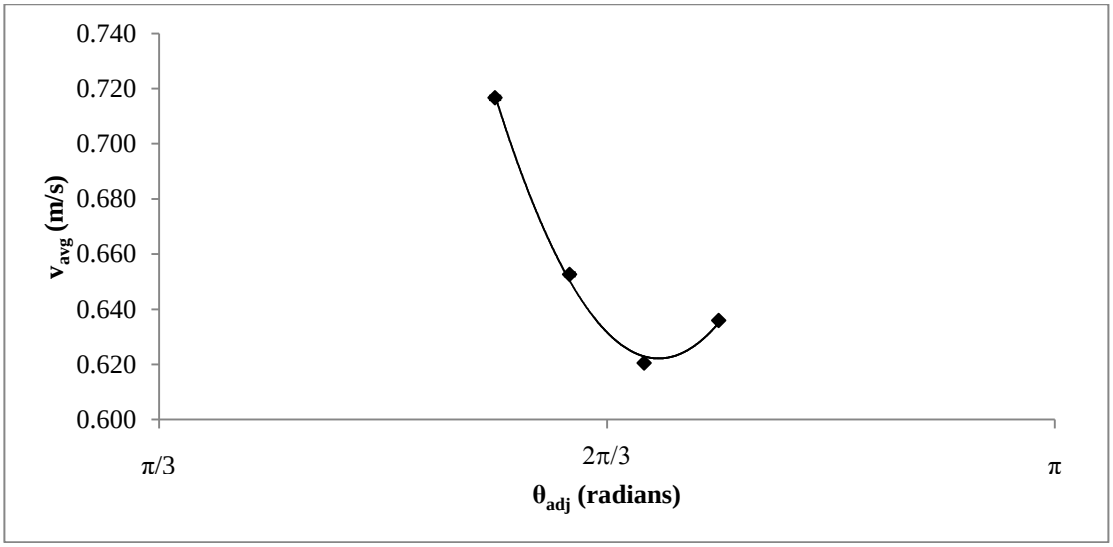

Figure 5.17: 'Instantaneous' average drop velocity, v_d, as a function of 'instantaneous' average adjusted phase, θ_{adj}, for 33.75 V (0-p) pulse, triggered at 5π/3 phase delay into the vibration waveform cycle. Trendline is a 2nd order polynomial line of best fit.

Figure 5.14 through Figure 5.17 appear to indicate that the drop velocity varies non-linearly with respect to time. Any data point with bars on it in Figure 5.14 through Figure 5.17 is an average velocity of all the 'instantaneous' mean drop velocities measured at that phase. The bars on these data points indicate the minimum to maximum spread of the 'instantaneous' mean drop velocities for this phase; these bars do not indicate either the propagated errors nor the statistical errors of the calculated average drop velocity for Figure 5.14 through Figure 5.17. The statistical errors for any of these data points would be considerably higher due to the limited sample size for each phase.

On the average, however, the velocity data for these drops are repeatable with a good degree of certainty. For Figure 5.14 through Figure 5.17, the instantaneous average velocity of the drop was calculated more than once for at least one of the phases at which data was collected. For example, Figure 5.14 has four velocity measurements at the same phase of 0.58π radians. As the spread bars indicate on Figure 5.14 for this averaged data point, the calculated velocities were all relatively close to one another. A larger sample size for each phase would allow for greater certainty in the velocity measurements by using the standard definition of the error of the mean.

Figure 5.14 through Figure 5.17 indicate a similar non-linear velocity versus phase behavior as Figure 5.11 and Figure 5.12. However, unlike the data in Figure 5.11 and Figure 5.12, Figure 5.14 through Figure 5.17 have only three or four different phases at which to compare velocities. Without additional phase resolution, it cannot

be definitively said that the trends for these figures are accurate. Higher order frequency dynamics could still be present and not observed. For example, Figure 5.15 may be similar to Figure 5.12 if there were additional phase resolution in the data for Figure 5.15. As such, the data for Figure 5.15 might be better predicted by a similar parabolic profile as is seen in Figure 5.12 than by the cubic trend included in Figure 5.15. The only thing that can be said for certain is that the instantaneous average velocity as a function of phase is non-linear. Greater resolution in phase for the data would be necessary before further conclusions could be made.

Given the earlier analysis for Figure 5.11 and Figure 5.12, it is likely that the observed trends in Figure 5.14 through Figure 5.17 do not fully capture the drop dynamics. In particular, the results from Figure 5.11 and Figure 5.12 indicate that the drop should be accelerating in the direction of its travel as the drop's flight time increases. However, the trend shown in Figure 5.16 directly contradicts the earlier result insomuch that the parabolic trend opens in the opposite direction to the parabolic trends observed in Figure 5.11 and Figure 5.12. Given that more data is available for Figure 5.11 and Figure 5.12, the error likely lies with Figure 5.16. If this is true for the Figure 5.16 trendline, it is likely that the other figures have a similar pitfall. Therefore, it can be concluded that more phase and/or time resolution is necessary for the cases reported in Figure 5.14 through Figure 5.17 in order to better define the instantaneous drop velocity behavior versus phase for the higher voltage, 33.75 V (0-p), drop formations.

5.2. ANALYTICAL MODEL COMPARISON TO EXPERIMENTAL RESULTS

The analytical model's predictive behavior has been compared to the experimental results in the roughly the same order as the experimental results were presented. First, however, the analytic model is compared with the experimental measurements for meniscus displacement as a function of time. Second, the analytical model's predictions for drop volume as a function of voltage will be compared to the experimental results presented for drop volume as a function of voltage. Finally, drop volume as a function of impulse phase in the vibrating waveform cycle will be presented for comparison to the experimental measurements of drop volume as a function of impulse phase.

5.2.1. MODEL VS EXPERIMENT - MENISCUS VIBRATIONS

Figure 5.18 compares the predictive model to the recorded experimental data of meniscus height displacement versus time. Qualitatively, the model can provide an approximation for the maximum displacement of the meniscus from an input waveform. In order to make comparisons simpler, the displacement of the meniscus for both the model and the experimental data reported here is scaled by the maximum recorded meniscus displacement from the set of experimental data. The peak model displacement is about 10% larger than the actual maximum displacement of the meniscus. However, as can be observed in Figure 5.18, the model over predicts the meniscus displacement rates, i.e. meniscus velocities. During the meniscus expansion, the model predicts that the meniscus will reach its maximum height in approximately two-thirds the time it actually takes according to the experimental data. Similarly, and

much more pronounced, the model indicates that the meniscus will return to less than 20% of the maximum displacement before 5 ms (1/4 of the waveform cycle) has passed. This differs significantly from the experimental data which shows that the meniscus returns to 20% of its maximum displacement only after about 8 ms. This indicates that there is an LEM element that was not included in the model that should have been, such as an inertial effect for the fluid behind the meniscus. Note that there is no data for negative meniscus displacements because the meniscus has retracted into the nozzle at these points and is therefore unable to be seen or measured.

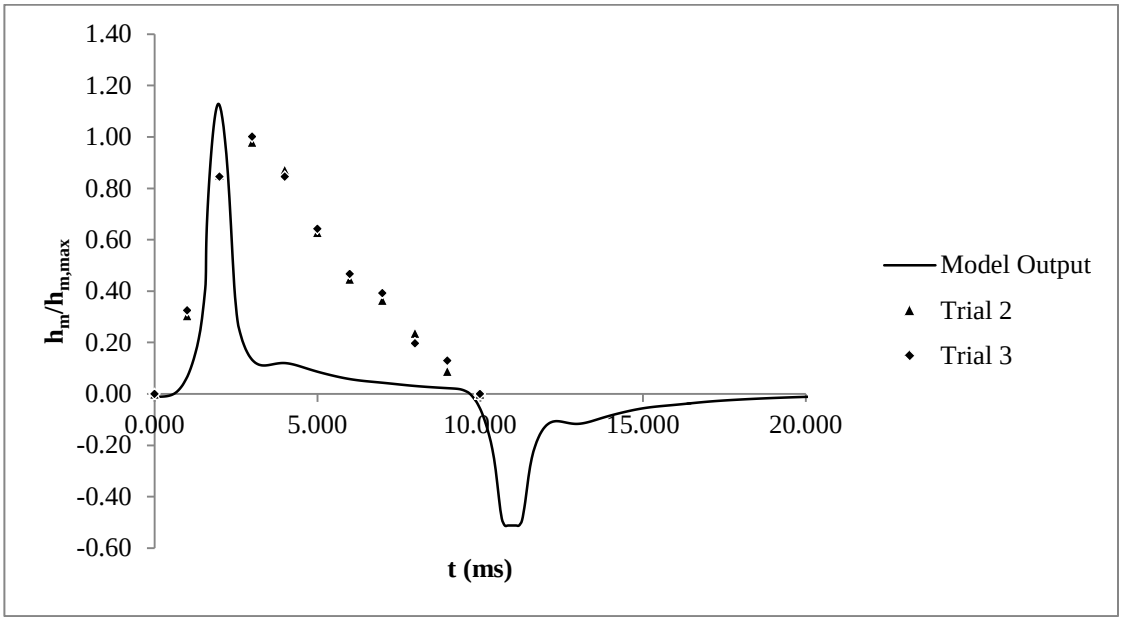

Figure 5.18: A comparative plot of the model output for meniscus vibrations as compared to the data recorded experimentally. The model output is plotted as a line, experimental data is plotted as individual points. The experimental and model data are for a driving vibration voltage of 11.25 V 0-p applied to the piezoelectric disk.

As outlined in the Literature Review, the LEM method has historical data backing it up, which would suggest that there is something missing in the LEM model

presented here which, if included, could fix the meniscus displacement discrepancy observed in Figure 5.18. The first thing to consider changing should be definition of the meniscus compliance. The model may have deviated from reality when choosing to go with the derived meniscus compliance over the meniscus compliance listed in Burr et al (1996). However, a change of this nature would require some explanation for why the meniscus compliance defined in Merhaut (1981) is incorrect. The second thing to consider would be to add an acoustic mass to the acoustic circuit that would represent the inertia of the fluid stored between the meniscus and the nozzle exit. Currently, there is no electroacoustic mass element modeling this region. However, as can be seen in the experimental and model results, a significant amount of volume accumulates in this region between the meniscus and the nozzle exit during normal meniscus vibration. Neglecting the effects of this inertial based acoustic mass may be one of the reasons that the model is failing to correctly predict meniscus vibrations.

5.2.2. MODEL VS EXPERIMENT - DROP VOLUME VS DRIVING VOLTAGE

The LEM model was run with driving drop formation voltages ranging from 18 V to 42 V (0-p) as applied to the piezoelectric disk in order to compare the results of the model to the experimental data for drop volume as a function of driving voltage (see Figure 5.1). The model output is plotted alongside the experimental data in Figure 5.19 below. For purposes of this comparison, both the experimental data and the model output have been scaled by the maximum recorded experimental drop volume. Notice how the model, the solid line, under predicts the experimental drop volume, the filled squares, by approximately one order of magnitude.

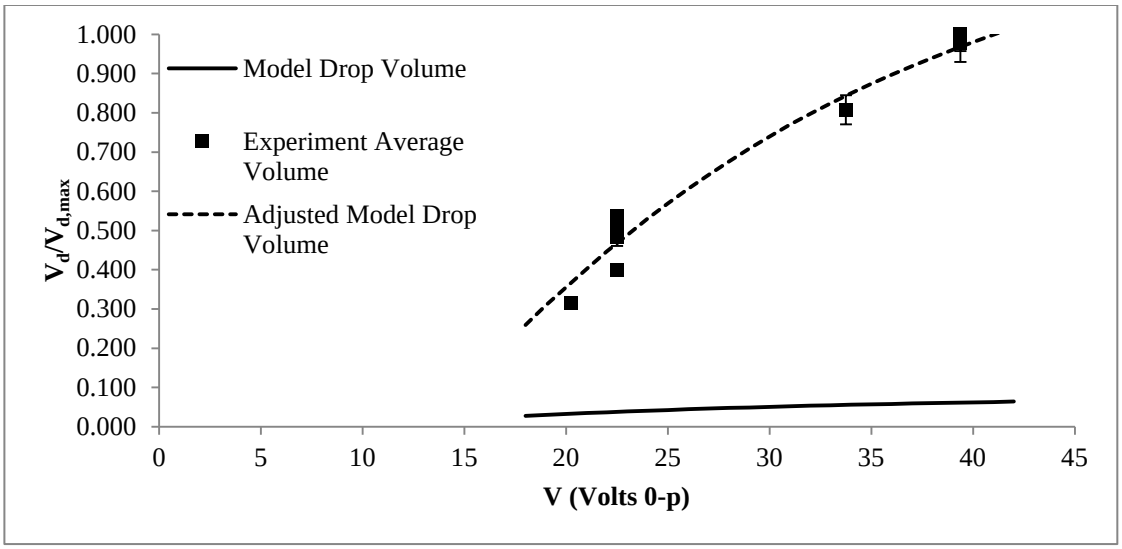

Figure 5.19: A comparative plot between the predictive LEM model and the experimental data. The drop volume has been scaled by the maximum recorded experimental drop volume for ease of comparison.

One reason this may occur is related to the results seen in Figure 5.18, which indicate that the model may have a faster time response to pressure changes than is observed experimentally. In Figure 5.18, this can be seen in the steep slopes of the meniscus displacement as a function of time. The shorter rise time, fall time, and overall duty time of the meniscus displacement seen in Figure 5.18 would translate in an equivalent manner to larger and steeper voltage pulses, such as the voltage pulses that generated the drop volumes reported in Figure 5.19. As a result, the drop volume calculation would be decreased, since it is measured by integrating the volume flow rate over time. The short time duration of the drop volume release-time in the model will result in a small integration domain and a small drop volume. Similar to the meniscus displacement discrepancies, the drop volume as a function of voltage

discrepancy might be solved by including an additional element that may have been left out.

Chief among the possible elements to fix would be those already mentioned that may fix the meniscus issue. If the meniscus issue is resolved, the applied fix may well fix the drop volume aspect of the model as well. Another possible cause for the discrepancy in drop volume could be two sources of error that originate with the LEM modeling of the drop formation process developed in section 3.1.2.4.

First, an incorrect threshold pressure for drop formation may have been used. The threshold pressure criterion used was taken from Burr et al. (1996). The criterion, $P = 4\sigma/D_n$, was derived from a force balance on a meniscus hanging with a contact angle of 90º. However, it was observed during experiments with the vibrating meniscus that the contact angle could actually grow beyond 90º and still not result in drop break-off. The second, most likely source for error, in the LEM modeling of the drop formation is the initial acoustic mass of the drop. The model development requires a constant non-zero acoustic mass to be defined for the drop formation element. Based on the theoretical derivation, this value should be zero, so the constant was made to be as small as reasonable; too small a value would cause the solution process to take too long. However, this derivation was based on the assumption that all the mass of fluid that is stored between the meniscus and the nozzle exit remains as part of the meniscus after drop break-off; only the excess fluid is what was assumed to form the drop. Experimental experience has indicated that this may not be the case. Changing this assumption would require one to determine a new constant value for the

acoustic mass that is related to the amount of volume stored behind the meniscus when drop formation begins.

In order to further explore the validity of the model for drop volume as a function of voltage, the model output was adjusted linearly to see what effect it would have on the predictive capabilities. The result of the linear adjustment can be seen in Figure 5.19. The process of adjustment was as follows: the model output data were multiplied by a constant and then vertically shifted by a separate constant. Note that the vertical shift was done after the linear scaling of model output. Due to the first order of magnitude difference in the data, the first exploration was to increase all the model output by a factor of ten. This yielded better results, but the slope of the curve was too shallow and the adjusted model still under predicted the experimental data. From this point, the slope of the curve was slowly increased until it approximated the same curve as the experimental data. Finally, the resulting adjusted model output was vertically shifted to bring the curve within the same range of values as the experimental data. The final result is what one observes in Figure 5.19 as the dotted line. The final linear scaling variables are a multiplication factor of 21 and a vertical shift of -0.25 μL. Note that these transformations were performed on the dimensional drop volumes, not the scaled drop volume. The resulting equation for the reported drop volume is:

$$V_{reported} = 21 \cdot V_{output} - 0.25 \qquad 5.2$$

Interestingly, the adjusted model output fits the low voltage drop volume data better than the straight trendline shown on Figure 5.1. If this output is reasonably accurate,

this may indicate that the drop volume as a function of voltage is not linear. It may also indicate that a corrected LEM model may be able to accurately predict drop volumes through proper calibration. In the next section, the same linear transformations is applied to the model output volumes for drops formed with a vibrating meniscus.

This adjustment may be justified by the sources of error specified earlier insomuch that the pressure required to form a drop is obviously larger than the initial threshold value. Also, the lack of a proper initial drop acoustic mass would cause the drop volume to be less since because the drop is assumed to start forming with an initial inertia of zero, which would result in a lower overall flow rate through the droplet element. Additional testing of the model would be necessary before either of these could be claimed for certain.

5.2.3. MODEL VS EXPERIMENT - VIBRATING MENISCUS EFFECTS ON DROP FORMATION

A comparison of the predictive model output to the measured experimental data is reported below in Figure 5.20 for different drop formation phase relationships. The figure shows how the drop volume is affected by the meniscus phase at which the drop formation is triggered. The result of the linear transformation of the LEM model output is reported in Figure 5.20 for both 22.5 V and 33.75 V (0-p) drop formation pulses. As was mentioned in section 5.1.2, the experimental data indicates an increase in the drop volume for drop formations triggered during the first half of the waveform cycle and a decrease in the drop volume for drop formations triggered during the latter half of the waveform cycle. The analytical model also tends to predict a similar

overall behavior for drops formed in the first half of the meniscus waveform cycle. However, the model under predicts the degree with which the drop volume is increased for drops formed between zero and π. Similarly, it also over predicts the drop volume for drops in the latter half of the waveform cycle, so much so that the drop volumes are practically equal to the neutral case during the latter half of the meniscus waveform cycle. Recall that there are no data for the 22.5 V (0-p) voltage pulses at 4π/3 and 5π/3 because meniscus vibrations completely prevented drop formation. Interestingly, the same behavior is observed in the model, but it is far in advance of the phases at which the experimental data indicated drop formation prevention.

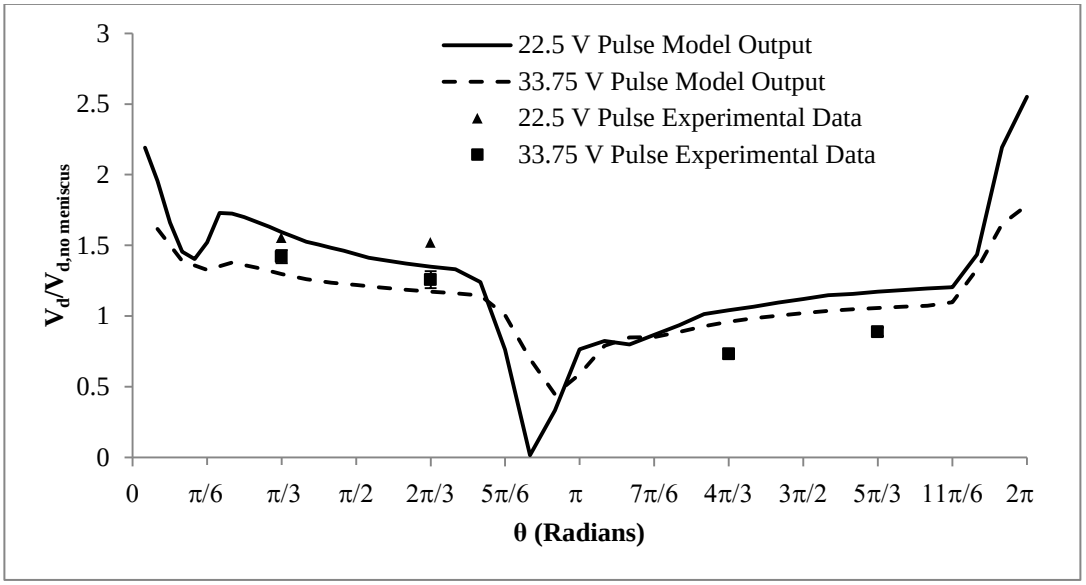

Figure 5.20: This figure is a comparative plot of the model output to experimental data for drop volume as a function of drop formation pulse phase within the vibrating waveform cycle. The values of drop volume have been scaled by the average drop volume for drops formed with the same pulse magnitude but without a vibrating meniscus.

The discrepancies between the model and the experimental data presented in Figure 5.20 can be explained by the results presented in sections 5.2.1 and 5.2.2. Due to the fast response of the meniscus to pressure changes in the system, the meniscus dynamics and overall displacement of the meniscus are suppressed in the model long before they are suppressed in the experiments. As a result, the meniscus effects on drop formation will be minimal once the drop formation pulse has moved beyond the dynamic region of meniscus vibrations. This is exemplified in Figure 5.20 by two regions, between 0 and about $\pi/6$ and again between $5\pi/6$ and $7\pi/6$, where the drop volume changes drastically with changes in drop formation pulse phase. These changes align with the general regions in which the meniscus dynamics are still strong in the model (see Figure 5.18). However, as was observed in Figure 5.18, the measured meniscus height as a function of time has a slower time response than is predicted by the model. The slower time response leads to larger meniscus displacements at the phases during which drop formations are triggered in Figure 5.20. This should result in increased experimental observations for drop volume over that of the model predictions, as is observed in Figure 5.20.

Interestingly, by scaling the predicted drop volumes by the average drop volume of drops formed with the same voltage pulse without a vibrating meniscus, one can more clearly see that the meniscus vibrations have a smaller affect on the drops formed when using larger voltage pulses. For example, the values for almost all the scaled drop volumes formed with the 33.75 V (0-p) pulse were closer to unity than the scaled drop volumes formed with the 22.5 V (0-p) pulse. This result of the

analytical model is consistent with the results observed earlier with respect to the experimental data reported in Figure 5.7. This indicates that despite being unable to quantitatively predict the drop formation, the current form of the LEM model is able to qualitatively predict drop formation characteristics. In particular, this suggests that the LEM model technique used in this study to predict drop formation may be corrected with future efforts to provide quantitatively correct drop volume predictions.

5.3. FLOW VISUALIZATION EXAMPLES

As mentioned in the experimental methods section, all the experimental data of the drop formation was collected via flow visualization of the drop formation. This section highlights a few examples of drop formations from different portions of this study. The remainder of the flow visualization images collected as experimental data points are included in APPENDIX G. Notice how the shape of the drop before and after break-off is affected by the presence and phase of a vibrating meniscus in Figure 5.21 through Figure 5.28.

5.3.1. DROP FORMATION WITHOUT A VIBRATING MENISCUS

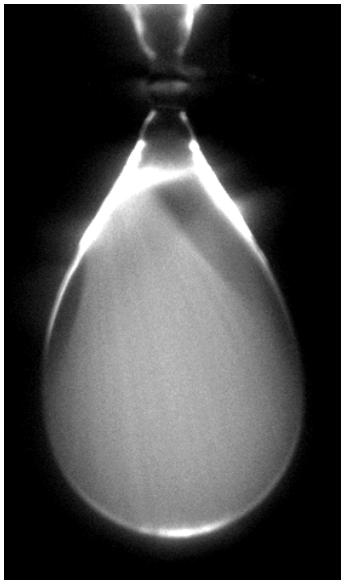

Figure 5.21: Drop formation with no vibration, 22.5 V pulse, just after break-off.

5.3.2. DROP FORMATION WITH A VIBRATING MENISCUS

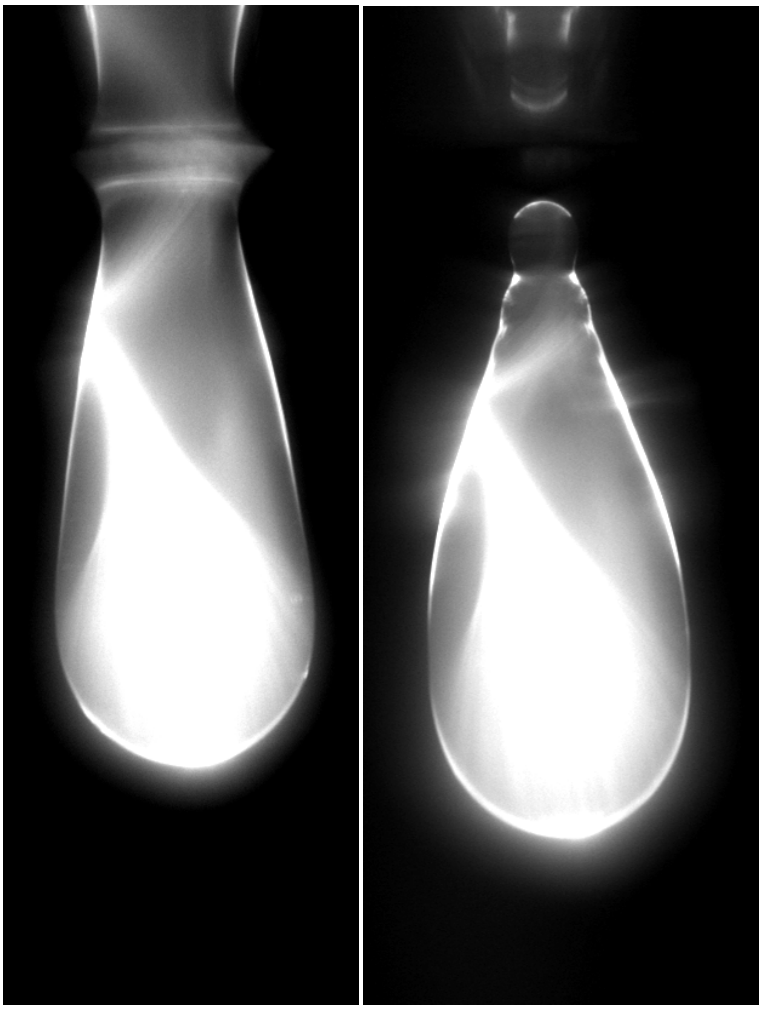

Figure 5.22: The image on the left is the drop just prior to break-off and the image on the right is the drop just after break-off. The drop here was created using a 22.5 V pulse waveform at $\pi/3$ phase shift from the start of the vibrating meniscus waveform.

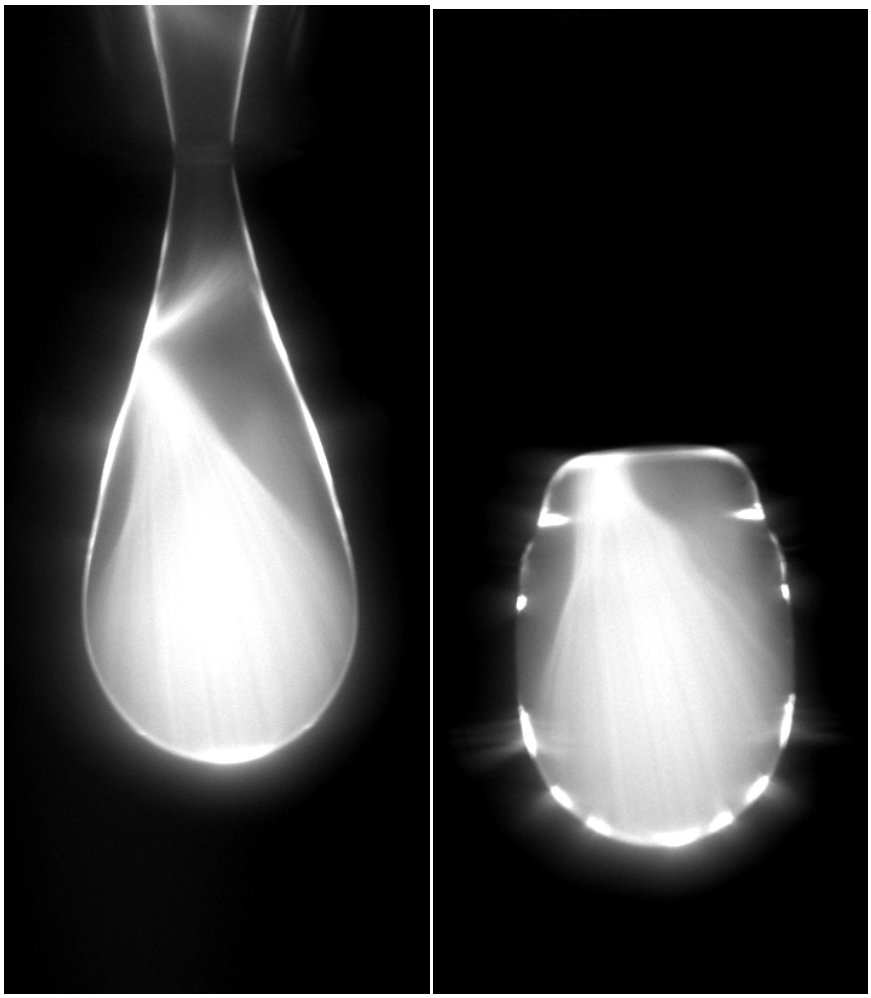

Figure 5.23: The image on the left is the drop just prior to break-off and the image on the right is the drop just after break-off. The drop here was created using a 22.5 V pulse waveform at $2\pi/3$ phase shift from the start of the vibrating meniscus waveform.

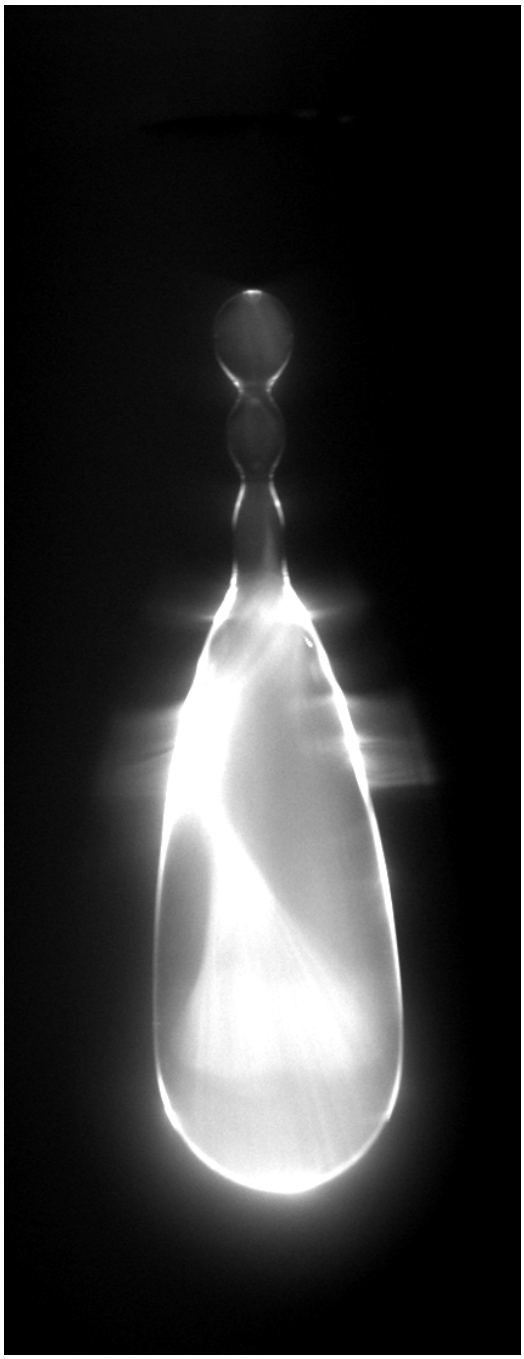

Figure 5.24: Drop formation with no vibration, 33.75 V pulse, just after break-off.

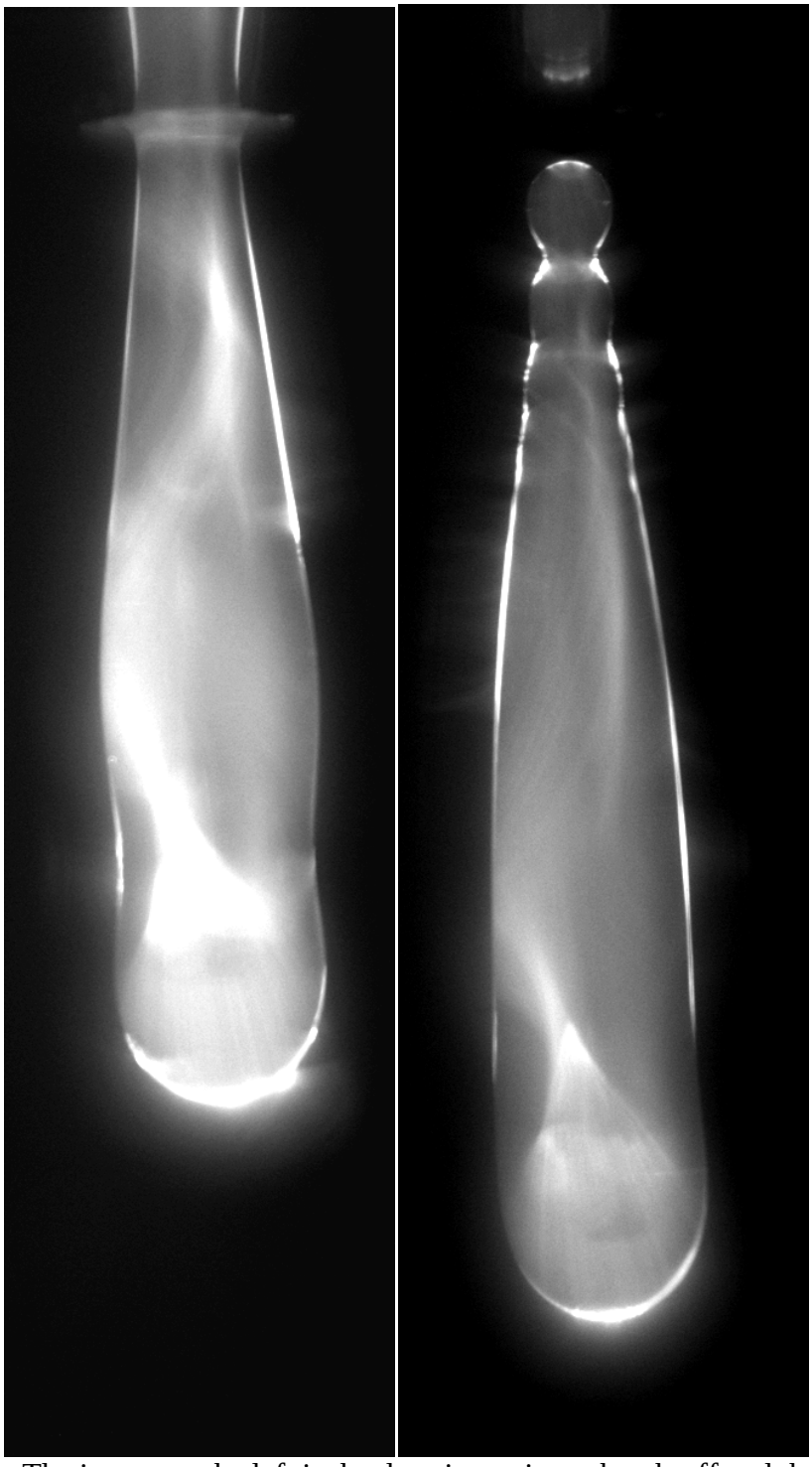

Figure 5.25: The image on the left is the drop just prior to break-off and the image on the right is the drop just after break-off. The drop here was created using a 33.75 V pulse waveform at $\pi/3$ phase shift from the start of the vibrating meniscus waveform.

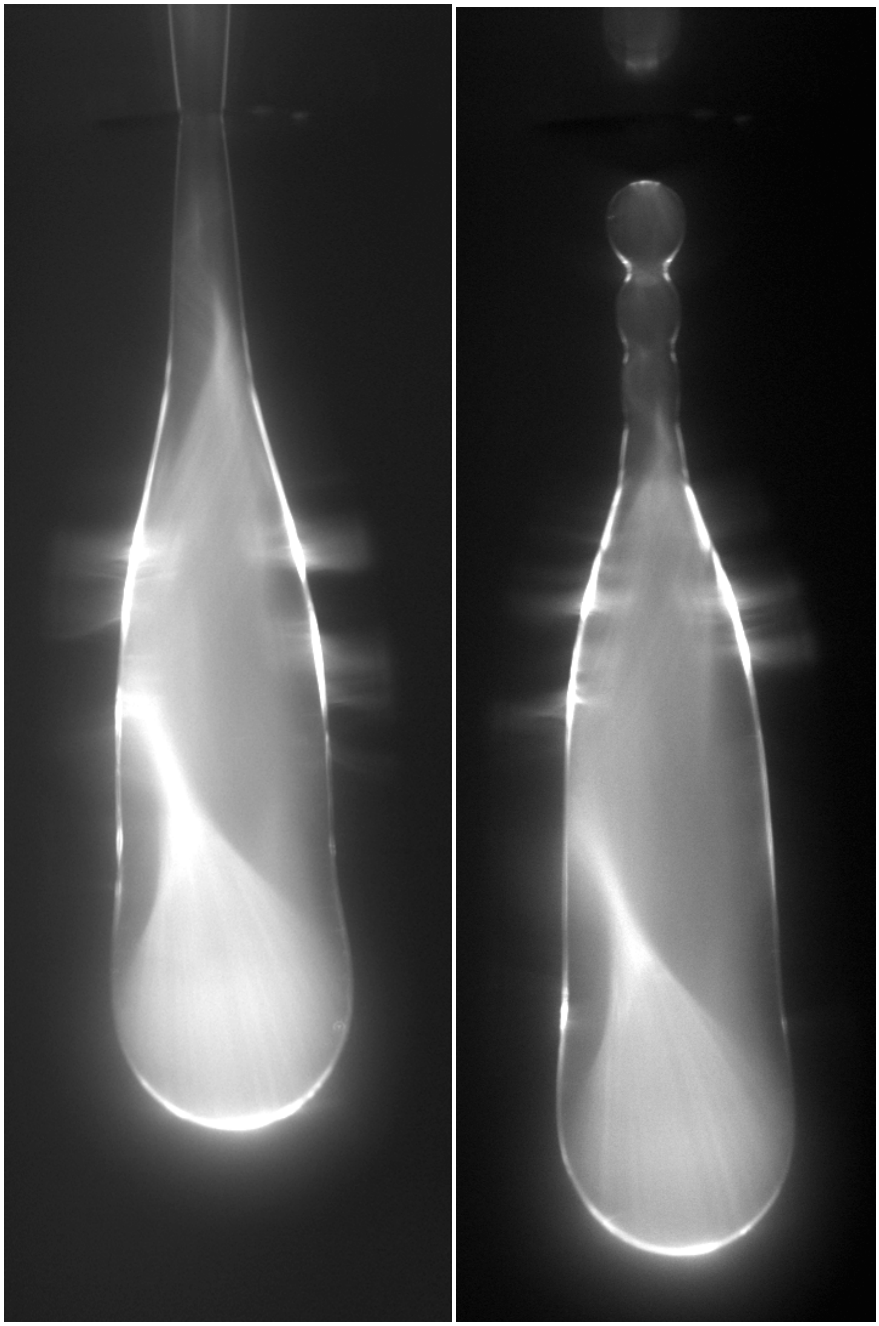

Figure 5.26: The image on the left is the drop just prior to break-off and the image on the right is the drop just after break-off. The drop here was created using a 33.75 V pulse waveform at $2\pi/3$ phase shift from the start of the vibrating meniscus waveform.

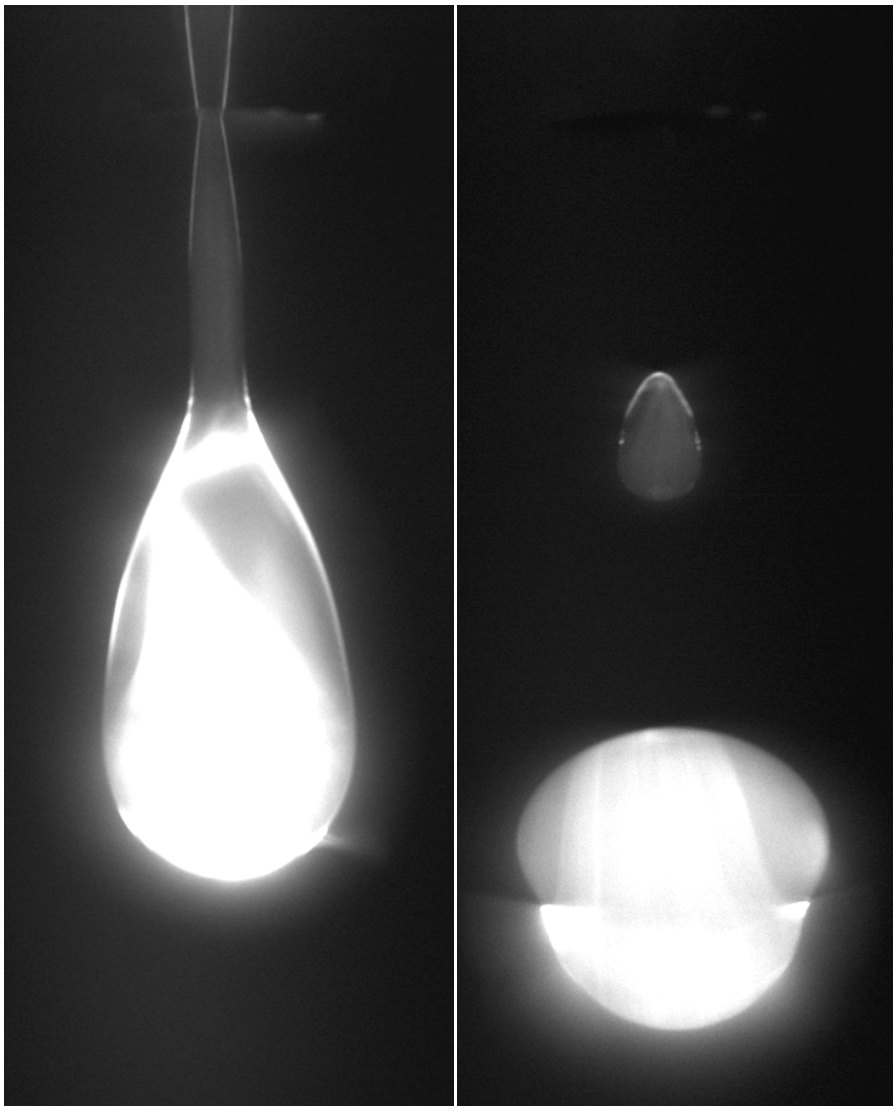

Figure 5.27: The image on the left is the drop just prior to break-off and the image on the right is the drop just after break-off. The drop here was created using a 33.75 V pulse waveform at $4\pi/3$ phase shift from the start of the vibrating meniscus waveform.

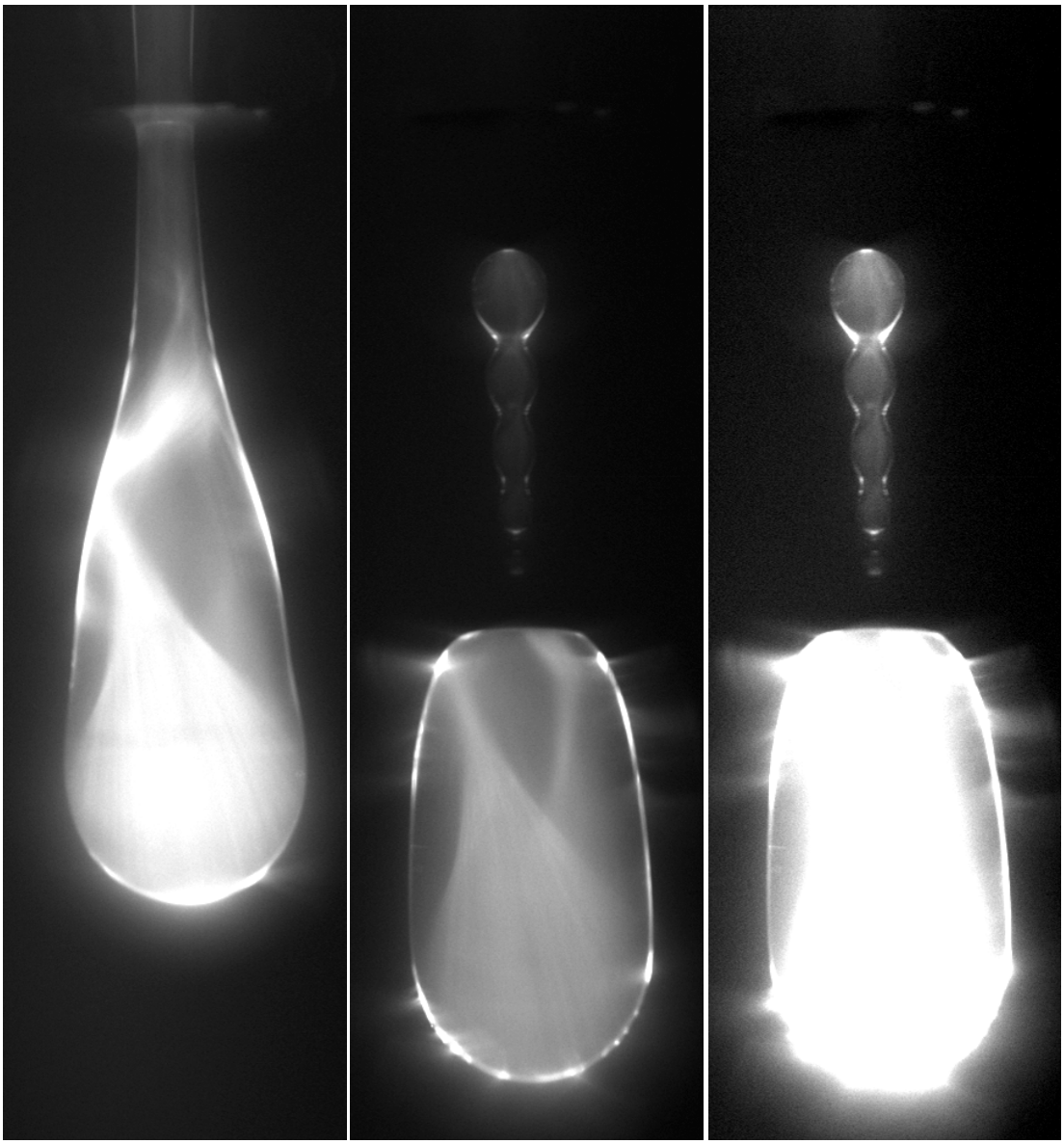

Figure 5.28: The image on the left is the drop just prior to break-off and the two images on the right are differently scaled versions of the same photo of the drop just after break-off. The drop here was created using a 33.75 V pulse waveform at $5\pi/3$ phase shift from the start of the vibrating meniscus waveform.

6. CONCLUSION

The goal of this study has been to explore the effects of a vibrating meniscus on drop formation. Within that context, experimental data was collected to observe the resulting drop formation effects and an analytic model was developed in an attempt to predict the results. After collecting, analyzing, and comparing the results, one can draw a number of conclusions on how drop formation is affected by meniscus vibrations.

6.1. THE EFFECT OF A VIBRATING MENISCUS

The most definitive observation one can take away from the experimental model results is that drop formation is affected by meniscus dynamics. The experimental data, collected in the form of flow visualization of drop formation, has shown visually and quantitatively that meniscus vibrations will change the volume and velocity of DOD drops. The experimental results also show that the vibrating meniscus phase is an important factor in determining how the drop formation is affected by the meniscus dynamics, not just the presence of a vibrating meniscus. From Figure 5.7 and Figure 5.10, one observes that the trial based drop volume and velocity are functions of the meniscus phase. This trend is most notable and statistically significant in Figure 5.7 where the results indicate a strong change of drop volume due to changes in meniscus phase. The model also indicates a similar dependency of drop formation on the presence and phase of a vibrating meniscus. Although the model may have shortcomings, it still indicates the same qualitative behavior that is observed in the experimental results. More specifically, the model

indicates an increase in drop volume during positive meniscus displacements and also indicates a decrease in drop volume during negative meniscus displacements.

Delving deeper into the analysis of the drop formation as a function of meniscus phase, one finds that positive meniscus displacements increase the drop volume over that of a drop formed without a vibrating meniscus, and vice versa. The effect of the vibrating meniscus is so strong that it can even completely suppress the formation of drops triggered by lower DOD voltage pulses (see the 22.5 V (0-p) series in Figure 5.7). It is also observed that drop velocity dynamics change as a result of the differing meniscus phases. For example, the velocity versus phase data in Figure 5.14 differs widely from the velocity versus phase data in Figure 5.15. The only change between the two figures is a change in the meniscus phase during drop formation. It can therefore be concluded that the drop dynamics post break-off are also affected by the meniscus phase, not just the drop dynamics while still attached to the meniscus. The trends indicated on the drop velocity versus drop phase figures (Figure 5.11, Figure 5.12, , and Figure 5.14 through Figure 5.17) imply some non-linear velocity trend; however, a higher resolution of time series data is required before this implication can be accepted with certainty. Figure 5.11 and Figure 5.12 indicate slight parabolic shapes could actually turn out to be straight lines with higher resolution data. And Figure 5.14 through Figure 5.17 only have enough data points to indicate that the drop velocity is not a constant. Following this same logic, future work with increased time resolution data could also allow one to perform a frequency analysis on the dynamics of the drop velocity. Given the addition of high enough time resolution data

for the meniscus dynamics, one may be able to seek a shared relationship between drop frequency dynamics and meniscus frequency dynamics.

The LEM model developed for this DOD system is also instructive to look at. Although it does not directly match the experimental data, it still lends an increased insight into the effect of a vibrating meniscus on drop formation. In particular, the model lends an insight into how one might expect drop volume to change as a function of meniscus displacement. Comparing Figure 5.18 to Figure 5.20, one may observe that the meniscus phases of the most significant increases and decreases in drop volume coincided with the largest meniscus vibration amplitudes. Assuming that the model is qualitatively correct, the higher resolution of the model output allows one to conclude that larger drop volumes coincide with positive meniscus displacements, and vice versa. While the experimental results would lead to the same conclusion, the time resolution is not fine enough to rule out higher frequency fluctuations away from a mean trend. The model, however, rules out this possibility because it does have a fine enough time resolution of data. However, since the model could not predict the experimental results, no further conclusions can be drawn from the model with relation to how the drop volume is dependent on the meniscus displacement. Furthermore, the model was not developed with the capability to observe drop dynamics post break-off, so qualitative model investigations cannot be done for drop velocity dynamics.

Beyond the meniscus vibration analysis, it was found that the drop volume appears to vary non-linearly as a function if input voltage to the piezoelectric disk.

This would be unexpected because one expects the piezoelectric disk to displace linearly with respect to input voltage. However, this assumption is precisely how the piezoelectric displacement was modeled in the LEM model, and after a linear transformation, it can be seen in Figure 5.19 that the drop volume as a function of input driving voltage varies non-linearly. In retrospect, this makes sense because one cannot expect one hundred percent of the pressure pulse to always go into forming the drop. With large pressure pulses, one may expect a greater amount of volume flow into the refill chamber and a greater compression of the fluid in the acoustic compliance elements. This diversion of the flow from the nozzle would therefore reduce the volume flow rate out of the nozzle and thus the total drop volume.

6.2. LESSONS LEARNED

From an experimental standpoint and in terms of the physical setup for the experiments, there are a number of lessons to be learned from this study. Perhaps the most noteworthy is evident in the flow visualizations of the drop formation process from chapter 5; the direction of lighting for flow visualization is an important factor in the quality of photos, particularly for any flow visualization of water drops. For all the flow visualization figures included in this study, the lighting for the drops was brought from the bottom right of the figure. For any configuration of light entering the drop, the drops surface will act as a lens and focus the light intensity toward a focal point inside or beyond the drop. The focusing of the light in this manner can be seen in many of the flow visualization figures in chapter 5. The light from the lower right of the figure enters the drop near the bottom and right side of the drops. Depending on

the shape of the drop at the time, the light is then dispersed or focused to different regions in the drop, and is sometimes reflected off the internal walls of the drop due to total or partial internal reflection.

For this study, the surface interactions resulted in a number of issues. The most notable affect of the surface-light interactions is seen in the reduced amount of laser light that could reach the tail end of any drop. In most cases with satellite drops, the surface interactions often made it nearly impossible to detect the satellite drops at all. This made it increasingly difficult for edge detection methods to find the true edges for the drop, the meniscus, and any satellite drops. For more uniform drop and satellite drop illumination, it would be beneficial to introduce the light into the system from the same direction of the camera of via back-lighting of the drop and meniscus region. It should be noted, however, that this will not eliminate this issue with refraction and reflection of light within the drop. Depending on the direction of lighting, it is likely that the drop size could be over predicted or under predicted due to reflection and refraction of the light near the drop edges. This effect might be enough to introduce a significant bias error depending on the radius of curvature of the drop in question.

Another key factor to consider when investigating any DOD drop formation is the supply line for fluid refill of the drop generator. In this study, the refill port was simplified to an extra plenum of fluid attached via an inlet port to the internal drop generator plenums. While this method of fluid replacement serves its purpose, it is not efficient. For the purposes of the LEM model, the effects of the refill port beyond the

drop generator outer boundary were considered to be a bulk compliance. However, in reality, the refill port is introducing what would be considered an acoustic transmission line into the LEM model for the fluid system. The introduction of such an element may defeat the purpose of the simplified solution technique of the LEM model. Also, the length of the refill port supply tube is much too long to still satisfy the fundamental assumption behind electroacoustic modeling, 3.2. Therefore, in retrospect, it would be better for the refill port to the drop generator to have a better design that can be more accurately modeled by the LEM method. Designing a better refill port could do more than potentially improve the model, it could also help stabilize the fluid system experimentally. Minor meniscus vibrations, gradual meniscus height changes over long periods of time, and refill port backflow conditions could all be mitigated with a better designed refill port. The majority of commercially available drop generators (i.e. print heads) usually have well designed refill ports for precisely these reasons.

From an analysis standpoint, one should notice that the accuracy of the velocity at any specific phase in the drop flight is much higher than the accuracy seen for the average velocity of an entire trial. For an example, one may compare the error of the mean for a trial based average velocity as reported in Figure 5.10 to the data spread presented in any of the velocity versus time plots in Figure 5.14 through Figure 5.17. The non-constant relationship between a drops' velocity and time will cause an overall average of drop velocity to be highly inaccurate. However, the drop velocity measured at an instant in time during the drop flight will have a much smaller

variation from test to test and the end result would be a much more accurate representation of a drop velocity repeatability. In addition to the greater accuracy of the drop velocity for a single instant in time, the trial-based mean drop velocity has another disadvantage due to the drop velocity dependence on time. Increasing the number of time series data collection will cause the overall average to increase or decrease with the overall trend of the drop velocity and will likely introduce even greater error. The best one can do with a trial based average of velocity is to use a constant time domain during which drop velocities are measured and restrict the averaging to that fixed time domain. However, this method introduces a number of additional sources for error that make it nearly as ineffective in quantitatively describing the drop velocity. The more accurate form of velocity measurement and velocity reporting is, therefore, a velocity versus time or velocity versus phase plot of the average drop velocity between two instances in time.

From the theoretical model perspective, there is a lot to be taken away from this study for continuous improvement to the LEM model. The most important thing to take note of is how much faster the model responded to system conditions than the experimental setup did. Given the history behind the LEM model and the support it has in accurately predicting acoustic system dynamics, it is unlikely that the model technique is flawed. Instead, it is more likely that an element was defined incorrectly or was left out entirely during this study. The fast time responses to pressure changes indicate a lack of acoustic mass in the model, since acoustic mass would generally be the greatest time based impedance to changes in flow rate and electroacoustic

voltages. Also, as was already mentioned, the modeling of the refill port may need some improvement. Finally, from a historical LEM model perspective, some additional changes and or additions to the current LEM model may also improve the model's performance and validity.

6.3. FUTURE RECOMMENDATIONS

Careful scrutiny of the experimental results, model output, and lessons learned during the study have lead to the following recommendations for model improvements and experimental improvements for future studies.

6.3.1. EXPERIMENTAL IMPROVEMENTS

To improve the lighting conditions for flow visualization, it is recommended that the laser light be directed through a set of optical equipment that allows for the laser lighting of the drop region to be illuminated from the same direction as the camera. The success of this method is ensured by the use of the Rhodamine 6G dye. The optical equipment should be setup to reflect the Nd:YAG laser light down the camera viewing angle toward the drop and meniscus field of view. The light reemitted by the Rhodamine 6G should then be able to pass through the same surface that acted as a mirror for the wavelength of light emitted by the Nd:YAG laser. This should allow for more uniform drop and satellite illumination. It should also reduce most or all drop shape distortion since the reemitted light being picked up by the camera will be primarily from Rhodamine 6G surface emissions of light. The light emitted at or near the surface should be minimally effected by the refraction of the laser light as it enters the drop, and it is the laser light refraction that appears to cause the majority of

the flow visualization issues, not the refraction of the light emitted by the Rhodamine 6G.

If forward lighting of the drop formation is not possible, it is recommended that future investigations attempt to calibrate the experimental setup for flow visualizations by determining the affect laser refraction has on image quality. It is suggested that one use a spherical bead or tear drop shape of known dimensions to calibrate the optical setup. By capturing a few control condition photos of the spherical bead or tear drop bead as illuminated by the laser light, one should be able to calibrate the images to the actual dimensions of the physical object, thus accounting for any distortion of the image or change to the apparent bead shape due to light refraction near the surface edges.

Future endeavors may also benefit from investigating what design constraints result in good refill port behavior. More time should be invested in designing a better overall in house droplet generator for research purposes, but special interest should be given to the refill port. In theory, the refill port should be highly resistive to back flow and relatively open to forward (into the drop generator) flow. A simple enough change to the inlet port may be to make it a diffuser for flow into the drop generator. A simple geometric change such as this may still be included in the LEM model but would allow for the inlet port to do a better job at fulfilling its intended purpose, which is to refill the drop generator with volume after a drop has been ejected. In addition to geometrical changes at the drop generator level, it is important the overall volume plenum available for the refill port be decreased in size and moved much closer to the

drop generator. Ideally, the characteristic length of any one of the elements leading to the final refill reservoir should still be much smaller than the wavelength of sound in the fluid at the operation frequency.

The experimental results of drop velocity have proven difficult to quantitatively compare across varying phases and voltages. Further research will be in want of a more accurate representation of the drop velocity for comparing drops formed at different phases in meniscus vibrations. Two methods such methods of comparison are recommended below.

The simpler of the two methods is to always measure the drop velocity at the same phase in the drops flight time. Collecting a number of data points at and around a single instant in time during the drop flight will allow one to hone in on a single velocity that could be used as a representative drop velocity for the trial condition in question. This method would greatly reduce the error of the mean for the drop velocity and should provide a relatively consistent comparative tool. However, this method would also be unable to capture an accurate representation of any higher order drop dynamics, such as any velocity versus time non-linearity. This could prove to be problematic since all the drop velocity trials indicated some form of non-linearity for the drop velocity as a function of time. Also, this method would be prone to report an incorrect ‘average’ of the drop velocity if any higher order oscillations of the drop velocity are not in phase with one another. Lastly, unless the 'drop phase' is measured from the start of the drop formation pulse, this method has the added difficulty of

requiring the experimentalist to find the exact time of drop break-off in order to establish the correct 'drop phase' scale for each drop trial.

The second more difficult but more accurate method of determining an appropriate representation for drop velocity would be to collect high time domain resolution data for velocity as a function of time. Multiple runs would allow for high accuracy at each time step in the drop flight and one could use the resulting output as a means of determining the velocity at a particular phase. By capturing the oscillatory dynamics of the drop velocity, one may also be able to find the mean velocity about which the velocity is oscillating and use this velocity as the representative velocity for a meniscus phase trial. The mean velocity trends for each of the different trials could then be compared on a single plot and used as the primary comparison tool for velocities of drops formed at different phases in the meniscus vibrations.

Finally, the effort but into the image analysis of the flow visualization yielded some important discoveries that would be good to consider during the initial stages of design for the experimental setup. The first has already been covered above in the discussion around the drop illumination setup. Due to the angle at which the light illuminated the drops in this study, it became very difficult to resolve even the edges of the primary drops at times. Concessions had to be made in the image analysis code that forced the code to not analyze satellite drops. The goal for future studies should be to increase the signal to noise gradient near drop edges. The easiest way would be to change the lighting condition as mentioned above. The end result of steeper edge gradients is a cleaner defined edge for the image analysis. With increased uniformity

in light emission, it will also be much simpler to include satellite volume and velocity determinations into the image analysis code.

Another possible way to increase the signal to noise ratio and obtain steep gradients would be to decrease the bit depth of the camera photos. For the image analysis performed in this study, 16-bit depth grayscale images were analyzed. While this provides a greater signal to noise ratio in general, it also causes the images to have more gradual intensity gradients due to the emission of light coming from the Rhodamine 6G dyed drops. If the grayscale images are reduced to 8-bit depth images, one can still have a good signal to noise ratio if the image is scaled properly. The optimum method for increasing the edge gradients would be to first scale a standard 16-bit grayscale image to the entire bit depth map. This process essentially takes the minimum and maximum measured values in the grayscale image and 'stretches' the image information in between to cover the entire 16-bit depth range. Converting the 16-bit image to an 8-bit image maintains the proper scaling but will result in steep gradients near edges due to the large decrease in available light intensities. Using this modified result as an input to an edge detection algorithm should yield better edge results than one may expect to find if the original 16-bit image were input to the edge detector without any post processing.

6.3.2. LEM MODEL IMPROVEMENTS

Section 5.2 discusses the shortcomings of the LEM model and the model's inability to accurately predict the volume of drops or the meniscus vibrations for the fluid system being studied. However, the historical data supporting the LEM method

would suggest that there is something missing in the LEM model presented here. A number of possible corrections or additions to the model are outlined below. Most of these corrections or additions are based off of previous studies and may aid in completely defining the acoustic fluid system.

The first piece of the LEM model that should be changed or considered is the meniscus compliance. Burr et al (1996) used a differing definition for the meniscus compliance, see section 3.1.2.3 and equation 3.18. It may be of value to modify the current LEM model to reflect the meniscus definition as provided by Burr et al (1996) and see how that changes the performance of the model as compared to the experimental results. The next most important elements to introduce or change would be the electroacoustic masses of the meniscus and drop. In the case of the meniscus, there is currently no electroacoustic mass for it. However, as is evident in both the experimental results and the model results, a significant amount of volume accumulates in the meniscus for the vibration amplitude studied. Neglecting the effects of an acoustic mass of this amount may be one of the reasons that the model is failing to correctly predict meniscus vibrations. Similarly, the acoustic mass of the drop is assumed to start at very near zero when volume first starts to flow out of the drop. It may be important to increase the acoustic impedance constant for the acoustic mass of the drop. Since the drop is considered to start forming at a certain meniscus displacement (i.e. back pressure), it reasons to say that the acoustic mass constant for the drop should be equal to the acoustic mass of the meniscus at the

instant in time that the back pressure is large enough to trigger the LEM model to redirect the flow through the drop element.

Two additional elements may also be needed to accurately represent the meniscus vibrations as they interact with the environment. The Yang and Liburdy (2007) LEM model includes acoustic mass and acoustic resistance radiation values for the meniscus. These additional elements represent the acoustic mass impedance and acoustic resistance impedance of energy transfer from the meniscus to the surrounding air.

Finally, it is suggested that a more comprehensive LEM parameterization for the piezoelectric disk be applied to the existing LEM model, such as applying the LEM modeling of a piezoelectric disk shown in Gallas et al (2003). The proper modeling of the piezoelectric disk will allow for the drop generator dynamics to interact concurrently with the piezoelectric disk in a couple fashion. The method used in this study restricts the piezoelectric disk to ideal behavior, which may be another cause for the discrepancies seen between the model and experimental results.

6.4. CLOSING STATEMENT

In conclusion, meniscus dynamics play an important role in the behavior of drop formation. Even at the very low frequencies studied, it was found that the phase of meniscus vibrations can significantly affect drop characteristics such as volumes and velocities. In some instances, it was found that the combined momentum and displacement of a vibrating meniscus can completely prevent drop formation. At the same time, an LEM model was developed and proposed for predicting the

experimental results. The qualitative relationships between the model and the experiments aligned well despite that the model was unable to accurately describe the meniscus dynamics and drop characteristics in a quantitative sense. The qualitative alignment indicates that continuous improvement of the LEM model presented may lead to a well behaved and robust predictive technique for DOD drop formation. Due to the model being designed in a commercially available circuit analyzer freeware, the model can be easily modified, adapted, or transferred to any other acoustic system.

7. REFERENCES

Berger, S.S., Burr, R.F., Padgett, J.D., and Tence, D.A., 1997 "Ink manifold design of phase change piezoelectric ink jets", International Conference on Digital Printing Technologies, 703-708

Burr, R.F., Berger, S.S., and Tence, D.A., 1996 "Overview of phase change piezoelectric ink jet fluids modeling and design", FED-Vol. 239, Fluids Engineering Conference, Vol. 4, pp 545-552

Brenner, M.P., Eggers, J., Joseph, K., Nagel, S.R., and Shi, X.D., 1997, "Breakdown of scaling in droplet fission at high Reynolds number", Phys. Fluids, Vol. 9, 1573-1590

Chaudhary, K.C. and Redekopp, L.G., 1980, "The nonlinear capillary instability of a liquid jet. Part 1. Theory", Journal of Fluid Mechanics, Vol. 96, pp 257-285

Chaudhary, K.C. and Maxworthy, T., 1980, "The nonlinear capillary instability of a liquid jet. Part 2. Experiments on jet behavior before droplet formation", Journal of Fluid Mechanics, Vol. 96, pp 275-286

Chaudhary, K.C. and Maxworthy, T., 1980, "The nonlinear capillary instability of a liquid jet. Part 3. Experiments on satellite drop formation and control", Journal of Fluid Mechanics, Vol. 96, pp 287-297

Chen, A.U. and Basaran, O.A., 2001, "A new method for significantly reducing drop radius without reducing nozzle radius in drop-on-demand drop production", Phys. Fluids, Vol. 14, pp L1-L4

Chen, A.U., Notz, P.K., and Basaran, O.A., 2002, "Computational and experimental analysis of pinch-off and scaling", Physical Review Letters, Vol. 88, pp 174501-1 through 174501-4

Chen, P.-H., Peng, H.-Y., Liu, H.-Y., Chang, S.-L., Wu, T.I., and Cheng, C.-H., 1998, "Pressure response and droplet ejection of a piezoelectric inkjet printhead", Inter. J. Mech. Sci., Vol. 41, pp 235-248

Christensen, C. M., 1997, The Innovator's Dilemma: When New Technologies Cause Great Firms to Fail, Harvard Business School Press

Cohen, I., Brenner, M.P., Eggers, J., Nagel, S.R., 1999 "Two fluid drop snap-off problem: Experiments and theory", Physical Review Letters, Vol. 83, pp 1147-1150

Daniels, B.J. and Liburdy, J.A., 2004, "Oscillatory free surface displacement of finite amplitude in a small orifice", Journal of Fluids Engineering, Vol. 126, pp 818-826

Eggers, J. and Dupont, T.F., 1994, "Drop formation in a one-dimensional approximation of the Navier-Stokes equation", J. Fluid Mechanics, Vol. 262, 205-221

Eggers, J., 1995, "Theory of Drop Formation", Phys. Fluids, Vol. 7, pp 941-953

Eggers, J., 1997, "Nonlinear dynamics of breakup and free-surface flows", Reviews of Modern Physics, Vol. 69, 865-928

Eggers, J., 2000, "Singularities in droplet pinching with vanishing viscosity", J. Appl. Math., Vol. 60, pp1997-2008

Gallas, Q., 2002, "Lumped element modeling of piezoelectric-driven synthetic jet actuators for active flow control", University of Florida

Gallas, Q., Carroll, B., Cattafesta, L., Holman, R., Nishida, T., Sheplak, M., 2003, "Lumped Element Modeling of Piezoelectric-Driven Synthetic Jet Actuators", American Institute of Aeronautics and Astronautics Journal, Vol. 41, pp 240-247

de Jong, J., de Bruin, G., Reinten, H., van der Berg, M., Wijshoff, H., Versluis, M., and Lohse, D., 2006, "Air entrapment in piezo-driven inkjet printheads", J. Acoust. Soc. Am., Vol. 120, pp 1257-1265

Englehardt, M., 2011 (Version 4.12u) [LTspice IV], Milpitas California: Linear Technology Corporation

Magnus, G. 1855, "Hydraulishe Untersuchungen" Ann. Phys. Chem., No. 95(171), pp 1-59

Merhaut, J., *Theory of Electroacoustics*, McGraw-Hill, New York, 1981

Strutt, J.W. and Rayleigh, L., 1878, "On the Instability of Jets", Proceedings of London Mathematical Society, Vol. 10, pp 4-13

Rutland, D. F., and Jameson, G. J., "A non-linear effect in the capillary instability of liquid jets", Journal of Fluid Mechanics, Vol. 46, pp 267-271

Sangplung, S., and Liburdy, J., 2009, "Droplet formation under the effect of a flexible nozzle plate", Journal of Colloid and Interface Science, Vol. 337, pp 145-154

Savart, F. 1833 "Memoire sur la constitution des veines liquides lancees par des orifices ciculares en mince paroi" Ann. du Chim., Vol. 53, pp 337-386

Shah, R.K. and London, A.L., 1978, "Laminar flow forced convection in ducts: A source book for compact heat exchanger analytical data", Academic Press, New York, 1978

Shield, T.W., Bogy, D.B., and Talke, F.E., 1986, "A numerical comparison of one-dimensional fluid jet models applied to drop-on-demand printing", Journal of Computational Physics, Vol. 67, 327-347

Shield, T.W., Bogy, D.B, and Talke, F.E., 1987, "Drop formation by DOD ink-jet nozzles: a comparison of experiments and numerical simulation", IBM J. Res. Dev. Vol. 31, pp 96-100

Groot Wassink, M.B., Zollner, F., Bosgra, O.H., Koekebakker, 2006 "Improving the drop-consistency of an inkjet printhead using meniscus-based Iterative Learning Control", Proceeding of the 2006 IEEE, International Conference on Control Applications, pp 2830-2835

Wilkes, E.D., Phillips, S.D., Basaran, O.A., 1999, "Computational and experimental analysis of dynamics of drop formation", Physics of Fluids, Vol. 11, pp 3577-3598

Yang, G., 2007, "Effect of PZT driving waveform and frequency on meniscus shape and drop-on-demand droplet formation parameters", Oregon State University

Yang, G. and Liburdy, J.L., 2004 "Droplet formation from a pulsed vibrating micro-nozzle", ASME Heat Transfer/Fluid Engineering Summer Conference, Division of Fluid Engineering, HT-FED2004-56272, July 11-15

Yang, G. and Liburdy, J.L., 2007 "The effects of driving waveform and frequency on the droplet formation process", International Mechanical Engineering Congress & Exposition, EMECE, November 11-16, pp 1-11

Yang, G., 2007, "Effect of PZT driving waveform and frequency on meniscus shape and drop-on-demand droplet formation parameters", Oregon State University Ph.D. Archives

Yang, A. and Tsai, W., 2006, "Ejection process simulation for a piezoelectric microdroplet generator", Journal of Fluids Engineering, Vol. 128, pp 1144-1152

Zhang, W.W., Lister, J.R., 1999 "Similarity solutions for capillary pinch-off in fluids of differing viscosity", Phys. Review Letters, Vol. 83, 1151-1154

Zhang, X., 1995, "An experimental study of dynamics of drop formation", Phys. Fluids, Vol. 7, pp 1184-1203

Zhang, X., 1998, "Dynamics of drop formation in viscous flows", Chemical Engineering Science, Vol. 54, pp1759-1774

APPENDICES

APPENDIX A

Drop generator dimensions

The drop generator used was the same as the drop generator used in Hawke (2006) with a few minor modifications. The first modification was to replace the nylon insert with an aluminum insert of a similar design. The second modification was to cut off a corner of the nozzle plate, done prior to this research by a previous research assistant. The aluminum insert may have effectively changed the internal plenum volumes, so the assembled drop generator was measured to determine the final dimensions. The nozzle plate modification in no way interacted with the fluid system, it was modified to make room for the refill port fitting in the assembled device. A digital scan of a drawing of the cross sectional area of the droplet generator is included on the next page. All dimensions necessary for calculating LEM parameters are shown on the drawing. Some additional engineering drawings are also included which pertain to the physical support structure. Engineering drawings of non-modified components of the drop generator can be found in Hawke (2006). The DropGenMount001 and DropGenMount002 parts were used to mount the drop generator to the vertical traverse system. The MountCap part was used to hold the drop generator in place against DropGenMount001. The Tubing Mount part was used to mount a support beam for the refill port to the work table.

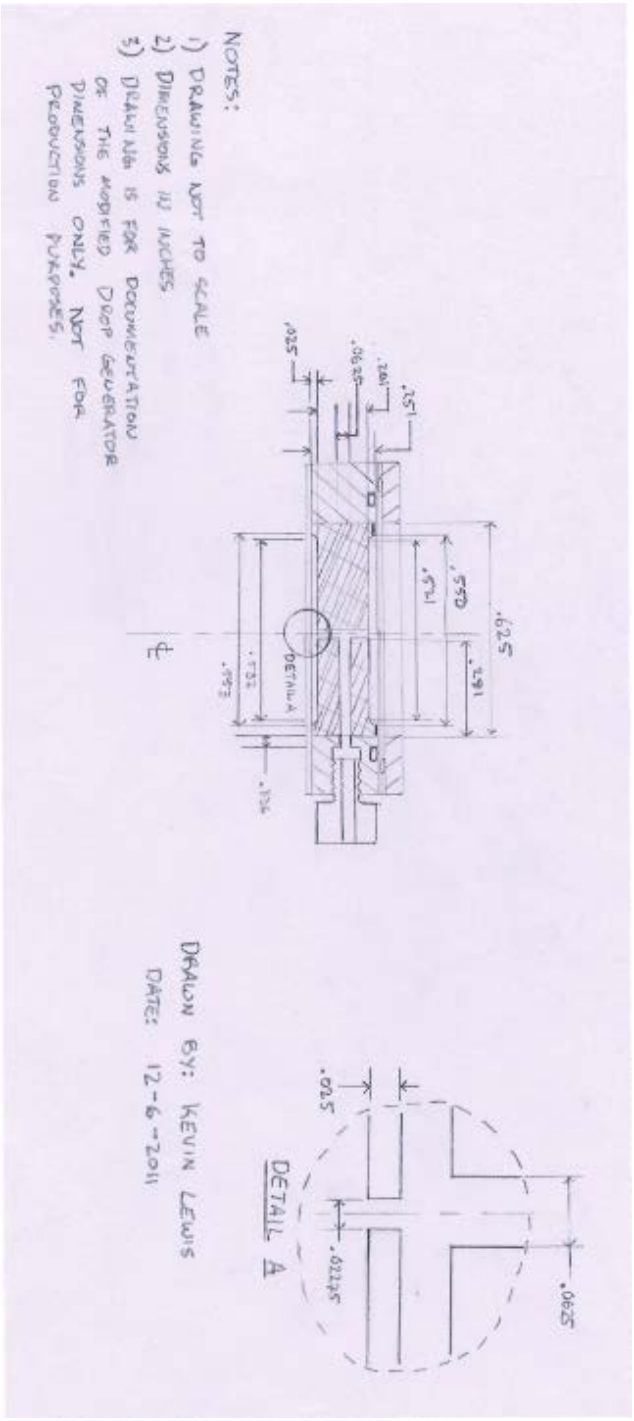

Figure A-1: A detailed drawing that lists the important physical dimensions used for calculating the lumped element parameters in the LEM model.

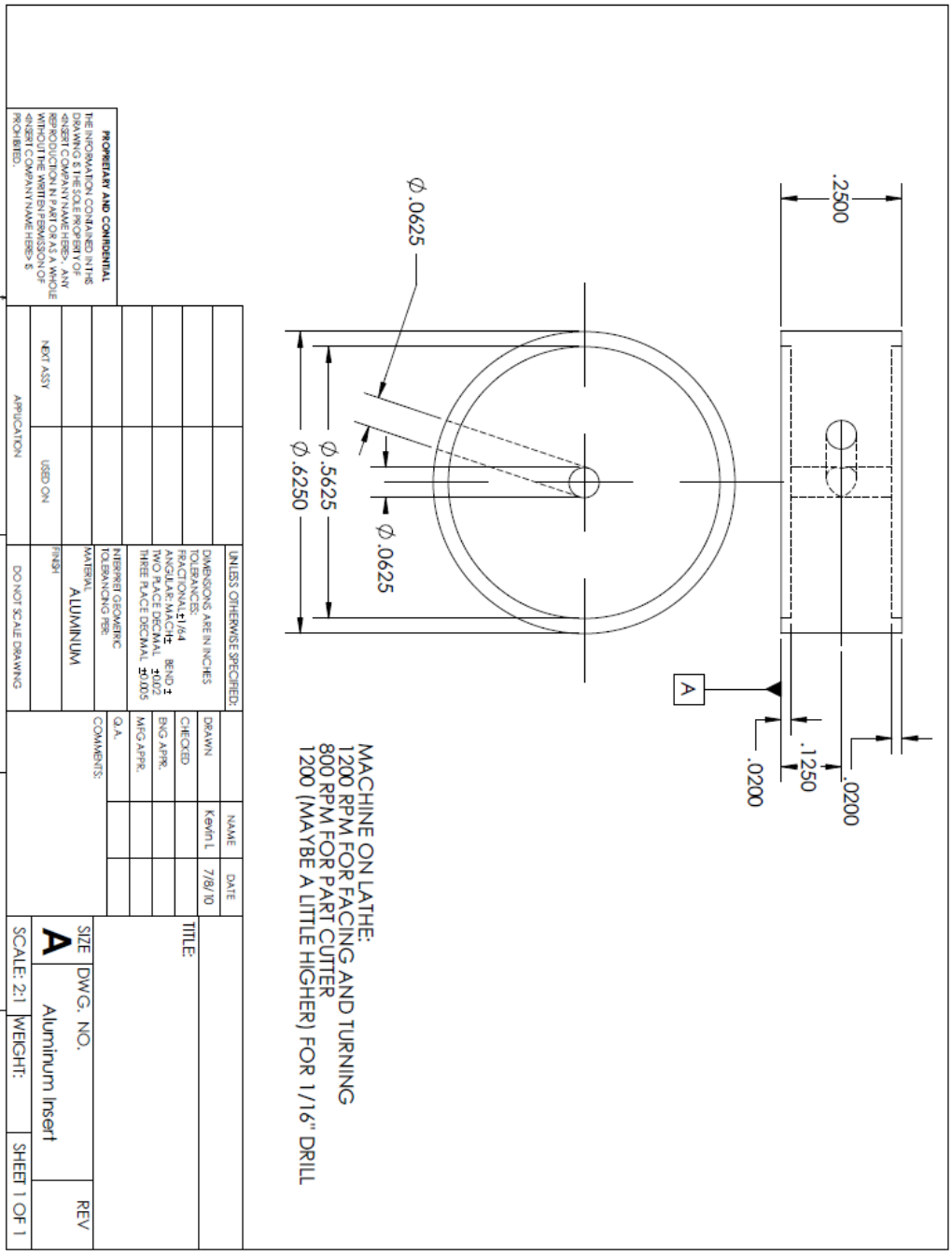
.2500
.0200
.1250
.0200
A
Ø.0625
Ø.5625
Ø.6250
Ø.0625
MACHINE ON LATHE:
1200 RPM FOR FACING AND TURNING
800 RPM FOR PART CUTTER
1200 (MAYBE A LITTLE HIGHER) FOR 1/16" DRILL
PROPRIETARY AND CONFIDENTIAL
THE INFORMATION CONTAINED IN THIS DRAWING IS THE SOLE PROPERTY OF <INSERT COMPANY NAME HERE>. ANY REPRODUCTION IN PART OR AS A WHOLE WITHOUT THE WRITTEN PERMISSION OF <INSERT COMPANY NAME HERE> IS PROHIBITED.
UNLESS OTHERWISE SPECIFIED:
DIMENSIONS ARE IN INCHES
TOLERANCES:
FRACTIONAL ±1/64
ANGULAR: MACH ± BEND ±
TWO PLACE DECIMAL ±0.02
THREE PLACE DECIMAL ±0.005
INTERPRET GEOMETRIC TOLERANCING PER:
MATERIAL
ALUMINUM
FINISH
DO NOT SCALE DRAWING
NAME
DATE
DRAWN
Kevin L
7/8/10
CHECKED
ENG APPR.
MFG APPR.
Q.A.
COMMENTS:
NEXT ASSY
USED ON
APPLICATION
TITLE:
SIZE
A
DWG. NO.
Aluminum Insert
REV
SCALE: 2:1
WEIGHT:
SHEET 1 OF 1

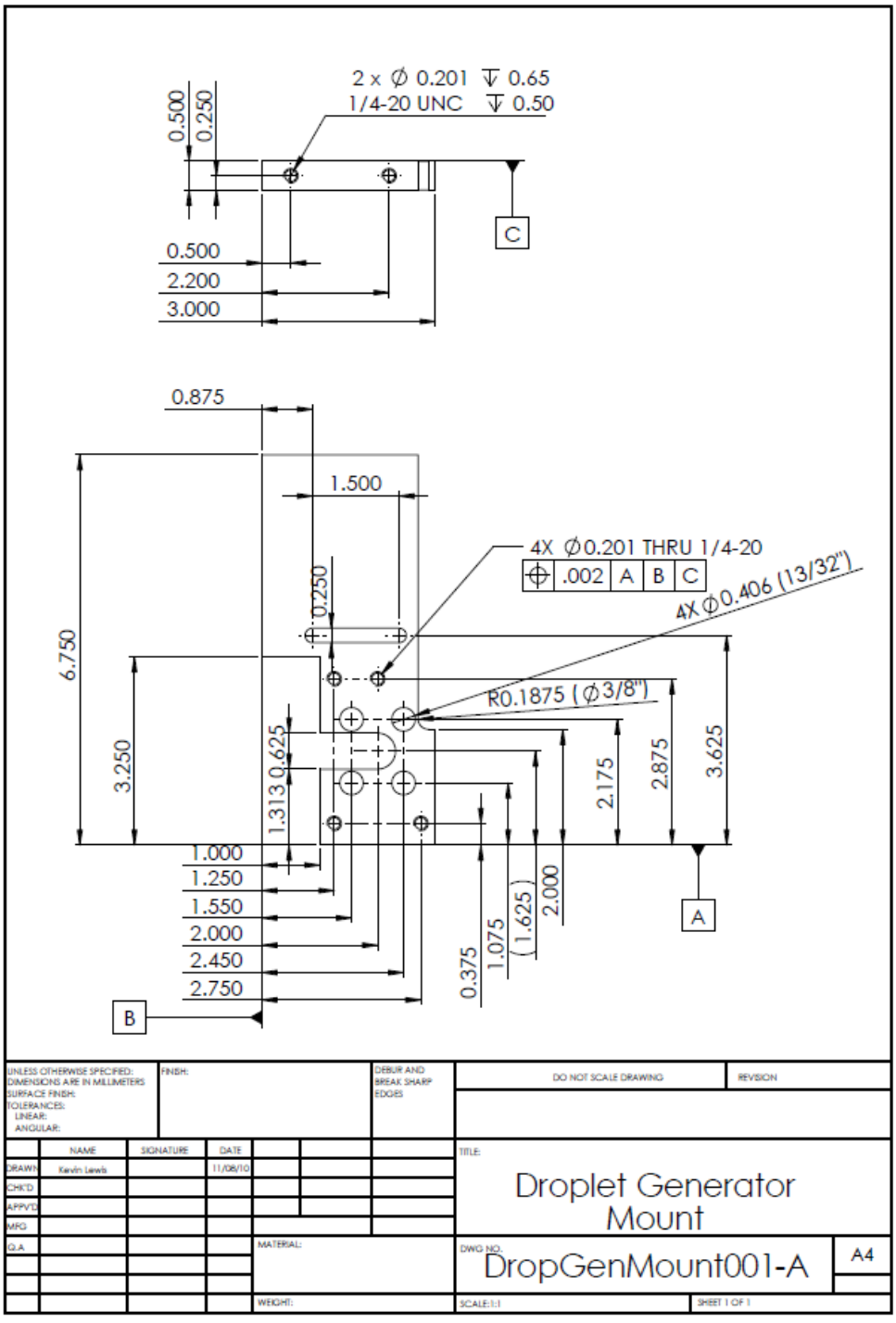
2 x ∅ 0.201 ↧ 0.65
1/4-20 UNC ↧ 0.50
0.500
0.250
C
0.500
2.200
3.000
0.875
1.500
4X ∅0.201 THRU 1/4-20
.002 A B C
4X ∅0.406 (13/32")
0.250
6.750
R0.1875 (∅3/8")
3.250
0.625
1.313
2.175
2.875
3.625
1.000
1.250
1.550
2.000
2.450
2.750
0.375
1.075
(1.625)
2.000
A
B
UNLESS OTHERWISE SPECIFIED:
DIMENSIONS ARE IN MILLIMETERS
SURFACE FINISH:
TOLERANCES:
LINEAR:
ANGULAR:
FINISH:
DEBUR AND BREAK SHARP EDGES
DO NOT SCALE DRAWING
REVISION
NAME
SIGNATURE
DATE
DRAWN
Kevin Lewis
11/08/10
CHK'D
APPV'D
MFG
Q.A
MATERIAL:
WEIGHT:
TITLE:
Droplet Generator Mount
DWG NO.
DropGenMount001-A
A4
SCALE:1:1
SHEET 1 OF 1

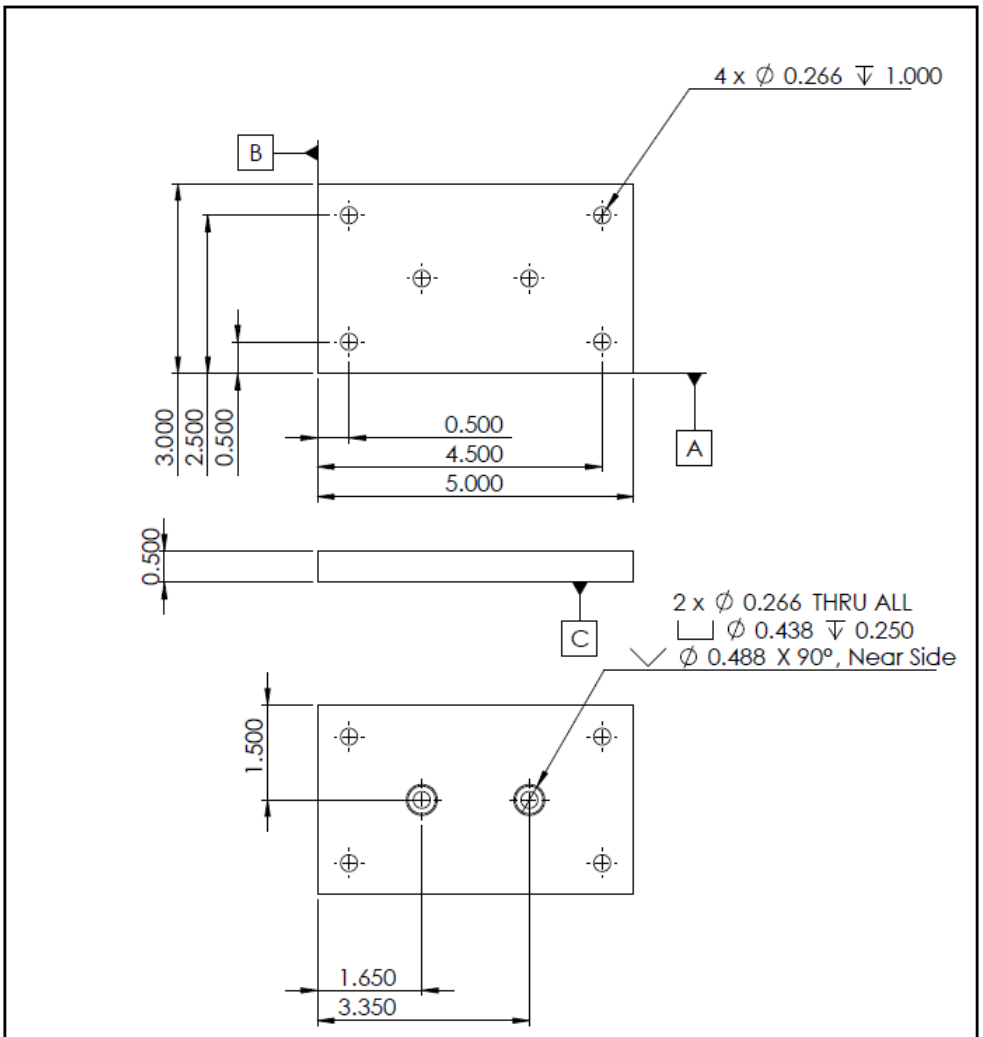

UNLESS OTHERWISE SPECIFIED: DIMENSIONS ARE IN MILLIMETERS SURFACE FINISH: TOLERANCES: LINEAR: ANGULAR:		FINISH:			DEBUR AND BREAK SHARP EDGES	DO NOT SCALE DRAWING	REVISION
	NAME	SIGNATURE	DATE			TITLE:	
DRAWN	Kevin Lewis		11/09/10				
CHK'D							
APPV'D							
MFG							
Q.A				MATERIAL:		DWG NO. DropGenMount002-A	A4
				WEIGHT:		SCALE:1:2	SHEET 1 OF 1

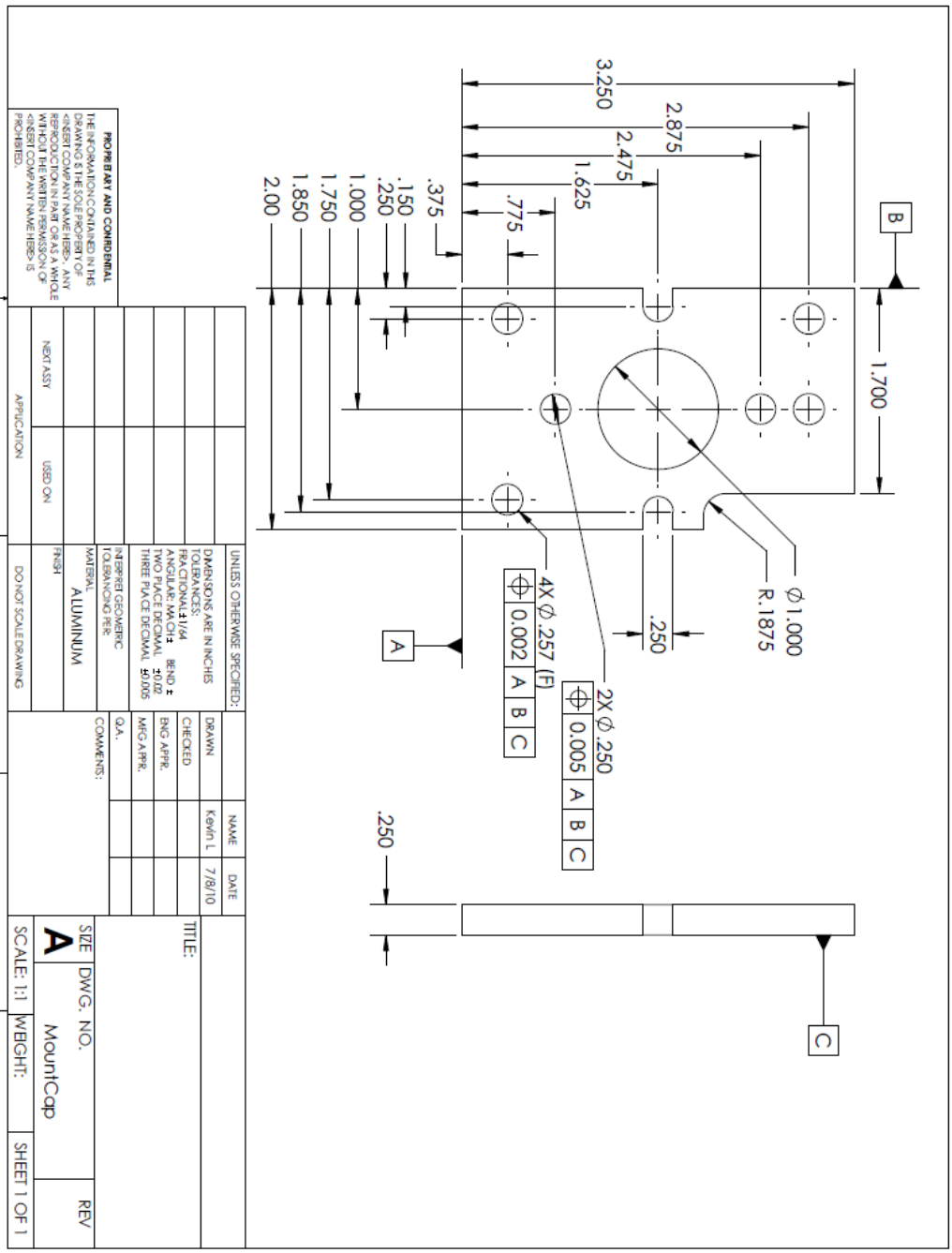
B
1.700
3.250
2.875
2.475
1.625
.775
.375
.150
.250
1.000
1.750
1.850
2.00
Ø1.000
R.1875
.250
2X Ø.250
0.005 A B C
4X Ø.257 (F)
0.002 A B C
A
.250
C
PROPRIETARY AND CONFIDENTIAL
THE INFORMATION CONTAINED IN THIS DRAWING IS THE SOLE PROPERTY OF <INSERT COMPANY NAME HERE>. ANY REPRODUCTION IN PART OR AS A WHOLE WITHOUT THE WRITTEN PERMISSION OF <INSERT COMPANY NAME HERE> IS PROHIBITED.
NEXT ASSY
USED ON
APPLICATION
DO NOT SCALE DRAWING
UNLESS OTHERWISE SPECIFIED:
DIMENSIONS ARE IN INCHES
TOLERANCES:
FRACTIONAL ± 1/64
ANGULAR: MACH ± BEND ± 1°
TWO PLACE DECIMAL ±0.02
THREE PLACE DECIMAL ±0.005
INTERPRET GEOMETRIC TOLERANCING PER:
MATERIAL
ALUMINUM
FINISH
Q.A.
COMMENTS:
DRAWN
CHECKED
ENG APPR.
MFG APPR.
NAME
Kevin L
DATE
7/8/10
TITLE:
SIZE
A
DWG. NO.
MountCap
REV
SCALE: 1:1
WEIGHT:
SHEET 1 OF 1

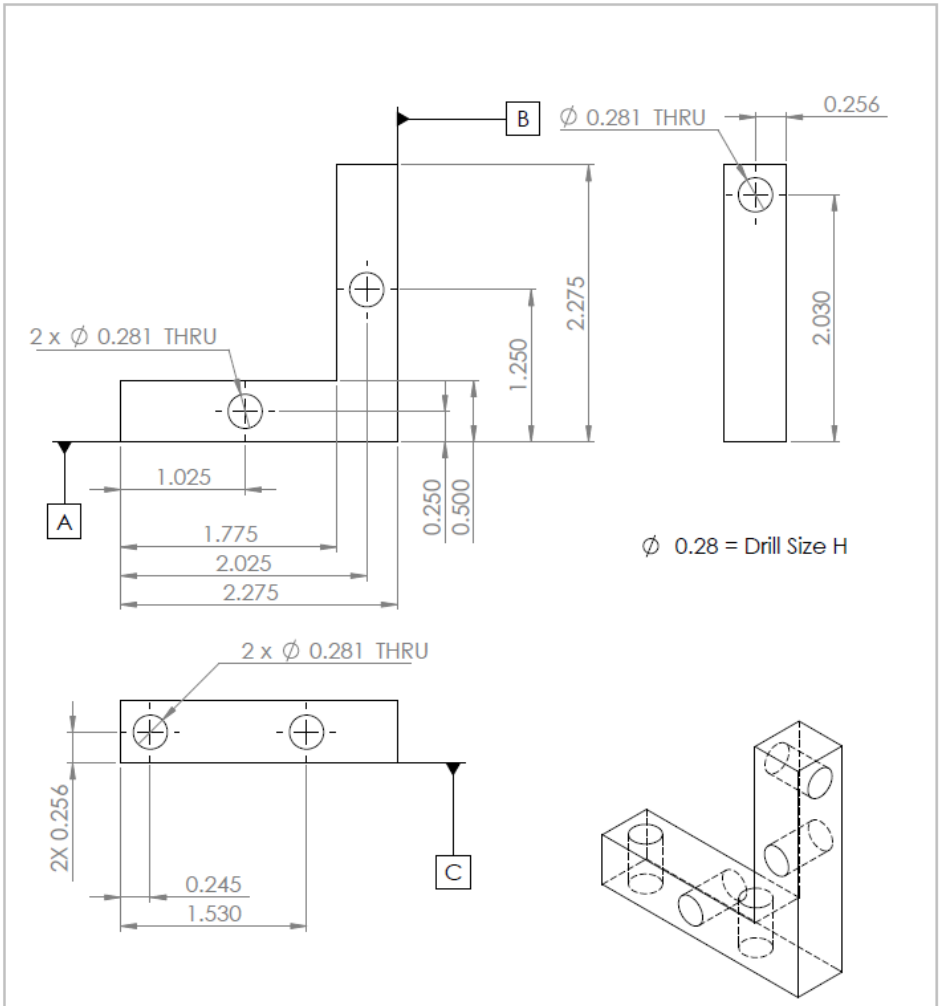

UNLESS OTHERWISE SPECIFIED: DIMENSIONS ARE IN MILLIMETERS SURFACE FINISH: TOLERANCES: LINEAR: ANGULAR:		FINISH: Machined		DEBUR AND BREAK SHARP EDGES	DO NOT SCALE DRAWING	REVISION
	NAME	SIGNATURE	DATE			TITLE:
DRAWN	Kevin L		3/30/2011			
CHK'D						
APPV'D						
MFG						
Q.A				MATERIAL: Aluminum	DWG NO. Tubing Mount	A4
				WEIGHT:	SCALE:1:1	SHEET 1 OF 1

APPENDIX B

Acoustic mass and acoustic resistance as functions of frequency

The acoustic mass and acoustics resistance equations for flow through a duct are copied from Yang (2007) below:

$$R = real\left(\frac{1}{\int_0^a j\cdot\frac{1}{\rho L\omega}\cdot\left[1-\frac{J_0\left(\sqrt{-j\cdot\frac{\omega r^2}{\nu}}\right)}{J_0\left(\sqrt{-j\cdot\frac{\omega a^2}{\nu}}\right)}\right]\cdot 2\pi r\cdot dr}\right) \quad \text{B-1}$$

$$M = imag\left(\frac{1}{\omega}\cdot\frac{1}{\int_0^a j\cdot\frac{1}{\rho L\omega}\cdot\left[1-\frac{J_0\left(\sqrt{-j\cdot\frac{\omega r^2}{\nu}}\right)}{J_0\left(\sqrt{-j\cdot\frac{\omega a^2}{\nu}}\right)}\right]\cdot 2\pi r\cdot dr}\right) \quad \text{B-2}$$

Where "real" and "imag" are the real and imaginary parts of the equations inside the brackets, ρ is the density, a is the radius of the geometry in question, L is the length of the geometry in question, r is the variable radius, ω is the frequency of oscillations, and ν is the kinematic viscosity.

APPENDIX C

LEM Model in LTspice IV

Appendix C is dedicated to the documentation of the LEM model. The model was generated in LTspice to take advantage of the software's analog circuit solver. This appendix will also document the displacement as a function of voltage look-up-table for the piezoelectric disk. It will also document the acoustic mass as a function of stokes number and acoustic resistance as a function of stokes number look-up-tables. The LTspice IV circuit is included as both the visual schematic and the spice netlist. The visual schematic is shown as the full circuit and also in sections so that the reader can better view the definitions of the elements.

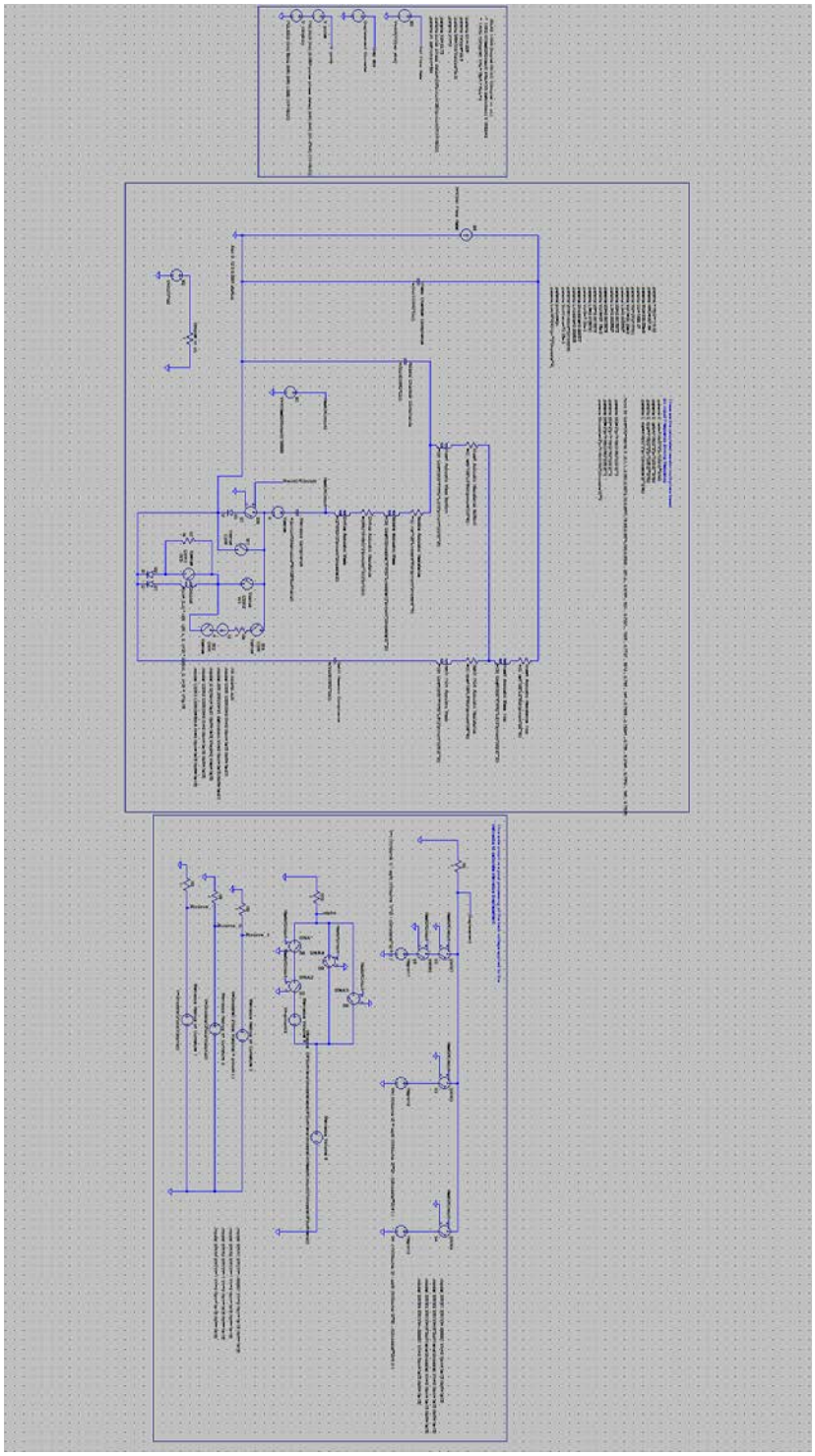

Figure C-1: This figure shows the full visual schematic for the LTspice IV LEM model.

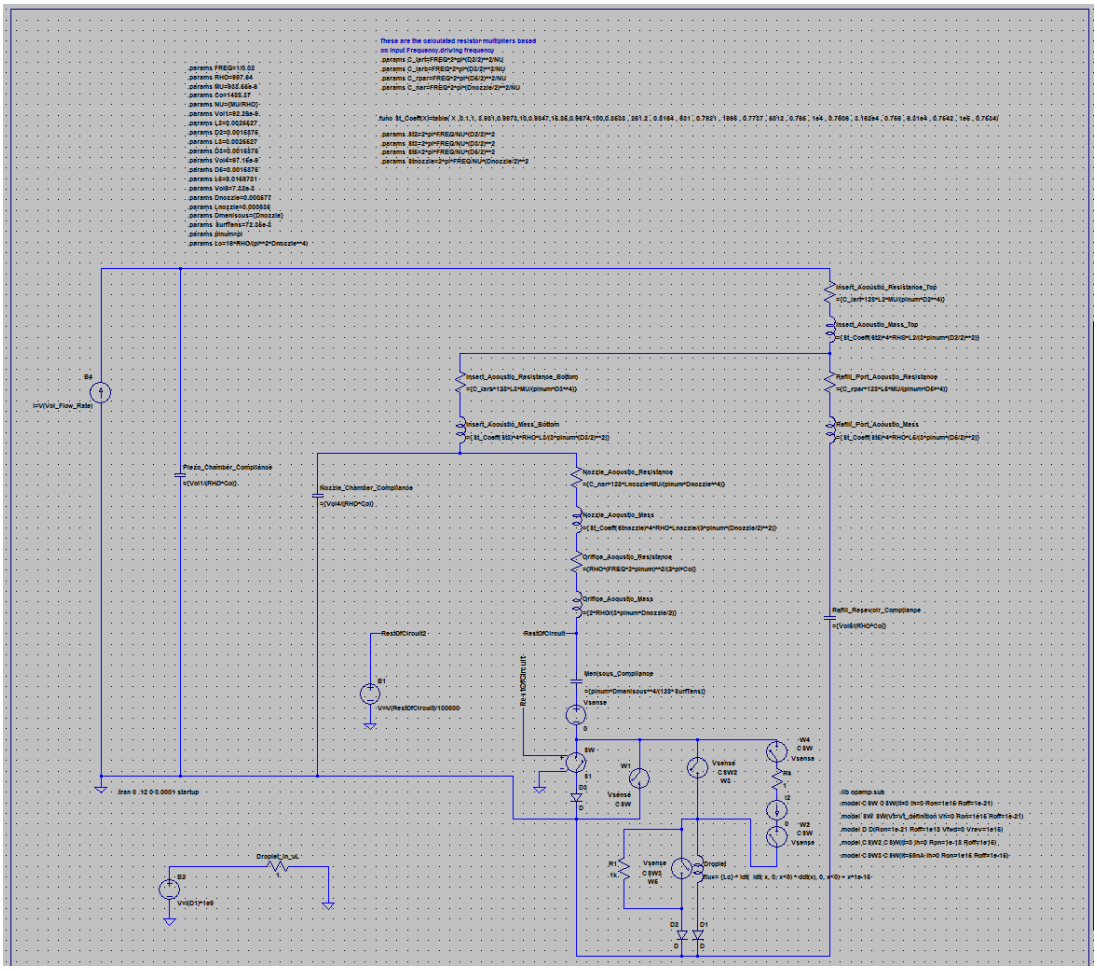

Figure C-2: A closer view of the LEM model for the droplet generator. Parameters and lookup tables are defined in the top portion of the figure. The circuit depicts the equivalent electroacoustic LEM circuit to the droplet generator.

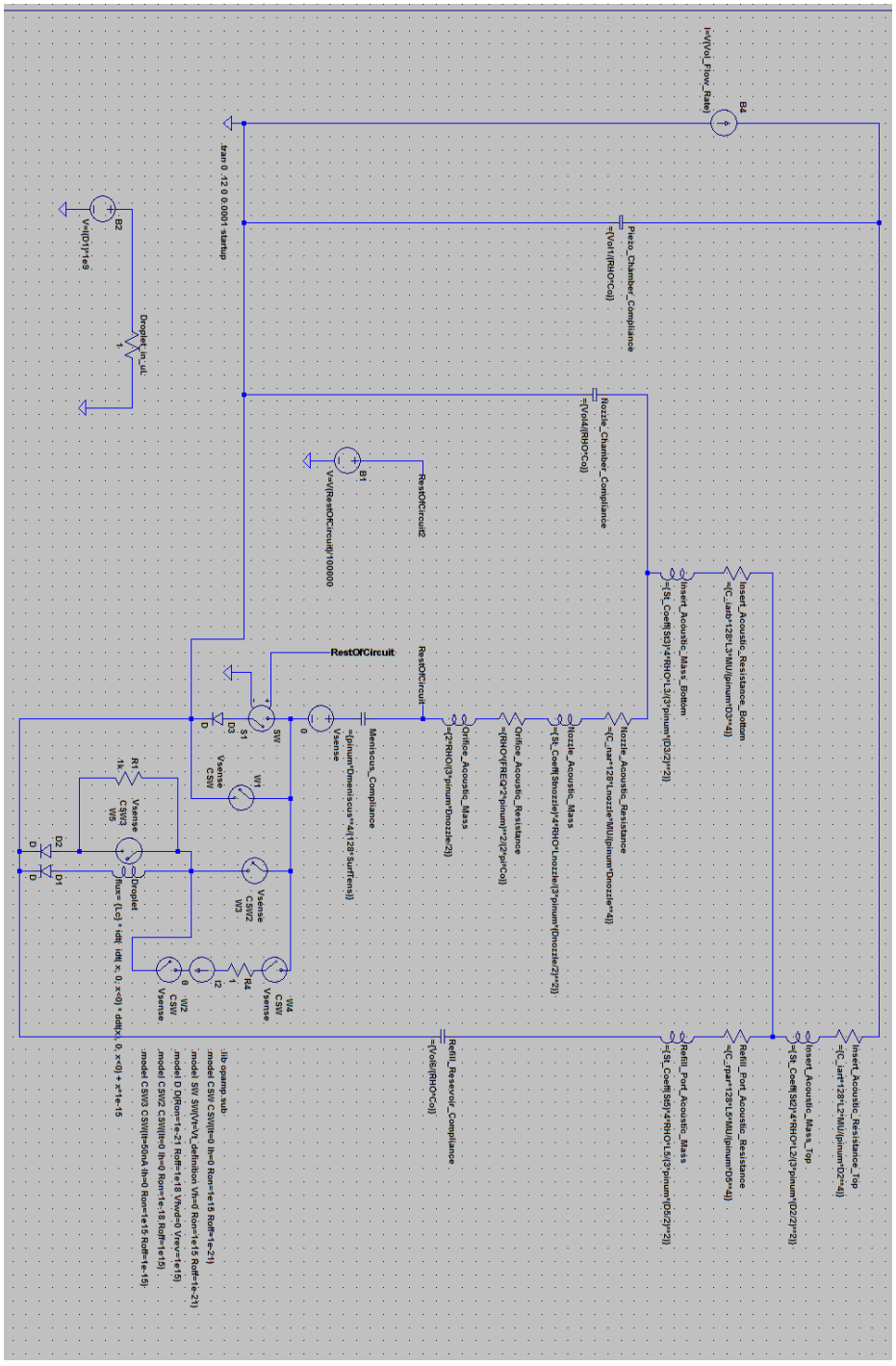

Figure C-3: This figure is a closer view of just the LEM model. Note that in the lower left corner of the figure, from a landscape perspective, there is a small circuit that converts the flow rate through the "Droplet" element from m3/s to µL/s.

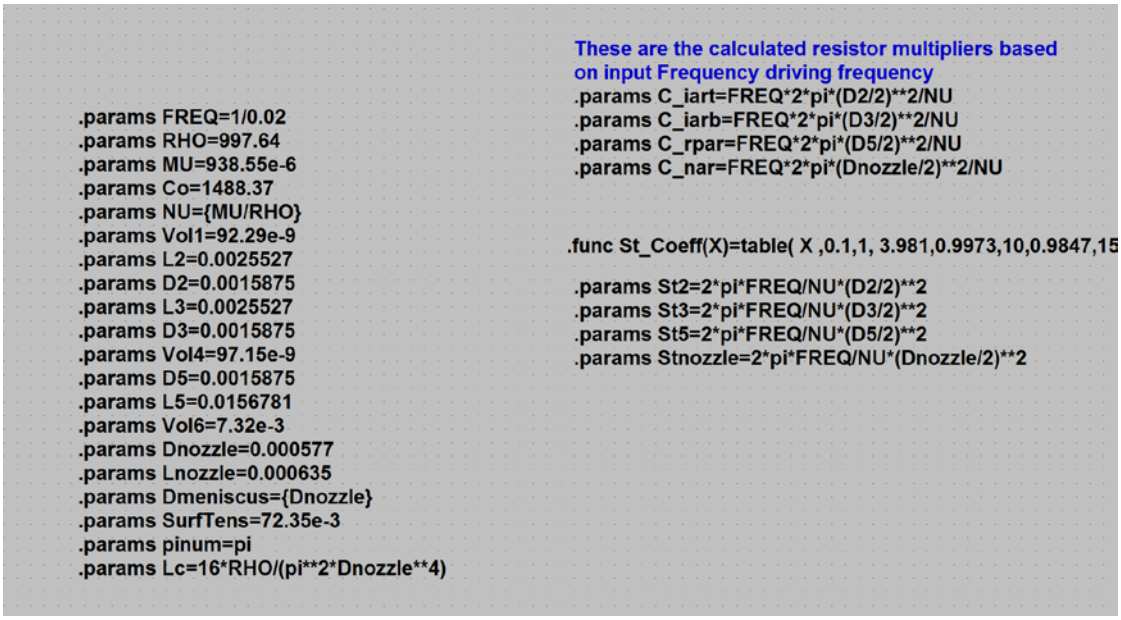

Figure C-4: This figure is a closer view of the LEM model parameter definitions. Each line is a different dimension, volume, or physical parameter used to calculate the value of the LEM elements shown in Figure C-3. The '.func' line that is cut off by the figure boundary is the look-up-table for the acoustic mass as a function of stokes number. This look-up-table is also shown in Table D-1.

Table C-1: The acoustic mass multiplier versus Stokes number look up table.

St, Stokes Number	C_m, Acoustic mass multiplier
0.1000×10^{-1}	1.000
3.981×10^{0}	0.9973
1.000×10^{1}	0.9847
1.585×10^{1}	0.9674
1.000×10^{2}	0.8538
2.512×10^{2}	0.8164
6.310×10^{2}	0.7921
1.995×10^{3}	0.7737
5.012×10^{3}	0.7650
1.000×10^{4}	0.7606
3.162×10^{4}	0.7560
6.310×10^{4}	0.7542
1.000×10^{5}	0.7534

Figure C-5 is a close up view of the driving waveform LEM circuitry. The voltages from the first two voltage sources, 'V_pulse' and 'V_vibration', are combined to form a single driving waveform 'V_comb'. This voltage is used as a variable in the voltage source 'Displacement_Converter' to calculate the piezoelectric disk volume displacement due to the voltage applied. This displacement is also output as a voltage ('Disp_abs'). Finally, the derivative of the volume displacement ('Disp_abs') with respect to time is performed with voltage source B3. The output is a new voltage value that represents the volume displacement rate as a function of time, i.e. volume flow rate as a function of time ('Vol_Flow_Rate'). The structure of this circuit allows for simple modifications to the input waveform to be quickly modeled in the program and translated into new driving volume flow rates. The displacement as a function of voltage determination is documented in more detail in APPENDIX D.

Lastly, Figure C-5 also lists the spice directive used to measure the drop volume. The first three lines near the top of Figure C-5 integrate the volume flow rate through the droplet over a designated time span. The time span is actively set by the program by starting the integration when the threshold pressure is surpassed and stopping the integration when the volume flow rate drops below 0.015 µL/s. This was set to remove the 'noise' of the circuit since the flow rate never truly drops back to zero; the value of the current approaches zero and may become negative, but never truly reaches zero again. Anything below 0.015 µL/s was assumed to be such a low

volume flow rate that the drop must have detached and the flow was once again contained to the meniscus oscillations.

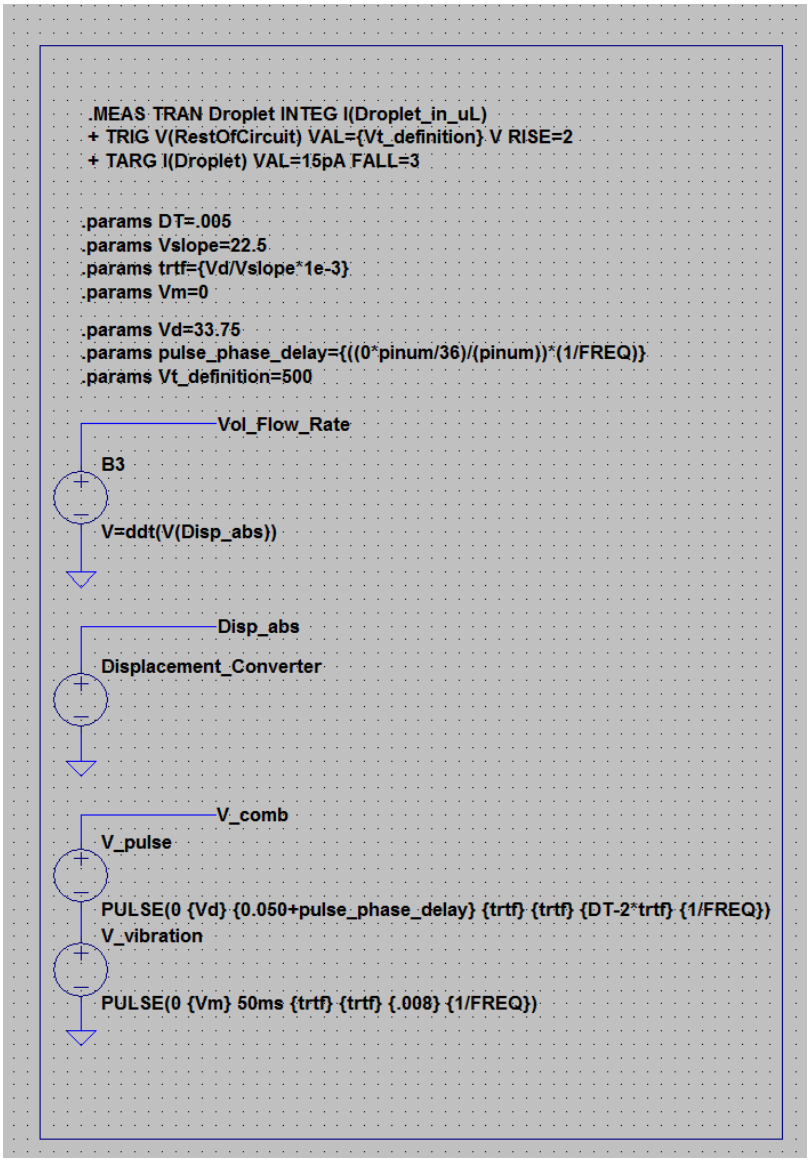

Figure C-5: This figure shows the driving waveform circuits. The voltage conditions into the piezoelectric disk are set in the lists of '.params' near the top. These values are used to output a combined meniscus vibration and pulse waveform ('V_comb'). The voltages propogate through the system to output a volume flow rate as a function of time. The top three lines in the figure are a spice directive used to integrate the volume flow rate over time through the droplet modeling element shown in Figure C-3 (the µL/s element in the lower left corner from a landscape perspective).

One of the variables of interest in the study was the meniscus displacement. As such, it was considered necessary to have the model calculate the meniscus height as a function of time. In concept, this is relatively easy because the meniscus, represented by a capacitor, expands as it fills with fluid stored between the surface and the nozzle exit to accommodate the applied pressure at the nozzle exit. This is analogous to the amount of charge stored on a capacitor to accommodate the voltage supplied to the capacitor. Therefore, the two could be related using electroacoustics to define the meniscus volume as the amount of fluid stored behind the meniscus in response to an applied back pressure, which could be extracted from the model as the applied voltage to the meniscus compliance.

A free body diagram (FBD) of the surface tension forces and the applied pressure was created to demonstrate the effect of the pressure on the meniscus displacement. The result was three distinct modes of meniscus operation: internal displacement, with negative displacement into the nozzle; standard meniscus displacement, with contact angles between 0 and $\pi/2$; and hyper extended meniscus displacements, with contact angles greater than $\pi/2$. The hyper extended meniscus displacement mode was first noted in experimental flow visualizations, so the model was adjusted to account for this mode of operation when calculating meniscus displacement. Using the nozzle exit pressure as an input control for the meniscus mode, the meniscus height was calculated with the assumption that the meniscus could be treated as the cap of a sphere. The contact angle was derived from the FBD based on the pressure, surface tension forces, the nozzle geometry, and the meniscus

mode. Using the contact angle, the Pythagorean theorem, the meniscus mode and the geometry of the nozzle, the electrical circuit shown in Figure C-6 calculates the meniscus displacement. The final meniscus displacement as a function of time can be measured at the output open node 'Displacement' in the circuit shown in Figure C-6.

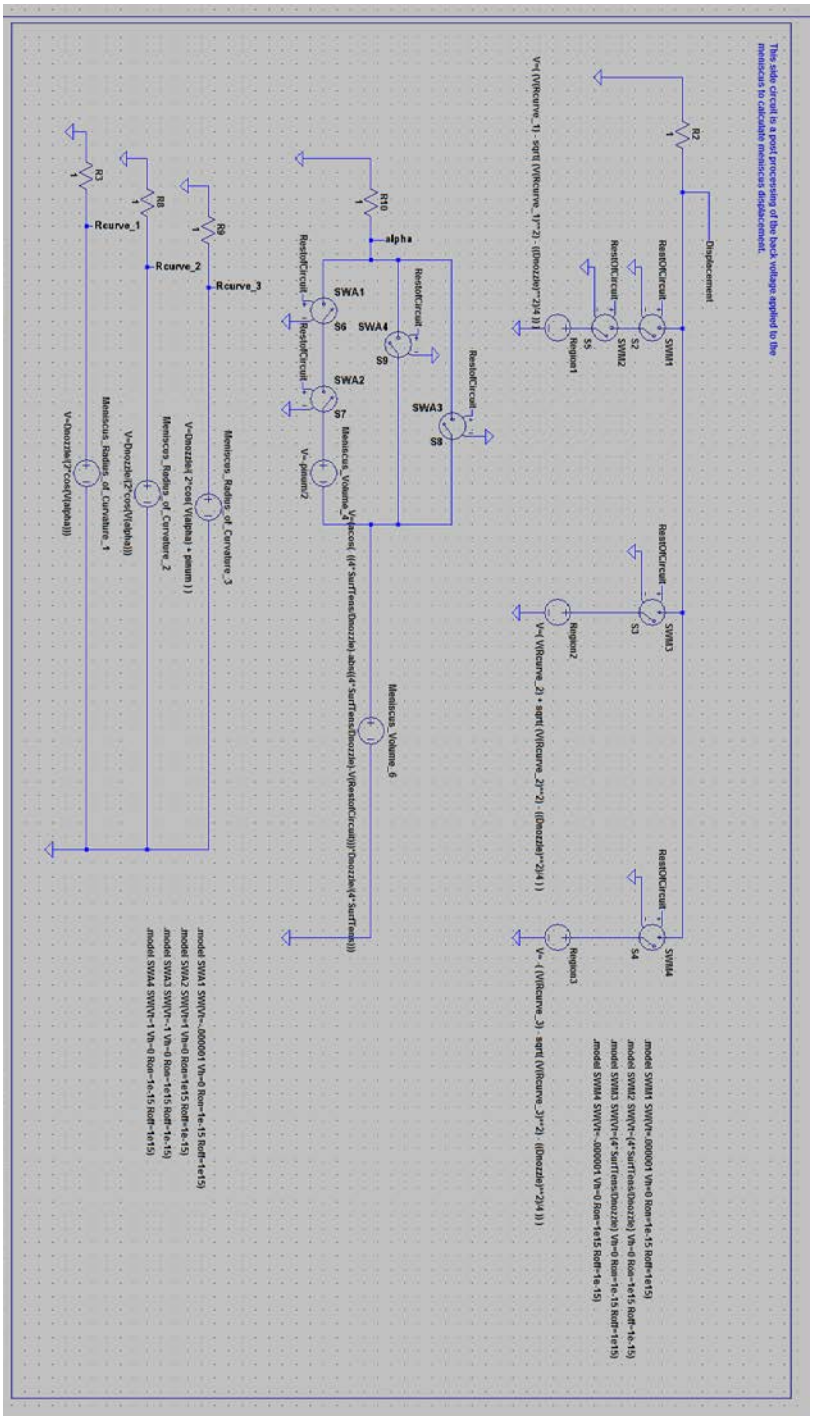

Figure C-6: A figure showing the meniscus-displacement calculation electrical circuit built into the model to facilitate easy measurements of the meniscus height versus time.

The individual elements of the LEM model were defined according to the methodology outlined in chapter 3. The LEM model diagrams above are just pictographic representations of the spice netlist shown below. Inside this netlist you may find the model definitions off all the elements, voltage sources, function based voltage sources, switches, and diodes. Theoretically, a SPICE netlist can be imported into any form of SPICE network analyzer and run the same way as it does in any other SPICE network analyzer, such as LTspice IV. This theory has not been tested with the following netlist.

Netlist:

```
* J:\THESIS BOX (mobile)\Spice Files\Final Code\LT Spice LEM Circuit
[Final] (Thesis Input).asc

R§Insert_Acoustic_Resistance_Top N001 N002
={C_iart*128*L2*MU/(pinum*D2**4)}

L§Insert_Acoustic_Mass_Top N002 N003
={St_Coeff(St2)*4*RHO*L2/(3*pinum*(D2/2)**2)}

R§Insert_Acoustic_Resistance_Bottom N003 N004
={C_iarb*128*L3*MU/(pinum*D3**4)}

Refill_Port_Acoustic_Resistance N003 N005
={C_rpar*128*L5*MU/(pinum*D5**4)}

L§Insert_Acoustic_Mass_Bottom N004 N006
={St_Coeff(St3)*4*RHO*L3/(3*pinum*(D3/2)**2)}

L§Refill_Port_Acoustic_Mass N005 N015
={St_Coeff(St5)*4*RHO*L5/(3*pinum*(D5/2)**2)}

C§Refill_Resevoir_Compliance N015 0 ={Vol6/(RHO*Co)}

C§Nozzle_Chamber_Compliance N006 0 ={Vol4/(RHO*Co)}

R§Nozzle_Acoustic_Resistance N006 N011
={C_nar*128*Lnozzle*MU/(pinum*Dnozzle**4)}
```

```
L§Nozzle_Acoustic_Mass N011 N012
={St_Coeff(Stnozzle)*4*RHO*Lnozzle/(3*pinum*(Dnozzle/2)**2)}

C§Meniscus_Compliance RestOfCircuit N019
={pinum*Dmeniscus**4/(128*SurfTens)}

L§Orifice_Acoustic_Mass N014 RestOfCircuit
={2*RHO/(3*pinum*Dnozzle/2)}

C§Piezo_Chamber_Compliance N001 0 ={Vol1/(RHO*Co)}

R§Orifice_Acoustic_Resistance N012 N014
={RHO*(FREQ*2*pinum)**2/(2*pi*Co)}

B1 RestOfCircuit2 0 V=V(RestOfCircuit)/100000

L§Droplet N023 N026 flux= {Lc} * idt( idt( x, 0, x<0) * ddt(x), 0,
x<0) + x*1e-15 Rser=0 Rpar=0 Cpar=0

S1 N021 N020 RestOfCircuit 0 SW
W1 N020 0 Vsense CSW
Vsense N019 N020 0
D1 N026 0 D
W4 P001 N020 Vsense CSW
I2 N022 P002 0
W2 N023 P002 Vsense CSW
R4 P001 N022 1
W3 N020 N023 Vsense CSW2
W5 N023 N025 Vsense CSW3
D2 N025 0 D
R1 N023 N025 1k
D3 N021 0 D

V_vibration N016 0 PULSE(0 {Vm} 50ms {trtf} {trtf} {.008} {1/FREQ})

V_pulse V_comb N016 PULSE(0 {Vd} {0.050+pulse_phase_delay} {trtf}
{trtf} {DT-2*trtf} {1/FREQ})

B§Displacement_Converter Disp_abs 0 V=8.3064858681e-12*V(V_comb)
B3 Vol_Flow_Rate 0 V=ddt(V(Disp_abs))

B4 0 N001 I=V(Vol_Flow_Rate)

R§Droplet_in_µL N024 0 1

B2 N024 0 V=I(D1)*1e9

R2 Displacement 0 1

B§Region1 N008 0 V=( (V(Rcurve_1) - sqrt( (V(Rcurve_1)**2) -
((Dnozzle)**2)/4 )) )

B§Region2 N009 0 V=( V(Rcurve_2) + sqrt( (V(Rcurve_2)**2) -
((Dnozzle)**2)/4 ) )
```

```
B§Region3 N010 0 V= -( (V(Rcurve_3) - sqrt( (V(Rcurve_3)**2) -
((Dnozzle)**2)/4 )) )

S2 N007 Displacement RestOfCircuit 0 SWM1
S3 N009 Displacement RestOfCircuit 0 SWM3
S4 N010 Displacement RestOfCircuit 0 SWM4
S5 N008 N007 RestOfCircuit 0 SWM2
R3 Rcurve_1 0 1

B§Meniscus_Radius_of_Curvature_1 Rcurve_1 0
V=Dnozzle/(2*cos(V(alpha)))

R8 Rcurve_2 0 1

B§Meniscus_Radius_of_Curvature_2 Rcurve_2 0
V=Dnozzle/(2*cos(V(alpha)))

R9 Rcurve_3 0 1

B§Meniscus_Radius_of_Curvature_3 Rcurve_3 0 V=Dnozzle/( 2*cos(
V(alpha) + pinum ) )

R10 alpha 0 1

B§Meniscus_Volume_6 N013 0 V=(acos( ((4*SurfTens/Dnozzle)-
abs((4*SurfTens/Dnozzle)-V(RestofCircuit)))*Dnozzle/(4*SurfTens)))

B§Meniscus_Volume_4 N018 N013 V=-pinum/2

S6 N017 alpha RestofCircuit 0 SWA1
S7 N018 N017 RestofCircuit 0 SWA2
S8 N013 alpha RestofCircuit 0 SWA3
S9 N013 alpha RestofCircuit 0 SWA4

.model D D
.lib C:\PROGRA~2\SPICEP~1\LTSPIC~1\lib\cmp\standard.dio

.params FREQ=1/0.02
.params RHO=997.64
.params MU=938.55e-6
.params Co=1488.37
.params NU={MU/RHO}
.params Vol1=92.29e-9
.params L2=0.0025527
.params D2=0.0015875
.params L3=0.0025527
.params D3=0.0015875
.params Vol4=97.15e-9
.params D5=0.0015875
.params L5=0.0156781
.params Vol6=7.32e-3
.params Dnozzle=0.000577
.params Lnozzle=0.000635
```

```
.params Dmeniscus={Dnozzle}
.params SurfTens=72.35e-3
.params pinum=pi
.params Lc=16*RHO/(pi**2*Dnozzle**4)
.params C_iart=FREQ*2*pi*(D2/2)**2/NU
.params C_iarb=FREQ*2*pi*(D3/2)**2/NU
.params C_rpar=FREQ*2*pi*(D5/2)**2/NU
.params C_nar=FREQ*2*pi*(Dnozzle/2)**2/NU

* These are the calculated resistor multipliers based\non input
Frequency driving frequency

.tran 0 .12 0 0.0001 startup

.func St_Coeff(X)=table( X ,0.1,1,
3.981,0.9973,10,0.9847,15.85,0.9674,100,0.8538 , 251.2 , 0.8164 , 631
, 0.7921 , 1995 , 0.7737 , 5012 , 0.765 , 1e4 , 0.7606 , 3.162e4 ,
0.756 , 6.31e4 , 0.7542 , 1e5 , 0.7534)

.params St2=2*pi*FREQ/NU*(D2/2)**2
.params St3=2*pi*FREQ/NU*(D3/2)**2
.params St5=2*pi*FREQ/NU*(D5/2)**2
.params Stnozzle=2*pi*FREQ/NU*(Dnozzle/2)**2

.model D D(Ron=1e-21 Roff=1e18 Vfwd=0 Vrev=1e15)
.model CSW CSW(It=0 Ih=0 Ron=1e15 Roff=1e-21)

.MEAS TRAN Droplet INTEG I(Droplet_in_µL)
+ TRIG V(RestOfCircuit) VAL={Vt_definition} V RISE=2
+ TARG I(Droplet) VAL=15pA FALL=3

.lib opamp.sub
.model SW SW(Vt=Vt_definition Vh=0 Ron=1e15 Roff=1e-21)
.model CSW2 CSW(It=0 Ih=0 Ron=1e-18 Roff=1e15)
.model CSW3 CSW(It=50nA Ih=0 Ron=1e15 Roff=1e-15)

.params DT=.005
.params Vslope=22.5
.params trtf={Vd/Vslope*1e-3}
.params Vm=0

* This side circuit is a post processing of the back voltage applied
to the \nmeniscus to calculate meniscus displacement.

.model SWM1 SW(Vt=.000001 Vh=0 Ron=1e-15 Roff=1e15)
.model SWM2 SW(Vt={4*SurfTens/Dnozzle} Vh=0 Ron=1e15 Roff=1e-15)
.model SWM3 SW(Vt={4*SurfTens/Dnozzle} Vh=0 Ron=1e-15 Roff=1e15)
.model SWM4 SW(Vt=-.000001 Vh=0 Ron=1e15 Roff=1e-15)
.model SWA1 SW(Vt=-.000001 Vh=0 Ron=1e-15 Roff=1e15)
.model SWA2 SW(Vt=1 Vh=0 Ron=1e15 Roff=1e-15)
.model SWA3 SW(Vt=-1 Vh=0 Ron=1e15 Roff=1e-15)
.model SWA4 SW(Vt=1 Vh=0 Ron=1e-15 Roff=1e15)

.params Vd=33.75
```

```
.params pulse_phase_delay={((0*pinum/36)/(pinum))*(1/FREQ)}
.params Vt_definition=500
.backanno
.end
```

APPENDIX D

Piezoelectric disk volume displacement as a function of voltage

As mentioned in chapter 3, the piezoelectric disk's displacement as a function of voltage was measured with a profilometer and the resulting volume displacement was calculated in a MATLAB code. This appendix outlines the process by which this one done and presents the MATLAB code used for the interested reader. The steps taken to reach the final volume displacement as a function of voltage relationship are as follows:

1. The profilometer was used to measure the entire positional domain of the visible piezoelectric disk. From this, it was found that the piezoelectric disk had a concave shape to it. Note that all piezoelectric disk displacements were measured from this local minima of the piezoelectric disk's profile.
2. A MATLAB code was used to determine the piezoelectric disks radial center for the concave shape. With the center as a reference point, the code numerically averages the piezoelectric disk's positional height as a function of radius.
3. The final piezoelectric disks positional height as a function of radius is exported from this first MATLAB code for analysis by a second MATLAB code.
4. A second MATLAB code, which already contains the piezoelectric disk's positional displacement as a function of voltage input seen Table D-1, imports the positional height as a function of radius from the last MATLAB program.
5. Assuming that the ratio of the displacement to the original position of the piezoelectric disk is the same as the ratio for any other radial position on the

piezoelectric disk, a numerical volume integral was performed on the resulting piezoelectric disk's profile for every voltage input. This volume displacement as a function of voltage was recorded into a string array in the MATLAB code.

6. Finally, a line of best fit was plotted to capture volume versus voltage relationship determined above. Given that a piezoelectric disk's displacement should theoretically be linear as a function of voltage, a first order polynomial was used to capture the relationship between piezoelectric volume displacement as a function of voltage.

The equation for the volume displacement as a function of voltage is shown below in D-1. A MATLAB plot of the voltage versus volume displacement for both the measured values and the line of best fit are shown in Figure D-1.

$$\text{Volume} = 8.306 \times 10^{-12} \cdot \text{Voltage} \qquad \text{D-1}$$

Table D-1: Input voltage versus piezoelectric disk displacement.

Voltage applied to piezoelectric disk (V)	Positional displacement (um)
0	0
1	0.3
3.17	0.6
5.05	0.8
6.85	0.95
9.01	1.1
9.88	1.3
12.47	1.6
15.34	1.8
17.69	2.1
20.3	2.3
23.5	2.6
27.4	2.9
32.1	3.3
36.1	3.7
40.1	4.1
49.7	4.8
60.5	5.5
70.1	6.2
80.0	6.8
90.5	7.7
100.0	8.6
119.7	10.4
140.1	13.5
150.1	13.8

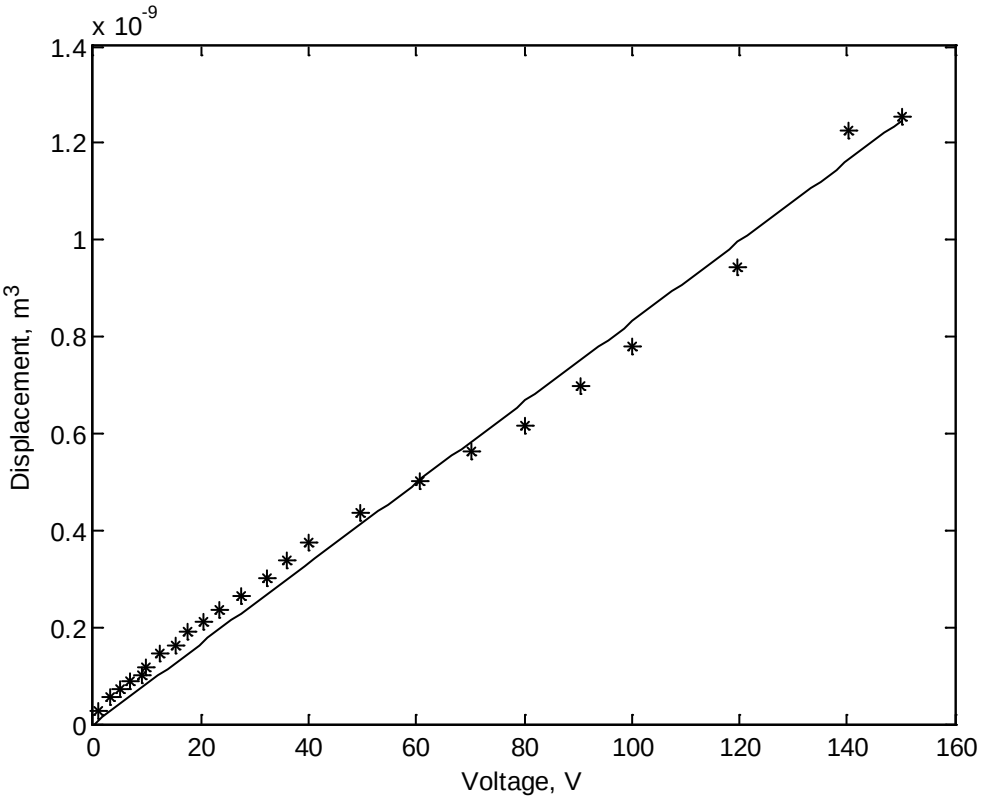

Figure D-1: This figure depicts the volume displacement of the piezoelectric disk (in m^3) as a function of the driving input voltage. The stars are the numerically calculated volumes based on the piezoelectric disk's profile and the line is the line of best fit described by equation D-1.

First MATLAB Code: This is the MATLAB code used to import the raw data from the profilometer and modify it until it could be reported as a radial based piezoelectric disk position/height.

```
%Kevin Lewis, 4/12/2011
%Importing and manipulating the piezoelectric disk's neutral profile.

clc
clear
close all

%No known global parameters to code.

%Define the ascii file and path.
[FileName, PathName] = uigetfile({'*.txt';'*.asc'},...
    'Retrieve the ascii file');
FullName=[PathName,FileName];

[Input] = importdata(FullName);
%For future reference:Data starts on line 16 (therefore
headernumber=15
%Also, the data is tab deliminated.

Data=[Input.data];
clear Input Garbage1 Garbage2 PathName FileName FullName

Data=Data(1:7529,1:7929);

%Imported Data set is still too huge.  Need to try and trim it down.
My
%idea is to first trim the data by removing rows and columns from the
data
%set, like only taking every other one, or one of every three, etc.
Then smooth
%the data out using a lagrangian averaging mask.

%First: Choose seven to make it ~1000x1000
%Next... Still too huge to handle in any kind of a timely
manner...try
%cutting it to something around 200x200 if that is possible and see
what
%the data looks like...
fraction=35;
DataNew=zeros(floor(size(Data,1)/fraction),floor(size(Data,2)/fractio
n));
%-----------------------------------------------------------------
----%
% for i=0:floor(length(Data(:,1))/fraction)-1
%     DataNew1(i+1,:)=Data(fraction*i+1,:);
```

```
% end
% DataNew2=zeros(floor(length(Data(:,1))/fraction),...
%     floor(length(Data(1,:))/fraction));
% for j=0:floor(length(Data(1,:))/fraction)-1
%     DataNew2(:,j+1)=DataNew1(:,j*fraction+1);
% end
%-------------------------------------------------------------------
----%
%The above works fine, but to get more accurate results, I will
average the
%35 skipped rows and cols into single data points using a nested for
loop.

for i=1:floor(size(DataNew,1))
    for j=1:floor(size(DataNew,2))
        DataNew(i,j)=mean(mean(Data((35*(i-1)+1):35*i,(35*(j-
1)+1):35*j)));
    end
end

clear Data
Data=DataNew;
clear i j DataNew

%-------------------------------------------------------------------
----%
%This subset looks good, but we see a lot of outliers that we want to
%remove.  Use a modified version of an old code used in ME 552.  This
code
%runs through pixels and compares the error between the center pixel
of a
%3x3 mask and the average of the surrounding nodes.  If the center
node is
%too different, it replaces it with the average of the other nodes.

rows=length(Data(:,1));
cols=length(Data(1,:));
DataNew=zeros(rows,cols);
for i=1:rows
    for j=1:cols
        clear DataComparator
        DataComparator=mean(nonzeros(MaskCode3(Data,j,i)...
        .*Data));
        if abs((Data(i,j)-DataComparator)/DataComparator)>=1.2 || ...
                abs((Data(i,j)-DataComparator)/DataComparator)<=0.8
            DataNew(i,j)=DataComparator;
        else
            DataNew(i,j)=Data(i,j);
        end
    end
end
%Good output, minor outliers have been smoothed.  The only remaining
```

```
%outliers that remain are the signal noise in the regime outside of
the
%measurement space.  How best to deal with these?  I think displacing
the
%plot first to make the minimum of the plot intersect zero will make
the
%signal to noise much stronger in these outer regions.  Then I could
%reapply the filter to see how well these signals are now damped out.

%-------------------------------------------------------------------
----%
% %Now we need to shift the 'out of range' data measurements and
unmeasured
% %space up to the piezo max height.  This should make visualization
easier
% %and hopefully make volume measurement easier.
% for i=1:rows
%     for j=1:cols
%         if DataNew(i,j)>=162.400 && DataNew(i,j)<=162.402
%             Data(i,j)=maxset;
%         else
%             Data(i,j)=DataNew(i,j);
%         end
%     end
% end
%Good, but now we have some of the outliers returning.  Smooth them
out for
%visual again.


%-------------------------------------------------------------------
----%
%Now we should displace the whole plot so that the minimum is aligned
with
%zero.
[minvector,ycenter]=min(DataNew);
[minimum,xcenter]=min(minvector);
ycenter=ycenter(xcenter);
Data=DataNew+abs(minimum);
%-------------------------------------------------------------------
----%
%The signal to noise ratio is now much better for the data we want to
%smooth.  Now to fix the data, I will need to refilter the data, this
time
%using the mode of the data set as the filter.  The following
repopulates
%the matrix with the old matrix unless the data point is within a +-
20%
%tolerance of the mode of the Data. If it is in this range, it finds
the
%mode of the masked region and if it is equal to the mode of the
data, it
```

```
%replaces the center node with the mode of the data.  This should
eliminate
%important data from being accidentally changed but still replace all
the
%noise in the outer region with a constant value.
modeset=mode(mode(Data));
for i=1:rows
    for j=1:cols
        if Data(i,j)<=1.3*modeset && Data(i,j)>=0.7*modeset
            if mode(nonzeros(MaskCode2(Data,j,i).*Data))==modeset;
                DataNew(i,j)=modeset;
            else
                DataNew(i,j)=Data(i,j);
            end
        else
            DataNew(i,j)=Data(i,j);
        end
    end
end
Data=DataNew;

%One last filter should remove the erroneous data points.
for i=1:rows
    for j=1:cols
        if mode(nonzeros(MaskCode2(Data,j,i).*Data))==modeset;
            if mean(nonzeros(MaskCode3(Data,j,i).*Data))==modeset;
                DataNew(i,j)=modeset;
            else
                DataNew(i,j)=Data(i,j);
            end
        else
            DataNew(i,j)=Data(i,j);
        end
    end
end
%Yup, it worked.
%-------------------------------------------------------------------
----%
%Now we have a really good smooth set of data showing the piezo and
the
%area at which point it has a step change in height (indicating the
edge of
%the plenum region. Replace all the erroneous Data Points with the
value of
%the neutral piezo position (zeroing to the amount the entire plot
was
%shifted by earlier.
% maxset=max(max(DataNew));
for i=1:rows
    for j=1:cols
        if DataNew(i,j)==modeset
            Data(i,j)=abs(minimum);
        else
```

```
            Data(i,j)=DataNew(i,j);
        end
    end
end
%-------------------------------------------------------------------
----%
%Now what we want to generate is a generic profile of the
piezoelectric
%disk. This can be best approximated by generating a
'Hieght'vs'Radius'
%plot from the given data set, and then manipulating that.  This was
also
%done in ME 552 for the IR lab, so I will pull most my basic code
%architecture from the old ME 552 IR Lab code.  The idea is to
average all
%the 'Height' values found along a circle of radius 'r'.  A linear 'h
vs r'
%plot is generated by repeating this for increasing values of 'r'
until the
%edge of the piezo domain is reached.

Radius=zeros(rows*cols,1);
Height=zeros(rows*cols,1);
Radius(1)=0;
Height(1)=0;
%Now in the old code I had an actual length to pixel ratio.  In this
case,
%I only really have a total radius length.  To get around this, I can
just
%generate a relative 'pixel distance' away from the center pixel for
all
%other pixels, and then multiply by a determinable factor at the end
of the
%process to get real values.

%The code below will insert the height value and corresponding radial
value
%into two parallel vectors for each data point.
clear i j
counter=1;
for i=1:cols
    for j=1:rows
        RadCalc=sqrt((i-xcenter)^2+(j-ycenter)^2);
        Radius(counter)=RadCalc;
        Height(counter)=Data(j,i);
        counter=counter+1;
    end
end
clear counter

%Now we have two vectors, side by side, where each entry in the
radius
```

```
%vector corresponds to an entry in the height vector at the same
position.
%In order to work any more with this data, we need to sort this data
by the
%radius vector in increasing magnitude and have the height vector
sort in
%parallel.
[r_sort,I]=sort(Radius,1,'ascend');
h_sort=Height(I);
Radius=r_sort;
Height=h_sort;
clear h_sort r_sort
%-------------------------------------------------------------------
----%

%The current plot would shows a slight divergence in the height from
a
%single line as you get further from the center.  This was expected
due to
%the inherent error in trying to level the piezo properly.  To get a
nice
%smooth single line, I need to radially average the height.
RadiusNew=zeros(ceil(max(Radius))+1,1);
HeightNew=zeros(ceil(max(Radius))+1,1);
Error=zeros(ceil(max(Radius))+1,1);
AveragingCell=zeros(length(Radius),1);
AveragingCell2=zeros(length(Radius),1);
Error(1)=0;
RadiusNew(1)=0;
HeightNew(1)=0;
for i=1:ceil(max(Radius))
    for j=1:length(Radius)
        if Radius(j)>=(i-0.5) && Radius(j)<=(i+0.5)
            if Height(j)==abs(minimum)
                AveragingCell(j)=0;
                AveragingCell2(j)=abs(minimum);
            else
                AveragingCell(j)=Height(j);
                AveragingCell2(j)=Height(j);
            end
        end
    end
    if (nnz(AveragingCell2)-
nnz(AveragingCell))>=0.80*nnz(AveragingCell2)
        HeightNew(i+1)=mean(nonzeros(AveragingCell2));
        Error(i+1)=(std(nonzeros(AveragingCell2))...
            *tinv(.975,length(AveragingCell2)-1))...
            /sqrt(length(AveragingCell2));
    else
        HeightNew(i+1)=mean(nonzeros(AveragingCell));
        Error(i+1)=(std(nonzeros(AveragingCell))...
            *tinv(.975,length(AveragingCell)-1))...
            /sqrt(length(AveragingCell));
```

```
    end
    RadiusNew(i+1)=i;
    AveragingCell=zeros(length(Radius),1);
    AveragingCell2=zeros(length(Radius),1);
end

%-------------------------------------------------------------------
----%

% %The above manages to create a descent graph, but has some problems
in that
% %the error diverges greatly from an average near the end of the
data set.
% %This is most likely due to the bias created in this region when
data was
% %not taken to fill out the circle.  I need to removed these data
points
% %that overly bias the average.
% %I will try to do this by finding all regions where the error is
greater
% %than 10% and remove the raw data that is at the 'default value'
for
% %unmeasured areas.  This should hopefully remove all the data
points that
% %overly skew the data to far inward of the actual step change in
height.
% %Need to scan the Error and HeightNew vectors for a %Error>10 and
store the
% %corresponding RadiusNew.
% Error_th=0.1;
% % Perc_Error=Error./HeightNew;
% % Bad_Radii=zeros(length(HeightNew),1);
% % for i=1:length(HeightNew)
% %     if Perc_Error(i)>=Error_th
% %         Bad_Radii(i)=Radius(i);
% %     end
% % end
% % Bad_Radii=nonzeros(Bad_Radii);
%
% %Now I need to redo the data averaging while ignoring any values of
Height
% %that are equal to the 'default value' that are also at radii that
had more
% %than 10% error.
% RadiusNew2=zeros(length(RadiusNew),1);
% HeightNew2=zeros(length(RadiusNew),1);
% Error2=zeros(length(RadiusNew),1);
% AveragingCell=zeros(length(Radius),1);
% Error2(1)=0;
% RadiusNew2(1)=0;
% HeightNew2(1)=0;
% for i=1:ceil(max(Radius))
%     for j=1:length(Radius)
```

```
%         if Radius(j)>=(i-0.5) && Radius(j)<=(i+0.5)
%             if Height(j)>=1.0460e5 && Height(j)<=1.0461e5 &&...
%                     (Height(j)-
HeightNew(i+1))/HeightNew(i+1)>Error_th
%                 AveragingCell(j)=0;
%             else
%                 AveragingCell(j)=Height(j);
%             end
%         end
%     end
%     HeightNew2(i+1)=mean(nonzeros(AveragingCell));
%     Error2(i+1)=std(nonzeros(AveragingCell));
%     RadiusNew2(i+1)=i;
%     AveragingCell=zeros(length(Radius),1);
% end

clf
figure(1), hold on
% plot(Radius,Height,'r.','MarkerSize',1),
plot(RadiusNew,HeightNew,'b-','LineWidth',2)
plot(RadiusNew,HeightNew+Error,'g--','LineWidth',1)
plot(RadiusNew,HeightNew-Error,'g--','LineWidth',1)

%-----------------------------------------------------------------------
----%
%Interesting results, but to continue according to plan, I want to
find the
%maximum in the averaged plot and call this the 'radial extent' of
what the
%profilometer was able to measure, i.e. our 0.625" diameter sight
region.
%This will allow us to finally scale the x-axis, at which point we
can then
%also scale the y axis into mm and output our final set of height vs
%distance from center data.

[h_max,r_max_loc]=max(HeightNew);
RadiusNew2=RadiusNew(1:r_max_loc);
HeightNew2=HeightNew(1:r_max_loc);
%Now scale HeightNew2 and RadiusNew2 to mm.
HeightNew2=HeightNew2/1e3; %Assuming the measurements were made in um
R_scaler=(0.625/(2*max(RadiusNew2)))*25.4;
RadiusNew2=RadiusNew2*R_scaler;

figure(2)
plot(RadiusNew2,HeightNew2,'-b','LineWidth',2)
xlabel('r (mm)')
ylabel('h (mm)')
%Now output the data for manually teasing out a proper curve fit
within
%excel.
dlmwrite('R vs
Disp.txt',[RadiusNew2,HeightNew2],'delimiter','\t','precision',5)
```

```
%-------------------------------------------------------------------
----%
%Now I think I want to develop the analysis of the data in a separate
file
%that reads the output of this one
```

Second MATLAB Code: This MATLAB code imports the exported file from the last MATLAB code and finds a line of best fit for the piezoelectric volume displacement as a function of input voltage.

```
%Kevin Lewis
%Import the simplified piezo height vs radius plot (output of the
%Piezo_Profile_Reader.m) and determine a volume displacement vs
voltage
%plot for the piezoelectric disk.

clc
clear
close all


%Define the file and path.
[FileName, PathName] = uigetfile({'*'},'Retrieve the ascii file');
FullName=[PathName,FileName];

Input = dlmread(FullName);
%Name of file you should be picking up is R vs Disp

%Split the 'Input' into its component vectors for the Radius (column
1) and
%the Height (column 2).
Radius=Input(:,1)*1e-3; %1e-3 converts this from mm to m
Height=Input(:,2)*1e-6; %1e-3 converts this from um to m

%File import works.
%-------------------------------------------------------------------
----%
%Hand input below the data for volt vs height of the piezo as
measured by
%the profilometer.

VoltagesDown=[0,1,3.17,5.05,6.85,9.01,9.88,12.47,15.34,17.69,20.3,23.
5,...

27.4,32.1,36.1,40.1,49.7,60.5,70.1,80.0,90.5,100.0,119.7,140.1,150.1]
;
VoltagesUp=[0,1,3.01,5.035,7.01,9.01,10.01,12.51,15.04,17.49,20.0,24,
28,...
    32.2,36.5,39.8,50.3,60.3,69.7,80.6,90.6,101.4,121.3,139.6,150.1];
PositionUp=[0,0.4,0.7,1,1.2,1.5,1.6,1.9,2.1,2.4,2.5,2.7,3.0,2.2,3.0,3
.2...
    ,4.3,5.4,7.0,8.3,9.3,10.7,13.4,15.9,17.3]*1e-6;
PositionDown=[3.5,3.8,4.1,4.3,4.45,4.6,4.8,5.1,5.3,5.6,5.8,6.1,6.4,6.
8,...
    7.2,7.6,8.3,9.0,9.7,10.3,11.2,12.1,13.9,17.0,17.3]*1e-6;
```

```
%
% plot(VoltagesUp,PositionUp,'b*'), hold on
% plot(VoltagesDown,PositionDown,'r*')

%Use only the VoltagesDown and the PositionDown vectors for the data
%adjustments.  This data set is obviously smoother and also had later
test
%points line up more accurately with this line than the other.
%-------------------------------------------------------------------
----%

%Need to adjust the Height vector such that each value is linearly
changed
%to match the change in maximum displacement height from the full map
test
%case to the final resting point of the tested piezo.
Height_ratio=(max(Height)-min(PositionDown))/max(Height);
%The above relationship should be a percentage decrease in the
maximum
%piezo height (at the radius zero) when 0 Volts are applied to the
piezo.
%This percentage can be multiplied by all the data points in the
Height
%vector to linearly reduce them all by this same percentage.  The
result
%will be our new Height vector that still corresponds with its
parallel
%radial vector at the neutral height of 0 applied volts.
Height=Height*Height_ratio;
Position=PositionDown'-min(PositionDown); %Start from 0 displacement
now
Voltage=VoltagesDown'; %Only use the Voltage Down and Position Down
vectors

%All the individual parameters have been set at neutral values and we
are
%ready to start performing integrations to determine volume
displacements
%of the piezo as a function of voltage.
%-------------------------------------------------------------------
----%

%For each displaced height, there will be a volume associated with
the
%space above the piezo.  This space will change as a function of the
%voltage applied to the piezo.  The goal for each displacement (or
%corresponding voltage) value is to determine how much more volume is
%displaced in the latter case when compared to the amount of volume
%available to displace in the neutral state (0 volts).  Before this
can be
%determined, we need to determine the volume above the piezo for each
%voltage case.  As outlined in the lab notebook, this will be done by
%performing a numerical integration of the radial profile.
```

```
%NOTE: The integration will be performed using the quad function in
matlab.
%This requires a function definition outside of this *.m file.  This
%requires that we generate a polynomial fit for every instance of the
data
%as manipulated by the change in height.  This means we must generate
the
%polynomial fit within matlab numerous time, using the matlab
function
%polyfit. All the curve fits will be 5th order polynomials (it was
%determined in Excel that these fit the data best).

%Degree of fit
degree=5;
%Reference outside self-made function that determines the polynomial
fit
%such that it always passes through (0,0).
A = poly_det(Radius,Height,degree);

Vol_quad=zeros(length(Voltage),1);

%Need to modify quad to reflect notes in lab book....
Vol_quad(1)=2*pi*quad(@(x)
Vol_quad_func(x,A,max(Height)),0,max(Radius));

%Seems to work for the first scenario (the neutral case).  Below is a
%for-loop that will do the same thing for each different displacement
of
%the piezo.  The end result will be a vector of the volume above the
piezo
%as a function of voltage.
HeightNew=Height;
for i=1:length(Position)
    Height_ratio = (max(Height)-Position(i))/max(Height);
    HeightNew = Height_ratio*Height;
    A = poly_det(Radius,HeightNew,degree);
    Vol_quad(i) = 2*pi*quad(@(x)
Vol_quad_func(x,A,max(HeightNew)),...
        0,max(Radius));
    clear HeightNew A Height_ratio
end

Vol_piezo=Vol_quad;
%-------------------------------------------------------------------
----%

%Now that the volumes are defined I can define the volume change from
the
%neutral to each voltage-applied displacement.
Displacement=Vol_piezo(1)-Vol_piezo;
```

```
%The 'Voltage' vector runs parallel to this 'Displacement', so we can
now
%generate a plot for displacement vs applied voltage.
figure(1)
plot(Voltage,Displacement,'k*'), hold on

%The plot looks right, it follows the same position vs voltage
behavior and
%should only be different in magnitude.  A curve fit can now be
generated
%for this data in excel or in matlab (using the self made poly_fit
%function).
%-----------------------------------------------------------------------
----%
Fit_degree=1;
Vol_func_of_Volt = poly_det(Voltage,Displacement,Fit_degree);
%Compare the polynomial function to the data below:
Prediction = polyval(Vol_func_of_Volt,linspace(0,max(Voltage)));
plot(linspace(0,max(Voltage)),Prediction,'k-')
ylabel('Displacement, m^3')
xlabel('Voltage, V')
hold off
%Convert this displacement vs Voltage plot into a 'Pressure' vs
'Voltage'
%plot using: P=dV*rho*c_o^2/V, where V=Vol_all(1)+Vol_plenum.
Vol_plenum=92.29e-9;
rho=997.64;
c_o=1488.37;
Pressure=Displacement*rho*c_o^2/(Vol_piezo(1)+Vol_plenum);
figure(2)
plot(Voltage,Pressure,'k*'), hold on
%Need to refit the data:
P_func_of_Volt = poly_det(Voltage,Pressure,Fit_degree);
Prediction2 = polyval(P_func_of_Volt,linspace(0,max(Voltage)));
plot(linspace(0,max(Voltage)),Prediction2,'k-')
ylabel('Pressure, Pa')
xlabel('Voltage, V')
clc
fprintf('The coefficients of the polynomial curve fit (Vol in mm^3 vs
V) are:\n\n')
fprintf('%10.10e\n',Vol_func_of_Volt)
fprintf('\nWhere the highest order of the polynomial is:
%2.0f.\n',Fit_degree)
fprintf('The coefficients of the polynomial curve fit (P in Pa vs V)
are:\n\n')
fprintf('%10.10e\n',P_func_of_Volt)
```

APPENDIX E

Mathematical derivation for the definition of meniscus compliance

The mathematical derivation of the meniscus compliance starts with the definition of the acoustic impedance of a meniscus as a function of the meniscus back pressure and the meniscus height, taken from Merhaut (1981):

$$\frac{1}{Z_{a,m}} = \frac{j\omega 2\pi}{P}\int_0^R \eta \, rdr \qquad \text{E-1}$$

Also from Merhaut (1981) is the definition of the meniscus displacement:

$$\eta = \frac{P}{k^2\sigma}\cdot\left(\frac{J_0(kr)}{J_0(kR)} - 1\right) \qquad \text{E-2}$$

where k is defined as:

$$k = \omega\sqrt{\frac{\rho}{\sigma}} \qquad \text{E-3}$$

For the purposes of this derivation, let $\beta = kR$. The derivation performed below is done in parallel with the derivation seen in Merhaut (1981). The key difference is that this derivation assumes a constant non-complex force per unit length for the surface tension whereas Merhaut derives a more universal equation.

$$\frac{1}{Z_{a,m}} = \frac{j\omega 2\pi}{P}\int_0^R \frac{PR^2}{\beta^2\sigma}\cdot\left(\frac{J_0\left(\beta\frac{r}{R}\right)}{J_0(\beta)} - 1\right) rdr \qquad \text{E-4}$$

$$\frac{1}{Z_{a,m}} = \frac{j\omega 2\pi R^2}{\beta^2\sigma}\int_0^R \left(\frac{J_0\left(\beta\frac{r}{R}\right)}{J_0(\beta)} - 1\right) rdr \qquad \text{E-5}$$

$$\frac{1}{Z_{a,m}} = \frac{j\omega 2\pi R^2}{\beta^2\sigma}\cdot\left[\frac{R^2 J_1(\beta)}{\beta J_0(\beta)} - \frac{R^2}{2}\right] \qquad \text{E-6}$$

$$\frac{1}{Z_{a,m}} = \frac{j\omega 2\pi R^4}{\beta^3\sigma}\cdot\left[\frac{J_1(\beta)}{J_0(\beta)} - \frac{\beta}{2}\right] \qquad \text{E-7}$$

which finally simplifies to:

$$Z_{a,m} = \frac{\beta^3\sigma}{2\pi\omega j R^4}\cdot\left[\frac{J_1(\beta)}{J_0(\beta)} - \frac{\beta}{2}\right]^{-1} \qquad \text{E-8}$$

Equation E-8 can be simplified further if one expands the Bessel functions in the definition by their infinite series representations. To do this, one must first simplify the latter half of equation E-8:

$$\left[\frac{J_1(\beta)}{J_0(\beta)} - \frac{\beta}{2}\right]^{-1} = \left[\frac{2J_1(\beta) - \beta J_0(\beta)}{2J_0(\beta)}\right]^{-1} \quad \text{E-9}$$

$$\therefore Z_{a,m} = \frac{\sigma}{\pi\omega j R^4} \cdot \frac{\beta^3 J_0(\beta)}{2J_1(\beta) - \beta J_0(\beta)} \quad \text{E-10}$$

$$2J_1(\beta) - \beta J_0(\beta) = \frac{2\beta^3}{2^2 \cdot 4} - \frac{4\beta^5}{2^2 \cdot 4^2 \cdot 6} + \frac{6\beta^7}{2^2 \cdot 4^2 \cdot 6^2 \cdot 8} - \frac{8\beta^9}{2^2 \cdot 4^2 \cdot 6^2 \cdot 8^2 \cdot 10} \mp \cdots \quad \text{E-11}$$

$$\therefore \frac{\beta^3 J_0(\beta)}{2J_1(\beta) - \beta J_0(\beta)} = \frac{J_0(\beta)}{\frac{2}{2^2 \cdot 4} - \frac{4\beta^2}{2^2 \cdot 4^2 \cdot 6} + \frac{6\beta^4}{2^2 \cdot 4^2 \cdot 6^2 \cdot 8} \mp \cdots} \quad \text{E-12}$$

When inspecting the denominator of equation E-12, note that the constant 1/8 can be pulled out of each term in the infinite series to yield:

$$\frac{2}{2^2 \cdot 4} - \frac{4\beta^2}{2^2 \cdot 4^2 \cdot 6} + \frac{6\beta^4}{2^2 \cdot 4^2 \cdot 6^2 \cdot 8} \mp \cdots = \frac{1}{8} \cdot \left(1 - \frac{2\beta^2}{4 \cdot 6} + \frac{3\beta^4}{4 \cdot 6^2 \cdot 8} \mp \cdots\right) \quad \text{E-13}$$

Combining equations E-10 through E-13 results in the following equation for acoustic impedance of the meniscus:

$$Z_{a,m} = \frac{8\sigma}{\pi\omega j R^4} \cdot \frac{J_0(\beta)}{\left(1 - \frac{2\beta^2}{4 \cdot 6} + \frac{3\beta^4}{4 \cdot 6^2 \cdot 8} \mp \cdots\right)} \quad \text{E-14}$$

Note that the limit of the second term in equation E-14 as β tends toward zero is equal to one. Since β is defined as kR and $k \propto \omega$, that must mean that $\beta \propto \omega$. Therefore, at low frequencies where $\omega \to 0$, the acoustic impedance of the meniscus is defined as:

$$Z_{a,m} = \frac{8\sigma}{\pi\omega j R^4} \quad \text{E-15}$$

Based on the definition of acoustic impedance defined in equation E-16 the acoustic compliance can be determined for the meniscus. The final definition for the compliance is therefore given in equation E-17.

$$Z_{a,m} = \frac{1}{j\omega C_m} = \frac{8\sigma}{\pi\omega j R^4} \quad \text{E-16}$$

$$\therefore C_m = \frac{\pi R^4}{8\sigma} = \frac{\pi D_{nozzle}}{2^4 \cdot 8\sigma} = \frac{\pi D_{nozzle}}{128\sigma} \quad \text{E-17}$$

This is the same acoustic compliance for the meniscus defined in equation 3.16 in chapter 3.

APPENDIX F

Image Analysis Introduction and Code

This appendix is dedicated to the documentation of the image analysis code used for calculating drop volumes and drop velocities. From an overall perspective, the code does the following:

1. The user is prompted to select an image file(s) for import into MATLAB
2. The user is prompted to select a save location for the final output of the code.
3. The code imports the selected image file(s) and applies a number of filters, scales the image, and adjusts the image to improve edge detection capability.
4. The code performs a series of edge detections to try and fully define the drop edge.
5. The multiple edge detection techniques are combined to yield a net edge of the drop.
6. The binary image of the edge of the drop is diluted a number of times to fill any missing gaps in the edge.
7. The interior of the drop is filled in order to represent the cross sectional area of the drop.
8. The drop image is then eroded by the same number of dilutions used on the original edges to close the gaps in the edge. Note that this should now return the drop project area to its actual size.
9. The centroid of the project area is determined with a Matlab function.
10. The volume (in terms of pix^3) is calculated in the program as outlined in section 4.5.

11. The centroid locations and drop volumes are stored in a matrix until the same analysis can be done for all the selected files.
12. Finally, the code exports an excel file for the user to work with that contains file names, drop volumes, and drop positions for every file selected at the beginning of the program.

Due to the development status and experimental nature of the MATLAB code, there are additional features that this MATLAB code attempted to handle but failed to do so. These lines of text may still be part of the code, or they may be commented to removed them from the processing stream, however they will not negatively affect the performance of the MATLAB code beyond increasing the time it takes to run the code. For example, it was embedded in the program the capability to detect satellite drops and to perform the same analysis on satellite drops as was performed on main drops. However, due to the poor quality of some of the images, the satellite code portion often would go unused. Also, due to the lack of satellite drop images, the code pertaining to the satellite drop calculations may need additional troubleshooting before it can properly determine satellite drop volumes and centroids.

```
%Kevin Lewis, 6-26-2011

%This file should do the following:
%       a) Opens TIFFS
%       b) Edge Detects TIFFS
%       c) Turns TIFFS image into Binary image of droplet
%       d) Outputs binary image for future data analysis

clc
clear
clf

%% Get JPEGS

%In opening JPEGS, I would like this code to be really fast and
capable of
%opening many files at once.  To be more precise, I would like to
select as
%many pictures as I want to load and have the program store their
names and
%locations in a matrix or array and then read them, analyze them, and
%output them as binary images one at a time.  I think this process of
doing
%one at a time, but having it be automated by the code once the user
select
%all the files, will avoid any memory issues and increase computation
%speed.

[filename, pathname, filterindex] = uigetfile(...
    {'*.tif', 'TIFF files (*.tif)'; ...
    '*.*', 'All Files'}, ...
    'Pick a file', ...
    'MultiSelect', 'on');
%Create a subfolder to save the new output in.  Call it 'Binary'
mkdir(pathname,'Binary')
savepath=[pathname,'/Binary'];

%The files are now loaded into an array for reference.

%% REPEATED LOOP
%The following sections are part of a repeated loop that will repeat
until
%all select files have been opened, modified and saved.
FileIndex=1;
check=isa(filename,'cell');
if check~=1
    files=1;
    info=imfinfo([pathname,filename]);
else
    files=length(filename);
    info=imfinfo([pathname,filename{FileIndex}]);
end
```

```
MinSampleValue=info(1).MinSampleValue;
MaxSampleValue=info(1).MaxSampleValue;
IMAGE=cell(1,2);      %Two images per file

%% Setup Variable for Excel Data Analysis Output
Centroid_exit=cell(1,files);
Volume_main_exit=cell(1,files);
Volume_second_exit=cell(1,files);
Volume_third_exit=cell(1,files);
Error_flag_exit=cell(1,files);
Satellite_pres_exit=cell(1,files);
Satellite_num_exit=cell(1,files);
Sat1_Centroid_out_exit=cell(1,files);
Sat2_Centroid_out_exit=cell(1,files);

%% While Loop (open and perform on all selected files)
while FileIndex<=files
    Centroid_out=zeros(2,2);
    Volume_main=zeros(2,1);
    Volume_second=zeros(2,1);
    Volume_third=zeros(2,1);
    Error_flag=zeros(2,1);
    Satellite_pres=zeros(2,5);
    Satellite_num=zeros(1,2);
    Sat1_Centroid_out=zeros(2,2);
    Sat2_Centroid_out=zeros(2,2);
    for i=1:2
        %% Load currently indexed file (2 images per file)
        if check==1
            IMAGE{i}=imread([pathname,filename{FileIndex}],'tif',...
                'Index',i);
        else
            IMAGE{i}=imread([pathname,filename],'tif',...
                'Index',i);
        end

        %% First the photo has to be filtered.
        %Filter Types to Consider:
        %Median Filtering (see medfilt2)
        %Linear Average Filtering (see filter2 as example)
        %Adaptive Linear Filtering (see wiener2)

        %Multiple filters are applied, and some a number of times, in
order
        %to generate the best possible representation of the photo
after
        %conversion to BW.

        %% Median Filter: removes 'Salt & Pepper' Noise
        IMAGE{i}=medfilt2(IMAGE{i});
        %% Linear Average Filtering: 1st Gaussian
        h=fspecial('gaussian',5);
        IMAGE{i}=imfilter(IMAGE{i},h);
```

```
        %% Linear Average Filtering: 1st Average
        h=fspecial('average',5);
        IMAGE{i}=imfilter(IMAGE{i},h);
        %% 1st Adaptive Linear Filtering: Increases edge sharpness
        IMAGE{i}=wiener2(IMAGE{i},[5,5]);
        %% Linear Scale - Adjust Image (need to adjust carefully)
        %Use the median pixel value as a low cut-off since all photos
have
        %mostly background noise. Use the maximum value as the
        %maximum.
        %Note that the code reads in uint16 from a Tiff file, so
        %at this point the data range is from 0 to 65535.  This needs
to be
        %scaled first to grayscale before it can be scaled to the
range as
        %set below.  The process for this was extracted from within
the
        %imadjust.m code.
        lowhigh_in=stretchlim(IMAGE{i},[0 1]);
        low_in=lowhigh_in(1);
        high_in=lowhigh_in(2);
        low_out=0;
        high_out=1;
        lut=linspace(0,1,2^16); %uint16 data
        lut=( ((lut-low_in) ./ (high_in-low_in)).*...
            (high_out-low_out) ) + low_out;
        lut=im2uint16(lut);
        IMAGE{i}=intlut(IMAGE{i},lut);
        %Current figure is not scaled to the full range for uint16.
The
        %rest of the code operates on the image being in Grayscale,
from 0
        %to 1.
        IMAGE{i}=mat2gray(IMAGE{i});

        %Now we can rescale the photo with the median as a zero
cutoff
        lowin=median(median(IMAGE{i}));
        highin=max(max(IMAGE{i}));
        %Map all values equal to or lesser than the cut-off value to
zero (i.e.
        %black). The new maximum output from imadjust can be anywhere
between 0
        %and 1.  Use gamma adjustment to accentuate the droplet and
        %suppress the background.
        lowout=0;
        highout=1;
        IMAGE{i}=imadjust(IMAGE{i},[lowin highin],[lowout
highout],0.75);
        IMAGE_save=IMAGE{i};

        %% Continue to filter/adjust image for better edge detection
```

```
        %See 'Detecting a Cell Using Image Segmentation' in the help
menu. Very
        %informative.

        %adapthisteq() prior to edge detect along with additional
filters might
        %help define satellite droplets better.
%         IMAGE{i}=adapthisteq(IMAGE{i},'NumTiles',[38
30],'Distribution',...
%             'exponential');

        %% New Idea (#101)
        %Remove drops to find background and use this to remove
background
        background=imopen(IMAGE{i},strel('disk',135));
        IMAGE{i}=IMAGE{i}-background;

        %% Smooth Background Noise near Signal
        for k=1:2
            %% Median Filter: removes 'Salt & Pepper' Noise
            IMAGE{i}=medfilt2(IMAGE{i});
            %% Linear Average Filtering: 2nd Gaussian
            %Smooth out regions after the adaptive histographic
contrast adjustment
            h=fspecial('gaussian',5);
            IMAGE{i}=imfilter(IMAGE{i},h);
            %% Linear Average Filtering: 1st Average
            h=fspecial('average',5);
            IMAGE{i}=imfilter(IMAGE{i},h);
            %% 1st Adaptive Linear Filtering: Increases edge
sharpness
            IMAGE{i}=wiener2(IMAGE{i},[5,5]);
            %% Sharpen Image for Better Edge Detect
            h=fspecial('unsharp');
            IMAGE{i}=mat2gray(filter2(h,IMAGE{i}));
        end

        %% Enhance Vertical and Horizontal Edges

        %% Use a Sobel Filter to Create Horizontal & Vertical Edge
Matrices
        h=fspecial('sobel');
        horiz_add=filter2(h,IMAGE{i});
        vert_add=filter2(h',IMAGE{i});
        Roberts_45 = [1 0;0 -1]; %Accentuate edges at 45 deg incline
        angle_add_45 = imfilter(IMAGE{i},Roberts_45,'replicate');
        angle_add_45 = angle_add_45 + abs(min(min(angle_add_45)));
        Roberts_135 = [0 1;-1 0]; %Accentuate edges at 135 deg
incline
        angle_add_135 = imfilter(IMAGE{i},Roberts_135,'replicate');
        angle_add_135 = angle_add_135 + abs(min(min(angle_add_135)));
```

```
        %% Scale the Horizontal Edge Matrix
        horiz_add=mat2gray(horiz_add);
        lowin=median(median(horiz_add));
        highin=max(max(horiz_add));
        horiz_add=imadjust(horiz_add,[lowin highin],[lowout
highout]);

        %% Scale the Vertical Edge Matrix
        vert_add=mat2gray(vert_add);
        lowin=median(median(vert_add));
        highin=max(max(vert_add));
        vert_add=imadjust(vert_add,[lowin highin],[lowout highout]);

        %% Scale the Angles Edge Matrices
        angle_add_45=mat2gray(angle_add_45);
        lowin=median(median(angle_add_45));
        highin=max(max(angle_add_45));
        angle_add_45=imadjust(angle_add_45,[lowin highin],[lowout
highout]);

        angle_add_135=mat2gray(angle_add_135);
        lowin=median(median(angle_add_135));
        highin=max(max(angle_add_135));
        angle_add_135=imadjust(angle_add_135,[lowin highin],[lowout
highout]);

        %% Combine Edge Accents with Original Image
%
IMAGE{i}=IMAGE{i}+2*vert_add+horiz_add+angle_add_45+angle_add_135;

        %% Rescale Edge Enhanced Image
        %Scale back all pixels such that maximum is 1.  Note, minimum
should be
        %zero so one can simply divide the data set by the intensity
of the
        %most intense pixel.
        IMAGE{i}=mat2gray(IMAGE{i});
        new_min=mode(mode(IMAGE{i}));
        new_max=max(max(IMAGE{i}));
        IMAGE{i}=imadjust(IMAGE{i},[new_min new_max],[]);

        %% (Another) NEW IDEA
        %Continue to filter the image in a while loop where you check
the
        %average intensity of the droplet to see if it is above a
        %threshold.  If it is, the while loop stops.  If it isn't,
the
        %image is increase in intensity by removing one more layer of
        %'background' by forcing it to zero.
        imageintensity=mean(nonzeros(IMAGE{i}));
        intensity_goal=0.5;
        breakchecker=0;
```

```
        slope = 0;
        while imageintensity < intensity_goal
            binedges=linspace(0,1,150);
            intensity_hist=histc(nonzeros(IMAGE{i}),binedges);
            [pixelsinbin position]=max(intensity_hist(2:length(...
                intensity_hist)));
            new_min=binedges(position+1);
            new_max=max(max(IMAGE{i}));
            NEW_IMAGE=imadjust(IMAGE{i},[new_min new_max],[0
1],0.99);
            newintensity=mean(nonzeros(NEW_IMAGE));
            slope=newintensity-imageintensity;
            if slope >= 0
                IMAGE{i}=NEW_IMAGE;
                imageintensity=newintensity;
            elseif slope < 0
                imageintensity=1;
            end
            if breakchecker>1e3
                break
            else
                breakchecker=breakchecker+1;
            end
        end

        %% Insert an Image Blurring Operation.
        %Blurred image should have steep gradients still where there
are
        %edges but should now have reduced noise from the background.
        blurfunc=fspecial('gaussian',8,12);
        for cntr=1:3
            IMAGE{i}=imfilter(IMAGE{i},blurfunc);
        end

        %% Re-sharpen vertical and angled edges from blurred image
        H = fspecial('sobel');
        vert_add = imfilter(IMAGE{i},H','replicate');
        vert_add = vert_add + abs(min(min(vert_add)));
        Roberts_45 = [1 0;0 -1]; %Accentuate edges at 45 deg incline
        angle_add = imfilter(IMAGE{i},Roberts_45,'replicate');
        angle_add = angle_add + abs(min(min(angle_add)));
        IMAGE{i} = IMAGE{i} + vert_add + angle_add;
        IMAGE{i} = mat2gray(IMAGE{i});
        IMAGE{i} = imadjust(IMAGE{i},[mode(mode((IMAGE{i}))),1],[]);

        %% More Blurring?  Focus on Intersection regions with
background...

        %% Edge Detection
        %Detect Droplet/Meniscus and Remove Small Noise
        [trash thresh1]=edge(IMAGE{i},'canny');
        [trash2
thresh2]=edge(IMAGE{i},'sobel','vertical','thinning');
```

```
        [trash3 thresh3]=edge(IMAGE{i},'roberts','thinning');
        [trash4 thresh4]=edge(IMAGE{i},'sobel','horizontal');
        IMAGE_1=edge(IMAGE{i},'canny',0.05*thresh1(2));

IMAGE_2=edge(IMAGE{i},'sobel',0.05*thresh2,'vertical','thinning');
        IMAGE_3=edge(IMAGE{i},'roberts',0.05*thresh3,'thinning');
        IMAGE_4=edge(IMAGE{i},'sobel',0.05*thresh4,'horizontal');

        %% Detected Edge Combination
        IMAGE{i}=IMAGE_1+IMAGE_2+IMAGE_3+IMAGE_4;
        IMAGE{i}=bwareaopen(IMAGE{i},15,8);
        IMAGE{i}=bwmorph(IMAGE{i},'dilate');
        IMAGE{i}=bwmorph(IMAGE{i},'bridge');
        IMAGE{i}=bwmorph(IMAGE{i},'diag');
        IMAGE{i}=imfill(IMAGE{i},'holes');
        IMAGE{i}=bwmorph(IMAGE{i},'erode');
        IMAGE{i}=bwareaopen(IMAGE{i},250,8);



        SE=strel('disk',5);
        loops=0;
        nozzle_height=120; %Estimate of the usual nozzle distance
from top
        %of the image in pixels.
        eulernumber=2;
        cntrreg=[450 580];
        realeuler=0;

        %% While Loop Erodes Image to Drop and Satellites only.
        min_erosion=3;
        while eulernumber>1 || loops<min_erosion
            if eulernumber==2 || eulernumber==3
                xycentroid=regionprops(IMAGE{i},'centroid');
                %In the centroid structure: First value is x, Second
is y
                %x and y are measured from top left.
                xposvec=zeros(1,length(xycentroid));
                yposvec=zeros(1,length(xycentroid));
                for cntr=1:length(xycentroid)
                    xposvec(cntr)=xycentroid(cntr).Centroid(1);
                    yposvec(cntr)=xycentroid(cntr).Centroid(2);
                end
                if min(ge(xposvec(:),cntrreg(1)))==1 && ...
                        min(le(xposvec(:),cntrreg(2)))==1 && ...
                        min(ge(yposvec(:),nozzle_height))==1
                    realeuler=eulernumber;
                    eulernumber=1;
                else
                    IMAGE{i}=imerode(IMAGE{i},SE);
                    loops=loops+1;
                    eulernumber=bweuler(IMAGE{i},8);
                end
            else
```

```
                IMAGE{i}=imerode(IMAGE{i},SE);
                loops=loops+1;
                eulernumber=bweuler(IMAGE{i},8);
            end
        end

        %% Include a For Loop to Refill the Eroded Image to Original
Size.
        for refill=1:loops
            IMAGE{i}=imdilate(IMAGE{i},SE);
        end

        %% Calculate Drop Volume for each Object
        %bwarea in thin bands (like 5 pixel bands) from bottom of
screen to
        %top and from centroid pixel out to edge. Divide reported
area of
        %each band by height of band to get radius of drop at said
        %location.  Then use equation: V=pi*sum(r^2*h) across all
disks for
        %an object to find the axisymmetric volume.  Repeat for the
other
        %side of the drop/object.  Compare and take the smaller of
the two
        %volumes.  Repeat for each object in an image in order to
include
        %satellite drops.
        objects=bwconncomp(IMAGE{i},8);
        object_data=regionprops(objects,'centroid');
        object_data_exact=struct('Centroid',{});
        for tic=1:objects.NumObjects

object_data_exact(tic).Centroid=object_data(tic).Centroid;

object_data(tic).Centroid=round(object_data(tic).Centroid);
        end
        bandwidth=5; %5 pixel disk heights for integral
        current_obj = zeros(size(IMAGE{i}));
        if objects.NumObjects==0
            object_vol = NaN;
        else
            object_vol = zeros(objects.NumObjects,1);
            for ph=1:(objects.NumObjects)
                current_obj(objects.PixelIdxList{ph}) = 1;
                axis_pos=object_data(ph).Centroid(1);
                int_vector=zeros(length(IMAGE{i}(:,1))/bandwidth,1);
                for intstep=(1:length(IMAGE{i}(:,1))/bandwidth)
                    band=(intstep*bandwidth-4):intstep*bandwidth;
                    crsec_area=bwarea(...

current_obj(band,axis_pos:length(IMAGE{i}(1,:))));
                    radius=crsec_area/bandwidth;
                    int_vector(intstep)=pi*radius^2*bandwidth;
```

```
                end
                object_vol(ph)=sum(int_vector);
                for intstep=(1:length(IMAGE{i}(:,1))/bandwidth)
                    band=(intstep*bandwidth-4):intstep*bandwidth;
                    crsec_area=bwarea(current_obj(band,axis_pos:-
1:1));
                    radius=crsec_area/bandwidth;
                    int_vector(intstep)=pi*radius^2*bandwidth;
                end
                checksum=sum(int_vector);
                if object_vol(ph)>checksum
                    object_vol(ph)=checksum;
                end
                current_obj = zeros(size(IMAGE{i}));
            end
        end

        %% Short if-statement to Remove 'Noise' based Satellites.
        [Main_vol Main_pos]=max(object_vol);
        Main_drop_y_pos=object_data(Main_pos).Centroid(2);
        comparator=zeros(1,length(object_data));
        for c=1:length(object_data)
            comparator(c)=object_data(c).Centroid(2);
        end
        %Main drop y position should be in front of (larger than) all
the
        %satellite drops y positions. If it is not, remove the
imaginary
        %Satellite drops from analysis.
        if min(ge(Main_drop_y_pos,comparator(:)))==1
            %Then its fine, do nothing.
        else
            clear object_vol
            object_vol=Main_vol;
            object.NumObjects=1;
        end

        %% Store Photo Characteristics for Export
        %Characteristics: Centroid, Volume, Satellite Prescence,
Satellite
        %Volume, Satellite Centroid
        if objects.NumObjects==0
        else
            %% Main Drop Volume and Centroid
            [Volume_main(i) pos1]=max(object_vol);
            % x-y pairs in each row, first col x
            Centroid_out(i,1)=object_data_exact(pos1).Centroid(1);
            Centroid_out(i,2)=object_data_exact(pos1).Centroid(2);
            %% Satellite Precence
            if objects.NumObjects>1
                Satellite_pres(i,:)='true ';
                Satellite_num(i)=objects.NumObjects-1;
            else
```

```
                Satellite_pres(i,:)='false';
                Satellite_num(i)=0;
            end
            %% Satellite Volume and Centroid Identification
            if Satellite_num(i)==1
                [Volume_second(i) pos2]=min(object_vol);

Sat1_Centroid_out(i,1)=object_data_exact(pos2).Centroid(1);

Sat1_Centroid_out(i,2)=object_data_exact(pos2).Centroid(2);
                Sat2_Centroid_out(i,1)=0;
                Sat2_Centroid_out(i,2)=0;
            elseif Satellite_num(i)==2
                [Volume_third(i) pos3]=min(object_vol);
                locater=object_vol;
                locater(pos1)=0;
                locater(pos3)=0;
                [Volume_second(i) pos2]=max(locater);

Sat1_Centroid_out(i,1)=object_data_exact(pos2).Centroid(1);

Sat1_Centroid_out(i,2)=object_data_exact(pos2).Centroid(2);

Sat2_Centroid_out(i,1)=object_data_exact(pos3).Centroid(1);

Sat2_Centroid_out(i,2)=object_data_exact(pos3).Centroid(2);
            elseif Satellite_num(i)>=3
                Error_flag(i)=1;  %indicates too many satellites to
resolve.
                Sat1_Centroid_out(i,1)=0;
                Sat1_Centroid_out(i,2)=0;
                Sat2_Centroid_out(i,1)=0;
                Sat2_Centroid_out(i,2)=0;
            else
                Sat1_Centroid_out(i,1)=0;
                Sat1_Centroid_out(i,2)=0;
                Sat2_Centroid_out(i,1)=0;
                Sat2_Centroid_out(i,2)=0;
            end
        end


%         %% Display Results for Code Debugging
%         overlay=imdilate(bwperim(IMAGE{i}),strel('disk',3));
%         subplot(1,2,1)
%         imshow(IMAGE_save+overlay,'InitialMagnification','fit')
%         title('Original Scaled Photograph')
%         subplot(1,2,2)
%         imshow(IMAGE{i},'InitialMagnification','fit')
%         title('Binary Output Image')
%
    %% Save Images in an Output File
```

```
    end

    %NOTE:  This for loop portion of the next few lines was added
after I
    %had finished all my post processing was complete.  In reviewing
the
    %code at a later date, I found that this image writing portion
was
    %outside the for loop above and also did not seem to step in i.
I
    %believe this should lead the code to not write one of the two
files
    %depending on what i was last (usually a 2).  However, the code
appears
    %to have worked fine.  Still, in the interest of robustness, the
for
    %loop portion was added here to ensure that the binary images
would be
    %written either way.
    for i=1:2
        cd(savepath)
        if i==1

imwrite(IMAGE{i},[filename{FileIndex}(1:length(filename{FileIndex})-
4)...
                ,' BW(a)'],'tif','WriteMode','overwrite')
        elseif i==2

imwrite(IMAGE{i},[filename{FileIndex}(1:length(filename{FileIndex})-
4)...
                ,' BW(b)'],'tif','WriteMode','overwrite')
        end
    end

    %% Export File's Data Set to the Outside of the While Loop.
    if isnan(object_vol)
        Centroid_exit{FileIndex}=NaN;
        Volume_main_exit{FileIndex}=NaN;
        Volume_second_exit{FileIndex}=NaN;
        Volume_third_exit{FileIndex}=NaN;
        Error_flag_exit{FileIndex}=NaN;
        Satellite_pres_exit{FileIndex}=NaN;
        Satellite_num_exit{FileIndex}=NaN;
        Sat1_Centroid_out_exit{FileIndex}=NaN;
        Sat2_Centroid_out_exit{FileIndex}=NaN;
    else
        Centroid_exit{FileIndex}=Centroid_out;
        Volume_main_exit{FileIndex}=Volume_main;
        Volume_second_exit{FileIndex}=Volume_second;
        Volume_third_exit{FileIndex}=Volume_third;
        Error_flag_exit{FileIndex}=Error_flag;
        Satellite_pres_exit{FileIndex}=Satellite_pres;
```

```
        Satellite_num_exit{FileIndex}=Satellite_num;
        Sat1_Centroid_out_exit{FileIndex}=Sat1_Centroid_out;
        Sat2_Centroid_out_exit{FileIndex}=Sat2_Centroid_out;
    end

    %% Index to the next file selected for analysis
    FileIndex=FileIndex+1;

end

%% Export the Drop Data into Excel
%Export the final collection of all data points with the folder into
an
%excel spreadsheet. Use xlswrite.  Before writing, however, we must
format
%the output to make sense and label each column.
%Initialize the matrix to write as having as many rows as there are
files
%(+1 for headers) and as many columns as there are data points to
write.
%Given x and y centroids for up to three drops in a picture x 2 pics
(12),
%volumes for those three drops (6), velocities (6), and markers to
indicate
%satellite presence (2), satellite number (2), and an error
%flag for too many satellite (2), there should be a minimum of 38
columns
%plus however many more are necessary for the filename.
Output=cell(files+1,31);

%% Column headers
Output(1,:)=   {'File name',...   %Important
    'Main Drop Volume 1',...   %Important
    'Main Drop Volume 2',...   %Important
    'Average Volume',...   %Important
    'Velocity from 1 to 2',...   %Important
    'Satellite Presence in 1',...   %Important
    'Satellite Presence in 2',...   %Important
    'Number of Satellites in 1',...
    'Number of Satellites in 2',...
    'Too many Satellites in 1?',...
    'Too many Satellites in 2?',...
    'Secondary Satellite Average Volume',...   %Important
    'Secondary Satellite Velocity from 1 to 2',...   %Important
    'Tertiary Satellite Average Volume',...   %Important
    'Tertiary Satellite Velocity from 1 to 2',...   %Important
    'Main Drop Centroid 1-x',...
    'Main Drop Centroid 1-y',...
    'Main Drop Centroid 2-x',...
    'Main Drop Centroid 2-y',...
    'Secondary Satellite Volume 1',...
    'Secondary Satellite Volume 2',...
    'Secondary Satellite Centroid 1-x',...
```

```
    'Secondary Satellite Centroid 1-y',...
    'Secondary Satellite Centroid 2-x',...
    'Secondary Satellite Centroid 2-y',...
    'Tertiary Satellite Volume 1',...
    'Tertiary Satellite Volume 2',...
    'Tertiary Satellite Centroid 1-x',...
    'Tertiary Satellite Centroid 1-y',...
    'Tertiary Satellite Centroid 2-x',...
    'Tertiary Satellite Centroid 2-y'};
%Now that the headers have been established, we need to fill the rest
of
%the Output matrix using 'for' loops that will load the data we saved
out
%of the 'while' loop into this matrix under the appropriate heading.
Some
%of these, such as the velocity, will need to be determined at this
%juncture.

%% Row filling
for row=1:files
    %Name the file
    Output(row+1,1)={filename(row)};
    %Determine the Average Volumes and Velocities here:
    Average_volume_main=mean(Volume_main_exit{row});
    Average_volume_second=mean(Volume_second_exit{row});
    Average_volume_third=mean(Volume_third_exit{row});
    %Note, all dual images analyzed by this code had a time
separation of
    %50us.  dt will need to be changed/changeable in the future
should new
    %data be taken with a different dt.
    dt=50e-6;
    Disp_main=sqrt((Centroid_exit{row}(2,1)-
Centroid_exit{row}(1,1))^2+...
        (Centroid_exit{row}(2,2)-Centroid_exit{row}(1,2))^2);
    Velocity_main=Disp_main/dt;
    Disp_second=sqrt((Sat1_Centroid_out_exit{row}(2,1)-...
        Sat1_Centroid_out_exit{row}(1,1))^2+...
        (Sat1_Centroid_out_exit{row}(2,2)...
        -Sat1_Centroid_out_exit{row}(1,2))^2);
    Velocity_second=Disp_second/dt;
    Disp_third=sqrt((Sat2_Centroid_out_exit{row}(2,1)-...
        Sat2_Centroid_out_exit{row}(1,1))^2+...
        (Sat2_Centroid_out_exit{row}(2,2)...
        -Sat2_Centroid_out_exit{row}(1,2))^2);
    Velocity_third=Disp_third/dt;

    %% Start filling out the row
    Output(row+1,1:7)={filename{row}(1,:),...
        Volume_main_exit{row}(1),...
        Volume_main_exit{row}(2),...
        Average_volume_main,...
        Velocity_main,...
```

```
        Satellite_pres_exit{row}(1,:),...
        Satellite_pres_exit{row}(2,:)};

    %% Check satellite presence and for too many satellites
    if isequal(Satellite_pres_exit{row}(1,:),'true ')==1 || ...
            isequal(Satellite_pres_exit{row}(2,:),'true ')==1
        Output(row+1,8:11)={Satellite_num_exit{row}(1),...
            Satellite_num_exit{row}(2),...
            Error_flag_exit{row}(1),...
            Error_flag_exit{row}(2)};
    end

    %% Skip all the data reporting of satellites if too many
    if Error_flag_exit{row}(1)==1 || Error_flag_exit{row}(2)==1
        %% Left blank to leave NaN's in matrix
    elseif Satellite_num_exit{row}(1)==1 &&
Satellite_num_exit{row}(2)==1
        %% One satellite Drop, just assign that satellites values
        Output(row+1,12:13)={Average_volume_second,Velocity_second};
        Output(row+1,20:25)={Volume_second_exit{row}(1),...
            Volume_second_exit{row}(2),...
            Sat1_Centroid_out_exit{row}(1,1),...
            Sat1_Centroid_out_exit{row}(1,2),...
            Sat1_Centroid_out_exit{row}(2,1),...
            Sat1_Centroid_out_exit{row}(2,2)};
    elseif Satellite_num_exit{row}(1)==2 &&
Satellite_num_exit{row}(2)==2
        %% Two satellites, assign all the values

Output(row+1,12:15)={Average_volume_second,Velocity_second,...
            Average_volume_third,Velocity_third};
        Output(row+1,20:31)={Volume_second_exit{row}(1),...
            Volume_second_exit{row}(2),...
            Sat1_Centroid_out_exit{row}(1,1),...
            Sat1_Centroid_out_exit{row}(1,2),...
            Sat1_Centroid_out_exit{row}(2,1),...
            Sat1_Centroid_out_exit{row}(2,2),...
            Volume_third_exit{row}(1),...
            Volume_third_exit{row}(2),...
            Sat2_Centroid_out_exit{row}(1,1),...
            Sat2_Centroid_out_exit{row}(1,2),...
            Sat2_Centroid_out_exit{row}(2,1),...
            Sat2_Centroid_out_exit{row}(2,2)};
    end

    %% Finally, include the main drop centroids in the output.
    Output(row+1,16:19)={Centroid_exit{row}(1,1),...
        Centroid_exit{row}(1,2),...
        Centroid_exit{row}(2,1),...
        Centroid_exit{row}(2,2)};
end

%% "Output" is now ready for exporting into Excel using xls write.
```

```
%Use user prompt at beginning of code for file name to save output
as.
xlswrite('Drop velocities and volumes.xlsx',Output,'Sheet1','B2');

%% End of code

%Notes on useful functions that may be needed for future code work.
%imlincomb  <-Possibly useful for future data analysis.  Linearly
combines
%images with scalings and addition.
%skeletinization might work
%Read on Morphological operations!
%Maybe some gamma adjustment of the image too.
%tabulate produces a frequency table
%bwconncomp will allow cycling through satellites and main drops
%bwarea can be used to measure the area between axis and curve for
each
%disk in a disk integration of the drop profile. :)
```

APPENDIX G

LT Spice IV Software Validation

Validation of the LT Spice IV software package for use with electroacoustics was performed for a simple scenario that could also be calculated by hand. The scenario is a constant pressure supplied to a pipe that has a step decrease in diameter. Given a constant back pressure to the pipes of 5 kPa gage and the pipe geometries shown in Figure G-1, the volume flow rate through the pipes and the pressure at the step change in diameter was calculated by hand. In the hand calculations, the loss coefficient of the contraction was ignored. An equivalent circuit for the system was created in LT Spice IV as well and can be seen in Figure G-2. This circuit was constructed using the same basic principles of conversion to the electroacoustic domain as outlined in Chapter 3.

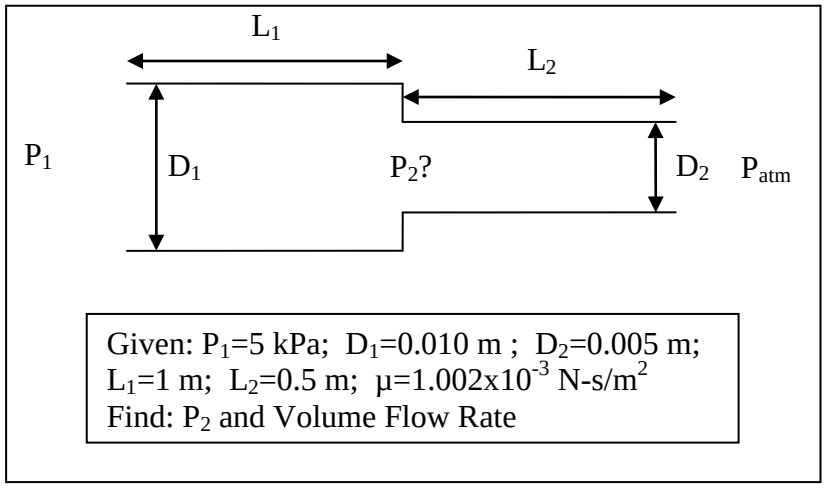

Figure G-1: Software validation test condition

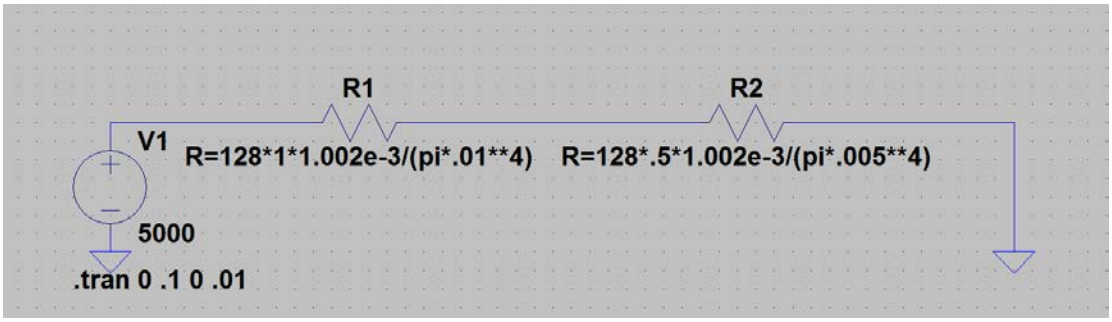

Figure G-2: Equivalent LT Spice IV circuit for the software validation test condition

The hand calculated volume flow rate of 136.1×10^{-6} m^3/s matched the predicted volume flow rate from the LT Spice IV model exactly. Also, the hand-calculated pressure of P_2=4444.4 Pa matched exactly the predicted pressure between the two pipes in the LT Spice IV model. From this simple validation, one can see that the model accurately predicts the pressure drops and volume flow rates of an electroacoustic system.

Note that it was assumed that the loss coefficients for the drop generator were negligible, and as such were not evaluated within the model. Similarly, the validation performed here did not seek to validate the model with the inclusion of loss coefficients for contractions or expansions. This assumption was based off the knowledge that the velocities within the drop generator were going to be small. In order to verify the validity of this assumption, a brief back of the envelope calculation was performed on the worst case scenario from the drop generator. Assuming a loss coefficient of 0.46 for a sudden contraction from one plenum into the aluminum insert, the maximum pressure loss from the contraction was approximated as 200×10^{-3} Pa by using the volume flow rates calculated in the LT Spice IV model. When compared to

the back pressure within the plenum at this same location, this pressure loss due to the contraction is less than 0.1% the magnitude of the back pressure. With such a small influence on the effective pressures within the drop generator, it is safe to assume that the pressure losses from sudden expansions or contractions can be ignored within the model.

APPENDIX H

Acoustic Mass of Meniscus Exploration

In accordance with the suggestions in the discussion and conclusion chapters of this study, a preliminary exploration into the affect of an meniscus acoustic mass on the system was performed. The meniscus acoustic mass was designed to include in the model a new element that represented the volume of fluid between the meniscus membrane and the nozzle exit. The goal of including this new element was to slow the response time of the meniscus to pressure changes. More specifically, the model appears to accurately predict the maximum meniscus displacement, but the time dependent behavior of the meniscus displacement was at too high a frequency to align with the measured real meniscus displacement as a function of time. In short, the model predicted too fast of a rise and too fast a fall of the meniscus displacement with respect to time. It was proposed that this was due to a lack of inertia modeling for the volume of fluid between the meniscus membrane and the nozzle exit.

The model for the meniscus inertia greatly resembled the model for the drop inertia. However, instead of determining the volume of the meniscus through an integral of the volume flow rate with respect to time, the volume of the meniscus was calculated using the geometrical definition of a spherical cap. The radius of curvature of the meniscus and the meniscus displacement have already been included in the model, and as such, it seemed prudent to use these same parameters to determine the volume of the meniscus. Figure H-1 is a screenshot of the new element added to the system to account for this inertia. The figure also show the meniscus element so that one can have a better idea of where in the model this new element was added.

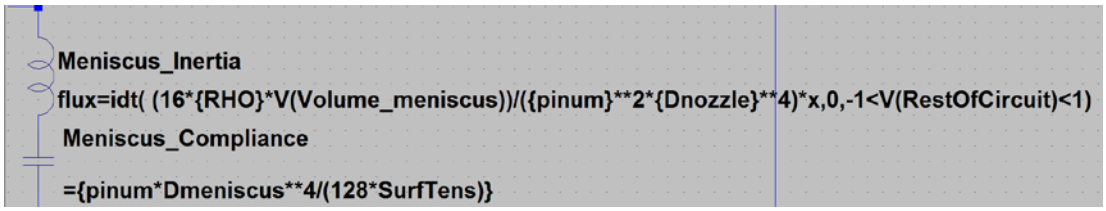

Figure H-1: New LT Spice IV element added to the model in order to model the inertia of the fluid between the meniscus membrane and the nozzle exit.

A number of observations were made from the inclusion of this element. The first observation, which cannot be captured visually, is that the solution time for the transient problem was greatly increased with the inclusion of this new element. This may be due to the new elements dependence on external calculation circuits, i.e. the V(Volume_meniscus) parameter is calculated externally from the element with the same circuit logic that calculated the meniscus height. It may also be due to the added complexity of having an element that is always time dependent on the circuit state, whereas the earlier circuit had mostly time-independent circuit elements, with the droplet element being the obvious exception. Whatever the cause, it is apparent that the new element must introduce a significant change for it to be worthwhile including it in the model.

The second observation pertains to the new model output for meniscus displacement versus time. The goal of including this new element was to improve the model's ability to predict the meniscus displacement versus time and thusly the drop volume. As a standard for comparison, the meniscus displacements versus time from the old and new models were plotted on the same graph. This was simpler than using the drop volume since one run provides a wide range of data over which to compare

the two outputs. The output results are shown in Figure H-2. Note that for these cases, the denominator coefficient for the meniscus displacement of 128 was used in both the old and new models.

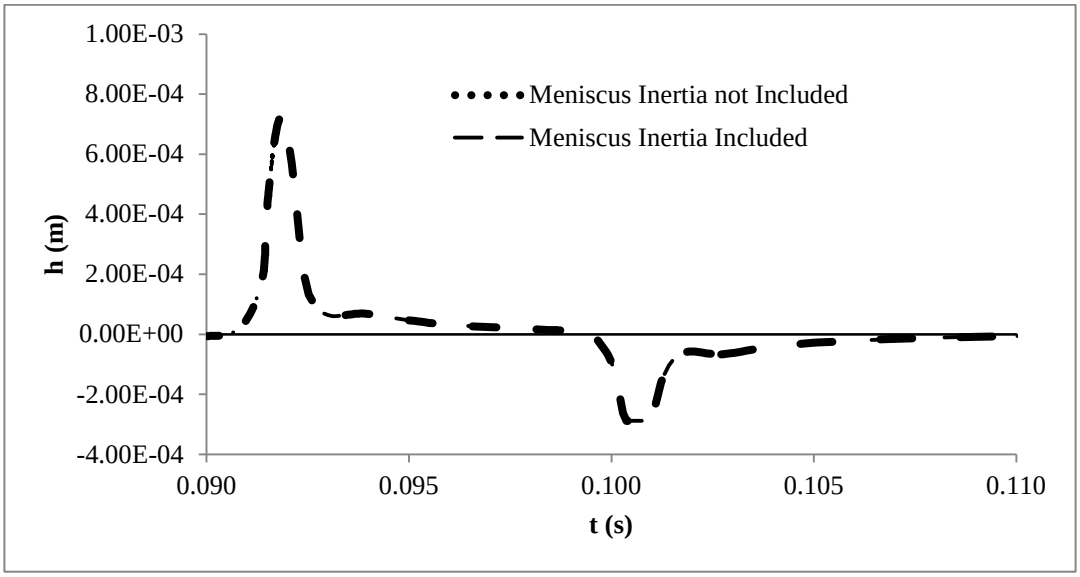

Figure H-2: Meniscus displacement, h, versus time, t, for models with and without the meniscus inertia element.

As can be seen in Figure H-2, the new element had a negligible effect on the behavior of the meniscus displacement. This indicates that although this element was left off initially, the added affect is so small that the element need not be included. Given how largely the new element negatively affected the solution time of the problem with little or no change to the output, it can be concluded that this inertial element is small enough to be ignored and should not be included in the model.

This element was supposed to slow the response time of the meniscus while maintaining its amplitude, but as can be seen in Figure H-2, this element did neither. From this result, it can be concluded that the behavior of the meniscus in the model is

more dependent on a different system element than the inertia of the meniscus. Since the droplet element does not come into play during standard meniscus vibrations, the only remaining source for the discrepancies observed in the meniscus displacement versus time is the modeling of the piezoelectric disk. In this study, the disk displacement was modeled as a current source. This was based on the assumption that the displacement versus time of the piezoelectric disk could be related to a volume flow rate current source in the LT Spice IV model. While this assumption is valid, it fails to capture the fact that the disk remains displaced until it returns to the neutral condition upon the release of the applied voltage.

The affect this could have on the system could result in what is observed in the meniscus displacement versus time. The experimental data indicated a slow decrease in meniscus displacement over time as the meniscus retracted into the nozzle. This slow retraction might be the result of forced back-flow into the refill port due to the pressures within the drop generator. This results from the increased pressure in the system due to decrease in volume from the piezoelectric displacement. However, the model does not capture the physically present disk displacement. The best recommendation to try and resolve this issue would be to model the piezoelectric disk and first plenum in the same way that Gallas et al (2003) modeled their piezoelectric disk. Given that most everything else has been eliminated from the possible sources for this discrepancy, this change will likely resolve the issue.

APPENDIX I

Flow Visualization Images

This appendix serves to document an abridged collection of flow visualization images collected as data for this study. The appendix is formatted in such a way so as to help readers navigate the data more easily. For each set of experimental conditions, the first page for the data set will list the experimental condition under which the following images were taken. The pages following the experimental condition description show the flow visualization images in a time series fashion, from left to right and top to bottom. Below each image will be the time of the exposure for the image. Each exposure time is a measure of the time delay between the image shown and the start of the driving waveform for the test condition. Additional flow visualization images and/or raw data images are available upon request from the author (e-mail: kevin.t.lewis.11@gmail.com) or Dr. James Liburdy (email: liburdy@engr.orst.edu).

Experimental Condition:

Data collection type: Meniscus vibrations

Oscillating Voltage: 11.25 V 0-p; controlling square-wave (see Figure 4.3)

Drop Formation Voltage: N/A

Drop Formation Phase: N/A

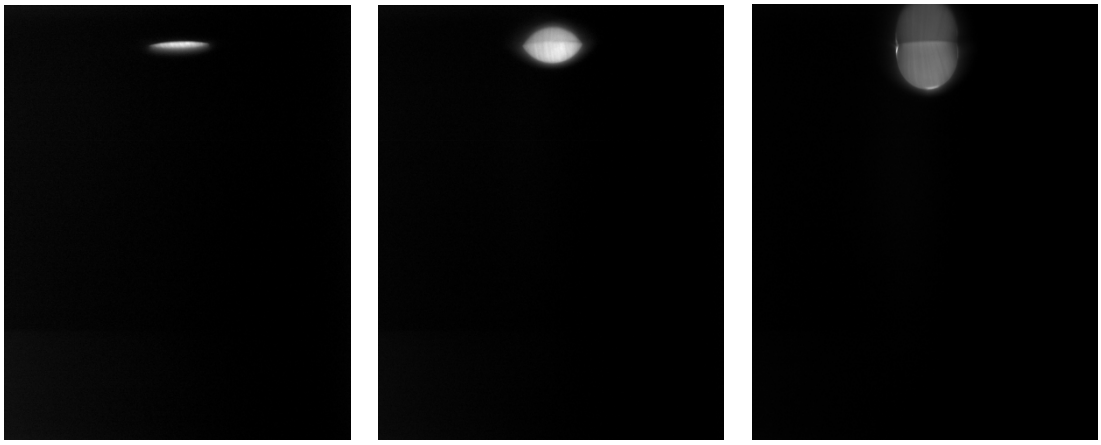

0ms 1ms 2ms

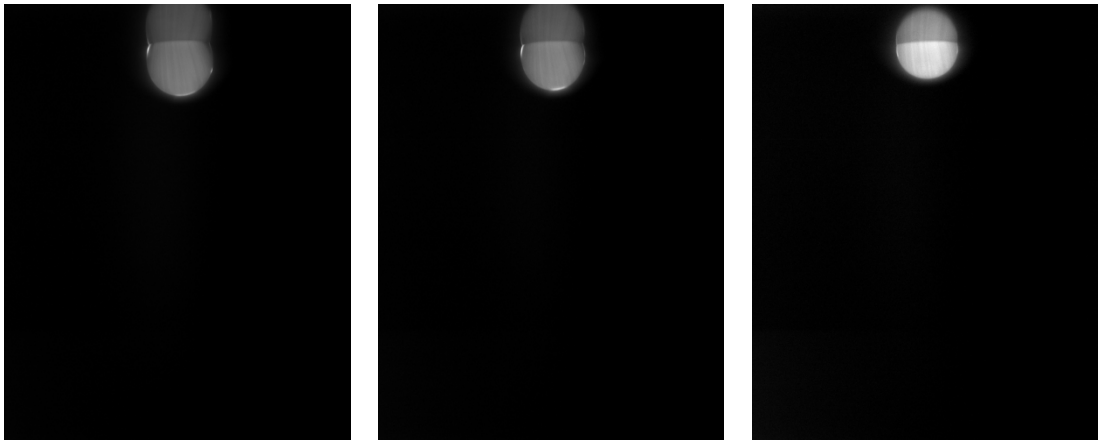

3ms 4ms 5ms

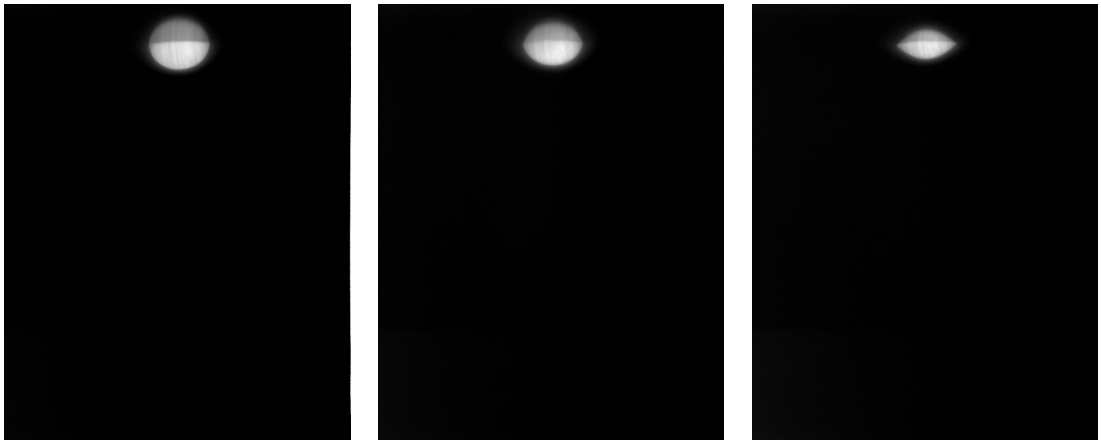

6ms 7ms 8ms

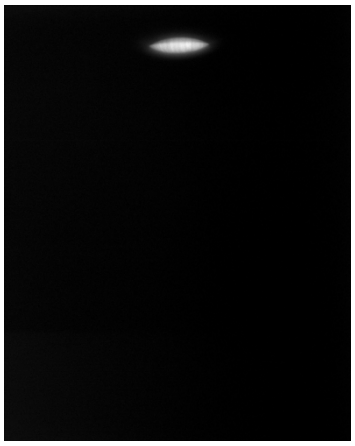

9ms

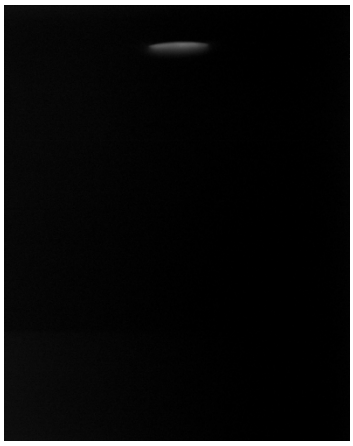

10ms

Experimental Condition(s):

Data collection type: Drop formation

Oscillating Voltage: N/A

Drop Formation Voltage: 22.5 V 0-p (see Figure 4.6)

Drop Formation Phase: N/A

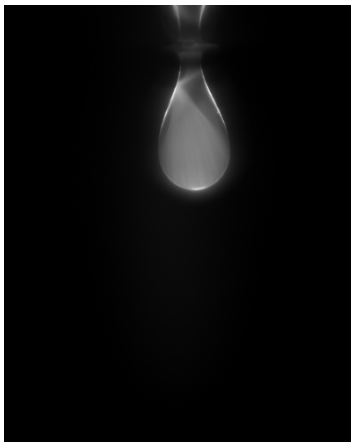
4.00ms

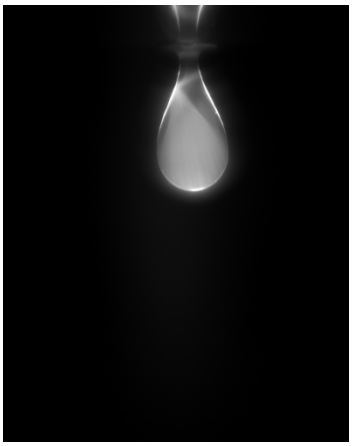
4.05ms

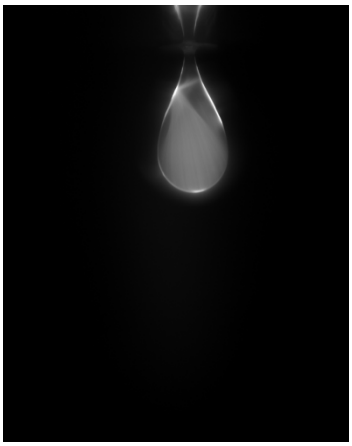
4.30ms


4.35ms

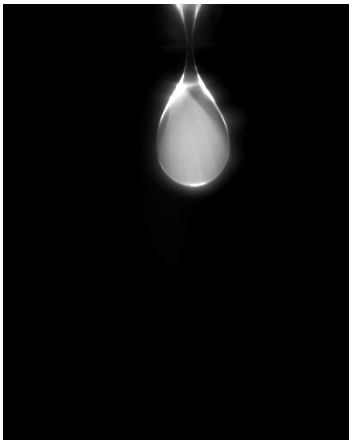
4.40ms


4.41ms

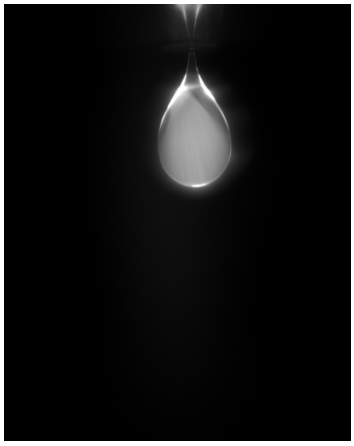
4.45ms


4.46ms

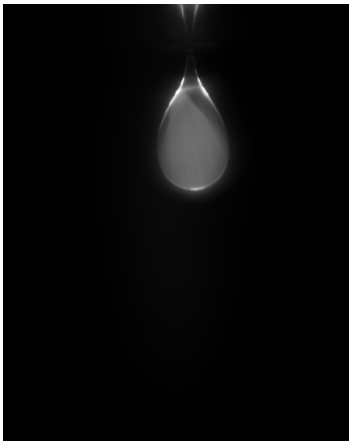
4.47ms


4.50ms


4.52ms


4.55ms

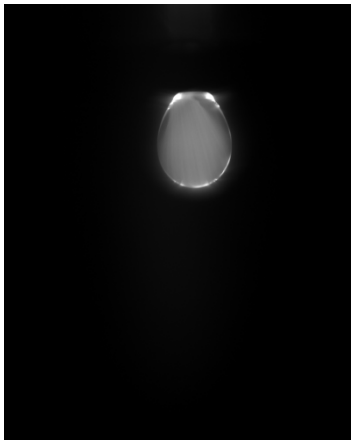
4.67ms

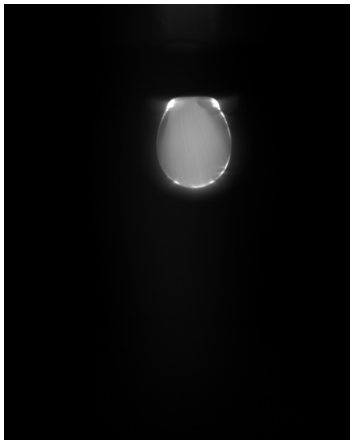
4.72ms

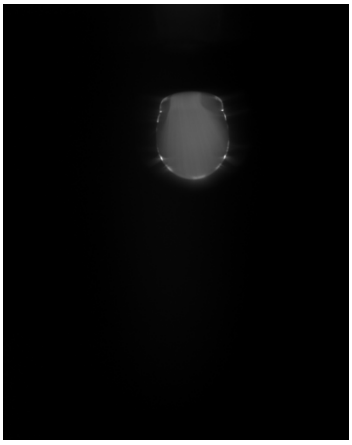
5.00ms

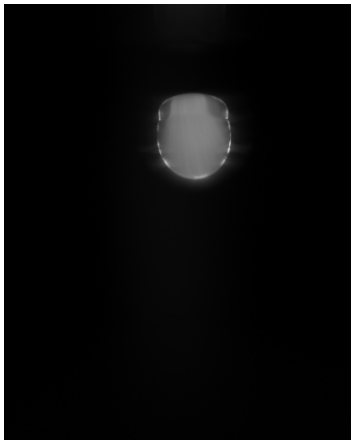
5.05ms

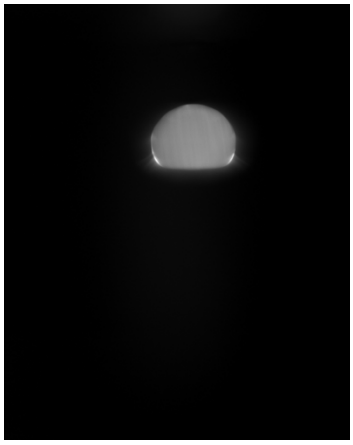
6.00ms

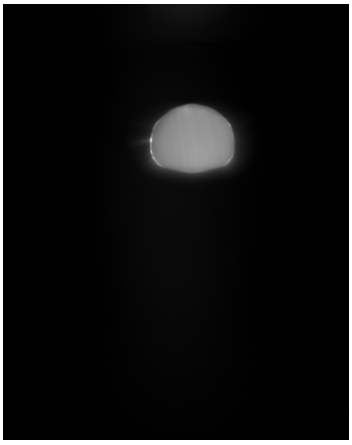
6.05ms

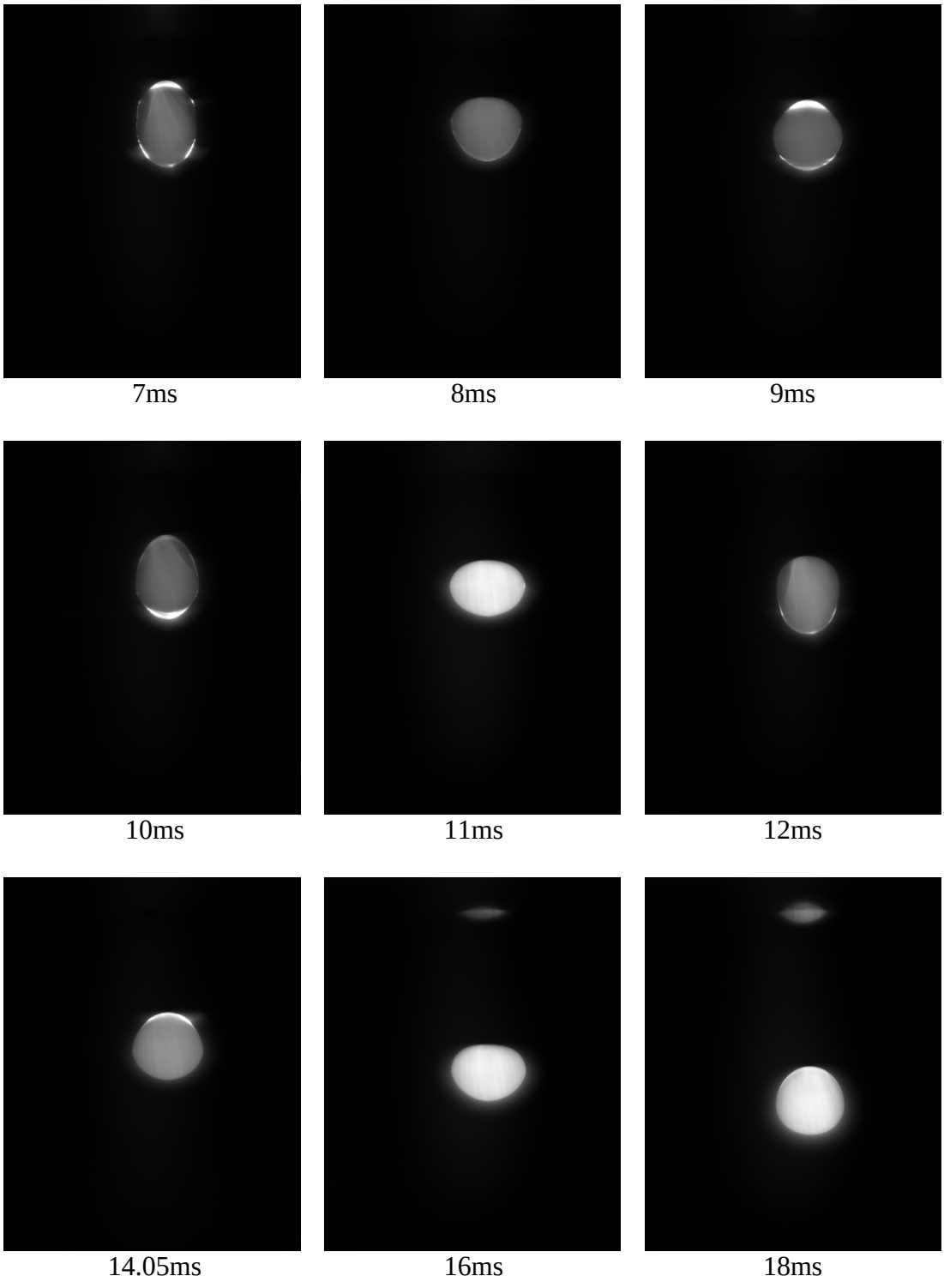

7ms 8ms 9ms

10ms 11ms 12ms

14.05ms 16ms 18ms

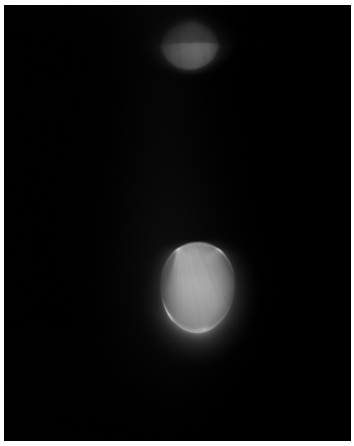

20ms

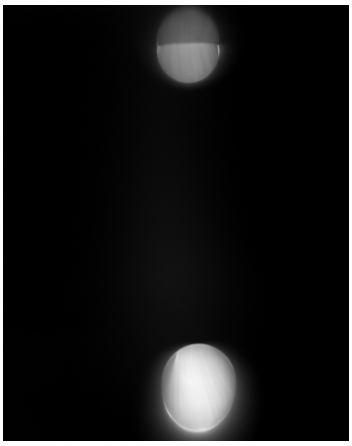

25ms

Experimental Condition(s):

Data collection type: Drop formation with meniscus vibration

Oscillating Voltage: 11.25 V 0-p, square-wave control

Drop Formation Voltage: 22.5 V 0-p

Drop Formation Phase: $2\pi/3$

Combined voltage waveform is shown in Figure 4.11.

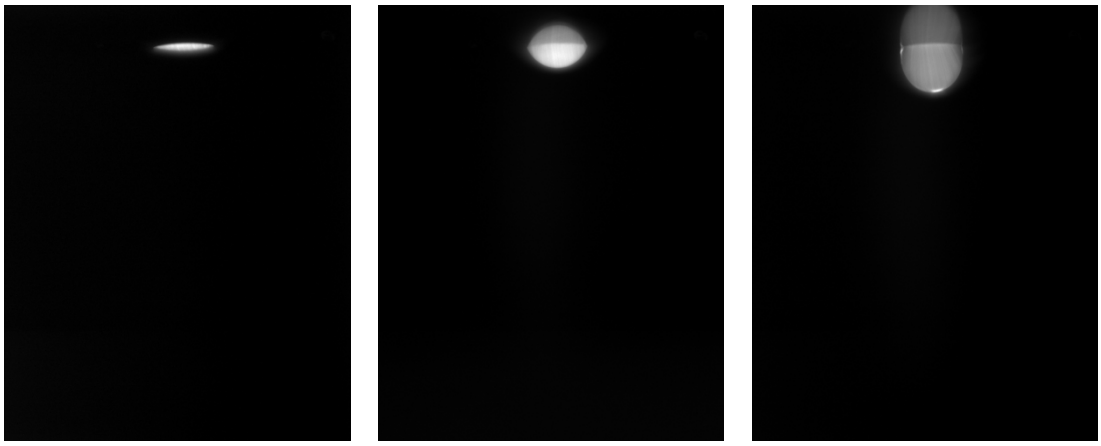

0ms 1ms 2ms

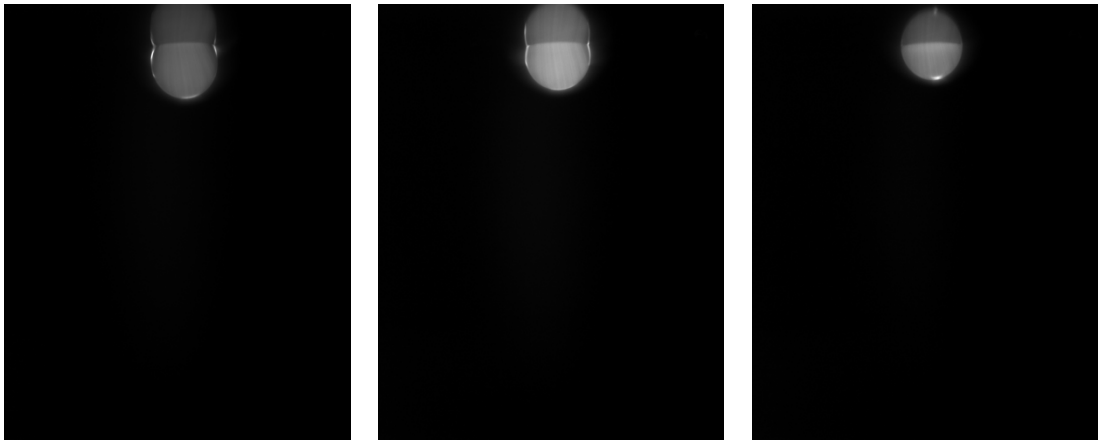

3ms 4ms 5ms

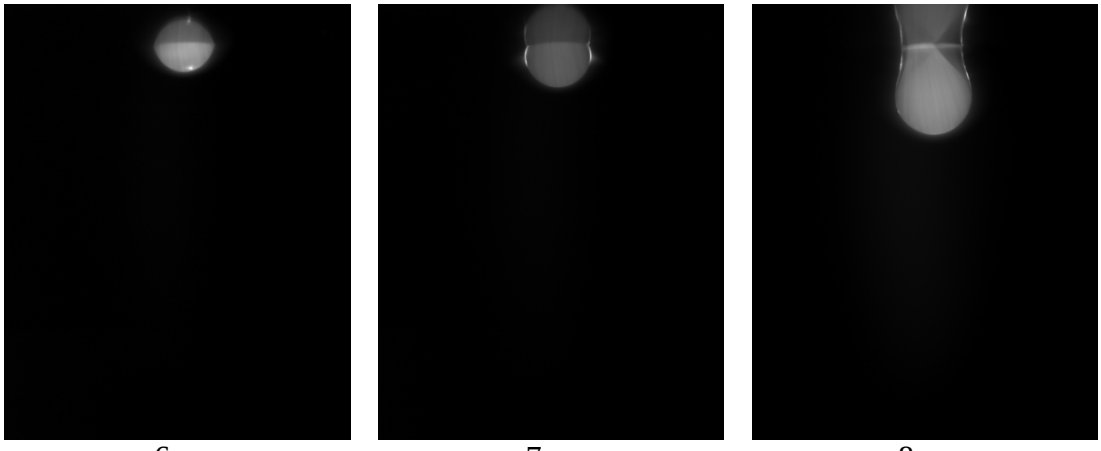

6ms 7ms 8ms

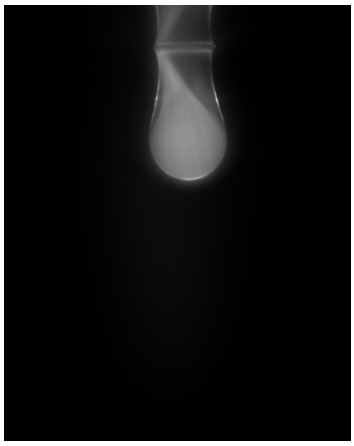
9ms


10ms

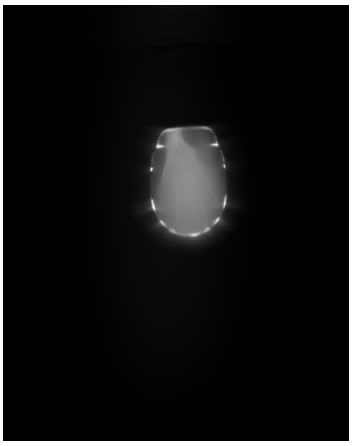
11ms

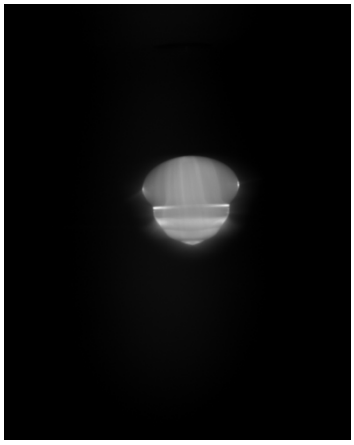
11.5ms

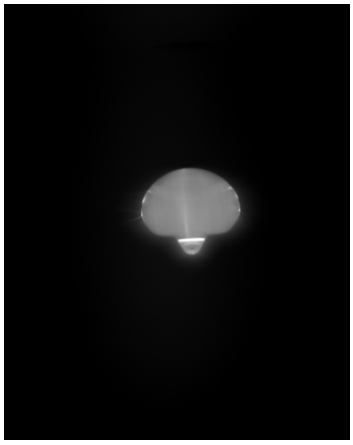
12ms

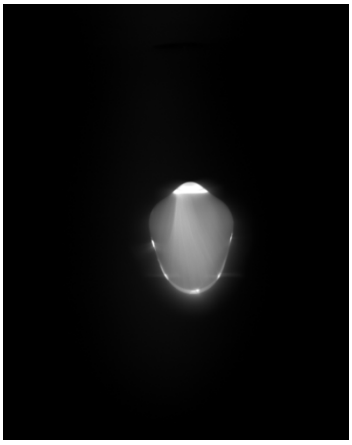
13ms

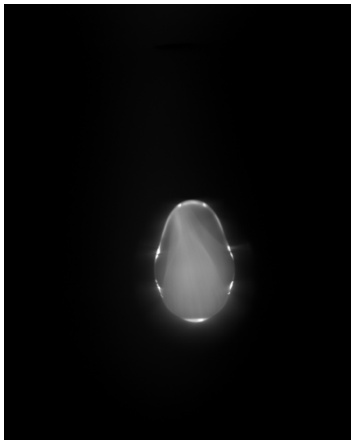
14ms

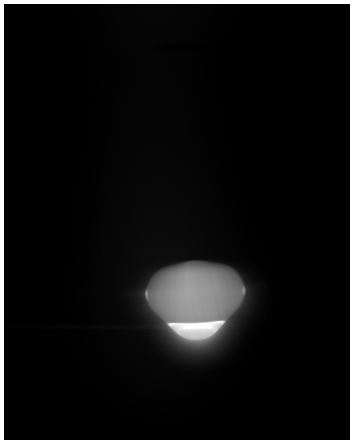
15ms

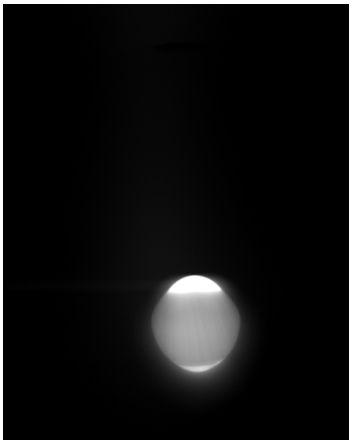
16ms

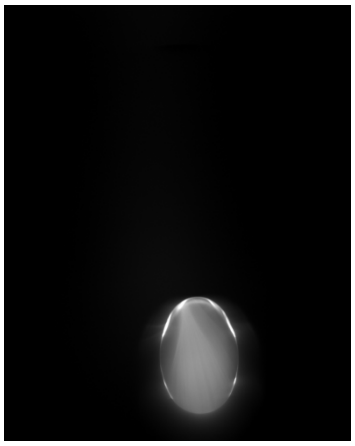

17ms

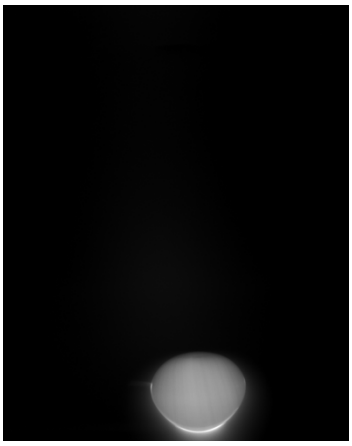

18ms

Experimental Condition(s):

Data collection type: Drop formation with meniscus vibration

Oscillating Voltage: 11.25 V 0-p, square-wave control

Drop Formation Voltage: 33.75 V 0-p

Drop Formation Phase: $2\pi/3$

7ms

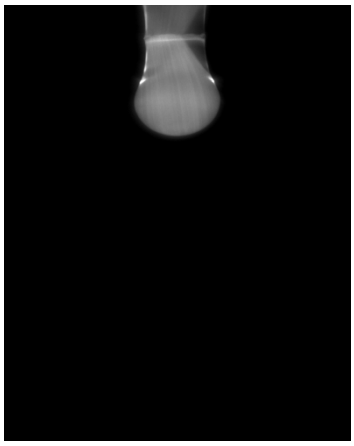

8ms

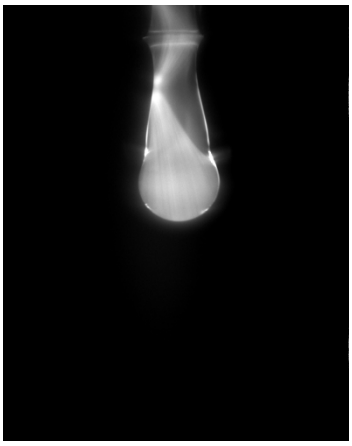

9ms

10ms

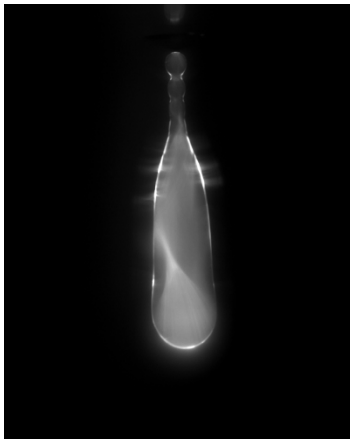

10.5ms

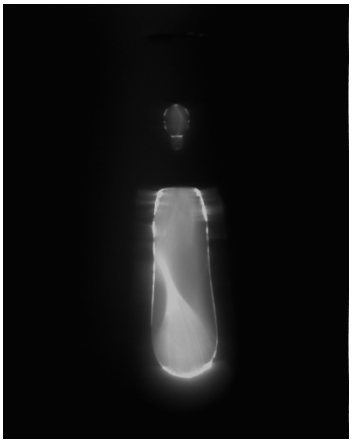

11ms

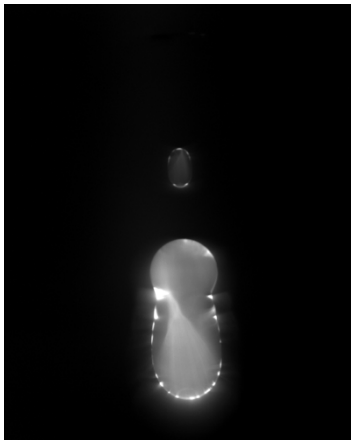

11.5ms

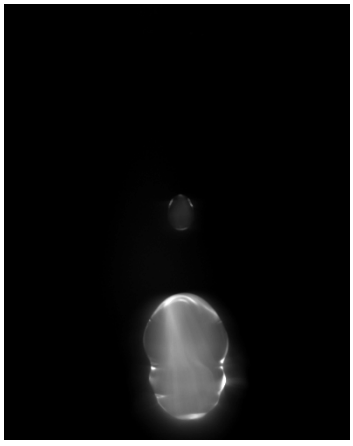

12ms

Experimental Condition(s):

Data collection type: Drop formation with meniscus vibration

Oscillating Voltage: 11.25 V 0-p, square-wave control

Drop Formation Voltage: 33.75 V 0-p

Drop Formation Phase: $4\pi/3$

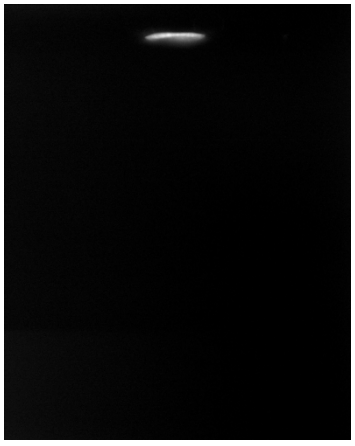

13ms

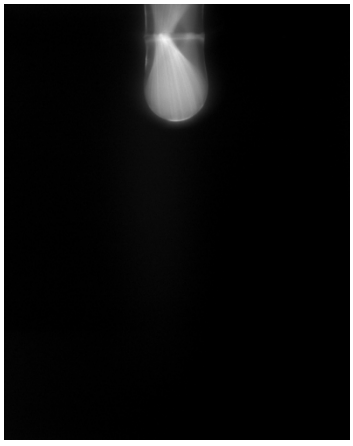

14ms

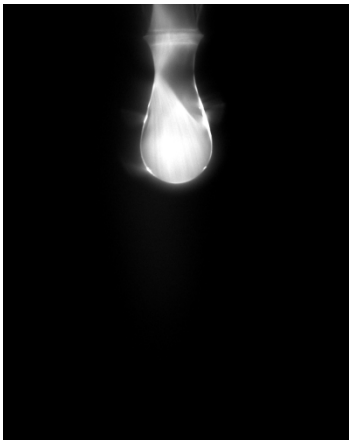

15ms

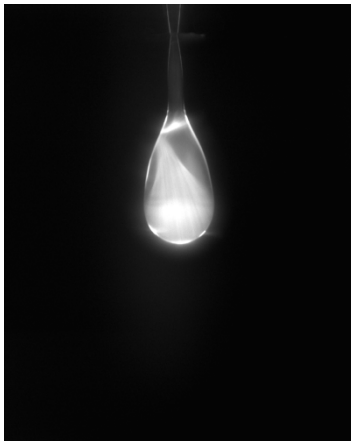

16ms

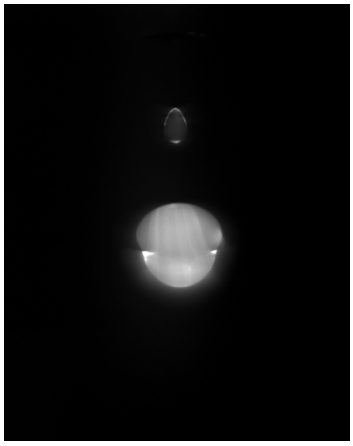

17ms

18ms

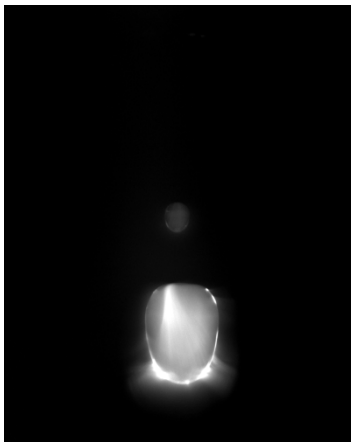

18.5ms

19ms